N°d'ordre NNT : 2022ISAL0077

THESE de DOCTORAT DE L'INSA LYON, membre de l'Université de Lyon

Ecole Doctorale N° EDA162
Mécanique – Energétique – Génie civil - Acoustique

Spécialité/ discipline de doctorat :

Acoustique

Soutenue publiquement le 22/09/2022, par :
Augustin Djibane Pouye

Source Array Optimization for the Synthesis of Random Pressure Fields for the Vibroacoustic Characterization of Structures

---

Devant le jury composé de :

Melon, Manuel	Professeur des Universités, Le Mans Université	Examinateur
De Rosa, Sergio	Professeur des Universités, Frédéric II Naples	Rapporteur
Ciappi, Elena	Docteure, INSEAN Rome	Rapportrice
Karimi, Mahmoud	Docteur, University of Technology Sydney	Examinateur
Maxit, Laurent	Maître de Conférences HDR, INSA Lyon	Directeur de thèse
Maury, Cédric	Professeur des Universités, Centrale Marseille	Co-directeur de thèse

Cette thèse est accessible à l'adresse : https://theses.insa-lyon.fr/publication/2022ISAL0077/these.pdf
© [A.D. Pouye], [2022], INSA Lyon, tous droits réservés

Cette thèse est accessible à l'adresse : https://theses.insa-lyon.fr/publication/2022ISAL0077/these.pdf
© [A.D. Pouye], [2022], INSA Lyon, tous droits réservés

Département FEDORA – INSA Lyon - Ecoles Doctorales

SIGLE	ECOLE DOCTORALE	NOM ET COORDONNEES DU RESPONSABLE
CHIMIE	**CHIMIE DE LYON** **https://www.edchimie-lyon.fr** Sec. : Renée EL MELHEM Bât. Blaise PASCAL, 3e étage secretariat@edchimie-lyon.fr	**M. Stéphane DANIELE** C2P2-CPE LYON-UMR 5265 Bâtiment F308, BP 2077 43 Boulevard du 11 novembre 1918 69616 Villeurbanne **directeur@edchimie-lyon.fr**
E.E.A.	**ÉLECTRONIQUE, ÉLECTROTECHNIQUE, AUTOMATIQUE** **https://edeea.universite-lyon.fr** Sec. : Stéphanie CAUVIN Bâtiment Direction INSA Lyon Tél : 04.72.43.71.70 secretariat.edeea@insa-lyon.fr	**M. Philippe DELACHARTRE** INSA LYON Laboratoire CREATIS Bâtiment Blaise Pascal, 7 avenue Jean Capelle 69621 Villeurbanne CEDEX Tél : 04.72.43.88.63 **philippe.delachartre@insa-lyon.fr**
E2M2	**ÉVOLUTION, ÉCOSYSTÈME, MICROBIOLOGIE, MODÉLISATION** **http://e2m2.universite-lyon.fr** Sec. : Sylvie ROBERJOT Bât. Atrium, UCB Lyon 1 Tél : 04.72.44.83.62 secretariat.e2m2@univ-lyon1.fr	**M. Philippe NORMAND** Université Claude Bernard Lyon 1 UMR 5557 Lab. d'Ecologie Microbienne Bâtiment Mendel 43, boulevard du 11 Novembre 1918 69 622 Villeurbanne CEDEX **philippe.normand@univ-lyon1.fr**
EDISS	**INTERDISCIPLINAIRE SCIENCES-SANTÉ** **http://ediss.universite-lyon.fr** Sec. : Sylvie ROBERJOT Bât. Atrium, UCB Lyon 1 Tél : 04.72.44.83.62 secretariat.ediss@univ-lyon1.fr	**Mme Sylvie RICARD-BLUM** Institut de Chimie et Biochimie Moléculaires et Supramoléculaires (ICBMS) - UMR 5246 CNRS - Université Lyon 1 Bâtiment Raulin - 2ème étage Nord 43 Boulevard du 11 novembre 1918 69622 Villeurbanne Cedex Tél : +33(0)4 72 44 82 32 **sylvie.ricard-blum@univ-lyon1.fr**
INFOMATHS	**INFORMATIQUE ET MATHÉMATIQUES** **http://edinfomaths.universite-lyon.fr** Sec. : Renée EL MELHEM Bât. Blaise PASCAL, 3e étage Tél : 04.72.43.80.46 infomaths@univ-lyon1.fr	**M. Hamamache KHEDDOUCI** Université Claude Bernard Lyon 1 Bât. Nautibus 43, Boulevard du 11 novembre 1918 69 622 Villeurbanne Cedex France Tél : 04.72.44.83.69 **hamamache.kheddouci@univ-lyon1.fr**
Matériaux	**MATÉRIAUX DE LYON** **http://ed34.universite-lyon.fr** Sec. : Yann DE ORDENANA Tél : 04.72.18.62.44 yann.de-ordenana@ec-lyon.fr	**M. Stéphane BENAYOUN** Ecole Centrale de Lyon Laboratoire LTDS 36 avenue Guy de Collongue 69134 Ecully CEDEX Tél : 04.72.18.64.37 **stephane.benayoun@ec-lyon.fr**
MEGA	**MÉCANIQUE, ÉNERGÉTIQUE, GÉNIE CIVIL, ACOUSTIQUE** **http://edmega.universite-lyon.fr** Sec. : Stéphanie CAUVIN Tél : 04.72.43.71.70 Bâtiment Direction INSA Lyon mega@insa-lyon.fr	**M. Jocelyn BONJOUR** INSA Lyon Laboratoire CETHIL Bâtiment Sadi-Carnot 9, rue de la Physique 69621 Villeurbanne CEDEX **jocelyn.bonjour@insa-lyon.fr**
ScSo	**ScSo*** **https://edsciencessociales.universite-lyon.fr** Sec. : Mélina FAVETON INSA : J.Y. TOUSSAINT Tél : 04.78.69.77.79 melina.faveton@univ-lyon2.fr	**M. Christian MONTES** Université Lumière Lyon 2 86 Rue Pasteur 69365 Lyon CEDEX 07 **christian.montes@univ-lyon2.fr**

*ScSo : Histoire, Géographie, Aménagement, Urbanisme, Archéologie, Science politique, Sociologie, Anthropologie

Cette thèse est accessible à l'adresse : https://theses.insa-lyon.fr/publication/2022ISAL0077/these.pdf
© [A.D. Pouye], [2022], INSA Lyon, tous droits réservés

Cette thèse est accessible à l'adresse : https://theses.insa-lyon.fr/publication/2022ISAL0077/these.pdf
© [A.D. Pouye], [2022], INSA Lyon, tous droits réservés

ABSTRACT

The reproduction of the vibration and acoustic responses of structures under random excitation such as the Diffuse Acoustic Field (DAF) or the Turbulent Boundary Layer (TBL) is of particular interest to researchers and the transportation industry (automobile, aeronautics, etc.). In practice, the characterization of structures under random excitations requires making *in-situ* measurements or using test facilities such as anechoic wind tunnels or the reverberant rooms, which are complex and costly methods. Based on the previous considerations, the necessity of finding simple, cost-efficient and reproducible alternative methods, becomes obvious. In this thesis, an alternative method called the Source Scanning Technique (SST) is presented. This solution is part of the methods that employ acoustic source arrays. However, SST is based on the use of a single monopole source along with the synthetic array principle: the monopole source is spatially displaced to an arbitrary number of different positions following a predefined spatial step, thereby creating a virtual array of monopole sources, overcoming limitations due to the source array density, the upper frequency range of the synthesis and the geometry of the test structure.

The first objective is to assess the validity of the proposed technique by comparing its results with numerical and experimental ones for simple structures such as Flat Rectangular Panels (FRPs). An academic case study consisting of a baffled and simply supported aluminum panel under diffuse acoustic field and turbulent boundary layer excitations is considered. After conducting parametric studies in order to define the optimal design parameters of the virtual array of monopoles, an experimental implementation of SST on FRPs is done. The experimental vibration response of the panel as well as the transmission loss using the proposed process are compared to results from random vibration theory on one hand. On the other hand, the same experimental results

Cette thèse est accessible à l'adresse : https://theses.insa-lyon.fr/publication/2022ISAL0077/these.pdf
© [A.D. Pouye], [2022], INSA Lyon, tous droits réservés

obtained using the SST are compared with results obtained with measurements in a reverberant room (DAF) and an anechoic wind tunnel (TBL). These comparisons show good agreement that validate SST for the considered panel.
In a second step, the goal is to extend SST to more complex structures such as Curved Rectangular Panels (CRPs). Although the principle of SST remains the same for these types of structures, one needs to determine the closed-form transfer functions between one source position and a point on the structure which are not as simple as the ones for FRPs. The closed-form solutions are determined for the two-dimensional case and the three-dimensional case and numerically validated using the Boundary Element Method (BEM). Afterwards, parametric studies similar to the ones conducted in the case of FRPs are done in order to investigate the optimal design parameters of the array of monopoles. Two monopole array – structure geometric configurations are studied: conformal configuration (monopole array with the same geometry as the test structure) and non-conformal (monopole array with a different geometry from the test structure). After defining an experimental setup for the application of SST on CRPs, the transfer functions are experimentally validated by comparing the measurements to the analytical solutions. The comparison shows very good agreement between both types of results. An experimental implementation of the source scanning technique is done for the two-dimensional case and the satisfying comparison between the target pressure fields and the synthesized ones show good promising applications of SST for convex curved structures.

RÉSUMÉ EN FRANÇAIS

La reproduction des réponses vibratoires et acoustiques de structures sous excitations aléatoires telles que le champ acoustique diffus ou la couche limite Turbulente intéresse particulièrement le monde de la recherche et l'industrie des transports (automobile, aéronautique. . .). En pratique, la caractérisation de structures sous excitations aléatoires

Cette thèse est accessible à l'adresse : https://theses.insa-lyon.fr/publication/2022ISAL0077/these.pdf
© [A.D. Pouye], [2022], INSA Lyon, tous droits réservés

nécessite de réaliser des mesures *in-situ* ou d'utiliser des moyens d'essais tels que les souffleries anéchoïques ou les salles réverbérantes, qui sont des méthodes complexes et coûteuses. Sur la base des considérations précédentes, la nécessité de trouver des méthodes alternatives simples, rentables et reproductibles, devient évidente. Dans cette thèse, une méthode alternative appelée la méthode de balayage de source ou *Source Scanning Technique* (en anglais) est présentée. Cette solution fait partie des procédés utilisant des réseaux de sources acoustiques. Cependant, contrairement aux autres techniques, la méthode de balayage de source est basée sur l'utilisation d'une seule source monopolaire en appliquant le principe du réseau synthétique : la source monopolaire est déplacée dans l'espace vers un nombre arbitraire de positions différentes suivant un pas spatial prédéfini, créant ainsi un réseau virtuel de sources, s'affranchissant des limitations dues à la densité du réseau de sources, à la gamme de fréquences supérieures de la synthèse et à la géométrie de la structure de test.

Le premier objectif est d'évaluer la validité de la technique proposée en comparant ses résultats avec des résultats numériques et expérimentaux pour des structures simples telles que les panneaux plans. Une étude de cas consistant en un panneau plan en aluminium en appuis simples et soumis à une excitation de types champ acoustique diffus et couche limite turbulente est considérée. Après avoir mené des études paramétriques afin de définir les paramètres de conception optimaux du réseau virtuel de monopoles, une implémentation expérimentale de la méthode de balayage de source sur le panneau plan en aluminium est réalisée. La réponse expérimentale aux vibrations du panneau ainsi que la perte en transmission sont comparées aux résultats de la théorie des vibrations aléatoires d'une part. D'autre part, ces mêmes résultats expérimentaux obtenus avec la méthode de balayage de source sont comparés aux résultats obtenus avec des mesures directes en salle réverbérante (champ acoustique diffus) et en soufflerie anéchoïque (couche limite turbulente). Ces comparaisons montrent un bon accord qui valide la méthode de balayage de source pour le panneau considéré.

Dans un second temps, le but est d'étendre la méthode de balayage de source à des structures plus complexes telles que les panneaux courbes. Bien que le principe de la méthode

Cette thèse est accessible à l'adresse : https://theses.insa-lyon.fr/publication/2022ISAL0077/these.pdf
© [A.D. Pouye], [2022], INSA Lyon, tous droits réservés

reste le même pour ces types de structures, il faut déterminer les fonctions de transfert analytiques entre une position source et un point d'un panneau courbe qui ne sont pas aussi simples que celles des panneaux plans. Les solutions analytiques sont déterminées pour le cas bidimensionnel et le cas tridimensionnel et validées numériquement à l'aide de la méthode des éléments de frontière. Ensuite, des études paramétriques similaires à celles menées dans le cas des panneaux plans sont réalisées afin de déterminer les paramètres de conception optimaux du réseau de monopoles. Deux configurations géométriques réseau monopolaire – structure sont étudiées : configuration conforme (réseau monopolaire avec la même géométrie que la structure test) et non conforme (réseau monopolaire avec une géométrie différente de la structure test). Après avoir défini un montage expérimental pour l'application de l'approche proposée à des panneaux courbes, les fonctions de transfert sont validées expérimentalement en comparant les mesures aux solutions analytiques. La comparaison montre un très bon accord entre les deux types de résultats. Une implémentation expérimentale de la technique de balayage de source est faite pour le cas bidimensionnel et la comparaison satisfaisante entre les champs de pression cibles et ceux synthétisés montre des applications prometteuses de la méthode de balayage de source pour les structures courbes convexes.

Cette thèse est accessible à l'adresse : https://theses.insa-lyon.fr/publication/2022ISAL0077/these.pdf
© [A.D. Pouye], [2022], INSA Lyon, tous droits réservés

CONTENTS

ABSTRACT v

RÉSUMÉ EN FRANÇAIS vi

CONTENTS ix

LIST OF FIGURES xiii

LIST OF TABLES xxvii

ACRONYMS xxvii

INTRODUCTION

I BACKGROUND AND PRESENTATION OF THE SOURCE SCANNING TECHNIQUE PROCESS

1 LITERATURE REVIEW 7

1.1 The excitation fields 8

1.1.1 Characterization of spatially correlated random pressure field . . 8

1.1.2 Diffuse acoustic field 10

1.1.3 Turbulent boundary layer 12

1.2 Standard test means 22

1.2.1 Diffuse acoustic field 22

1.2.2 Turbulent boundary layer 23

1.3 Alternative approaches to standard test means 25

1.3.1 Reciprocity method 25

1.3.2 Wave Field Synthesis 26

1.3.3 Planar Near-field Acoustical Holography 27

1.3.4 Least Squares Technique 28

Cette thèse est accessible à l'adresse : https://theses.insa-lyon.fr/publication/2022ISAL0077/these.pdf
© [A.D. Pouye], [2022], INSA Lyon, tous droits réservés

1.3.5 Source Scanning Technique 29
1.4 Objectives of this thesis 30
1.5 Dissertation outline 30
2 SOURCE SCANNING TECHNIQUE 33
2.1 Synthetic array principle 33
2.2 Wavenumber formulation and quantities of interest 35
2.3 Wall-pressure plane waves 39
2.3.1 Definition 39
2.3.2 Uncorrelated WPPWs and TBL excitation 40
2.3.3 Generating WPPWs 41
2.4 Description of the SST approach 42
2.5 Summary 47
II APPLICATION ON FLAT RECTANGULAR PANELS
3 SST ON FLAT RECTANGULAR PANELS: THEORY AND NUMERICAL STUDIES 51
3.1 Problem statement 51
3.2 Theoretical responses 53
3.2.1 Vibration response - Sensitivity functions 53
3.2.2 Transmission loss 53
3.3 SST on flat rectangular panels: parametric studies 54
3.3.1 Cutoff wavenumber and wavenumber resolution 55
3.3.2 Interplanar distance 56
3.4 Summary 62
4 SST ON PANELS: EXPERIMENTS 63
4.1 Experimental implementation 64
4.1.1 Measurement devices 64
4.1.2 Experimental setup 65
4.2 Results and discussion 72
4.2.1 Numerical validation 72

Cette thèse est accessible à l'adresse : https://theses.insa-lyon.fr/publication/2022ISAL0077/these.pdf
© [A.D. Pouye], [2022], INSA Lyon, tous droits réservés

4.2.2 Validation with direct measurements in standard test facilities . . 76
4.3 Summary 77

III EXTENSION TO CURVED RECTANGULAR PANELS

5 SST ON CURVED RECTANGULAR PANELS: THEORY AND NUMERICAL STUDIES 81
5.1 Scattering by a rigid and curved rectangular panel: transfer functions . . 82
5.1.1 Two-dimensional case 83
5.1.2 Three-dimensional case 87
5.1.3 Validation of the solutions 91
5.2 SST on curved rectangular panels: parametric studies 94
5.2.1 Two-dimensional case 94
5.2.2 Three-dimensional case 111
5.3 Summary 124
6 SST ON CURVED RECTANGULAR PANELS: EXPERIMENTS 125
6.1 Experimental implementation 126
6.1.1 Measurement devices 126
6.1.2 Experimental setup 128
6.2 Results and discussion 134
6.2.1 Two dimensional case: validation of the transfer functions and experimental SST 134
6.2.2 Three dimensional case: validation of the transfer functions 139
6.3 Summary 141

CONCLUSION

APPENDICES

A VELOCITY SENSITIVITY FUNCTIONS 151
B RADIATED POWER BY A PANEL 153
C INVARIANCE PRINCIPLE 157

Cette thèse est accessible à l'adresse : https://theses.insa-lyon.fr/publication/2022ISAL0077/these.pdf
© [A.D. Pouye], [2022], INSA Lyon, tous droits réservés

D VALIDATION OF THE TRANSFER FUNCTIONS FOR CURVED PANELS 159
D.1 Two dimensional case . . . 159
D.1.1 Convergence of the harmonic expansion . . . 159
D.1.2 Comparison with OpenBEM . . . 167
D.2 Three dimensional case . . . 171
D.2.1 Integration domain . . . 171
D.2.2 Validation with OpenBEM . . . 175
E RÉSUMÉ ÉTENDU EN FRANÇAIS 181
E.1 Contexte de la thèse . . . 181
E.2 Technique de balayage de source . . . 183
E.3 Application à des panneaux plans . . . 186
E.4 Extension à des panneaux courbes . . . 188
E.5 Conclusions générales . . . 189

BIBLIOGRAPHY

Cette thèse est accessible à l'adresse : https://theses.insa-lyon.fr/publication/2022ISAL0077/these.pdf
© [A.D. Pouye], [2022], INSA Lyon, tous droits réservés

LIST OF FIGURES

Figure 1.1 DAF description 11
Figure 1.2 TBL description 14
Figure 1.3 Schematic of the characteristic regions of a wavenumber-frequency spectrum at a constant frequency 18
Figure 2.1 Difference between (a) an actual array of monopoles and (b) a synthetic array using only one mobile monopole. 34
Figure 2.2 Structure under random pressure field where p_b represents the blocked pressure at the surface Σ_s. 36
Figure 2.3 Description of the transfer function $G_{ps}(\omega)$ 43
Figure 2.4 Description of the velocity FRF $\Gamma_v^s(\mathbf{x}, \omega)$ 45
Figure 2.5 Description of the distance d between the structure and the synthetic monopole array and that of the distance d_m between two adjacent monopole positions in the x and y directions. 46
Figure 3.1 Simply supported panel subject to an excitation p_b. 52
Figure 3.2 Optimal interplanar distance: (a) logarithm of the condition number ($\log_{10}(\kappa)$) of the transfer matrix, (b) reproduction error e_p (dB, ref. 1) on the reconstructed pressure field according to Eq. (3.6) for $k_x = k_{max}$ and $k_y = 0$. Both quantities are plotted as functions of frequency and the interplanar distance normalized by the smallest wavelength to be synthesized. 58

Cette thèse est accessible à l'adresse : https://theses.insa-lyon.fr/publication/2022ISAL0077/these.pdf
© [A.D. Pouye], [2022], INSA Lyon, tous droits réservés

Figure 3.3 Reproduction error e_p (dB, ref. 1) in the wavenumber-frequency domain for two different interplanar distances. (a) along k_x, $k_y = 0$ and (b) along k_y, $k_x = 0$ for $d = \frac{\lambda_{min}}{10}$. (c) along k_x, $k_y = 0$ and (d) along k_y, $k_x = 0$ for $d = \frac{\lambda_{min}}{4}$. 59

Figure 3.4 Reproduction error e_p (dB, ref. 1) in the wavenumber domain at (a) $f = 200\,\text{Hz}$, (b) $f = 500\,\text{Hz}$, (c) $f = 1000\,\text{Hz}$ and (d) $f = 2000\,\text{Hz}$ for $d = \frac{\lambda_{min}}{4}$. 60

Figure 3.5 Pressure fields (Pa) in the spatial domain at a frequency $f = 2000\,\text{Hz}$ for the plane wave defined by $\left(k_x = 50, k_y = 50\right)\,\text{rad}\,\text{m}^{-1}$: (a) target, (b) reconstructed for $d = \frac{\lambda_{min}}{10}$ and (c) reconstructed for $d = \frac{\lambda_{min}}{4}$. 61

Figure 4.1 Microflown mid-high frequency volume velocity source. (1) high impedance loudspeaker, (2) flexible hose and (3) nozzle with sensor. 65

Figure 4.2 Roga RG-50 1/4" ICP microphone. 66

Figure 4.3 Bruel & Kjær accelerometer. 66

Figure 4.4 Baffled simply supported panel setup for the SST process. (1) aluminum panel, (2) nozzle component of the monopole source mounted on the $3D$ Cartesian robot, (3) 5 cm thick plywood baffle and (4) sound absorbing foam. 68

Figure 4.5 Measurement of the transfer functions G_{ps}: experimental setup. (1) $3D$ Cartesian robot, (2) linear array of 20 microphones, (3) front view of the flush mounted microphones and (4) back view of the flush mounted microphones. 69

Figure 4.6 Measurement of the particle velocity with the two microphone method, S_1 and S_2 are discretized surfaces consisting of two identical grids of R points. 70

Figure 4.7 Particle velocity measurements: experimental setup. (1) linear array of microphones mounted on the $2D$ Cartesian robot and (2) $2D$ Cartesian robot. 71

Cette thèse est accessible à l'adresse : https://theses.insa-lyon.fr/publication/2022ISAL0077/these.pdf
© [A.D. Pouye], [2022], INSA Lyon, tous droits réservés

Figure 4.8 Velocity sensitivity functions $\left|H_v\left(\mathbf{x}, k_x, k_y = 0, \omega\right)\right|^2$ (dB, ref. $1\,\mathrm{m^3\,s^{-1}\,Pa^{-1}}$): (a) numerical and (b) SST. Continuous white line: acoustic wavenumber k_0. Dashed white line: panel flexural wavenumber k_f. 72

Figure 4.9 Velocity ASD function $S_{vv}(\mathbf{x}, \omega)$ (dB, ref. $1\,\mathrm{m^2\,s^{-2}\,Hz^{-1}}$) of the panel subjected to a DAF excitation: numerical (thin black line), SST (thick gray line). 73

Figure 4.10 Velocity ASD function $S_{vv}(\mathbf{x}, \omega)$ (dB, ref. $1\,\mathrm{m^2\,s^{-2}\,Hz^{-1}}$) of the panel subjected to a TBL excitation: numerical (thin black line), SST (thick gray line). 74

Figure 4.11 Transmission loss $\mathrm{TL}(\omega)$ (dB, ref. 1) of the panel under DAF excitation: numerical (thin black line), SST (thick gray line). 75

Figure 4.12 Transmission loss $\mathrm{TL}(\omega)$ (dB, ref. 1) of the panel under TBL excitation: numerical (thin black line), SST (thick gray line). 75

Figure 4.13 Velocity ASD function $S_{vv}(\mathbf{x}, \omega)$ (dB, ref. $1\,\mathrm{m^2\,s^{-2}\,Hz^{-1}}$) of the panel subjected to a DAF excitation: reverberant chamber measurements at the University of Sherbrooke [57] (thin black line), SST (thick gray line). 76

Figure 4.14 Velocity ASD function $S_{vv}(\mathbf{x}, \omega)$ (dB, ref. $1\,\mathrm{m^2\,s^{-2}\,Hz^{-1}}$) of the panel subjected to a TBL excitation: wind tunnel measurements at the University of Sherbrooke [58] (thin black line), SST (thick gray line). 77

Figure 5.1 Problem geometry and parameters. 82

Figure 5.2 Problem geometry and parameters: section view of the $3D$ case. The z-axis is outgoing. 88

Cette thèse est accessible à l'adresse : https://theses.insa-lyon.fr/publication/2022ISAL0077/these.pdf
© [A.D. Pouye], [2022], INSA Lyon, tous droits réservés

Figure 5.3 Comparison between the amplitudes and phases of the wall-pressure obtained with OpenBEM (gray continuous line) and those obtained using the developed analytical solution in Eq. (5.16) (dash-dotted black line) for one position of the monopole source $\left(r_0 = 1\,\text{m}, \theta_0 = \frac{\pi}{4}\right)$ at a frequency $f = 1000\,\text{Hz}$: two-dimensional case. (a) amplitudes (b) phases. 92

Figure 5.4 Comparison between the magnitudes and phases of the wall-pressure obtained with OpenBEM (gray continuous line) and those obtained using the developed analytical solution in Eq. (5.30) (dash-dotted black line) for one position of the monopole source $\left(r_0 = 0.6\,\text{m}, \theta_0 = \frac{\pi}{4}, z_0 = 0.5\,\text{m}\right)$ and at a frequency $f = 2000\,\text{Hz}$: three-dimensional case. The distance along the z-axis between the plane of the monopole source and that of the observation points is $|z - z_0| = 0.3\,\text{m}$. 93

Figure 5.5 Section view of the SST setup for CRPs. 95

Figure 5.6 Reproduction error in the frequency-wavenumber domain: (a) $n_s = 1$, (b) $n_s = 2$, (c) $n_s = 3$ and (d) $n_s = 4$. 97

Figure 5.7 Real part of the target pressure field (continuous grey line) and the reconstructed pressure (dashed black line) of the WPPW defined by the wavevector $(-50, 50)\,\text{rad}\,\text{m}^{-1}$ at a frequency $f = 2000\,\text{Hz}$: (a) $n_s = 1$, (b) $n_s = 2$, (c) $n_s = 3$ and (d) $n_s = 4$. 98

Figure 5.8 Imaginary part of the target pressure field (continuous grey line) and the reconstructed pressure (dashed black line) of the WPPW defined by the wavevector $(-50, 50)\,\text{rad}\,\text{m}^{-1}$ at a frequency $f = 2000\,\text{Hz}$: (a) $n_s = 1$, (b) $n_s = 2$, (c) $n_s = 3$ and (d) $n_s = 4$. 99

Cette thèse est accessible à l'adresse : https://theses.insa-lyon.fr/publication/2022ISAL0077/these.pdf
© [A.D. Pouye], [2022], INSA Lyon, tous droits réservés

Figure 5.9 Parametric studies for $h = 5$ cm: (a) real part and (b) imaginary part of the target pressure (continuous grey line) and reconstructed pressure (dashed black line) of the WPPW defined by the wavevector $(-50, 50)$ rad m^{-1} at a frequency $f = 2000$ Hz and (c) reproduction error. 101

Figure 5.10 Condition number ($\log_{10}(\kappa)$) of the transfer matrix $\mathbf{G}$ for three different radial heights: (a) $h = 5$ cm, (b) $h = 10$ cm and (c) $h = 20$ cm. 102

Figure 5.11 Parametric studies for an added normally distributed noise which values vary between 0 and 0.01. Reproduction errors in the frequency-wavenumber domain for (a) $h = 5$ cm, (b) $h = 10$ cm and (c) $h = 20$ cm. 103

Figure 5.12 Parametric studies for an added normally distributed noise which values vary between 0 and 0.01. Real part of the target pressure (continuous grey line) and reconstructed pressure (dashed black line) for (a) $h = 5$ cm, (b) $h = 10$ cm and (c) $h = 20$ cm. The WPPW is defined by the wavevector $(-50, 50)$ rad m^{-1} at a frequency $f = 2000$ Hz. 104

Figure 5.13 Parametric studies for an added normally distributed noise which values vary between 0 and 0.01. Imaginary part of the the target pressure (continuous grey line) and reconstructed pressure (dashed black line) for (a) $h = 5$ cm, (b) $h = 10$ cm and (c) $h = 20$ cm. The WPPW is defined by the wavevector $(-50, 50)$ rad m^{-1} at a frequency $f = 2000$ Hz. 105

Figure 5.14 Section view of the non conformal SST geometry setup for CRPs. . 106

Cette thèse est accessible à l'adresse : https://theses.insa-lyon.fr/publication/2022ISAL0077/these.pdf
© [A.D. Pouye], [2022], INSA Lyon, tous droits réservés

Figure 5.15 Parametric studies for a non conformal geometry configuration and for $h' = 55\,\text{cm}$: (a) reproduction error, (b) logarithm of the condition number ($\log_{10}\kappa$), (c) real part and (d) imaginary part of the target pressure (continuous grey line) and reconstructed pressure (dashed black line) of the WPPW defined by the wavevector $(-50, 50)\,\text{rad}\,\text{m}^{-1}$ at a frequency $f = 2000\,\text{Hz}$. 107

Figure 5.16 Parametric studies for a non conformal geometry configuration and for $h' = 60\,\text{cm}$: (a) reproduction error, (b) logarithm of the condition number ($\log_{10}\kappa$), (c) real part and (d) imaginary part of the target pressure (continuous grey line) and reconstructed pressure (dashed black line) of the WPPW defined by the wavevector $(-50, 50)\,\text{rad}\,\text{m}^{-1}$ at a frequency $f = 2000\,\text{Hz}$. 108

Figure 5.17 Parametric studies for a non conformal geometry configuration and for $h' = 70\,\text{cm}$: (a) reproduction error, (b) logarithm of the condition number ($\log_{10}\kappa$), (c) real part and (d) imaginary part of the target pressure (continuous grey line) and reconstructed pressure (dashed black line) of the WPPW defined by the wavevector $(-50, 50)\,\text{rad}\,\text{m}^{-1}$ at a frequency $f = 2000\,\text{Hz}$. 109

Figure 5.18 Comparison between the reproduction error induced by the (a) conformal geometry configuration and the (b) non-conformal configuration in the frequency-wavenumber domain. 110

Figure 5.19 Parametric studies: influence of the density of the array of monopoles on the reproduction error e_p at a frequency $f = 500\,\text{Hz}$. (a) $n_s = 1$, (b) $n_s = 2$, (c) $n_s = 3$ and (a) $n_s = 4$. 113

Figure 5.20 Parametric studies: influence of the density of the array of monopoles on the reproduction error e_p at a frequency $f = 1000\,\text{Hz}$. (a) $n_s = 1$, (b) $n_s = 2$, (c) $n_s = 3$ and (a) $n_s = 4$. 114

Cette thèse est accessible à l'adresse : https://theses.insa-lyon.fr/publication/2022ISAL0077/these.pdf
© [A.D. Pouye], [2022], INSA Lyon, tous droits réservés

Figure 5.21 Parametric studies: influence of the density of the array of monopoles on the reproduction error e_p at a frequency $f = 2000$ Hz. (a) $n_s = 1$, (b) $n_s = 2$, (c) $n_s = 3$ and (a) $n_s = 4$. 115
Figure 5.22 Target WPPW defined by the wavevector $(50, 50)$ rad m^{-1} mapped on the surface of the half-cylindrical structure. 116
Figure 5.23 Parametric studies: influence of the density of the array of monopoles on the reconstructed pressure fields at a frequency $f = 500$ Hz. (a) $n_s = 1$, (b) $n_s = 2$, (c) $n_s = 3$ and (a) $n_s = 4$. 117
Figure 5.24 Parametric studies: influence of the density of the array of monopoles on the reconstructed pressure fields at a frequency $f = 1000$ Hz. (a) $n_s = 1$, (b) $n_s = 2$, (c) $n_s = 3$ and (a) $n_s = 4$. 118
Figure 5.25 Parametric studies: influence of the density of the array of monopoles on the reconstructed pressure fields at a frequency $f = 2000$ Hz. (a) $n_s = 1$, (b) $n_s = 2$, (c) $n_s = 3$ and (a) $n_s = 4$. 119
Figure 5.26 Influence of the radial height on the reproduction error at a frequency $f = 500$ Hz for two different radial heights: (a) $h = 5$ cm and (b) $h = 10$ cm. 120
Figure 5.27 Influence of the radial height on the reproduction error at a frequency $f = 1000$ Hz for two different radial heights: (a) $h = 5$ cm and (b) $h = 10$ cm. 121
Figure 5.28 Influence of the radial height on the reproduction error at a frequency $f = 2000$ Hz for two different radial heights: (a) $h = 5$ cm and (b) $h = 10$ cm. 121
Figure 5.29 Reconstructed pressure fields using SST at a frequency $f = 500$ Hz for two different radial heights: (a) $h = 5$ cm and (b) $h = 10$ cm. . . 122
Figure 5.30 Reconstructed pressure fields using SST at a frequency $f = 1000$ Hz for two different radial heights: (a) $h = 5$ cm and (b) $h = 10$ cm. . . 122
Figure 5.31 Reconstructed pressure fields using SST at a frequency $f = 2000$ Hz for two different radial heights: (a) $h = 5$ cm and (b) $h = 10$ cm. . . 123

Cette thèse est accessible à l'adresse : https://theses.insa-lyon.fr/publication/2022ISAL0077/these.pdf
© [A.D. Pouye], [2022], INSA Lyon, tous droits réservés

Figure 6.1 Siemens mid-high frequency volume source used during the SST process for CRPs. 126
Figure 6.2 CTTM 1/4″ microphones. 127
Figure 6.3 Eight channel conditioner with a Harting connector output. . . . 127
Figure 6.4 five degrees-of-freedom robot arm. 128
Figure 6.5 Sketch of the experimental setup for the SST process on CRPs. . . 129
Figure 6.6 Monopole source mounted on the robot arm. 130
Figure 6.7 Chosen location of the semi-circular array of 63 microphones flush-mounted on the rigid half cylinder. The reference (green) position is where the microphones are actually located and the edge (red) corresponds to the farthest location from the reference where one needs to measure the transfer functions. 131
Figure 6.8 Optimal location of the semi-circular array of 63 microphones on the rigid half cylinder which reduces the diffraction effects on the measurements. 132
Figure 6.9 Flush-mounted microphones on the rigid open half cylinder. Left: view in *chamber 1* in Fig. 6.5. Right: view in *chamber 2* in Fig. 6.5. 132
Figure 6.10 Experimental setup: simply supported rigid open half cylinder. The monopole source (7) is mounted on the robot arm (8) which can slide along the rail (9) and supported by the truss structure (1). The 63 microphones (3) are flush-mounted on the rigid open half cylinder (4) baffled by the half polystyrene cylinders (2) and (5). (6) corresponds to the robot arm control unit. 133

Cette thèse est accessible à l'adresse : https://theses.insa-lyon.fr/publication/2022ISAL0077/these.pdf
© [A.D. Pouye], [2022], INSA Lyon, tous droits réservés

Figure 6.11 Pressure at the surface of the structure at two frequencies: (a) $f = 500\,\text{Hz}$ and (b) $f = 2000\,\text{Hz}$, for a radial height $h = 5\,\text{cm}$ and source angular position $\theta_0 = \frac{\pi}{2}$. Comparison between the analytical results (dash-dotted black line) and the experimental measurements (continuous gray line, the red dots correspond to the positions of the measurement points) for the two-dimensional case. 135

Figure 6.12 Pressure at the surface of the structure at two frequencies: (a) $f = 500\,\text{Hz}$ and (b) $f = 2000\,\text{Hz}$, for a radial height $h = 5\,\text{cm}$ and source angular position $\theta_0 = \frac{\pi}{4}$. Comparison between the analytical results (dash-dotted black line) and the experimental measurements (continuous gray line, the red dots correspond to the positions of the measurement points) for the two-dimensional case. 135

Figure 6.13 Pressure at the surface of the structure at two frequencies: (a) $f = 1000\,\text{Hz}$ and (b) $f = 1500\,\text{Hz}$, for a radial height $h = 10\,\text{cm}$ and source angular position $\theta_0 = \frac{\pi}{2}$. Comparison between the analytical results (dash-dotted black line) and the experimental measurements (continuous gray line, the red dots correspond to the positions of the measurement points) for the two-dimensional case. 136

Figure 6.14 Pressure at the surface of the structure at two frequencies: (a) $f = 500\,\text{Hz}$ and (b) $f = 2000\,\text{Hz}$, for a radial height $h = 20\,\text{cm}$ and source angular position $\theta_0 = \frac{\pi}{2}$. Comparison between the analytical results (dash-dotted black line) and the experimental measurements (continuous gray line, the red dots correspond to the positions of the measurement points) for the two-dimensional case. 136

Cette thèse est accessible à l'adresse : https://theses.insa-lyon.fr/publication/2022ISAL0077/these.pdf
© [A.D. Pouye], [2022], INSA Lyon, tous droits réservés

Figure 6.15 Condition number ($\log_{10}\kappa$) of the experimental transfer matrix $\mathbf{G}$ between the 50 monopole positions and the 63 microphone positions. 137

Figure 6.16 Comparison between the target pressure (dash-dotted black line) and the synthesized one (continuous gray line, the red dots correspond to the positions of the measurement points) using experimental SST at a frequency $f = 2000\,\text{Hz}$ for a radial height $h = 5\,\text{cm}$ and for three different Wall-Pressure Plane Waves (WPPWs): (a) and (b): $k_\theta = 5\,\text{rad}\,\text{m}^{-1}$, (c) and (d): $k_\theta = 25\,\text{rad}\,\text{m}^{-1}$, (e) and (f): $k_\theta = 50\,\text{rad}\,\text{m}^{-1}$. Left column: real part of the pressure. Right column: imaginary part. 138

Figure 6.17 Pressure at the surface of the structure at two frequencies: (a) $f = 500\,\text{Hz}$ and (b) $f = 2000\,\text{Hz}$, for a radial height $h = 5\,\text{cm}$ and source angular position $\theta_0 = \frac{\pi}{2}$. Comparison between the analytical results (dash-dotted black line) and the experimental measurements (continuous gray line, the red dots correspond to the positions of the measurement points) for the three-dimensional case. The observation points are on a different section from the source's plane/section, i.e. $|z - z_0| = 50\,\text{cm}$. 139

Figure 6.18 Pressure at the surface of the structure at two frequencies: (a) $f = 500\,\text{Hz}$ and (b) $f = 2000\,\text{Hz}$, for a radial height $h = 10\,\text{cm}$ and source angular position $\theta_0 = \frac{\pi}{4}$. Comparison between the analytical results (dash-dotted black line) and the experimental measurements (continuous gray line, the red dots correspond to the positions of the measurement points) for the three-dimensional case. The observation points are on a different section from the source's plane/section, i.e. $|z - z_0| = 25\,\text{cm}$. 140

Figure C.1 Frequency Response Functions (FRFs) measurements using a non-displaceable microphone array 157

Cette thèse est accessible à l'adresse : https://theses.insa-lyon.fr/publication/2022ISAL0077/these.pdf
© [A.D. Pouye], [2022], INSA Lyon, tous droits réservés

Figure D.1 Localization of arbitrarily chosen test points $\mathbf{x}_1$, $\mathbf{x}_2$, $\mathbf{x}_3$ and $\mathbf{x}_4$ where the pressure is plotted in order to study the number of necessary harmonics for a convergence of the pressure. 160

Figure D.2 Evolution of the pressure at four different points (see Fig. D.1) on the structure as a function of the source position r_0 for $\theta_0 = \frac{\pi}{2}$ and the number of harmonics N_h used in Eq. (5.15) at a frequency $f = 100\,\text{Hz}$ (a) $\mathbf{x}_1$, (b) $\mathbf{x}_2$, (c) $\mathbf{x}_3$, and (d) $\mathbf{x}_4$. 161

Figure D.3 Evolution of the pressure at four different points (see Fig. D.1) on the structure as a function of the source position r_0 for $\theta_0 = \frac{\pi}{2}$ and the number of harmonics N_h used in Eq. (5.15) at a frequency $f = 1000\,\text{Hz}$ (a) $\mathbf{x}_1$, (b) $\mathbf{x}_2$, (c) $\mathbf{x}_3$, and (d) $\mathbf{x}_4$. 162

Figure D.4 Evolution of the pressure at four different points (see Fig. D.1) on the structure as a function of the source position r_0 for $\theta_0 = \frac{\pi}{2}$ and the number of harmonics N_h used in Eq. (5.15) at a frequency $f = 2000\,\text{Hz}$ (a) $\mathbf{x}_1$, (b) $\mathbf{x}_2$, (c) $\mathbf{x}_3$, and (d) $\mathbf{x}_4$. 163

Figure D.5 Evolution of the pressure at four different points (see Fig. D.1) on the structure as a function of the source position θ_0 for $r_0 = 0.8\,\text{m}$ and the number of harmonics N_h used in Eq. (5.15) at a frequency $f = 100\,\text{Hz}$ (a) $\mathbf{x}_1$, (b) $\mathbf{x}_2$, (c) $\mathbf{x}_3$, and (d) $\mathbf{x}_4$. 164

Figure D.6 Evolution of the pressure at four different points (see Fig. D.1) on the structure as a function of the source position θ_0 for $r_0 = 0.8\,\text{m}$ and the number of harmonics N_h used in Eq. (5.15) at a frequency $f = 1000\,\text{Hz}$ (a) $\mathbf{x}_1$, (b) $\mathbf{x}_2$, (c) $\mathbf{x}_3$, and (d) $\mathbf{x}_4$. 165

Figure D.7 Evolution of the pressure at four different points (see Fig. D.1) on the structure as a function of the source position θ_0 for $r_0 = 0.8\,\text{m}$ and the number of harmonics N_h used in Eq. (5.15) at a frequency $f = 2000\,\text{Hz}$ (a) $\mathbf{x}_1$, (b) $\mathbf{x}_2$, (c) $\mathbf{x}_3$, and (d) $\mathbf{x}_4$. 166

Cette thèse est accessible à l'adresse : https://theses.insa-lyon.fr/publication/2022ISAL0077/these.pdf
© [A.D. Pouye], [2022], INSA Lyon, tous droits réservés

Figure D.8 Comparison between the amplitudes ((a), (c) and (e)) and phases ((b), (d) and (f)) of the transfer functions obtained with OpenBEM (gray continuous line) and those obtained using the developed analytical solution (dash-dotted black line) for one position of the unit amplitude monopole source ($r_0 = 1\,\text{m}, \theta_0 = 0$) and at three different frequencies. (a) and (b): $f = 2000\,\text{Hz}$; (c) and (d): $f = 1000\,\text{Hz}$ and (e) and (f): $f = 100\,\text{Hz}$. 168

Figure D.9 Comparison between the amplitudes ((a), (c) and (e)) and phases ((b), (d) and (f)) of the transfer functions obtained with OpenBEM (gray continuous line) and those obtained using the developed analytical solution (dash-dotted black line) for one position of the unit amplitude monopole source $\left(r_0 = 1\,\text{m}, \theta_0 = \frac{\pi}{4}\right)$ and at three different frequencies. (a) and (b): $f = 2000\,\text{Hz}$; (c) and (d): $f = 1000\,\text{Hz}$ and (e) and (f): $f = 100\,\text{Hz}$. 169

Figure D.10 Comparison between the amplitudes ((a), (c) and (e)) and phases ((b), (d) and (f)) of the transfer functions obtained with OpenBEM (gray continuous line) and those obtained using the developed analytical solution (dash-dotted black line) for one position of the unit amplitude monopole source $\left(r_0 = 1\,\text{m}, \theta_0 = \frac{\pi}{2}\right)$ and at three different frequencies. (a) and (b): $f = 2000\,\text{Hz}$; (c) and (d): $f = 1000\,\text{Hz}$ and (e) and (f): $f = 100\,\text{Hz}$. 170

Figure D.11 Values of $I(k_z)$ for $k_z \in [-k_z^{max}, k_z^{max}]$: (a) real part and (b) imaginary part at a frequency $f = 500\,\text{Hz}$ and for a source position defined by $\left(r_0 = 0.7\,\text{m}, \theta_0 = \frac{\pi}{2}, z_0 = 0.5\,\text{m}\right)$. The observation point located at $(r = 0.5\,\text{m}, \theta = 0, z = 0.5\,\text{m})$ and the dashed black lines correspond to values of the acoustic wavenumber at the considered frequency. 172

Cette thèse est accessible à l'adresse : https://theses.insa-lyon.fr/publication/2022ISAL0077/these.pdf
© [A.D. Pouye], [2022], INSA Lyon, tous droits réservés

Figure D.12 Values of $I(k_z)$ for $k_z \in [-k_z^{max}, k_z^{max}]$: (a) real part and (b) imaginary part at a frequency $f = 2000\,\text{Hz}$ and for a source position defined by $\left(r_0 = 0.7\,\text{m}, \theta_0 = \frac{\pi}{2}, z = 0.5\,\text{m}\right)$. The observation point located at $(r = 0.5\,\text{m}, \theta = 0, z_0 = 0.5\,\text{m})$ and the dashed black lines correspond to values of the acoustic wavenumber at the considered frequency. 172

Figure D.13 Values of $I(k_z)$ for $k_z \in [-k_z^{max}, k_z^{max}]$: (a) real part and (b) imaginary part at a frequency $f = 500\,\text{Hz}$ and for a source position defined by $\left(r_0 = 0.7\,\text{m}, \theta_0 = \frac{\pi}{2}, z_0 = 0.5\,\text{m}\right)$. The observation point located at $\left(r = 0.5\,\text{m}, \theta = \frac{\pi}{2}, z = 0.5\,\text{m}\right)$ and the dashed black lines correspond to values of the acoustic wavenumber at the considered frequency. 173

Figure D.14 Values of $I(k_z)$ for $k_z \in [-k_z^{max}, k_z^{max}]$: (a) real part and (b) imaginary part at a frequency $f = 2000\,\text{Hz}$ and for a source position defined by $\left(r_0 = 0.7\,\text{m}, \theta_0 = \frac{\pi}{2}, z_0 = 0.5\,\text{m}\right)$. The observation point located at $\left(r = 0.5\,\text{m}, \theta = \frac{\pi}{2}, z = 0.5\,\text{m}\right)$ and the dashed black lines correspond to values of the acoustic wavenumber at the considered frequency. 173

Figure D.15 Values of $I(k_z)$ for $k_z \in [-k_z^{max}, k_z^{max}]$: (a) real part and (b) imaginary part at a frequency $f = 2000\,\text{Hz}$ and for a source position defined by $\left(r_0 = 0.7\,\text{m}, \theta_0 = \frac{\pi}{3}, z_0 = 0.5\,\text{m}\right)$. The observation point located at $\left(r = 0.5\,\text{m}, \theta = \frac{\pi}{2}, z = 0.75\,\text{m}\right)$ and the dashed black lines correspond to values of the acoustic wavenumber at the considered frequency. 174

Figure D.16 Generated mesh for OpenBEM computations. 175

Cette thèse est accessible à l'adresse : https://theses.insa-lyon.fr/publication/2022ISAL0077/these.pdf
© [A.D. Pouye], [2022], INSA Lyon, tous droits réservés

Figure D.17 Comparison between the magnitudes ((a), (c) and (e)) and phases ((b), (d) and (f)) of the transfer functions obtained with OpenBEM (gray continuous line) and those obtained using the developed analytical solution (dash-dotted black line) for one position of the unit amplitude monopole source $\left(r_0 = 0.6\,\text{m}, \theta_0 = \frac{\pi}{2}, z_0 = 0.5\,\text{m}\right)$ and at three different frequencies. (a) and (b): $f = 500\,\text{Hz}$; (c) and (d): $f = 1000\,\text{Hz}$ and (e) and (f): $f = 2000\,\text{Hz}$. The observation points are on the same section as the source, i.e. $z = z_0$. 176

Figure D.18 Comparison between the magnitudes (a) and phases (b) of the transfer functions obtained with OpenBEM (gray continuous line) and those obtained using the developed analytical solution (dash-dotted black line) for one position of the unit amplitude monopole source $\left(r_0 = 0.6\,\text{m}, \theta_0 = \frac{\pi}{2}, z_0 = 0.5\,\text{m}\right)$ and at the frequency $f = 2000\,\text{Hz}$. The observation points are on a different section from the source's plane/section, i.e. $|z - z_0| = 0.1\,\text{m}$. 177

Figure D.19 Comparison between the magnitudes ((a), (c) and (e)) and phases ((b), (d) and (f)) of the transfer functions obtained with OpenBEM (gray continuous line) and those obtained using the developed analytical solution (dash-dotted black line) for one position of the unit amplitude monopole source $\left(r_0 = 0.6\,\text{m}, \theta_0 = \frac{\pi}{4}, z_0 = 0.5\,\text{m}\right)$ and at two different frequencies. (a) and (b): $f = 1000\,\text{Hz}$ and (c) and (d): $f = 2000\,\text{Hz}$. The observation points are on a different section from the source's, i.e. $|z - z_0| = 0.3\,\text{m}$. 178

Cette thèse est accessible à l'adresse : https://theses.insa-lyon.fr/publication/2022ISAL0077/these.pdf
© [A.D. Pouye], [2022], INSA Lyon, tous droits réservés

Figure D.20 Comparison between the magnitudes (a) and phases (b) of the transfer functions obtained with OpenBEM (gray continuous line) and those obtained using the developed analytical solution (dash-dotted black line) for one position of the unit amplitude monopole source $\left(r_0 = 1\,\text{m}, \theta_0 = \frac{\pi}{2}, z_0 = 0.5\,\text{m}\right)$ and at the frequency $f = 2000\,\text{Hz}$. The observation points are on a different section from the source's and close to the edge, i.e. $|z - z_0| = 0.4\,\text{m}$. 179

LIST OF TABLES

Table 1.1 Complementary TBL parameters 15
Table 3.1 Panel parameters 55
Table 4.1 Measurement times during the experimental SST process. 78
Table 5.1 Transfer functions computation times. 94
Table 5.2 Dimensions of the rigid half-cylinder. 111
Table 5.3 Values of the condition number ($\log \kappa$) of the transfer matrix $\mathbf{G}$ for each frequency and radial height setup. 123
Table D.1 Geometrical properties of the structure 160

ACRONYMS

ANR French National Research Agency or *Agence Nationale de la Recherche* (in French)

ASD Auto-Spectral Density

ASTM American Society for Testing and Materials

BEM Boundary Element Method

CHIEF Combined Helmholtz Integral Equation Formulation

Cette thèse est accessible à l'adresse : https://theses.insa-lyon.fr/publication/2022ISAL0077/these.pdf
© [A.D. Pouye], [2022], INSA Lyon, tous droits réservés

CRP Curved Rectangular Panel

CSD Cross-Spectral Density

CTTM Center for Transfer of Technologies of Le Mans or *Centre de Transfert de Techonologie* in French

DAF Diffuse Acoustic Field

FRF Frequency Response Function

FRP Flat Rectangular Panel

ISO International Organization for Standardization

MSE Mean Square Error

NAH Nearfield Acoustic Holography

PNAH Planar Nearfield Acoustical Holography

PSD Power Spectral Density

RANS Reynolds-Averaged Navier-Stokes

SRI Sound Reduction Index

SST Source Scanning Technique

TBL Turbulent Boundary Layer

TL Transmission Loss

WFS Wave Field Synthesis

WPF Wall-Pressure Fluctuations

WPPW Wall-Pressure Plane Wave

Cette thèse est accessible à l'adresse : https://theses.insa-lyon.fr/publication/2022ISAL0077/these.pdf
© [A.D. Pouye], [2022], INSA Lyon, tous droits réservés

INTRODUCTION

Cette thèse est accessible à l'adresse : https://theses.insa-lyon.fr/publication/2022ISAL0077/these.pdf
© [A.D. Pouye], [2022], INSA Lyon, tous droits réservés

Cette thèse est accessible à l'adresse : https://theses.insa-lyon.fr/publication/2022ISAL0077/these.pdf
© [A.D. Pouye], [2022], INSA Lyon, tous droits réservés

Nowadays, in the framework of developing more sustainable transportation means, new materials which are usually very light with good mechanical properties are spreading very fast. However, these new materials often have very poor acoustic properties. In order to improve the acoustic properties of these new materials, it is necessary to experimentally determine their vibroacoustic behavior when subjected to complex excitations such as the turbulent boundary layer excitation in the aeronautical transportation industry. There are currently available experimental facilities that allow one to determine the vibroacoustic properties of such structures but these are often very expensive and the reproducibility of the measurements performed in these facilities can be questioned, making it difficult to compare different solutions. It is therefore of considerable interest to have at disposal an experimental tool or process that can be used during the design stage of the considered structures and that allows one to accurately and cost-efficiently assess the vibroacoustic properties of the structures of interest. All the above reasons gave birth to the VIRTECH (VIRTualization of Experimental facilities in structural aCoustics by wall pressure syntHesis) project funded by the French National Research Agency or *Agence Nationale de la Recherche* (in French) (ANR). One of the main objectives of VIRTECH is the optimization of source networks to synthesize a wall-pressure field having the characteristics of a Diffuse Acoustic Field (DAF) or a Turbulent Boundary Layer (TBL) over the surface of a given structure, and by leveraging the filtering phenomena of structures in the wavenumber domain, determine their vibroacoustic responses with respect to the excitation of interest. The optimization will focus on various criteria: speed of implementation, spatial resolution, error sensitivity, cost and reproducibility. Another goal of the VIRTECH project consists in identifying the useful components of the acoustic field through direct measurements using microphones and through indirect measurement by examining the vibroacoustic behavior of the tested structure supplemented by an analysis of a numerical model of the pressure field.

The work presented in this thesis is part of the component of the VIRTECH project that aims at optimizing source networks for the synthesis of random excitations in order to determine the vibroacoustic behavior of structures under random pressure fields

Cette thèse est accessible à l'adresse : https://theses.insa-lyon.fr/publication/2022ISAL0077/these.pdf
© [A.D. Pouye], [2022], INSA Lyon, tous droits réservés

through the structural and acoustic responses for instance and with a particular focus on the DAF and TBL excitations. As stated earlier, the experimental characterization of structures under DAF and TBL excitations is of great interest to researchers as well as the transportation industry for acoustic comfort reasons mainly. The objective of this research work is to establish an experimental process allowing to determine the vibroacoustic responses of structures using the Source Scanning Technique (SST) that was introduced a few years ago.

The manuscript is organized as follows. After this general introduction and contextualization of the subject, a literature review on the excitations of interest and the existing methods used for the vibroacoustic characterization of structures is proposed in Part I. This first part also includes a chapter dedicated to a detailed description of the SST approach and its parameters. Part II is devoted to a numerical and experimental study of SST applied on flat rectangular panels. Then Part III proposes an extension of the method to curved rectangular panels.

Cette thèse est accessible à l'adresse : https://theses.insa-lyon.fr/publication/2022ISAL0077/these.pdf
© [A.D. Pouye], [2022], INSA Lyon, tous droits réservés

Part I

BACKGROUND AND PRESENTATION OF THE SOURCE SCANNING TECHNIQUE PROCESS

Cette thèse est accessible à l'adresse : https://theses.insa-lyon.fr/publication/2022ISAL0077/these.pdf
© [A.D. Pouye], [2022], INSA Lyon, tous droits réservés

Cette thèse est accessible à l'adresse : https://theses.insa-lyon.fr/publication/2022ISAL0077/these.pdf
© [A.D. Pouye], [2022], INSA Lyon, tous droits réservés

1 LITERATURE REVIEW

1.1 The excitation fields 8
1.1.1 Characterization of spatially correlated random pressure field . . 8
1.1.2 Diffuse acoustic field 10
1.1.3 Turbulent boundary layer 12
1.2 Standard test means 22
1.2.1 Diffuse acoustic field 22
1.2.2 Turbulent boundary layer 23
1.3 Alternative approaches to standard test means 25
1.3.1 Reciprocity method 25
1.3.2 Wave Field Synthesis 26
1.3.3 Planar Near-field Acoustical Holography 27
1.3.4 Least Squares Technique 28
1.3.5 Source Scanning Technique 29
1.4 Objectives of this thesis 30
1.5 Dissertation outline 30

This chapter is dedicated to an overview of the different aspects related to the proposed testing method. It concerns the reproduction of random pressure fields and the determination of the vibroacoustic properties of the structure. The main quantities of interest are the vibration response and the sound transmission of a given structure. We start by presenting the two excitations of interest and how they are mathematically modeled. Then a discussion on the standard test means that are currently used in order to experimentally reproduce the DAF and TBL excitations for the assessment of the vi-

Cette thèse est accessible à l'adresse : https://theses.insa-lyon.fr/publication/2022ISAL0077/these.pdf
© [A.D. Pouye], [2022], INSA Lyon, tous droits réservés

broacoustic properties of the considered structure is given. Afterwards, a brief overview on other experimental methods that have been suggested over the years and aiming at synthesizing the pressure fluctuations due to the two types of excitations of interest is presented. The chapter ends with a presentation of the outline for the remainder of the manuscript.

1.1 THE EXCITATION FIELDS

In general, there are two stochastic excitations that are of interest in several industrial applications

- the DAF excitation which is namely used in the building sector as an acoustic source for the characterization of the sound transmission loss of the walls,
- the TBL excitation which is generally used in the transportation industry (aeronautics, naval and automobile sectors) in order to represent the pressure fluctuations induced by the flow on the vibrating structures.

In the following, we propose an overview on the characterization of random pressure fields using stochastic tools before describing the two random pressure fields of interest.

1.1.1 Characterization of spatially correlated random pressure field

The following convention is used for Fourier temporal and spatial transforms.

TEMPORAL FOURIER TRANSFORM

$$\mathcal{F}\left[f\left(t\right)\right] = F\left(\omega\right) = \int_{-\infty}^{+\infty} f\left(t\right) \mathrm{e}^{-\mathrm{i}\omega t} \mathrm{d}t \tag{1.1}$$

Cette thèse est accessible à l'adresse : https://theses.insa-lyon.fr/publication/2022ISAL0077/these.pdf
© [A.D. Pouye], [2022], INSA Lyon, tous droits réservés

$$\mathcal{F}^{-1}\left[F\left(\omega\right)\right] = f\left(t\right) = \frac{1}{2\pi}\int_{-\infty}^{+\infty} F\left(\omega\right)\mathrm{e}^{\mathrm{i}\omega t}\mathrm{d}\omega \tag{1.2}$$

SPATIAL FOURIER TRANSFORM

$$\mathcal{F}\left[f\left(x\right)\right] = F\left(k\right) = \int_{-\infty}^{+\infty} f\left(x\right)\mathrm{e}^{-\mathrm{i}kx}\mathrm{d}x \tag{1.3}$$

$$\mathcal{F}^{-1}\left[F\left(k\right)\right] = f\left(x\right) = \frac{1}{2\pi}\int_{-\infty}^{+\infty} F\left(k\right)\mathrm{e}^{\mathrm{i}kx}\mathrm{d}k \tag{1.4}$$

where $\mathcal{F}$ represents the Fourier transform.

The early studies on Wall-Pressure Fluctuations (WPF) were based on wind tunnel measurements or flight tests. Pressure transducers were used to measure the pressure time signal at one point in space, $p_b\left(\mathbf{x},t\right)$, the statistics of which are usually assumed to be both stationary and homogeneous up to order 2 [87]. The autocorrelation function of this signal is defined as

$$R_{p_bp_b}\left(\mathbf{x},\tau\right) = \left\langle p_b\left(\mathbf{x},t\right)p_b\left(\mathbf{x},t+\tau\right)\right\rangle \tag{1.5}$$

where $\langle\bullet\rangle$ represents an average over time.

The wavenumber-frequency spectrum of the blocked pressure $p_b\left(\mathbf{x},t\right)$, denoted $S_{p_bp_b}\left(\mathbf{k},\omega\right)$ is defined as the space-time Fourier transform of the autocorrelation function $R_{p_bp_b}\left(\mathbf{x},\tau\right)$, that is, in terms of the space-frequency spectrum, $S_{p_bp_b}\left(\mathbf{x},\omega\right)$ of the blocked pressure

$$S_{p_bp_b}\left(\mathbf{k},\omega\right) = \iint_{\Sigma_s} S_{p_bp_b}\left(\mathbf{x},\omega\right)\mathrm{e}^{-\mathrm{i}\omega\mathbf{x}}\mathrm{d}\mathbf{x} \tag{1.6}$$

and

$$S_{p_bp_b}\left(\mathbf{x},\omega\right) = \iint_{-\infty}^{+\infty} R_{p_bp_b}\left(\mathbf{x},t\right)\mathrm{e}^{-\mathrm{i}\omega t}\mathrm{d}t \tag{1.7}$$

Cette thèse est accessible à l'adresse : https://theses.insa-lyon.fr/publication/2022ISAL0077/these.pdf
© [A.D. Pouye], [2022], INSA Lyon, tous droits réservés

where Σ_s is the surface of the structure.

Eq. (1.7) provides information on the energy of the TBL excitation at one specific point over the surface. By inferring that the convected pressure field is statistically homogeneous on the surface of the structure, the Fourier transform of the autocorrelation function of the WPF, also known as the wall-pressure auto-spectrum or single point wall-pressure spectrum, can be determined by integrating the wavenumber-frequency spectrum over the entire range of wavenumbers $\left(k_x, k_y\right)$

$$S_{p_b p_b}(\omega) = \int_{-\infty}^{+\infty} S_{p_b p_b}(\mathbf{k}, \omega)\, \mathrm{d}\mathbf{k} \tag{1.8}$$

As spatial homogeneity is assumed, the dependence of the wall-pressure ASD function on x is no longer specified as in Eq. (1.8).

1.1.2 Diffuse acoustic field

The term *diffuse acoustic field* has been defined from several approaches in the literature. However, the following formulation appears to have gained acceptance in the acoustical community:

In a diffuse acoustic field, there should be equal probability of energy flow in all possible directions, which means at a given position, sound waves are approaching with random phases (incoherent), and the probabilities of approaching from all possible directions are equal [50]. *It indicates that the time-averaged intensity is zero at all positions and, hence, the field is isotropic in nature. At the same time, there should be uniform energy density at all positions, ensuring homogeneous characteristics of the field* [50, 83]. *Once the field is isotropic and homogeneous, another criterion of diffuse acoustic field — constant irradiation from each volume element — will be fulfilled automatically* [89].

Cette thèse est accessible à l'adresse : https://theses.insa-lyon.fr/publication/2022ISAL0077/these.pdf
© [A.D. Pouye], [2022], INSA Lyon, tous droits réservés

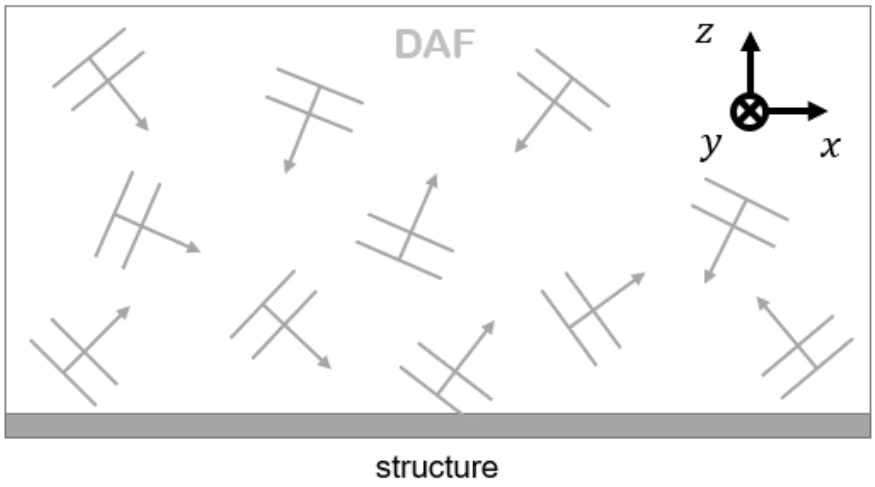

Figure 1.1: DAF description

A DAF is often described by a correlation function [26, 52, 67] but in the following, the Cross-Spectral Density (CSD) function, which is the temporal Fourier transform of the correlation function, defined by Eq. (1.9) will be used.

$$S_{p_b p_b}\left(\left|\mathbf{r}-\mathbf{r}'\right|,\omega\right) = S_{p_b p_b}(\omega)\,\frac{\sin\left(k_0\left|\mathbf{r}-\mathbf{r}'\right|\right)}{k_0\left|\mathbf{r}-\mathbf{r}'\right|} \tag{1.9}$$

where $\mathbf{r}$ and $\mathbf{r}'$ are the position vectors of two points; ω is the frequency; $k_0 = \omega/c_0$ is the acoustic wavenumber and c_0 the speed of sound in the medium. $S_{p_b p_b}(\omega)$ designates the wall-pressure Auto-Spectral Density (ASD) function which is actually a two-sided ASD as a function of the angular frequency ω expressed in $\mathrm{Pa^2 rad^{-1} s}$ and related to the more physically meaningful one-sided ASD (or Power Spectral Density (PSD)) $W_{p_b p_b}$ as a function of the frequency f and expressed in $\mathrm{Pa^2 Hz^{-1}}$ through the following equation

$$W_{p_b p_b}(f) = 4\pi S_{p_b p_b}(\omega) \tag{1.10}$$

Cette thèse est accessible à l'adresse : https://theses.insa-lyon.fr/publication/2022ISAL0077/these.pdf
© [A.D. Pouye], [2022], INSA Lyon, tous droits réservés

It is also possible to define the CSD function of the excitation in the frequency-wavenumber domain:

$$S_{p_b p_b}(\mathbf{k},\omega) = \begin{cases} S_{p_b p_b}(\omega)\,\dfrac{2\pi}{k_0}\,\dfrac{1}{\sqrt{k_0^2 - |\mathbf{k}|^2}} & \text{if } |\mathbf{k}| < k_0 \\ 0 & \text{if } |\mathbf{k}| \geq k_0 \end{cases} \tag{1.11}$$

where $|\mathbf{k}| = \sqrt{k_x^2 + k_y^2}$, k_x and k_y are the wavenumbers in the x and y directions, respectively.

$S_{p_b p_b}(\mathbf{k},\omega)$ is simply a two dimensional spatial Fourier transform of the CSD function written in the space-frequency domain.

The DAF excitation is generally used to determine the sound transmission of a given structure or material in building acoustics for airborne sound insulation purposes [49]. It is used in the transportation industry (aeronautics, automobile, etc.) as well.

1.1.3 Turbulent boundary layer

1.1.3.1 Description

When a fluid flows along an object or when an object is moving through a fluid, as a consequence of the viscosity of the fluid, there is internal friction between adjacent layers starting from the wall(s) of the considered object. The layer below the top layer will be dragged in the forward direction by the layer above it, but at a velocity somewhat less than the velocity of the layer above. This layer, in turn, will exert a forward drag on the layer beneath it at reduced velocity and so on through the entire fluid layer up until the wall(s) of the object: a boundary layer is forming.

The boundary layer is a well known concept in many fields (mechanical, aeronautical, naval, etc.) and has been the subject of increasing interest from the scientific community. This concept was initiated by Prandtl [73] in the beginning of the past century where he

Cette thèse est accessible à l'adresse : https://theses.insa-lyon.fr/publication/2022ISAL0077/these.pdf
© [A.D. Pouye], [2022], INSA Lyon, tous droits réservés

built a bridge between the two major disciplines of fluid dynamics: hydrodynamics at that moment which was developed from Euler's theory of inviscid flows and hydraulics which relied on a large amount of experimental data to tackle practical engineering problems. In his 1904 paper, Prandtl stated that however small the viscosity of a fluid in motion may be, it cannot be ignored. Over the years, this led to the development of the boundary layer theory. A simple definition of the boundary layer would be (according to Prandtl):
The boundary layer is a region of the flow with non-negligible effects of viscosity separating a solid body and a free flow which corresponds to the inviscid limiting solution.
The flow within the boundary layer can be considered *laminar* or *turbulent* depending on the value of the Reynolds number Re defined by the following equation

$$Re = \frac{UL}{\nu} \tag{1.12}$$

ν is the kinematic viscosity of the fluid, U and L are the characteristic streamwise velocity and length, respectively.
When the Reynolds number increases, the regime of the boundary layer transitions from laminar to turbulent leading to much more complex flow patterns and a thickening of the boundary layer.

1.1.3.2 TBL parameters

The main parameters allowing the description of a TBL excitation are presented hereunder. This type of excitation is illustrated in Fig. 1.2 along with two parameters that describe the excitation.

Physical domain

When a fluid is flowing around a structure (or the structure is moving through a fluid) at a certain velocity U_∞, an area with a velocity gradient can be observed: the fluid velocity $U(z)$ gradually increases away from the structure until it reaches the outer

Cette thèse est accessible à l'adresse : https://theses.insa-lyon.fr/publication/2022ISAL0077/these.pdf
© [A.D. Pouye], [2022], INSA Lyon, tous droits réservés

velocity U_∞. This area is called the *boundary layer* and has a thickness δ. The transition from boundary layer flow to outer flow takes place continuously (at least in the case of laminar flows), so that a precise boundary cannot, in principle, be given. However, the concept of boundary layer thickness is very often used in practice. Frequently the boundary layer thickness is arbitrarily given as being at the point where the velocity reaches a certain percentage of the outer velocity, e.g. 99%. This is translated by Eq. (1.13) below

$$U(\delta) = 0.99 U_\infty \tag{1.13}$$

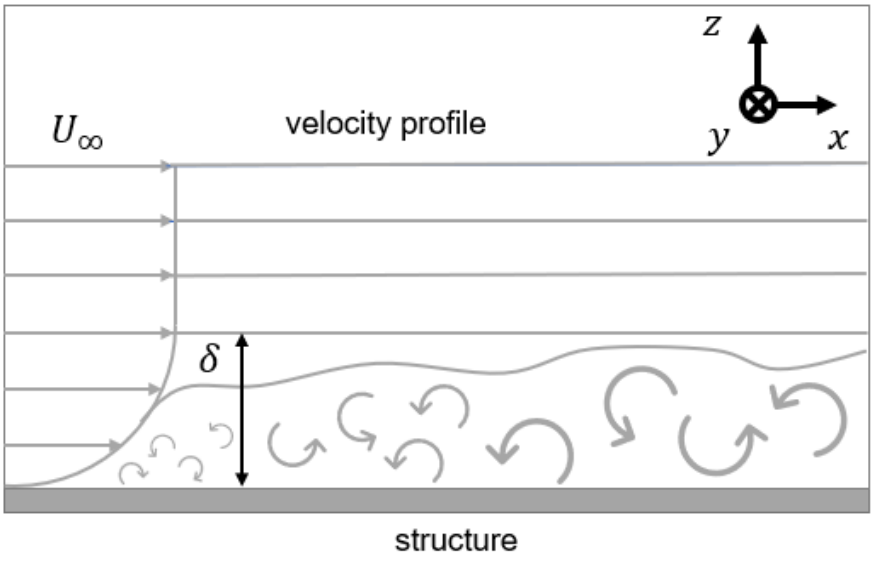

Figure 1.2: TBL description

A more precise and physical definition of the boundary layer thickness is given by the *displacement thickness*, $\delta_\star$, which is the distance by which the external potential flow is displaced outwards due to the decrease in velocity in the boundary layer

$$\delta_\star = \int_0^\infty 1 - \frac{U(z)}{U_\infty} \mathrm{d}z \tag{1.14}$$

Cette thèse est accessible à l'adresse : https://theses.insa-lyon.fr/publication/2022ISAL0077/these.pdf
© [A.D. Pouye], [2022], INSA Lyon, tous droits réservés

Following the analogy of the displacement thickness, a momentum thickness may be defined. The momentum thickness θ is the distance by which a surface would have to be moved parallel to itself towards the reference plane in an inviscid fluid stream of velocity U_∞ to give the same total momentum as exists between the surface and the reference plane in a real fluid

$$\theta = \int_0^\infty \frac{U(z)}{U_\infty}\left(1 - \frac{U(z)}{U_\infty}\right)\mathrm{d}z \tag{1.15}$$

The other parameters allowing the description of TBL excitation are given in Table 1.1.

Name	Equation	Comments
Wall shear stress	$\tau_w = \mu\left(\frac{\partial u}{\partial z}\right)_w \approx \mu\frac{U_\infty}{\delta}$	According to Newton's law of friction. The index w denotes the value at the wall and μ is the dynamic viscosity.
Friction velocity	$u_\tau = \sqrt{\frac{\tau_w}{\rho}}$	ρ is the fluid density.
Shape factor	$H = \frac{\delta_\star}{\theta}$	$\delta_\star$ is the displacement thickness and θ is the momentum thickness.

Table 1.1: Complementary TBL parameters

The higher the value of H, the stronger the adverse pressure gradient. A high adverse pressure gradient can greatly reduce the Reynolds number at which transition into turbulence may occur. Conventionally, $H = 2.59$ (Blasius boundary layer) is typical of laminar flows, while $H = 1.3 - 1.4$ is typical of turbulent flows. For more details concerning the TBL excitation, see reference [80].

Wavenumber-frequency spectrum

The WPF induced by a TBL excitation are usually modeled in the wavenumber-frequency domain through their CSD function $S_{p_b p_b}(\mathbf{k}, \omega)$ which gives information about the wavenumber components of the pressure field. Generally, it is represented in the

Cette thèse est accessible à l'adresse : https://theses.insa-lyon.fr/publication/2022ISAL0077/these.pdf
© [A.D. Pouye], [2022], INSA Lyon, tous droits réservés

wavenumber domain and three main regions can be distinguished from a schematic representation of $S_{p_b p_b}(\mathbf{k}, \omega)$ (see Fig. 1.3)

- The *acoustic region*: it is located in the low wavenumbers region ($|\mathbf{k}| \leq k_0$, k_0 is the acoustic wavenumber), has low energy levels and is associated to the compressibility effects of the fluid. However, if the fluid is considered incompressible, the wall-pressure CSD function tends toward 0 when the wavenumber tends toward 0. This property known as the Kraichnan-Phillips theorem [54, 71] means that the eddies constituting the boundary layer can only be of finite size as the boundary layer is of finite dimensions.

- The *convective region* ($|\mathbf{k}| \approx k_c$, k_c represents the convective wavenumber and is defined by Eq. (1.16)): it corresponds to the region defined by the convective ridge in the high wavenumbers region, has substantial energy levels and corresponds to the mass convection of the fluid.

- The *transitional region* ($k_0 < |\mathbf{k}| < k_c$): it is the region that connects the acoustic and the convective regions. Up until now, this region is not well known because the energy levels of the convective ridge are very high making it difficult to measure the energy levels in this region.

The distinction between these different regions of the spectrum is fundamental as Hwang and Maidanik showed it in their paper [48]: the contribution of the low wavenumber region to the response of the structure under TBL excitation can be significant in some cases. This phenomenon is known as the filtering effect of the structure under TBL forcing and will be discussed in Part II, Chapter 3.

Let us develop a little more on the acoustic and convective regions of the WPF CSD function starting by the former.

The acoustic component of the TBL excitation corresponds to the pressure fluctuations of the acoustic radiation of the eddies in the fluid. It is characterized by the acoustic wavenumber k_0 defined previously. This acoustic component has lower energetic levels

Cette thèse est accessible à l'adresse : https://theses.insa-lyon.fr/publication/2022ISAL0077/these.pdf
© [A.D. Pouye], [2022], INSA Lyon, tous droits réservés

compared to the convective component and is generally located in the low wavenumber domain. It is often represented in the wavenumber domain by a disk centered at $\left(k_x = 0, k_y = 0\right)$ and of radius k_0 (see Fig. 1.3). In fact, the acoustic component corresponds to waves propagating in all directions which can be assimilated to a DAF [4].
The convective component corresponds to the pressure fluctuations due to the mass convection. In the wavenumber domain, it is defined by the convective wavenumber given by the following equation

$$k_c = \frac{\omega}{U_c} \tag{1.16}$$

where ω is the angular frequency and $U_c = KU_\infty$ is the convective velocity. K is an experimentally determined coefficient [5] and its values lie in the interval $[0.7, 0.8]$. This component of the TBL excitation is the most energetic part and is usually located in the high wavenumbers domain depending on the free stream velocity U_∞. It can be represented by an ellipse centered at $k_x = k_c$ (x being the streamwise direction) in the wavenumber domain whose parameters (length Δk_x and width Δk_y) are given by the bandwidth at −3dB around the convective ridge along k_x and k_y [17] as illustrated in Fig. 1.3. These two lengths Δk_x and Δk_y are respectively given by the following equations

$$\Delta k_x = \frac{2\omega\alpha_x}{U_c} \quad \text{and} \quad \Delta k_y = \frac{2\omega\alpha_y}{U_c} \tag{1.17}$$

where α_x and α_y are called the Corcos coefficients and account for the spatial coherence of the TBL WPF along the streamwise and spanwise directions, respectively.

1.1.3.3 TBL models

Up to now, there is no closed-form analytical model that describes a typical TBL excitation. However, the TBL parameters can be estimated numerically through analytical models on simple structures or Reynolds-Averaged Navier-Stokes (RANS) equations for more complex structures. For example, Peltier and Hambric [70] developed a statistical model allowing to obtain the spatial correlation functions using data computed from RANS

Cette thèse est accessible à l'adresse : https://theses.insa-lyon.fr/publication/2022ISAL0077/these.pdf
© [A.D. Pouye], [2022], INSA Lyon, tous droits réservés

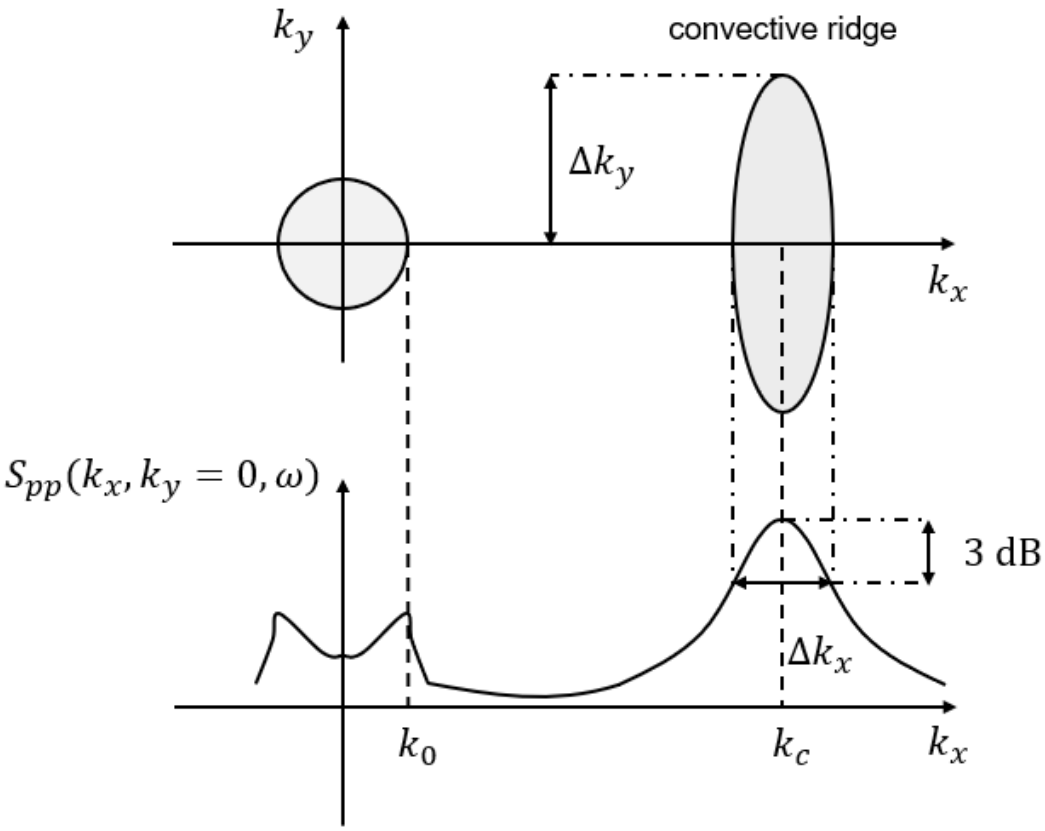

Figure 1.3: Schematic of the characteristic regions of a wavenumber-frequency spectrum at a constant frequency

equations and taking into account a pressure gradient. These numerical models are often complex to implement and costly in terms of computing time. Thus our interest concerns empirical and semi-empirical models that can describe the TBL fluctuations provided that some adjustments are done. Historically, it has not been obvious to measure the WPF induced by a TBL [21, 47]. This fact led to the introduction of the normalized cross-spectrum, usually denoted $\Phi_{p_b p_b}(\mathbf{k}, \omega)$, and which is a ratio between the cross-spectrum itself $S_{p_b p_b}(\mathbf{k}, \omega)$ and the auto-spectrum $S_{p_b p_b}(\omega)$. In this section, the two types of spectra are discussed: on one hand, the auto-spectrum of the TBL WPF and on the other hand, the cross-spectrum.

Cette thèse est accessible à l'adresse : https://theses.insa-lyon.fr/publication/2022ISAL0077/these.pdf
© [A.D. Pouye], [2022], INSA Lyon, tous droits réservés

Single point wall-pressure spectrum

The single point wall-pressure spectrum has been the object of many investigations and numerous models came out of those studies. One can cite the model of Robertson [74] based on data from supersonic NASA-Ames measurements, that of Willmarth-Amiet-Roos [3] based on measurements by Willmarth and Roos [97] over a flat plate, the model of Goodwin [41] based on flight test data on three supersonic aircraft: XB-70, A3J and Concorde, etc. As an example, one can take a look at the model of Goody [42] considered as the model that matches the most the experimental measurements performed in the case of a TBL excitation characterization as it takes into account a large number of measurements, those of seven different research teams [47]. This model takes into account the influence of the Reynolds number through the parameter R_T

$$S_{p_b p_b}(\omega) = \frac{3\tau_w^2 \delta \left(\frac{\omega\delta}{U_\infty}\right)^2}{U_\infty \left(\left[0.5 + \left(\frac{\omega\delta}{U_\infty}\right)^{0.75}\right]^{3.7} + \left[1.1 R_T^{-0.57}\left(\frac{\omega\delta}{U_\infty}\right)\right]^7\right)} \tag{1.18}$$

where $R_T = \frac{\delta u_\tau^2}{U_\infty \nu}$ is a ratio between two time scales: $\frac{\delta}{U_\infty}$ and $\frac{\nu}{u_\tau^2}$. The model is valid for a large range of Reynolds number: $1400 < Re < 23400$ and has inspired the models established by Rozenberg [78], Catlett [22] and Klabes [53] for the single point wall-pressure spectrum of a TBL excitation.

Now let us take a look at some cross-spectrum models non-exhaustively listed below.

Two point wall-pressure spectrum

corcos (1963) From the analysis of experimental results obtained by Willmarth and Wooldridge [98], Corcos proposed the following model for the WPF CSD function of a TBL [27]:

$$S_{p_b p_b}\left(\xi_x, \xi_y, \omega\right) = S_{p_b p_b}(\omega) \mathrm{e}^{-|\xi_x|/L_x} \mathrm{e}^{-\left|\xi_y\right|/L_y} \mathrm{e}^{-\mathrm{i}\omega|\xi_x|/U_c} \tag{1.19}$$

Cette thèse est accessible à l'adresse : https://theses.insa-lyon.fr/publication/2022ISAL0077/these.pdf
© [A.D. Pouye], [2022], INSA Lyon, tous droits réservés

where ξ_x and ξ_y are streamwise and spanwise distances, respectively. L_x is the correlation length in the streamwise or x-direction and L_y is the correlation length in the spanwise or y-direction, U_c is the convection velocity and $S_{p_b p_b}(\omega)$ corresponds to the WPF ASD function and will be developed later. As suggested by Corcos, the correlation lengths are assumed to be inversely proportional to frequency, and have the form

$$L_x = \frac{U_c}{\omega \alpha_x} \quad \text{and} \quad L_y = \frac{U_c}{\omega \alpha_y} \tag{1.20}$$

where α_x and α_y are the decay rates of the spatial coherence and correspond to empirical constants previously introduced as the Corcos coefficients.

The spatial Fourier transform of Eq. (1.19) yields the CSD function in the wavenumber domain:

$$S_{p_b p_b}(\mathbf{k}, \omega) = S_{p_b p_b}(\omega) \left(\frac{U_c}{\omega} \right)^2 \frac{4 \alpha_x \alpha_y}{\left[\alpha_x^2 + \left(1 - \frac{k_x}{k_c} \right)^2 \right] \left[\alpha_y^2 + \left(\frac{k_y}{k_c} \right)^2 \right]} \tag{1.21}$$

where k_x and k_y are the streamwise and spanwise wavenumbers, respectively.

This model describes the convective ridge accurately. However, the simplicity of the model proposed by Corcos limits its validity domain to the wavenumbers around he convective ridge [17]. In fact, on one hand, the model proposed by Corcos assumes that the correlation lengths L_x and L_y do not depend on the thickness δ of the TBL which leads to an underestimation of the convective ridge width when the spatial separations ξ_x and ξ_y become large. On the other hand, this model also assumes a separation between the streamwise and spanwise directions which constitutes a strong hypothesis.

Other models (Efimtsov [31], Smol'yakov and Tkachenko [86], etc.) which propose improvements of the Corcos model can be found in the literature.

MELLEN (1990) The model proposed by Mellen [65] is a readjustment of the Corcos model. The separation of the components along the streamwise axis x and the spanwise axis y induces the diamond shaped convective ridge of the Corcos model in the

Cette thèse est accessible à l'adresse : https://theses.insa-lyon.fr/publication/2022ISAL0077/these.pdf
© [A.D. Pouye], [2022], INSA Lyon, tous droits réservés

wavenumber domain. The Mellen model combines both components and as a result, the convective ridge is oval shaped which is a more appropriate representation with respect to actual experimental measurements. The level of the spectrum in the convective ridge is then estimated better or in other words, less overestimated compared to that of the Corcos model. The Mellen model is defined by the following equation:

$$S_{p_b p_b}\left(k_x, k_y, \omega\right) = S_{p_b p_b}\left(\omega\right) \frac{2\pi \left(\alpha_x \alpha_y k_c^2\right)^2}{\left[\left(\alpha_x \alpha_y k_c^2\right)^2 + \left(\alpha_x k_c k_y\right)^2 + \left(\alpha_y k_c\right)^2 \left(k_c - k_x\right)^2\right]^{3/2}} \tag{1.22}$$

where $\alpha_x = 0.116$ and $\alpha_y = 0.7$ [65]. Note that these exponential decay rates α_x and α_y can be modified to fit flow measurements.

Now, let us summarize this discussion on TBL models. It is important to note that the TBL ASD function sorts the energy into frequencies while the normalized wavenumber-frequency spectrum (CSD function normalized by the ASD function) sorts the energy into wavenumbers. There are numerous models available and aiming at characterizing a TBL excitation but none of them do fit exactly to experimental measurements without some adjustments. The list of models presented previously is far from being exhaustive. Hereafter are two references that discuss TBL models more thoroughly. Bull [21] has done an extensive study on WPF beneath a TBL by looking at the statistical parameters inherent to the WPF of a TBL, its frequency spectrum and the mean square pressure from which one can define the ASD function of the WPF. Miller [66], in her PhD thesis, was also interested in the analysis of three types of TBL models from a theoretical to a practical point of view.

Cette thèse est accessible à l'adresse : https://theses.insa-lyon.fr/publication/2022ISAL0077/these.pdf
© [A.D. Pouye], [2022], INSA Lyon, tous droits réservés

1.2 STANDARD TEST MEANS

In this section, a brief overview on the standard experimental methods used to study the vibroacoustic properties of a given structure under stochastic excitation is presented for both the DAF and TBL cases. In order to assess the vibroacoustic behavior of a given structure, two quantities are considered: the structural or vibration response and the sound transmission of the structure.

1.2.1 Diffuse acoustic field

The experimental reproduction of a DAF excitation is generally done in a reverberant room also called reverberation room. The purpose of a reverberation room is to create a highly diffuse acoustic measurement environment, defined as a sound field in which the acoustic energy flows equally in all directions as stated earlier in Sec. 1.1.2.
Reverberant rooms are involved in several standardized measurements such as the sound absorption of materials, the sound power of noise sources or the sound insulation of partitions [23]. They are also used for high-intensity noise level fatigue testing of, for example, aircraft and spacecraft components analysis [99].
In order to determine the sound transmission of a given structure using a reverberant room in which the DAF is experimentally created by a source emitting broadband noise (this room is referred to as the sending room), it is usually coupled to another reverberant room or an anechoic room which is referred to as the receiving room. The sound transmission of the structure is measured through the Transmission Loss (TL) if one is using the American Society for Testing and Materials (ASTM) standards [30] or the Sound Reduction Index (SRI) if one is using the European International Organization for Standardization (ISO) standards [1]. It should be noted that the main difference between these two quantities resides in the fact that the SRI value has been developed to approximate the performance of a material in reducing the transmission of speech, and

Cette thèse est accessible à l'adresse : https://theses.insa-lyon.fr/publication/2022ISAL0077/these.pdf
© [A.D. Pouye], [2022], INSA Lyon, tous droits réservés

therefore, does not give a true idea with respect to non-speech sounds such as music, traffic, trains, aircraft, etc.

Although the use of reverberant rooms is widely spread, there are some limitations inherent to these types of installation. In fact, it has been experimentally proven that the field in the reverberant room can be considered as a DAF only above a cutoff frequency [51, 81] also known as the Schroeder frequency. It marks the transition from individual, well-separated resonances (that dominate the pressure field which is thus not diffuse) to many overlapping normal modes [82]. Another limitation is the strong variability of the results obtained between different facilities. These differences are mainly due to test conditions, mounting conditions of test structures, geometry of the reverberant room, measurement strategies, etc.

1.2.2 Turbulent boundary layer

In Sec. 1.1.3.1, it is stated that a boundary layer arises when a fluid is moving around a structure or the structure is moving through a fluid at a certain speed. Naturally, there is mainly two experimental solutions for the characterization of the vibroacoustic behavior of a structure under TBL excitation: the wind tunnel (air flowing around an object) and the *in situ* or in-flight measurements (object moving through air).

1.2.2.1 Wind tunnel

The wind tunnel is the most commonly used method for the determination of the vibroacoustic behavior of structures under TBL excitation. Wind tunnels are large ducts with air flowing inside and are used to reproduce the interaction between a flow and a full or downscaled object. The measurements, which can be complex to perform, are done in a small section of the tunnel. In fact, while making measurements inside a wind tunnel, it is important to have control over the flow velocity and the pressure inside the tunnel on one hand. On the other, one must make sure to homogenize the flow with honeycomb grids and decouple the structure to be tested from the flow vein.

Cette thèse est accessible à l'adresse : https://theses.insa-lyon.fr/publication/2022ISAL0077/these.pdf
© [A.D. Pouye], [2022], INSA Lyon, tous droits réservés

The experimental setup, the transducers used for the measurement of the parameters of interest as well as the flow quality have a direct impact on the measurements done in a wind tunnel [69, 98], thus justifying the numerous TBL models present in the literature. As one can notice, wind tunnel measurements can be expensive and delicate to implement.

1.2.2.2 In situ tests

The other standard solution for the determination of the TBL induced noise and vibrations is *in situ* or in flight measurements where an aircraft is equipped with numerous transducers. These allow one to measure the turbulent flow and the vibrations at some regions of the aircraft as well as an estimation of the cabin noise. One can cite the work of Bhat [15] who carried out exterior WPF measurements on a Boeing model 737 airplane in two separate flight tests and at two different Mach numbers. Subsequently, he and Wilby [16] studied the interior noise radiated by an airplane fuselage subjected to a TBL excitation and evaluated the effectiveness of some noise reduction treatments. However, the flight test data were in poor agreement with available wind tunnel measurements. Afterwards, Wilby and Gloyna [94] measured the response of an airplane (Boeing model 737) fuselage structure to a TBL excitation for two locations on the fuselage and three flight Mach numbers. Although in flight measurements are popular, they are costly and complicated to set up. Also, as the measurements are done during flight, they are polluted by other noise sources present in the aircraft.

Wind tunnel and *in situ* measurements have been widely used over the years and almost all the TBL models that can be found in the literature were established using these measurements. However there are inherent drawbacks to these *standard* methods. Namely: cost, complexity, reproducibility of the results, etc. These reasons motivated researchers to propose alternatives to the standard test means and which will be discussed in the following section.

Cette thèse est accessible à l'adresse : https://theses.insa-lyon.fr/publication/2022ISAL0077/these.pdf
© [A.D. Pouye], [2022], INSA Lyon, tous droits réservés

1.3 ALTERNATIVE APPROACHES TO STANDARD TEST MEANS

The possibility of synthesizing the vibroacoustic response of structures under stochastic excitations using an array of acoustic sources was theoretically shown some decades ago [33]. But due to technical limitations, this method could not experimentally be validated. Since then, several techniques have been proposed over the years. Hereunder, a non-exhaustive list of alternative techniques for the reproduction of the vibroacoustic behavior of structures under DAF and TBL excitation are presented.

1.3.1 Reciprocity method

Recently, a new methodology based on the reciprocity principle was proposed by Marchetto *et al.* for the experimental characterization of flat rectangular panels under DAF [57] and TBL [58] excitations. This approach is based on the concept that the panel response at a given point on the panel to a random pressure field depends on two quantities in the wavenumber domain: first, the wall-pressure CSD function, which characterizes the excitation, and, second, the so-called "sensitivity function" determined at point, which characterize the dynamic behavior of the panel. Those sensitivity functions can be determined using the reciprocity principle, which states that they are equivalent to the panel velocity FRF when the panel is excited by a normal force at the point of interest, expressed in the wavenumber domain. The authors compared the vibration response and the transmission loss determined using the proposed approach and those determined using standard test means (reverberant room and wind tunnel). The results obtained in both papers [57, 58] show good agreement, thus validating the proposed approach. Other than the limitations inherent to the mathematical formulation of the problem (linearity, time invariance, etc.), the authors stated that the methodology can be costly in terms of measurement time. However, this limitation can be overcome with the recently developed full-field vibration measuring techniques.

Cette thèse est accessible à l'adresse : https://theses.insa-lyon.fr/publication/2022ISAL0077/these.pdf
© [A.D. Pouye], [2022], INSA Lyon, tous droits réservés

1.3.2 Wave Field Synthesis

Wave Field Synthesis (WFS) is one of the most well-known sound field reproduction techniques. It was introduced at the Delft University of Technology by Berkhout in 1988 in a greatly cited paper [11] where he suggested the term *acoustic control system* and not yet WFS. In fact, the term WFS was introduced later on as *wave front synthesis* [12] and subsequently as *wave field synthesis* [13]. Since then, many researchers have investigated this new method and a large number of publications on WFS is now available. A substantial number of PhD theses have also been written in the context of WFS as well, see for example Ref. [29, 37, 39, 68, 76, 79, 88, 91, 92].

This sound reproduction technique is based on the wave theory concept of Huygens [46] which was originally described for water waves and optics. The construction principle postulated by Huygens states that each point on a wavefront can be regarded as a point source and that all these secondary sources combine to form subsequent wavefronts which are the same as the the wavefronts generated by the original source. This principle can be mathematically formulated using the Kirchhoff-Helmholtz integral representation which states that the sound pressure is completely determined in a volume if the sound pressure and the velocity are determined on the surface delimiting the volume. This integral is usually simplified *via* the first Rayleigh integral (for monopole-like sources) and the second Rayleigh integral (for dipole-like sources) which explicitly define the signals which are to be fed to the loudspeakers in terms of the normal derivative of the target pressure field to be synthesized. This representation formula is the basis of WFS where an array of equally spaced loudspeakers is used to reproduce a given pressure field.

For practical reasons, the implementation of WFS is usually limited to sound field reproduction on a plane using a finite size of loudspeaker array, thus implying a discretization of the ideally continuous distribution of secondary sources from Huygens principle. Other methods have been developed in order to extend this reproduction technique to arrays of different shape: a relevant example is the so called *2.5 operator* derived from

Cette thèse est accessible à l'adresse : https://theses.insa-lyon.fr/publication/2022ISAL0077/these.pdf
© [A.D. Pouye], [2022], INSA Lyon, tous droits réservés

a stationary phase approximation of the three dimensional free-field Green function applied to two dimensional arrays, see for instance Ref. [88].
Berry *et al.* [14] proposed a numerical study aiming at reproducing three types of excitation using WFS: propagating plane wave, diffuse acoustic field and wall-pressure in subsonic or supersonic TBL. They examined the accuracy of the reproduction in terms of the size of the source and reproduction planes, their separation and the number of reproduction sources required per acoustic wavelength. In their paper, they show that the approach is well suited to the reproduction of a DAF excitation or a supersonic TBL excitation (for which most of the wall-pressure energy is contained in the acoustic wavenumber domain) with a minimum of two reproduction monopoles per acoustic wavelength in the streamwise and crosswise directions. However, the reproduction approach has inherent limitations in the case of the small wavelength components of subsonic turbulent boundary layers, which are known to contribute to sound transmission.

1.3.3 Planar Near-field Acoustical Holography

Acoustical holography is a process by which the measurement of the pressure at a set of points on a surface in the vicinity of an acoustically radiating object is analyzed to yield the velocity vector field, the acoustic pressure, and the acoustic intensity map in three-dimensional space. This technique which appeared in the mid 1960s [45] is only an approximation of the inverse problem of reconstructing sound fields. If the measurement points are recorded on a surface located at a distance of at least one acoustic wavelength from the vibrating surface, then the processing of the data results in an acoustic image that can only resolve sources that are separated by at least one acoustic wavelength, in other words, only source details greater than the acoustic wavelength can be retrieved in this procedure. However, if the measurement points are taken in the nearfield of the source region, then the spatial resolution can be reduced to a fraction of a wavelength [43], resulting in what is known as Nearfield Acoustic Holography (NAH)

Cette thèse est accessible à l'adresse : https://theses.insa-lyon.fr/publication/2022ISAL0077/these.pdf
© [A.D. Pouye], [2022], INSA Lyon, tous droits réservés

which appeared in the 1980s [64, 96]. The surface containing the measurement points is called the hologram surface. For more details on the theoretical foundations, the theory in different coordinate systems (planar, cylindrical and spherical) and the applications of NAH, see Ref. [64].

Planar Nearfield Acoustical Holography (PNAH) is a method of imaging the source field of a planar or *near* planar vibrating structure and the three-dimensional half-space in front of the structure. The hologram is thus a plane of measurement points. PNAH is usually used to determine the pressure and velocity distributions on a plane knowing the pressure distribution on a parallel plane. However, it can also be used for the reproduction of a target pressure field on a plane as shown by Robin *et al.* [75]. In their paper, they considered the reproduction of random pressure fields based on PNAH for the measurement of the vibroacoustic properties of plane panels. The numerical simulation showed a good reproduction of the wall-pressure fluctuations inside the acoustic circle for the considered three types of excitation: DAF, supersonic TBL and subsonic TBL. However, the system should involve a density of at least 400 monopoles per square meter for the test of a panel up to a frequency of 1 kHz in the case of a subsonic TBL. Thus PNAH is very well adapted to the synthesis of a DAF excitation or a supersonic TBL excitation.

1.3.4 Least Squares Technique

Bravo and Maury [61], Elliott *et al.* [32], Maury and Bravo [18] and Maury *et al.* [62] have widely discussed the reproduction of random excitations using an array of acoustic sources. This alternative method which uses a two-dimensional array of loudspeakers whose control filters are determined using the least squares method by minimizing the error between the desired target signals and the generated ones, hence the name *least squares technique* of this approach. It was established that this method works well when it comes to the reproduction of a DAF excitation but due to the limited number of sources in the array, it fails to simulate the WPF of a subsonic TBL excitation because of the high

Cette thèse est accessible à l'adresse : https://theses.insa-lyon.fr/publication/2022ISAL0077/these.pdf
© [A.D. Pouye], [2022], INSA Lyon, tous droits réservés

wavenumbers involved meaning that a denser source array would be required. A criteria of approximately four sources per smallest wavelength was derived in the literature in order to reproduce the small correlation lengths of the surface pressure field induced by the TBL [6, 62]. As frequency increases, the number of required sources becomes very large and as one is limited by the size of the sources, the frequency range that can be studied with a given source is also limited. In order to circumvent this issue, Maury and Bravo [60] proposed a focused synthesis of the TBL excitation over a subdomain of the simulation surface. While this method allows to reach higher frequencies and ensures correct reproduction of the TBL excitation, it also limits the observation area to a fraction of the actual panel. Always in the framework of the least squares technique, Bravo and Maury [19] proposed another alternative which consists in the reproduction of TBL-induced vibroacoustic response of a flat panel. However, this alternative requires a prior modal analysis of the panel.

1.3.5 Source Scanning Technique

We have seen that all of the methods using arrays of sources presented above are able to synthesize a DAF-like pressure fields but most of them fail to reproduce a TBL-like excitation due to the limited number of sources in the arrays. This results in a limitation in the wavenumber/frequency range that can be covered by these solutions. In order to circumvent this issue, Aucejo *et al.* introduced the Source Scanning Technique (SST) [6–8] which involves the synthetic array principle and a monopole source that is spatially displaced at predefined positions in order to virtually create a full array of sources. However, the proposed approach was only partially validated through qualitative comparisons on a rectangular steel panel for a limited frequency range (up to 300 Hz). This partial validation of SST concerned only flat panels and the process was not automatized. Furthermore, only the vibration response of the steel panel was determined.

Cette thèse est accessible à l'adresse : https://theses.insa-lyon.fr/publication/2022ISAL0077/these.pdf
© [A.D. Pouye], [2022], INSA Lyon, tous droits réservés

1.4 OBJECTIVES OF THIS THESIS

SST, as it was presented some years ago, is a promising which allows to overcome the limitations inherent to the other alternative techniques using full arrays of sources by using only one source and displacing it which means that one has much more flexibility on the spacing between two adjacent source positions. However, there were still several points to be clarified and improved for the approach to be used at industrial level.
The first task at hand is therefore the validation of SST on flat rectangular panels through a parametric study on a wider frequency range for the DAF and the TBL excitations and automatizing the process using robots. The design parameters of the synthetic array will be studied in order to define optimal values for these parameters and determine accurately the vibration response as well as the power radiated by the panel (allowing to determine the transmission loss). The results obtained using SST will then be compared to results directly measured in a reverberant room in the case of the DAF excitation and in an anechoic wind tunnel for the TBL excitation.
Once SST is completely validated for flat rectangular panels, an extension of the method to more complex structures will be proposed. This is motivated by the fact that the structures found in the transportation industry are seldom flat and that it is also interesting to explore the validity of SST for other geometrical configurations. The ultimate goal being for the method to be adopted as an alternative or complementary measurement process to the standard test means.

1.5 DISSERTATION OUTLINE

The remainder of the thesis is organized as follows. Chapter 2 of Part I is dedicated to a general presentation of the Source Scanning Technique (SST) in a theoretical point of view. Then, Part II deals with the application of SST on FRPs: Chapter 3 starts with a presentation of the study case and the theoretical background concerning panels.

Cette thèse est accessible à l'adresse : https://theses.insa-lyon.fr/publication/2022ISAL0077/these.pdf
© [A.D. Pouye], [2022], INSA Lyon, tous droits réservés

This is followed by a parametric study of the design parameters of SST. In Chapter 4, a presentation of the experimental SST setup followed by a comparison of the results to numerical and/or experimental results from direct measurement in standard facilities is proposed. In Part III, an extension of the SST process to Curved Rectangular Panels (CRPs) is proposed. First the study case and the theoretical background on CRPs are presented in Chapter 5. Subsequently is Chapter 6 where an experimental validation of SST on CRPs is proposed: the experimental setup is presented first before going through the results and discussion. Following this, a general conclusion and a discussion on future work on this topic close the main body of the manuscript. Following the main body of this thesis are several appendices with additional information and a bibliography.

Cette thèse est accessible à l'adresse : https://theses.insa-lyon.fr/publication/2022ISAL0077/these.pdf
© [A.D. Pouye], [2022], INSA Lyon, tous droits réservés

Cette thèse est accessible à l'adresse : https://theses.insa-lyon.fr/publication/2022ISAL0077/these.pdf
© [A.D. Pouye], [2022], INSA Lyon, tous droits réservés

2 SOURCE SCANNING TECHNIQUE

2.1 Synthetic array principle 33
2.2 Wavenumber formulation and quantities of interest 35
2.3 Wall-pressure plane waves 39
2.3.1 Definition 39
2.3.2 Uncorrelated WPPWs and TBL excitation 40
2.3.3 Generating WPPWs 41
2.4 Description of the SST approach 42
2.5 Summary 47

This chapter is dedicated to the presentation of the source scanning technique from a theoretical point of view. First we will talk about the synthetic array principle and the wavenumber formulation on which the SST approach is based. In particular, we will discuss how the response of structures under stochastic excitations are derived using random vibration theory along with the filtering effect. Then we will formerly introduce the SST process and its parameters. For the sake of simplicity, the structures illustrated in this chapter are flat and rectangular.

2.1 SYNTHETIC ARRAY PRINCIPLE

The synthetic array principle is inspired by the concept of the synthetic aperture radar, invented in the 1950s by Carl A. Wiley [95], and which consists in post-processing

Cette thèse est accessible à l'adresse : https://theses.insa-lyon.fr/publication/2022ISAL0077/these.pdf
© [A.D. Pouye], [2022], INSA Lyon, tous droits réservés

the signals received by a moving radar to produce fine resolution images from an intrinsically resolution-limited radar system in the along-track direction [9, 28].

Linearity is one of the most useful features that a system can have, and there is an entire branch of mathematics devoted to linear systems theory. With that in mind, what makes a system linear? Simply put, a system is considered linear if the equations that govern it follow the simple rule that the sum of the inputs to the system yields the sum of the outputs. Put mathematically, if $g(x)$ describes our system, and a and b are our inputs, then $g(a+b) = g(a) + g(b)$. In our case, the acoustic medium and the structure are assumed to behave linearly which means that the technique will not work for high sound levels or large displacements/deformations of the structure.

The synthetic array principle, which assumes a linear system, consists in using one monopole source that is spatially displaced in the desired positions in order to virtually create an array of monopole sources. Hence, the response to a full array of monopole sources is obtained by adding up the individual responses due to each monopole position. Using an actual array allows one to simultaneously drive all of the sources and proceed with an online process whereas in the case of the synthetic array, the process is an offline one.

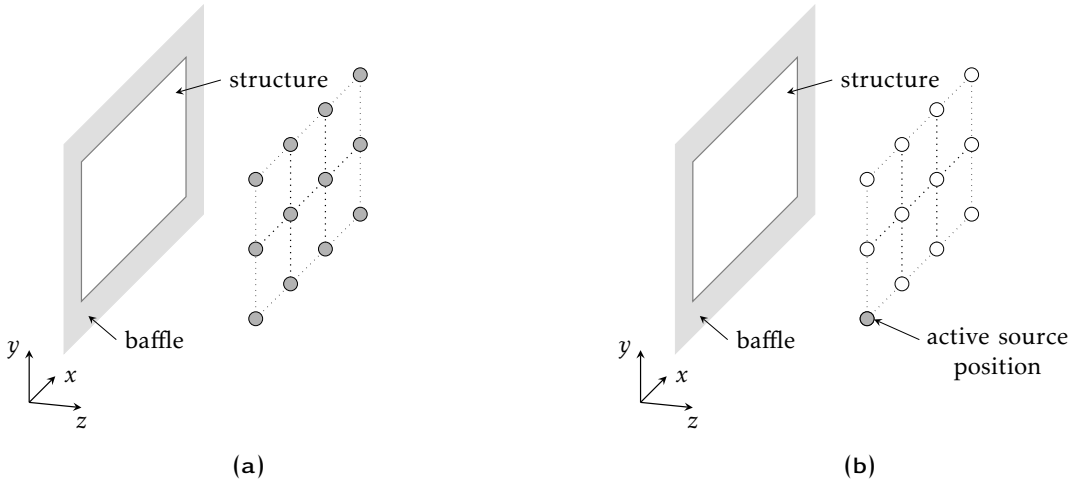

Figure 2.1: Difference between (a) an actual array of monopoles and (b) a synthetic array using only one mobile monopole.

Cette thèse est accessible à l'adresse : https://theses.insa-lyon.fr/publication/2022ISAL0077/these.pdf
© [A.D. Pouye], [2022], INSA Lyon, tous droits réservés

It is important to note that with the synthetic array approach, one needs to add a post-processing step in order to obtain the response of the structure due to the actual array using the linearity assumption stated earlier at the beginning of Sec. 2.1.

2.2 WAVENUMBER FORMULATION AND QUANTITIES OF INTEREST

This analysis considers the response of structures to random pressure fields assumed to be stationary in time and homogeneous in space, as described in [59]. Basically, this means that the our system is in a steady state response and that the forcing function time history repeats itself for all time.

Let us consider the structure of surface Σ_s illustrated in Fig. 2.2 and under random pressure field. In the following, we will assume that the wall-pressure fluctuations are not affected by the vibrations of the structure which means that the excitation is not modified by the structural response. This assumption holds as long as the flow-induced displacements are much smaller than the characteristic length scales of the flow and as long as we are further downstream from the transitional boundary layer, so that the flow is robust to small perturbations due to the vibrations of the structure [90]. This approximation makes the problem more tractable, and suitable for the derivation of analytical expressions. Thus the random excitations considered here are modeled by the wall pressure fluctuations that would be observed on a smooth rigid wall, also known as the *blocked pressure* p_b [35].

The time response of a structure, when excited by the blocked pressure p_b, is denoted $\alpha(\mathbf{x}, t)$ in general. This quantity designates either the structural velocity response $v(\mathbf{x}, t)$ or the radiated pressure by the structure $p(\mathbf{x}, t)$ or the particle velocity response $v_0(\mathbf{x}, t)$. Note that,in the first case, $\mathbf{x}$ is located on the Σ_s and in the last two cases, $\mathbf{x}$ is located

Cette thèse est accessible à l'adresse : https://theses.insa-lyon.fr/publication/2022ISAL0077/these.pdf
© [A.D. Pouye], [2022], INSA Lyon, tous droits réservés

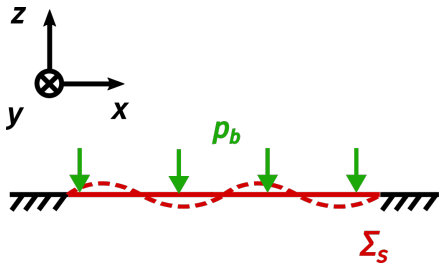

Figure 2.2: Structure under random pressure field where p_b represents the blocked pressure at the surface Σ_s.

inside the fluid domain and on the radiating side of the structure. The time response α is given by the following convolution product [59]

$$\alpha(\mathbf{x},t) = \int_{-\infty}^{+\infty} \iint_{\Sigma_s} \gamma_\alpha(\mathbf{x},\mathbf{y},t-\tau)\, p_b(\mathbf{y},\tau)\, \mathrm{d}\mathbf{x}\mathrm{d}\tau \tag{2.1}$$

where $\gamma_\alpha(\mathbf{x},\mathbf{y},t)$ is the space-time impulse response of the structure at point $\mathbf{x}$ when excited by a normal unit force at point $\mathbf{y}$. Considering the random process as ergodic, the cross-correlation function $R_{\alpha\alpha'}(\mathbf{x},t)$ can be written

$$R_{\alpha\alpha'}(\mathbf{x},t) = \int_{-\infty}^{+\infty} \alpha(\mathbf{x},t)\, \alpha'(\mathbf{x},t+\tau)\, \mathrm{d}\tau \tag{2.2}$$

where α' also designates v, p or v_0. Performing a time-Fourier transform of the cross-correlation function after introducing Eq. (2.1) in Eq. (2.2) yields the following space-frequency spectrum of the response of the structure [59, 63]

$$S_{\alpha\alpha'}(\mathbf{x},\omega) = \iint_{\Sigma_s} \iint_{\Sigma_s} \Gamma_\alpha(\mathbf{x},\mathbf{y},\omega)\, S_{p_b p_b}(\mathbf{y},\mathbf{z},\omega)\, \Gamma^*_\alpha(\mathbf{x},\mathbf{z},\omega)\, \mathrm{d}\mathbf{y}\mathrm{d}\mathbf{z} \tag{2.3}$$

where $\Gamma_\alpha(\mathbf{x},\mathbf{y},\omega)$ is the time-Fourier transform of $\gamma_\alpha(\mathbf{x},\mathbf{y},t)$ and corresponds to the FRF of the structure at point $\mathbf{x}$ when excited by a unit normal point force at point $\mathbf{y}$; $S_{p_b p_b}(\mathbf{y},\mathbf{z},\omega)$ is the time-Fourier transform of the blocked pressure cross-correlation function and the superscript "*" represents the complex conjugate.

Cette thèse est accessible à l'adresse : https://theses.insa-lyon.fr/publication/2022ISAL0077/these.pdf
© [A.D. Pouye], [2022], INSA Lyon, tous droits réservés

Defining the wavenumber-frequency spectrum of the blocked pressure $S_{p_b p_b}(\mathbf{k}, \omega)$ as the wavenumber transform of its space-frequency spectrum $S_{p_b p_b}(\mathbf{x}, \mathbf{y}, \omega)$ yields

$$S_{p_b p_b}(\mathbf{x}, \mathbf{y}, \omega) = \frac{1}{4\pi^2} \iint_{-\infty}^{+\infty} S_{p_b p_b}(\mathbf{k}, \omega) \, \mathrm{e}^{\,\mathrm{i}\mathbf{k}(\mathbf{x}-\mathbf{y})} \mathrm{d}\mathbf{k} \tag{2.4}$$

Introducing Eq. (2.4) in Eq. (2.3) and re-arranging, one obtains the following expression of the response of the structure

$$S_{\alpha\alpha'}(\mathbf{x}, \omega) = \frac{1}{4\pi^2} \iint_{-\infty}^{+\infty} H_\alpha(\mathbf{x}, \mathbf{k}, \omega) \, S_{p_b p_b}(\mathbf{k}, \omega) \, H^*_{\alpha'}(\mathbf{x}, \mathbf{k}, \omega) \, \mathrm{d}\mathbf{k} \tag{2.5}$$

where

$$H_\alpha(\mathbf{x}, \mathbf{k}, \omega) = \iint_{\Sigma_s} \Gamma_\alpha(\mathbf{x}, \mathbf{y}, \omega) \, \mathrm{e}^{\,-\mathrm{i}\mathbf{k}\mathbf{y}} \mathrm{d}\mathbf{y} \tag{2.6}$$

represents the sensitivity function and characterizes the vibroacoustic behavior of the structure. From Eq. (2.6), one can deduce that it corresponds to the response of the considered system at point $\mathbf{x}$ when it is excited by a unit WPPW of wavevector $\mathbf{k}$ at the angular frequency ω. In practice, the following discretized version of Eq. (2.5) is used

$$S_{\alpha\alpha'}(\mathbf{x}, \omega) \approx \frac{1}{4\pi^2} \sum_{\mathbf{k} \in \Omega_\mathbf{k}} H_\alpha(\mathbf{x}, \mathbf{k}, \omega) \, S_{p_b p_b}(\mathbf{k}, \omega) \, H^*_{\alpha'}(\mathbf{x}, \mathbf{k}, \omega) \, \delta\mathbf{k} \tag{2.7}$$

where $\Omega_\mathbf{k}$ is a set of properly chosen wavevectors.
The two quantities of interest being the vibration response as well as the transmission loss of the structure, let us introduce them hereunder.

VIBRATION RESPONSE The velocity response of the structure at a given point $\mathbf{x}$ is obtained by replacing α and α' with v in Eq. (2.7)

$$S_{vv}(\mathbf{x}, \omega) \approx \frac{1}{4\pi^2} \sum_{\mathbf{k} \in \Omega_\mathbf{k}} S_{p_b p_b}(\mathbf{k}, \omega) \left| H_v(\mathbf{x}, \mathbf{k}, \omega) \right|^2 \delta\mathbf{k} \tag{2.8}$$

Cette thèse est accessible à l'adresse : https://theses.insa-lyon.fr/publication/2022ISAL0077/these.pdf
© [A.D. Pouye], [2022], INSA Lyon, tous droits réservés

Looking at the previous equation, one can conclude that the velocity sensitivity functions $H_v(\mathbf{x}, \mathbf{k}, \omega)$ have to be determined in order to estimate the velocity response ASD function $S_{vv}(\mathbf{x}, \omega)$ and the way to do so will be discussed in Sec. 2.4.

TRANSMISSION LOSS The sound transmission loss, denoted TL, is a measure of the performance of a structure in preventing transmission of sound from one space to another. It is defined as ten times the logarithm in base ten of the ratio of the sound power incident on the structure to the sound power radiated by the structure on the receiving side, as indicated by the following equation

$$\mathrm{TL}(\omega) = 10 \log_{10} \left[\frac{\Pi_i(\omega)}{\Pi_r(\omega)} \right] \tag{2.9}$$

where Π_i and Π_r denote the incident power and the radiated power by the structure, respectively.

The incident power will be discussed in Chapter 3 and Chapter 5 for each of the considered random pressure fields. The radiated power is defined by the following equation

$$\Pi_r(\omega) = \iint_{\Sigma_p} I_{act}(\mathbf{x}, \omega) \, \mathrm{d}\mathbf{x} \tag{2.10}$$

where $\mathrm{d}\mathbf{x}$ is the surface element and $I_{act}(\mathbf{x}, \omega)$ is the normal component of the active sound intensity at point $\mathbf{x}$. The active sound intensity is directly related to the CSD function $S_{pv_0}(\mathbf{x}, \omega)$ between the sound pressure and the particle velocity at point $\mathbf{x}$ [36]

$$I_{act}(\mathbf{x}, \omega) = \mathfrak{Re}\left[S_{pv_0}(\mathbf{x}, \omega) \right] \tag{2.11}$$

where $\mathfrak{Re}$ designates the real part and from Eq. (2.7), replacing α by p and α' by v_0 one has

Cette thèse est accessible à l'adresse : https://theses.insa-lyon.fr/publication/2022ISAL0077/these.pdf
© [A.D. Pouye], [2022], INSA Lyon, tous droits réservés

$$S_{pv_0}(\mathbf{x},\omega) \approx \frac{1}{4\pi^2} \sum_{\mathbf{k}\in\Omega_\mathbf{k}} H_p(\mathbf{x},\mathbf{k},\omega)\, S_{pp}(\mathbf{k},\omega)\, H^*_{v_0}(\mathbf{x},\mathbf{k},\omega)\, \delta\mathbf{k} \tag{2.12}$$

In practice, a discretized version of Eq. (2.10) will be used

$$\Pi_r(\omega) \approx \sum_{\mathbf{x}\in\Sigma_r} I_{act}(\mathbf{x},\omega)\, \delta\mathbf{x} \tag{2.13}$$

where Σ_r is a virtual surface at a certain distance z on the radiating side of the structure. Here again, in order to compute the CSD function between the radiated pressure by the structure and the particle velocity on the radiating side of the structure $S_{pv_0}(\mathbf{x},\omega)$, one will need to determine the radiated pressure sensitivity function $H_p(\mathbf{x},\mathbf{k},\omega)$ and the particle velocity sensitivity function $H_{v_0}(\mathbf{x},\mathbf{k},\omega)$. As for the velocity sensitivity function, these two other types of sensitivity function will be determined using the SST approach.

2.3 WALL-PRESSURE PLANE WAVES

Here, we will answer the following questions: What is a Wall-Pressure Plane Wave (WPPW)? How can we use them in order to model a TBL pressure field through the CSD function? How can we experimentally generate them?

2.3.1 Definition

In room acoustics, a diffuse field can be approximated by adding up the effect of an infinite number of acoustic plane waves having the same amplitudes and emanating from all directions [72]. A WPPW is defined as the blocked pressure acting at the surface of a structure when excited by a pressure field due to a DAF or TBL excitations for instance.

Cette thèse est accessible à l'adresse : https://theses.insa-lyon.fr/publication/2022ISAL0077/these.pdf
© [A.D. Pouye], [2022], INSA Lyon, tous droits réservés

As for a plane wave, the pressure induced by a WPPW η is defined by an amplitude A_η and a two-dimensional wavevector $\mathbf{k}_\eta = \left(k_x^\eta, k_y^\eta\right)$. Hence, it can be defined as follows

$$p_\eta(\mathbf{x}, t) = A_\eta(t)\, \mathrm{e}^{-\mathrm{i}\mathbf{k}_\eta \mathbf{x}} \tag{2.14}$$

where $A_\eta(t)$ is a random variable.
It is important to note that WPPWs are only defined at the very surface of the structure and do not depend on the acoustic propagation as for a simple plane wave. The pressure CSD function corresponding to the WPPW is therefore

$$S_{p_\eta p_\eta}(\boldsymbol{\xi}, \omega) = S_{A_\eta A_\eta}(\omega)\, \mathrm{e}^{-\mathrm{i}\mathbf{k}_\eta \boldsymbol{\xi}} \tag{2.15}$$

where $\boldsymbol{\xi} = \left(\xi_x, \xi_y\right)$ is the vector representing the spatial shift between two points on the surface of the structure and $S_{A_\eta A_\eta}(\omega)$ is the ASD function of the amplitude of the WPPWs. Let us suppose a rigid surface excited by a set of uncorrelated WPPWs. The total pressure $p(\mathbf{x}, t)$ is given by

$$p(\mathbf{x}, t) = \sum_\eta p_\eta(\mathbf{x}, t) \tag{2.16}$$

As the WPPWs are supposed uncorrelated, one has $S_{A_\eta A'_\eta}(\omega) = 0$ if $\eta \neq \eta'$. Consequently, the CSD function of the total pressure $p(\mathbf{x}, t)$ is

$$S_{pp}(\boldsymbol{\xi}, \omega) = \sum_\eta S_{A_\eta A_\eta}(\omega)\, \mathrm{e}^{-\mathrm{i}\mathbf{k}_\eta \boldsymbol{\xi}} \tag{2.17}$$

2.3.2 Uncorrelated WPPWs and TBL excitation

The goal here is to establish a relationship between uncorrelated WPPWs and the TBL excitation through their CSD functions. The CSD function of the TBL excitation $S_{pp}(\boldsymbol{\xi}, \omega)$

Cette thèse est accessible à l'adresse : https://theses.insa-lyon.fr/publication/2022ISAL0077/these.pdf
© [A.D. Pouye], [2022], INSA Lyon, tous droits réservés

in the space-frequency domain is related to that in the wavenumber-frequency domain $S_{pp}(\mathbf{k},\omega)$ by the following inverse space-Fourier transform

$$S_{pp}(\boldsymbol{\xi},\omega) = \frac{1}{4\pi^2}\iint_{-\infty}^{+\infty} S_{pp}(\mathbf{k},\omega)\,\mathrm{e}^{-\mathrm{i}\mathbf{k}\boldsymbol{\xi}}\mathrm{d}\mathbf{k} \tag{2.18}$$

In practice, a discretized version of Eq. (2.18) is used

$$S_{pp}(\boldsymbol{\xi},\omega) = \frac{1}{4\pi^2}\sum_{\Omega_{\mathbf{k}}} S_{pp}(\mathbf{k},\omega)\,\mathrm{e}^{-\mathrm{i}\mathbf{k}\boldsymbol{\xi}}\Delta\mathbf{k} \tag{2.19}$$

where $\Omega_{\mathbf{k}}$ represents a set of wavevectors and $\Delta\mathbf{k} = \delta k_x \delta k_y$ with δk_x and δk_y corresponding to the wavenumber resolutions in the x and y directions, respectively.
Equalizing Eq. (2.17) and Eq. (2.19) and assuming that the sums are both defined over the same set of wavevectors $\Omega_{\mathbf{k}}$, one can establish the following relation between the ASD function of the amplitude of the WPPW and the CSD function of the TBL excitation in the wavenumber-frequency domain

$$S_{A_\eta A_\eta}(\omega) = \frac{1}{4\pi^2} S_{pp}(\mathbf{k},\omega)\,\Delta\mathbf{k} \tag{2.20}$$

where $\mathbf{k} \in \Omega_{\mathbf{k}}$. This set $\Omega_{\mathbf{k}}$ is chosen depending on what one wants to achieve by approximating the TBL excitation with uncorrelated WPPWs.

2.3.3 Generating WPPWs

In the following, the generation of WPPWs is discussed. To begin with, let us remember that a WPPW and an acoustic plane wave are two different concepts. Let us consider an acoustic plane wave of unit amplitude, the pressure induced by this wave can be written as

$$p_{ac}(\mathbf{x},t) = \mathrm{e}^{-\mathrm{i}\mathbf{k}\mathbf{x}} \tag{2.21}$$

Cette thèse est accessible à l'adresse : https://theses.insa-lyon.fr/publication/2022ISAL0077/these.pdf
© [A.D. Pouye], [2022], INSA Lyon, tous droits réservés

where $\mathbf{k} = \left(k_x, k_y, k_z\right)$ and $\mathbf{x} = (x, y, z)$.

It is important to note that, in this case, the components of the three-dimensional wavevector $\mathbf{k}$ must satisfy the following dispersion relation of the Helmholtz equation

$$k_x^2 + k_y^2 + k_z^2 = k_0^2 \tag{2.22}$$

where k_0 represents the acoustic wavenumber in the considered medium.

In the case of a WPPW η, as the wavenumbers in the x and y directions are *a priori* known (as discussed in Sec. 2.3.2), the wavenumber in the direction perpendicular to the surface of the structure must satisfy

$$k_z^\eta = \begin{cases} \pm\sqrt{k_0^2 - {k_x^\eta}^2 - {k_y^\eta}^2} & \text{if } k_0 > {k_x^\eta}^2 + {k_y^\eta}^2 \\ \pm \mathrm{i}\sqrt{{k_x^\eta}^2 + {k_y^\eta}^2 - k_0^2} & \text{if } k_0 < {k_x^\eta}^2 + {k_y^\eta}^2 \end{cases} \tag{2.23}$$

The previous equation clearly indicates that wall-pressure fields corresponding to those of propagating (k_z^η is real) and evanescent (k_z^η is complex) acoustic plane waves must be generated to simulate a TBL wall-pressure field from uncorrelated WPPWs. It is very difficult to experimentally create evanescent plane waves normal to the surface of the structure. However, one can achieve this by using an array of monopole sources by simulating the required near-field interferential conditions.

2.4 DESCRIPTION OF THE SST APPROACH

The proposed approach is based on the mathematical formulation of the problem in the wavenumber domain. This formulation is appropriate because it allows, through Eq. (2.5), an explicit separation of the contributions of the excitation *via* the wall-pressure CSD function from those of the vibroacoustic behavior of the structure *via* the sensitivity functions discussed above.

Cette thèse est accessible à l'adresse : https://theses.insa-lyon.fr/publication/2022ISAL0077/these.pdf
© [A.D. Pouye], [2022], INSA Lyon, tous droits réservés

Let us consider a unit WPPW characterized by the wavevector $\mathbf{k}$ and the angular frequency ω. The pressure at the surface of the structure that will be referred to as the reproduction surface is simply given by $p(\mathbf{x}, \mathbf{k}, \omega) = e^{-i\mathbf{kx}}$. The SST process can be divided into four main steps that will allow us to reproduce this target pressure field from S positions of the monopole source.

1. **Definition of the target pressure at the observation points:** one supposes that the reproduction surface is regularly discretized in P observation points and one defines the target pressure vector as the vector with the components corresponding to the pressure of the unit WPPW at the P points. The spacing between the points should be sufficiently small to describe the spatial variation of the WPPW.

2. **Characterization of the acoustic source:** one determines the transfer functions (G_{ps}) between source positions $s \in [1, S]$ and observation points $p \in [1, P]$ on the structure as shown in Fig. 2.3, and define the transfer function matrix $\mathbf{G}$ as the matrix having the transfer functions G_{ps} as components.

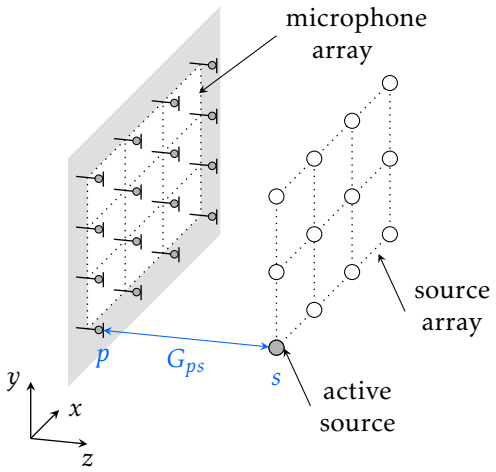

Figure 2.3: Description of the transfer function $G_{ps}(\omega)$

Cette thèse est accessible à l'adresse : https://theses.insa-lyon.fr/publication/2022ISAL0077/these.pdf
© [A.D. Pouye], [2022], INSA Lyon, tous droits réservés

3. **Computation of the vector of source amplitudes q** by inverting the following matrix equation

$$\mathbf{Gq} = \mathbf{p} \tag{2.24}$$

that can be rewritten explicitly as

$$\sum_{s=1}^{S} G_{ps}(\omega)\, q_s(\mathbf{k},\omega) = p_p(\mathbf{k},\omega),\ \forall p \in [1,P] \tag{2.25}$$

where $q_s(\mathbf{k},\omega)$ is the amplitude of the source at position s and $p_p(\mathbf{k},\omega) = \mathrm{e}^{-\mathrm{i}\left(k_x x_p + k_y y_p\right)}$ represents the target pressure at the observation point p whose coordinates are x_p and y_p on the structure.

When the number of observation points P is less than the number of source positions S, the system in Eq. (2.24) is underdetermined and has an infinite number of solutions. However, when $P > S$, the system is overdetermined and does not have one single exact solution. Nevertheless, a solution minimizing the error between the target pressure and the synthesized one can be determined. The matrix **G** is then rectangular, therefore Eq. (2.24) is solved in the least squares sense as

$$\mathbf{q} = \mathbf{G}^{\dagger}\mathbf{p} \tag{2.26}$$

The dagger symbol in Eq. (2.26) indicates the Moore-Penrose pseudo-inverse. The reproduction of a target pressure field using an array of acoustic sources is thus an inverse problem which leads to some issues that will be discussed later on.

4. **Synthesis of the target pressure field and of the sensitivity function:** in order to assess the quality of the reconstructed pressure field, one considers Q points on the reproduction surface. These Q points must be different from the P reference points in order to estimate the ability of the technique to reproduce correctly the pressure field between the reference points. After the transfer function matrix $\hat{\mathbf{G}}$

Cette thèse est accessible à l'adresse : https://theses.insa-lyon.fr/publication/2022ISAL0077/these.pdf
© [A.D. Pouye], [2022], INSA Lyon, tous droits réservés

between the S source positions and the Q reconstruction points is determined, the vector of the reconstructed pressure $\hat{\mathbf{p}}$ can be computed with the following expression: $\hat{\mathbf{p}} = \hat{\mathbf{G}}\mathbf{q}$. One will use this expression in the following to estimate the efficiency of the SST and to define the optimal parameters of the synthetic array. However, in practice, it will not be used, as only the sensitivity functions are of interest to estimate the response of the structure to the stochastic excitation. The sensitivity functions are given by the following equation

$$H_\alpha(\mathbf{x}, \mathbf{k}, \omega) = \sum_{s=1}^{S} q_s(\mathbf{k}, \omega) \Gamma_\alpha^s(\mathbf{x}, \omega) \tag{2.27}$$

where $\alpha = (v, p, v_0)$ and $\Gamma_\alpha^s(\mathbf{x}, \omega)$ represents the FRF between point $\mathbf{x}$ and the source at position s and is defined as the response α at point $\mathbf{x}$ when the source is located at point s.

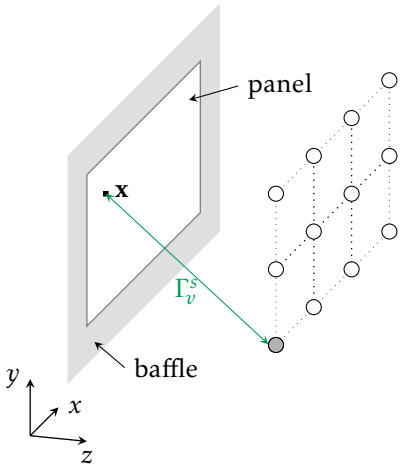

Figure 2.4: Description of the velocity FRF $\Gamma_v^s(\mathbf{x}, \omega)$

Step 2 is generally achieved only one time whereas the other steps can be repeated to cover the set of wavevectors of interest in Eq. (2.5). Once the sensitivity functions have been determined using Eq. (2.27) for the set of wavevectors of interest, the response of the structure to the stochastic excitation can be estimated with Eq. (2.7) and the model

Cette thèse est accessible à l'adresse : https://theses.insa-lyon.fr/publication/2022ISAL0077/these.pdf
© [A.D. Pouye], [2022], INSA Lyon, tous droits réservés

of the wall-pressure field as described in the Sec. 1.1.2 and Sec. 1.1.3 for the DAF and the TBL, respectively.

Naturally, there are design parameters that are inherent to this approach and whose values need to be carefully chosen for a good reproduction process. These parameters are

- the cutoff wavenumber $\bar{k}$ which allows one to define the set of wavevectors $\Omega_{\mathbf{k}}$ over which one has an accurate synthesis of the response of the structure,
- the distance d_m between two adjacent monopole positions (see Fig. 2.5), and
- the distance d between the structure and the array of monopoles which will be determined through an analysis of the condition number of the transfer matrix $\mathbf{G}$ and the relative mean square error between the target WPPWs and the synthesized ones. See Fig. 2.5 for a depiction of this distance.

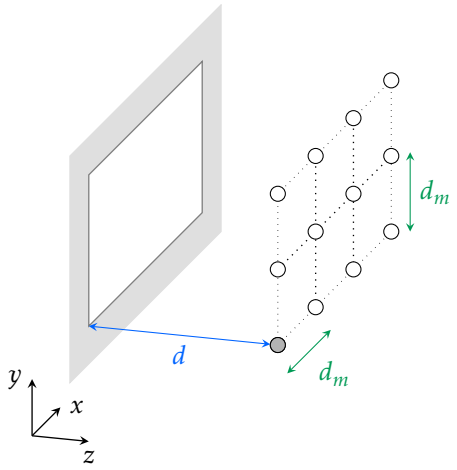

Figure 2.5: Description of the distance d between the structure and the synthetic monopole array and that of the distance d_m between two adjacent monopole positions in the x and y directions.

Cette thèse est accessible à l'adresse : https://theses.insa-lyon.fr/publication/2022ISAL0077/these.pdf
© [A.D. Pouye], [2022], INSA Lyon, tous droits réservés

2.5 SUMMARY

This chapter was dedicated to the presentation of the SST approach and its theoretical background. The method is based on the synthetic array principle where one monopole source is spatially displaced in several positions in order to reconstruct the effect of a full array of monopoles. The technique relies on a formulation of the vibroacoustic problem in the wavenumber domain: this allows one to be able to simulate a TBL excitation through uncorrelated WPPWs. The same can be done for the DAF excitation. Apart from the CSD functions of the DAF and TBL, the other difference originating from the modeling of these two excitations through uncorrelated WPPWs is in the very nature of the waves. In the case of the DAF, only propagating waves are needed whereas in the TBL case, one also needs to produce evanescent waves. The main design parameters of the synthetic monopole array have been presented: a study of the influence of these parameters is done in Chapter 3 and Chapter 5 for rectangular panels and open circular cylindrical shells, respectively.

Cette thèse est accessible à l'adresse : https://theses.insa-lyon.fr/publication/2022ISAL0077/these.pdf
© [A.D. Pouye], [2022], INSA Lyon, tous droits réservés

Cette thèse est accessible à l'adresse : https://theses.insa-lyon.fr/publication/2022ISAL0077/these.pdf
© [A.D. Pouye], [2022], INSA Lyon, tous droits réservés

Part II

APPLICATION ON FLAT RECTANGULAR PANELS

Cette thèse est accessible à l'adresse : https://theses.insa-lyon.fr/publication/2022ISAL0077/these.pdf
© [A.D. Pouye], [2022], INSA Lyon, tous droits réservés

Cette thèse est accessible à l'adresse : https://theses.insa-lyon.fr/publication/2022ISAL0077/these.pdf
© [A.D. Pouye], [2022], INSA Lyon, tous droits réservés

3 SST ON FLAT RECTANGULAR PANELS: THEORY AND NUMERICAL STUDIES

3.1 Problem statement 51
3.2 Theoretical responses 53
3.2.1 Vibration response - Sensitivity functions 53
3.2.2 Transmission loss 53
3.3 SST on flat rectangular panels: parametric studies 54
3.3.1 Cutoff wavenumber and wavenumber resolution 55
3.3.2 Interplanar distance 56
3.4 Summary 62

The next two chapters are dedicated to the application of SST on flat panels: theoretical background and parametric study in Chapter 3, and experimental validation in Chapter 4. The case study concerns a rectangular aluminum flat panel simply supported on its edges. In this chapter, the problem of interest is described in a first step. Secondly, a theoretical background on mechanics of panels and the computation of the quantities of interest (vibration response and transmission loss) are presented. Afterwards, a parametric study on the design parameters of the synthetic array of monopoles is proposed before closing the chapter with a brief summary.

3.1 PROBLEM STATEMENT

This analysis considers the response of two-dimensional rectangular planar structures to a random pressure field excitation. This pressure field is assumed to be stationary in time

Cette thèse est accessible à l'adresse : https://theses.insa-lyon.fr/publication/2022ISAL0077/these.pdf
© [A.D. Pouye], [2022], INSA Lyon, tous droits réservés

and homogeneous in space. We will be interested in two types of random excitations: the diffuse acoustic field and the turbulent boundary layer excitations. The quantities of interest will be the ASD function of the velocity at one point on the panel and the sound transmission loss of the considered panel.

The geometric configuration of the studied structure of surface Σ_p is shown in Fig. 3.1. The geometric parameters characterizing the panel are the length L_x, the width L_y and the thickness h.

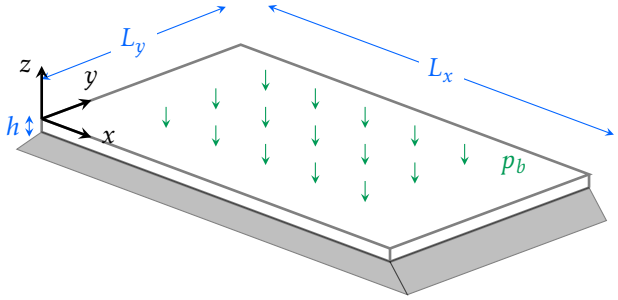

Figure 3.1: Simply supported panel subject to an excitation p_b.

In the following, we will assume that the WPFs are not affected by the vibrations of the structure which means that the excitation is not modified by the structural response. Thus the random excitations considered in this paper are modeled by the WPFs that would be observed on a smooth rigid wall, also known as the *blocked pressure* p_b [35].

The goal here is to determine the vibroacoustic responses of the panel by reproducing WPFs that are close enough to the target WPFs using SST. The transverse velocity $v_z(\mathbf{x}, t)$, which will be simply written as $v(\mathbf{x}, t)$ throughout this dissertation, represents the vibration response of the panel when excited by a normal random pressure field $p_b(\mathbf{x}, t)$. The transmission loss denoted $\mathrm{TL}(\omega)$, introduced in Sec. 2.2, gives a measure in decibels (dB) of the ability of the structure to reduce sound energy transmission. In a first step, let us briefly derive the expression of these two quantities of interest for the considered panel.

Cette thèse est accessible à l'adresse : https://theses.insa-lyon.fr/publication/2022ISAL0077/these.pdf
© [A.D. Pouye], [2022], INSA Lyon, tous droits réservés

3.2 THEORETICAL RESPONSES

3.2.1 Vibration response - Sensitivity functions

The ASD function of the vibration response of a given structure under random excitation was derived in Chapter 2 and is given by Eq. (2.8) which is rewritten hereunder

$$S_{vv}(\mathbf{x},\omega) \approx \frac{1}{4\pi^2} \sum_{\mathbf{k}\in\Omega_{\mathbf{k}}} S_{p_b p_b}(\mathbf{k},\omega) |H_v(\mathbf{x},\mathbf{k},\omega)|^2 \, \delta\mathbf{k}$$

The previous equation clearly shows that one needs to estimate the velocity sensitivity functions $H_v(\mathbf{x},\mathbf{k},\omega)$ in order to determine the ASD function of the vibration response. These functions are theoretically determined using a modal expansion method. In general, the standard expression of the velocity sensitivity functions $H_v(\mathbf{x},\mathbf{k},\omega)$ written using a modal expansion is given by Eq. (A.1) and all the details about the computation of these functions are also given in Appendix A.

3.2.2 Transmission loss

The transmission loss was also introduced in Chapter 2 through Eq. (2.9) rewritten below

$$\mathrm{TL}(\omega) = 10\log_{10}\left[\frac{\Pi_i(\omega)}{\Pi_r(\omega)}\right]$$

In order to determine the radiated power $\Pi_r(\omega)$ defined by Eq. (2.13), one needs to determine the pressure sensitivity function $H_p(\mathbf{x},\mathbf{k},\omega)$ and the particle velocity sensitivity function $H_{v_0}(\mathbf{x},\mathbf{k},\omega)$. However, as can be observed in Appendix B, one can use only one of these two types of sensitivity functions as they are related through Eq. (B.13), in order to determine the CSD function $S_{pv_0}(\mathbf{x},\omega)$ between the pressure and the particle velocity

Cette thèse est accessible à l'adresse : https://theses.insa-lyon.fr/publication/2022ISAL0077/these.pdf
© [A.D. Pouye], [2022], INSA Lyon, tous droits réservés

at point **x**. Appendix B also shows the derivation of the theoretical power radiated by the panel.

Now, let us talk about the incident power on the panel $\Pi_i(\omega)$. Its expression depends on the type of excitation. For a panel excited by a DAF in a reverberant room, the incident power corresponds to the power in the reverberant room, far away from the surface of the panel. According to Sabine's theory, the incident power depends on the ASD function $S_{p_b p_b}(\omega)$ of the acoustic pressure, the celerity of sound c_0, the density of the medium ρ_0 and the surface of the panel Σ_p through the following equation [34]

$$\Pi_i(\omega) = \frac{S^{DAF}_{p_b p_b}(\omega)\,\Sigma_p}{8\rho_0 c_0} \tag{3.1}$$

For a TBL, there is no incident acoustic pressure in the farfield. Nevertheless, in order to compare both excitation fields, we define an equivalent incident power $\Pi^{eq}_i(\omega)$, which will be the one of a DAF having a sound power CSD function equal to $S^{TBL}_{pp}(\omega)$ on the plate surface. The equivalent incident power is thus given by the following equation

$$\Pi^{eq}_i(\omega) = \frac{S^{TBL}_{p_b p_b}(\omega)\,\Sigma_p}{8\rho_0 c_0} \tag{3.2}$$

where $S^{TBL}_{p_b p_b}(\omega)$ corresponds, this time, to the ASD function of the TBL WPF.

3.3 SST ON FLAT RECTANGULAR PANELS: PARAMETRIC STUDIES

In the following, some parametric investigations on the SST are proposed. These studies aim at determining the optimal parameters of the array of sources for an accurate reproduction of the vibroacoustic response of the structure. The numerical simulations presented in this section concern a panel with the same geometrical and mechanical properties (see Table 3.1) as the one considered for the experimental work presented

Cette thèse est accessible à l'adresse : https://theses.insa-lyon.fr/publication/2022ISAL0077/these.pdf
© [A.D. Pouye], [2022], INSA Lyon, tous droits réservés

in Chapter 4. The panel is supposed simply supported on its four edges. The normal modes are then calculated analytically and the sensitivity functions can be estimated using the modal expansion method as described in Sec. 3.2.1 and more thoroughly in Appendix A.

Table 3.1: Panel parameters

Parameter	Symbol	Value
Young modulus	E	68.9 GPa
Poisson ratio	ν	0.3
Mass density	ρ	2740 kg m^{-3}
Length	L_1	0.48 m
Width	L_2	0.42 m
Thickness	h	3.17 mm

3.3.1 Cutoff wavenumber and wavenumber resolution

The minimum separation between the source positions is derived from the maximum wavenumber or the minimum wavelength to be synthesized. For frequencies well above the hydrodynamic coincidence frequency and accordingly to Marchetto et al. [58], the wavenumber domain $\Omega_{\mathbf{k}}$ over which Eq. (2.7) is calculated must at least include the flexural wavenumber of the panel at the highest frequency of interest. The natural flexural wavenumber of a thin panel is given by the following equation

$$k_f(\omega) = \sqrt[4]{\omega^2 \frac{\rho h}{D}} \tag{3.3}$$

where $D = \dfrac{Eh^3}{12(1-\nu^2)}$ is the flexural rigidity of the panel.
Thus the smallest cutoff wavenumber from which the spacing δ_s between the source positions is defined is set to

$$k_{max} = \beta k_f(\omega_{max}) \tag{3.4}$$

Cette thèse est accessible à l'adresse : https://theses.insa-lyon.fr/publication/2022ISAL0077/these.pdf
© [A.D. Pouye], [2022], INSA Lyon, tous droits réservés

where β is a safety coefficient such that $\beta > 1$ and ω_{max} corresponds to the maximum frequency of interest.

The spacing between two adjacent source positions is then defined using the criteria of four monopoles per smallest wavelength (as shown in previous studies [6, 62])

$$\delta_s = \frac{\lambda_{min}}{4} \tag{3.5}$$

where $\lambda_{min} = 2\pi/k_{max}$.

Let us now talk about the wavenumber resolution. Numerical simulations do not show that the wavenumber resolution is a critical parameter as $H_\alpha(\mathbf{x}, \mathbf{k}, \omega)$ and $S_{p_b p_b}(\mathbf{k}, \omega)$ do not vary quickly with respect to the wavenumber. Moreover, SST can deal with fine resolution as the wavenumber resolution only affects the post-processing steps. In the following, the wavenumber resolution is set to $\delta k_{x,y} = 1\,\mathrm{rad\,m^{-1}}$.

3.3.2 Interplanar distance

The interplanar distance represents the distance between the source array plane and the panel plane (or reproduction plane). The study presented in this section aims at defining the optimal interplanar distance ensuring an accurate pressure synthesis.

In order to assess the quality of the reproduction process, two different parameters are examined:

- The condition number of the transfer matrix $\mathbf{G}$ denoted $\kappa(\mathbf{G})$ which is a measure of the sensitivity of the sought parameters (i.e. the amplitudes of the sources) with respect to perturbations in the input data and round-off errors made while solving Eq. (2.24) for $\mathbf{q}$.

  The condition number of a matrix $\mathbf{A}(m \times n)$ is defined as follows

$$\kappa(\mathbf{A}) = \frac{\sigma_1}{\sigma_n} \quad \text{with} \quad \sigma_1 >> 1 >> \sigma_n > 0$$

Cette thèse est accessible à l'adresse : https://theses.insa-lyon.fr/publication/2022ISAL0077/these.pdf
© [A.D. Pouye], [2022], INSA Lyon, tous droits réservés

where σ_1 and σ_n are the greatest and the smallest singular values of matrix $\mathbf{A}$ and are determined from the singular value decomposition of matrix $\mathbf{A}$.

When the condition number is large, the computed solution of the system may be in error. Values of the condition number near one indicate a well-conditioned matrix whereas large values indicate an ill-conditioned matrix [24].

- The Mean Square Error (MSE) on the synthesized pressure field denoted e_p is defined by the following equation

$$e_p\left(k_x, k_y, \omega\right) = \frac{E\left[\left\|\mathbf{p}\left(\mathbf{x}, k_x, k_y, \omega\right) - \hat{\mathbf{p}}\left(\mathbf{x}, k_x, k_y, \omega\right)\right\|\right]^2}{\left\|\mathbf{p}\left(\mathbf{x}, k_x, k_y, \omega\right)\right\|^2} \tag{3.6}$$

where $\mathbf{p}\left(\mathbf{x}, k_x, k_y, \omega\right)$ and $\hat{\mathbf{p}}\left(\mathbf{x}, k_x, k_y, \omega\right)$ are the target and reconstructed pressure vectors, respectively, $\|\bullet\|$ represents the Euclidean norm and $E[\bullet]$ represents an ensemble average also referred to as the mathematical expectation (or expected value) of the considered parameter. Note that the relative MSE is a spatial average over the panel. An arbitrary threshold of -10 dB (corresponding to a relative MSE of 10%) is chosen in order to gauge the accuracy of the reproduction process. As long as the relative MSE (which will be called the reproduction error in the following) is less than that threshold, the pressure field synthesis will be considered accurate.

Fig. 3.2 shows the two quantities presented above plotted as functions of frequency and the normalized interplanar distance (with respect to λ_{min}). In Fig. 3.2a, one can notice that the condition number of the transfer matrix is almost frequency independent but increases when the interplanar distance increases. This means that the closer the array of acoustic sources is to the panel plane, the less sensitive the system is to noise. In order to avoid large condition numbers, an upper limit of the interplanar distance d is set to $\frac{\lambda_{min}}{2}$. Concerning the mean square error in Fig. 3.2b, one observes that it is roughly constant as a function of the frequency for a given interplanar distance. On the contrary, its evolution as a function of the interplanar distance for a given frequency is

Cette thèse est accessible à l'adresse : https://theses.insa-lyon.fr/publication/2022ISAL0077/these.pdf
© [A.D. Pouye], [2022], INSA Lyon, tous droits réservés

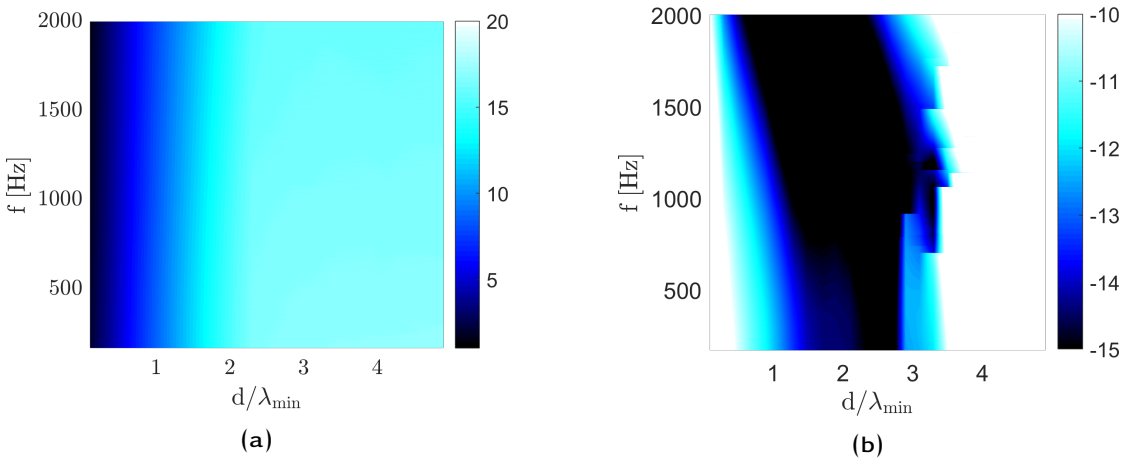

Figure 3.2: Optimal interplanar distance: (a) logarithm of the condition number ($\log_{10}(\kappa)$) of the transfer matrix, (b) reproduction error e_p (dB, ref. 1) on the reconstructed pressure field according to Eq. (3.6) for $k_x = k_{max}$ and $k_y = 0$. Both quantities are plotted as functions of frequency and the interplanar distance normalized by the smallest wavelength to be synthesized.

similar to a U-shaped valley: the error is relatively high when the interplanar distance is small, typically smaller than $\frac{\lambda_{min}}{10}$ or larger than $3\lambda_{min}$. Between these two limits (i.e. for $d \in \left]\frac{\lambda_{min}}{10}, 3\lambda_{min}\right[$), the reproduction error for the maximum wavenumber considered is less than the threshold defined earlier. In the end, the optimal interval for the interplanar distance d and for an accurate reproduction process is defined by the intersection of the previous intervals defined from Fig. 3.2a and Fig. 3.2b: $I_{opt} = \left]\frac{\lambda_{min}}{10}, \frac{\lambda_{min}}{2}\right[$.
On Fig. 3.3 the reproduction error e_p is plotted as a function of frequency and wavenumbers in both directions (i.e. k_x for Fig. 3.3a, 3.3c and k_y for Fig. 3.3b, 3.3d) and for two interplanar distances: one outside the interval I_{opt} and the other within I_{opt}. There is an almost identical evolution of the reproduction error along k_x and k_y directions. One can notice that although the reproduction error in Fig. 3.3a and 3.3b complies with the criterion (less than −10 dB) for wavenumbers in the interval $[-30, 30]\,\mathrm{rad\,m^{-1}}$, it is not the case for wavenumbers outside this interval. This result was expected as the corresponding interplanar distance is not within I_{opt}. On the contrary, in Fig. 3.3c and 3.3d, one can observe that the reproduction is accurate for all the wavenumbers of

Cette thèse est accessible à l'adresse : https://theses.insa-lyon.fr/publication/2022ISAL0077/these.pdf
© [A.D. Pouye], [2022], INSA Lyon, tous droits réservés

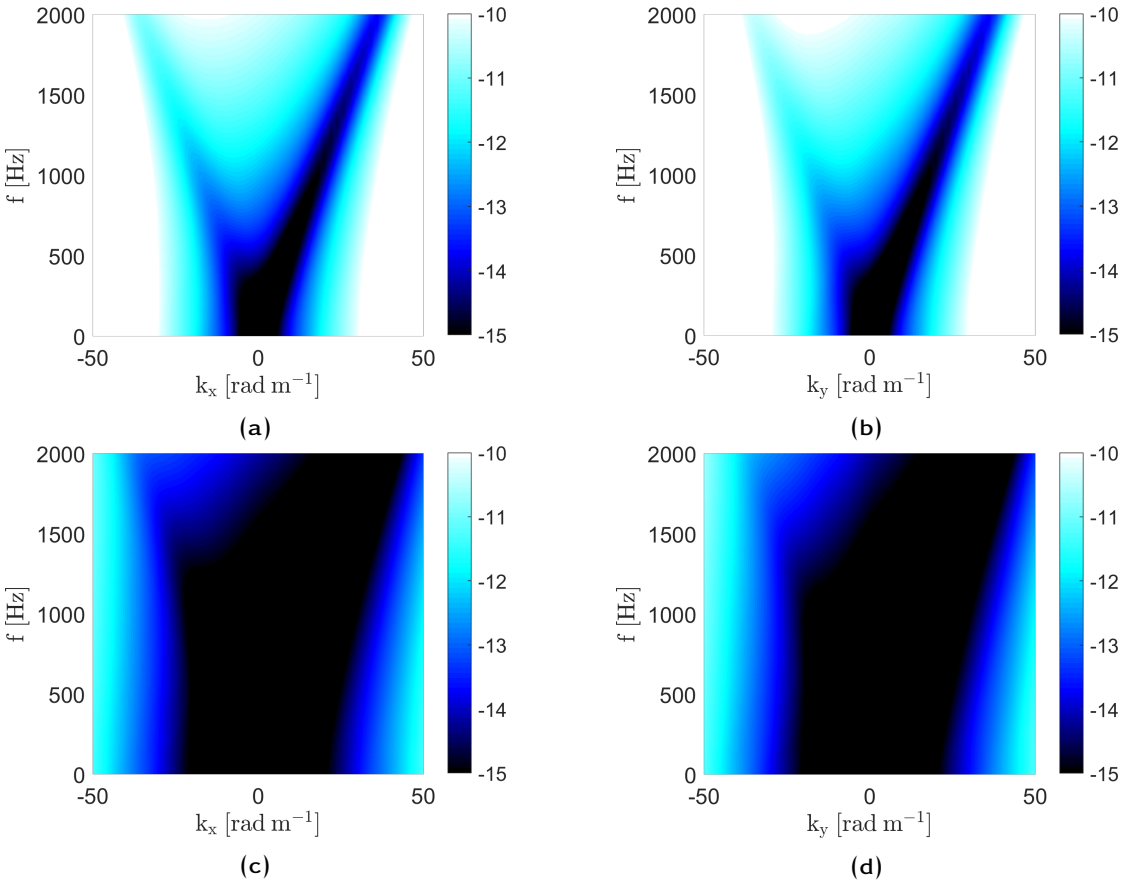

Figure 3.3: Reproduction error e_p (dB, ref. 1) in the wavenumber-frequency domain for two different interplanar distances. (a) along k_x, $k_y = 0$ and (b) along k_y, $k_x = 0$ for $d = \frac{\lambda_{min}}{10}$. (c) along k_x, $k_y = 0$ and (d) along k_y, $k_x = 0$ for $d = \frac{\lambda_{min}}{4}$.

interest and that it is in agreement with the proposed criterion as the corresponding interplanar distance is within I_{opt}.

Fig. 3.4 shows the reproduction error for the same interplanar distance as in Fig. 3.3c and 3.3d but in the wavenumber domain and at four different frequencies. One observes that the reproduction error is always below the threshold (see Eq. (3.6) and discussion). This confirms the consistency of the proposed criterion: for an accurate synthesis, it is preferable to choose the interplanar distance such that $d \in I_{opt}$.

Cette thèse est accessible à l'adresse : https://theses.insa-lyon.fr/publication/2022ISAL0077/these.pdf
© [A.D. Pouye], [2022], INSA Lyon, tous droits réservés

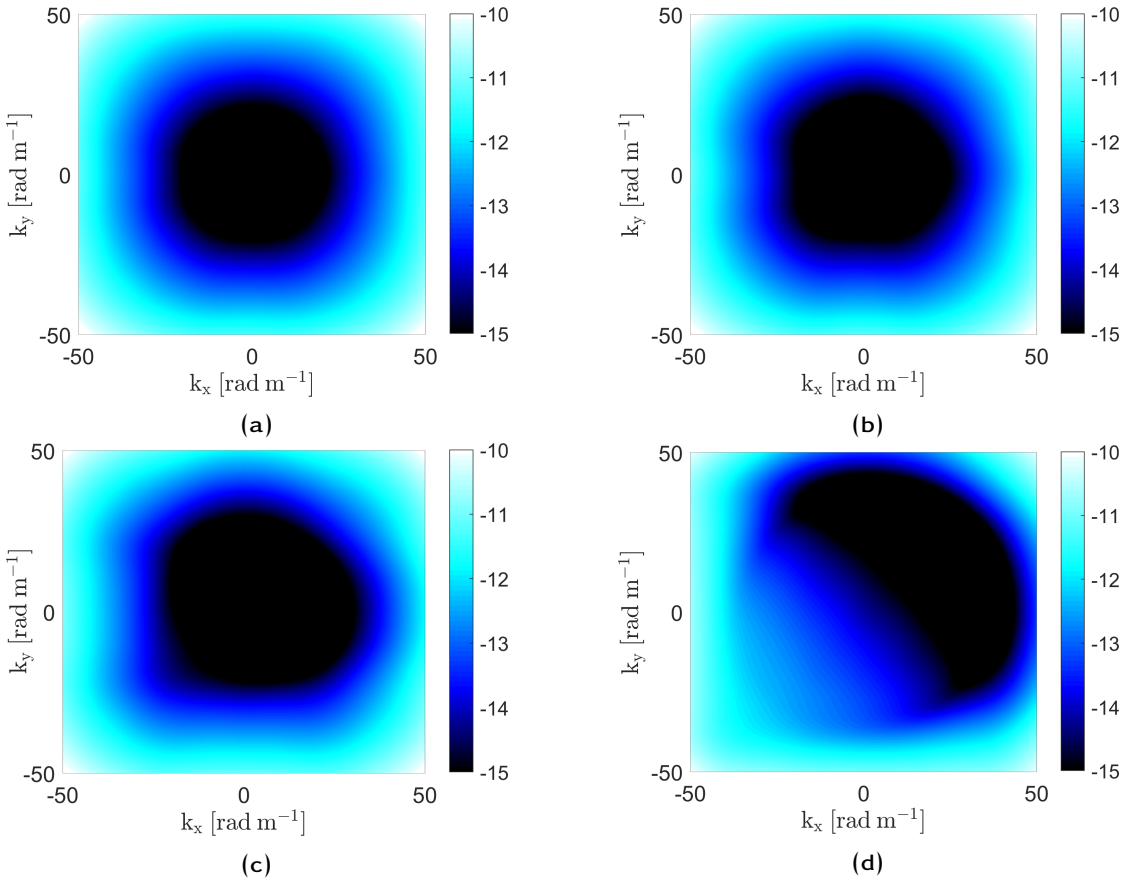

Figure 3.4: Reproduction error e_p (dB, ref. 1) in the wavenumber domain at (a) $f = 200$ Hz, (b) $f = 500$ Hz, (c) $f = 1000$ Hz and (d) $f = 2000$ Hz for $d = \frac{\lambda_{min}}{4}$.

Fig. 3.5 shows three pressure fields in the spatial domain for a plane wave defined by the wave-vector $\left(k_x = 50, k_y = 50\right)$ rad m^{-1} at $f = 2000$ Hz. This is the most constraining plane wave to reconstruct using the proposed approach as the wavenumbers k_x and k_y correspond to the maximum wavenumber value used to define the number of source positions. Fig. 3.5a corresponds to the target pressure field whereas Fig. 3.5b and 3.5c correspond to the reconstructed pressure field for an interplanar distance outside and inside I_{opt}, respectively. One can notice that although the reproduction error corresponding to the reconstructed pressure field on Fig. 3.5b does not comply with the set criterion on the entire wavenumber domain (see Fig. 3.3a and 3.3b), the proposed

Cette thèse est accessible à l'adresse : https://theses.insa-lyon.fr/publication/2022ISAL0077/these.pdf
© [A.D. Pouye], [2022], INSA Lyon, tous droits réservés

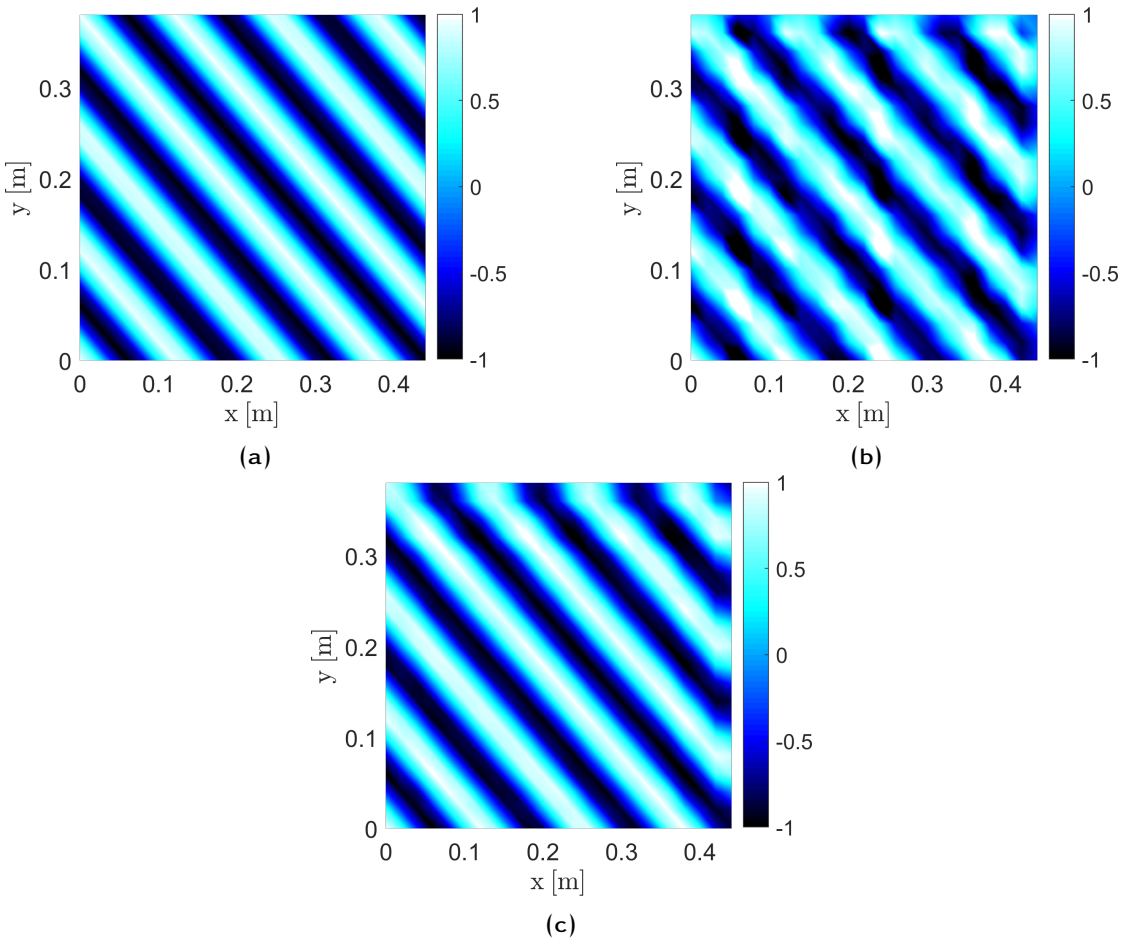

Figure 3.5: Pressure fields (Pa) in the spatial domain at a frequency $f = 2000\,\text{Hz}$ for the plane wave defined by $\left(k_x = 50, k_y = 50\right)\,\text{rad}\,\text{m}^{-1}$: (a) target, (b) reconstructed for $d = \frac{\lambda_{min}}{10}$ and (c) reconstructed for $d = \frac{\lambda_{min}}{4}$.

method succeeds relatively well to reconstruct the target plane wave. Some errors can be noticed on the amplitude but the shape of the wave is correctly described. On Fig. 3.5c where the interplanar distance is taken from the interval I_{opt}, the synthesized pressure field is almost identical to the target pressure field. These observations thus validate the chosen interval I_{opt} from which one can choose a value for the interplanar distance.
For the experimental study presented in the following chapter, the parameters of the array are set to the following values: $k_{max} = 50\,\text{rad}\,\text{m}^{-1}$, $\delta_s = 3\,\text{cm}$ and $d = 3\,\text{cm}$.

Cette thèse est accessible à l'adresse : https://theses.insa-lyon.fr/publication/2022ISAL0077/these.pdf
© [A.D. Pouye], [2022], INSA Lyon, tous droits réservés

3.4 SUMMARY

In this chapter, a brief review on the theoretical vibroacoustic responses of panels under random excitations was presented. The quantities of interest were the vibration/velocity response and the transmission loss of the panel subject to a DAF or TBL pressure field. Afterwards, parametric studies on the SST process were done in order to determine the optimal values of the design parameters of the synthetic array for an accurate synthesis process. These design parameters are the cutoff wavenumber $\bar{k}$ of and the interplanar distance d between the plane of the panel and the plane of the synthetic array.

Cette thèse est accessible à l'adresse : https://theses.insa-lyon.fr/publication/2022ISAL0077/these.pdf
© [A.D. Pouye], [2022], INSA Lyon, tous droits réservés

4 SST ON PANELS: EXPERIMENTS

4.1 Experimental implementation 64
4.1.1 Measurement devices 64
4.1.2 Experimental setup 65
4.2 Results and discussion 72
4.2.1 Numerical validation 72
4.2.2 Validation with direct measurements in standard test facilities . . 76
4.3 Summary 77

In this chapter, the vibroacoustic response of the aluminum flat panel is experimentally determined using SST. In a first step, the various devices used during the experiment as well as the experimental setup are presented in Sec. 4.1. Afterwards, the experimental results in terms of vibration response and transmission loss of the panel are compared to theoretical results on one hand and to direct measurements in standard test facilities on the other hand for each of the two excitations of interest (DAF and TBL) in Sec. 4.2. The chapter is closed with a brief summary.

Cette thèse est accessible à l'adresse : https://theses.insa-lyon.fr/publication/2022ISAL0077/these.pdf
© [A.D. Pouye], [2022], INSA Lyon, tous droits réservés

4.1 EXPERIMENTAL IMPLEMENTATION

4.1.1 Measurement devices

4.1.1.1 *Monopole source*

The excitation device used during the SST process is a mid-high frequency monopole source manufactured by Microflown Technologies [20] and shown in Fig. 4.1. This monopole source is composed of a simple flexible hose at the end of which there is a 15 mm diameter nozzle with a reference sensor at the output and the whole is driven with a high impedance loudspeaker. The source (volume velocity) was calibrated by measuring the radiated sound pressure at a given distance in anechoic conditions for a given input voltage and using the theoretical model of a monopole in free field conditions in order to verify the relation between the radiated sound pressure and the volume velocity.

4.1.1.2 *Microphones*

In order to determine the transfer functions G_{ps} between the S source positions and the P observation points, 20 1/4″ microphones were used. They were all calibrated using a sound level calibrator.
These microphones were also used to measure the transfer functions $\Gamma_{\alpha}^{s}(\mathbf{x}, \omega)$ (for $\alpha = p$ and $\alpha = v_0$) needed in order to determine the sensitivity functions as described by Eq. (2.27) in Chapter 2.

4.1.1.3 *Accelerometer*

A z-axis Bruel & Kjær accelerometer was used for the measurement of the transfer functions $\Gamma_{v}^{s}(\mathbf{x}, \omega)$ allowing to determine the velocity sensitivity functions $H_v(\mathbf{x}, \mathbf{k}, \omega)$.

Cette thèse est accessible à l'adresse : https://theses.insa-lyon.fr/publication/2022ISAL0077/these.pdf
© [A.D. Pouye], [2022], INSA Lyon, tous droits réservés

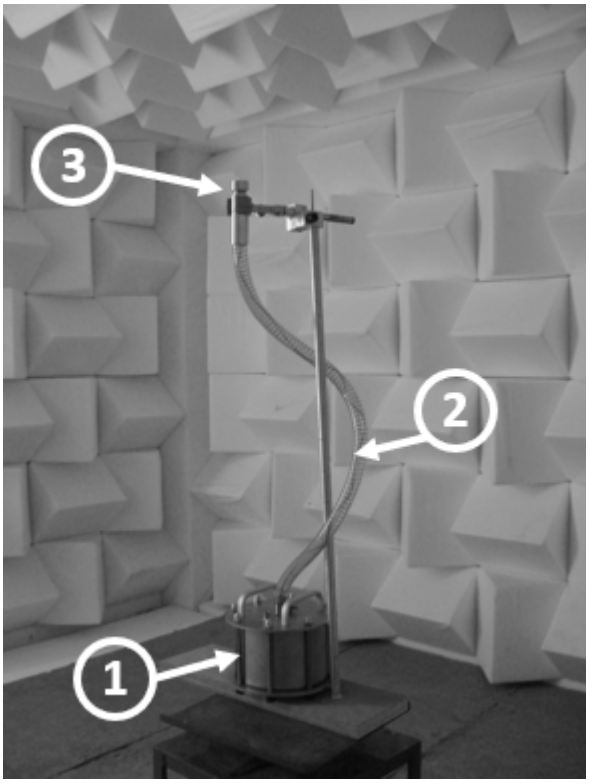

Figure 4.1: Microflown mid-high frequency volume velocity source. (1) high impedance loudspeaker, (2) flexible hose and (3) nozzle with sensor.

4.1.2 Experimental setup

The SST process described in Chapter 2 has been applied on a simply supported aluminum panel. The characteristics of the panel are the same as the one considered in the numerical simulation in Chapter 3. To simulate the appropriate boundary conditions (i.e. simply supported), the panel was mounted using the protocol presented by Robin *et al.* [77] and was placed in a baffle consisting of a 2 cm thick square plywood with a 1 m side and in which there is an aperture the size of the panel, see Fig. 4.4. The measurements were done in a room where the walls are covered with absorbing wedges and 10 cm thick absorbing foam panels were placed on the floor and around the structure inside the baffle in order to prevent the potential reflections and noises coming from the robot and acquisition system from polluting the measurements.

Cette thèse est accessible à l'adresse : https://theses.insa-lyon.fr/publication/2022ISAL0077/these.pdf
© [A.D. Pouye], [2022], INSA Lyon, tous droits réservés



Figure 4.2: Roga RG-50 1/4" ICP microphone.

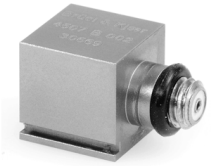

Figure 4.3: Bruel & Kjær accelerometer.

The monopole source was placed on the arm of a 3 axis Cartesian robot controlled by a MATLAB script in order to automatize the displacement of the source. It is important to note that this source was only efficient from 300 Hz to 7000 Hz. The considered positions of the source correspond to a regular mesh grid having the size of the panel and located in a plane at $d = 3\,\text{cm}$ of the panel (which is in the interval I_{opt} defined previously in Chapter 3). The spacing between two adjacent points is $\delta_s = 3\,\text{cm}$ in the x and y directions. One then has 15 different positions along the x direction and 13 different positions along the y direction, which makes an overall of 195 source positions. The SST process requires measuring two types of transfer functions

- In step 2 of the SST process presented in Sec. 2.4, the transfer functions G_{ps} between source positions s and observation points p are measured considering a 2 cm thick square plywood at the location of the panel as shown in Fig. 4.4. A linear array of 1/4" ROGA RG-50 microphones flush-mounted at $x = 2\,\text{cm}$ is considered for the measurement of the wall pressure. The microphone spacing is $\delta_p = 2\,\text{cm}$,

Cette thèse est accessible à l'adresse : https://theses.insa-lyon.fr/publication/2022ISAL0077/these.pdf
© [A.D. Pouye], [2022], INSA Lyon, tous droits réservés

ensuring a number of observation points P greater than the number of source positions S. Considering what we call the *property of invariance in translation* of the considered system (i.e. source exciting the baffled flat panel in a semi-anechoic room), one deduces the pressure distribution on the reconstruction surface for a given source position from measurements with the linear microphone array at different source positions along the x axis with a spacing of $\delta_p = 2\,\text{cm}$ instead of using a rectangular array of microphones. This technical aspect is described in more detail in Appendix C. At the end, we obtained the transfer functions G_{ps} between the $S = 15 \times 13 = 195$ source positions and the $P = 18 \times 20 = 360$ observation points with a frequency resolution of 0.625 Hz. This step is time consuming (i.e. approximately 13 hours for the presented measurement) but it should be achieved only one time to characterize the acoustical environment (i.e. source radiating in the semi-anechoic chamber with the baffle plane). This means that for the characterization of a second structure presenting dimensions smaller or equal to the present one, the same transfer matrix $\mathbf{G}$ could be used, albeit with a smaller number of microphone positions over its surface.

- In step 4 of the SST process presented in Sec. 2.4, $\Gamma_\alpha^s(\mathbf{x}, \omega)$, the FRFs between point $\mathbf{x}$ and the source at position s are determined: they were measured when the test panel was mounted in the baffle as shown in Fig. 4.5. Two cases depending of the final quantities of interest were considered
  - to evaluate the velocity sensitivity function $H_v(\mathbf{x}, \mathbf{k}, \omega)$ at a point $\mathbf{x}$ on the panel, the acceleration response at point $\mathbf{x}$ was measured using one Bruel&Kjaer type 4508 accelerometer. The FRFs $\Gamma_\gamma^s(\mathbf{x}, \omega)$ corresponding to the acceleration of the panel at point $\mathbf{x}$ for a monopole source at position s were measured for the $S = 195$ monopole positions. It took approximately 45 minutes to measure all the FRFs $\Gamma_\gamma^s(\mathbf{x}, \omega)$. These latter were used with Eq. (2.27) to estimate the acceleration sensitivity functions of the panel at point $\mathbf{x}$, $H_\gamma(\mathbf{x}, \mathbf{k}, \omega)$ for $\mathbf{k}$ in $\Omega_\mathbf{k}$ defined in Sec. 2.2. Finally, the velocity sensitivity functions were de-

Cette thèse est accessible à l'adresse : https://theses.insa-lyon.fr/publication/2022ISAL0077/these.pdf
© [A.D. Pouye], [2022], INSA Lyon, tous droits réservés

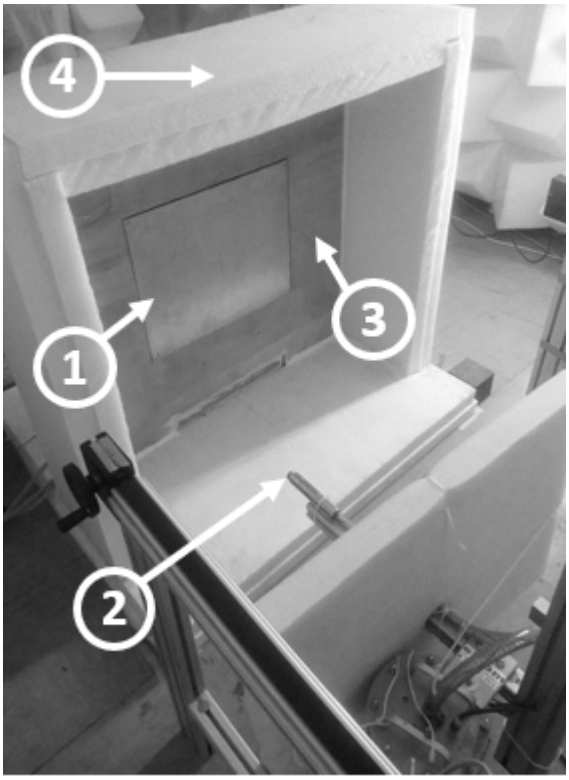

Figure 4.4: Baffled simply supported panel setup for the SST process. (1) aluminum panel, (2) nozzle component of the monopole source mounted on the 3*D* Cartesian robot, (3) 5 cm thick plywood baffle and (4) sound absorbing foam.

termined using the relation $H_v(\mathbf{x},\mathbf{k},\omega) = \frac{1}{\mathrm{i}\omega} H_\gamma(\mathbf{x},\mathbf{k},\omega)$ and these quantities were introduced in Eq. (2.7) with the appropriate model of the wall-pressure fluctuations in order to deduce the PSD of the velocity at point $\mathbf{x}$ when the panel is excited by the considered stochastic excitation. It is important to note that the velocity sensitivity functions $H_v(\mathbf{x},\mathbf{k},\omega)$ are determined here using the direct interpretation of Eq. (2.6) in contrast with the results in [58] where the *reciprocity principle* was used by exciting the panel with a shaker at the point of interest $\mathbf{x}$ and the response of the panel was measured on a grid of points using a laser vibrometer. In our case, the grid of monopole source positions constitute the excitation and the response is measured at only one point, the point of interest $\mathbf{x}$, using one accelerometer.

Cette thèse est accessible à l'adresse : https://theses.insa-lyon.fr/publication/2022ISAL0077/these.pdf
© [A.D. Pouye], [2022], INSA Lyon, tous droits réservés

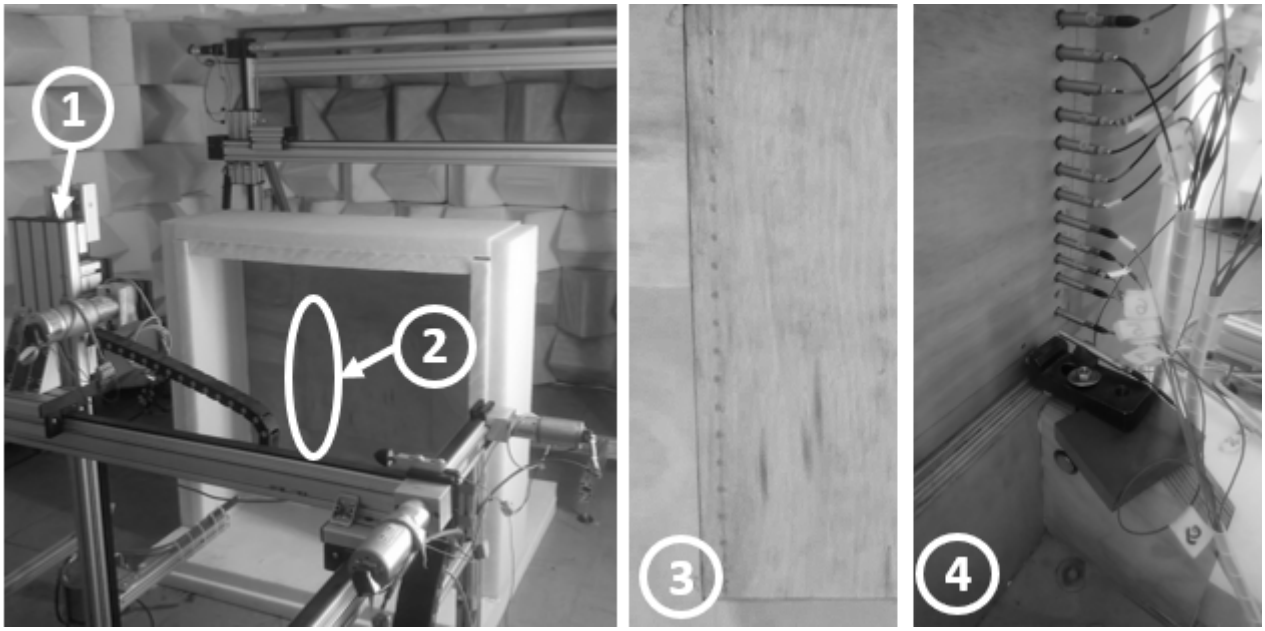

Figure 4.5: Measurement of the transfer functions G_{ps}: experimental setup. (1) 3D Cartesian robot, (2) linear array of 20 microphones, (3) front view of the flush mounted microphones and (4) back view of the flush mounted microphones.

– to evaluate the radiated power by the plate. In accordance with Eq. (2.10) to (2.13), the sensitivity functions in term of the radiated pressure and of the particle velocity along the z-axis should be estimated for the $R = 9 \times 20 = 180$ points discretizing Σ_r. A linear array of microphones close to the panel (at a distance of approximately 7 cm from the panel plane on the radiating side, corresponding to $z = -7$ cm as defined in Sec. 2.2) was used as shown in Fig. 4.7 to measure the pressure at each point r of Σ_r. To evaluate the particle velocity, an estimation of the pressure gradient was considered.

With the time dependence $e^{i\omega t}$, the particle velocity at direction z can be written

$$v_0^z = -\frac{i}{\rho_0 \omega} \frac{\partial p}{\partial z} \tag{4.1}$$

Cette thèse est accessible à l'adresse : https://theses.insa-lyon.fr/publication/2022ISAL0077/these.pdf
© [A.D. Pouye], [2022], INSA Lyon, tous droits réservés

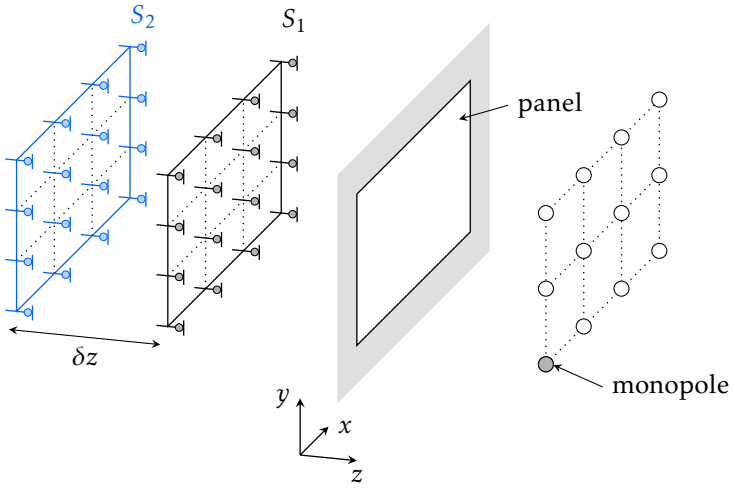

Figure 4.6: Measurement of the particle velocity with the two microphone method, S_1 and S_2 are discretized surfaces consisting of two identical grids of R points.

Thus, the particle velocity can be obtained by evaluating the pressure gradient $\partial p/\partial z$ [10, 72] by using the two point finite difference method

$$v_0^z \approx -\frac{\mathrm{i}}{\rho_0 \omega} \frac{p_2 - p_1}{\delta z} \tag{4.2}$$

where p_1 and p_2 are pressure measurements at two adjacent positions on surface S_1 and on surface S_2, respectively, as shown in Fig. 4.6. δz is the spacing between the two surfaces S_1 and S_2 and is also the distance between two microphone positions on the grid. δz must be large enough to induce a sufficient pressure difference in order to determine the particle velocity but it also must be small enough for the approximation in Eq. (4.2) to be valid. Some trial and error tests with the monopole source were made in order to define an adequate spacing between the two planes where the pressure would be measured and it was found that a separation of $\delta z \approx 2\,\mathrm{cm}$ was ideal for these measurements. Normally, the finite difference method suffers from robustness issue against sensor noise and mismatch but the latter is avoided here as the particle velocity at one position of the grid in Fig. 4.6 is obtained using two pressure measurements of the same microphone at the designated position (see Fig. 4.6 for an illustration of the proposed

Cette thèse est accessible à l'adresse : https://theses.insa-lyon.fr/publication/2022ISAL0077/these.pdf
© [A.D. Pouye], [2022], INSA Lyon, tous droits réservés

methodology). In the experimental setup, only one linear array of 20 microphones is used to accomplish these pressure measurements on the two surfaces S_1 and S_2. In fact the linear array of microphone is mounted on a $2D$ Cartesian robot allowing us to sweep through a given surface on the radiating side of the panel. Measuring the transfer functions $\Gamma_p^s(\mathbf{x},\omega)$ (radiated pressure) and $\Gamma_{v_0}^s(\mathbf{x},\omega)$ (particle velocity) at point $\mathbf{x}$, now located on the discretized surface Σ_r, allows us to determine the pressure sensitivity functions $H_p(\mathbf{x},\mathbf{k},\omega)$ and the particle velocity sensitivity functions $H_{v_0}(\mathbf{x},\mathbf{k},\omega)$ used in Eq. (2.12). The measurement of all the transfer functions needed in the determination of the radiated power by the panel took approximately 46 hours.

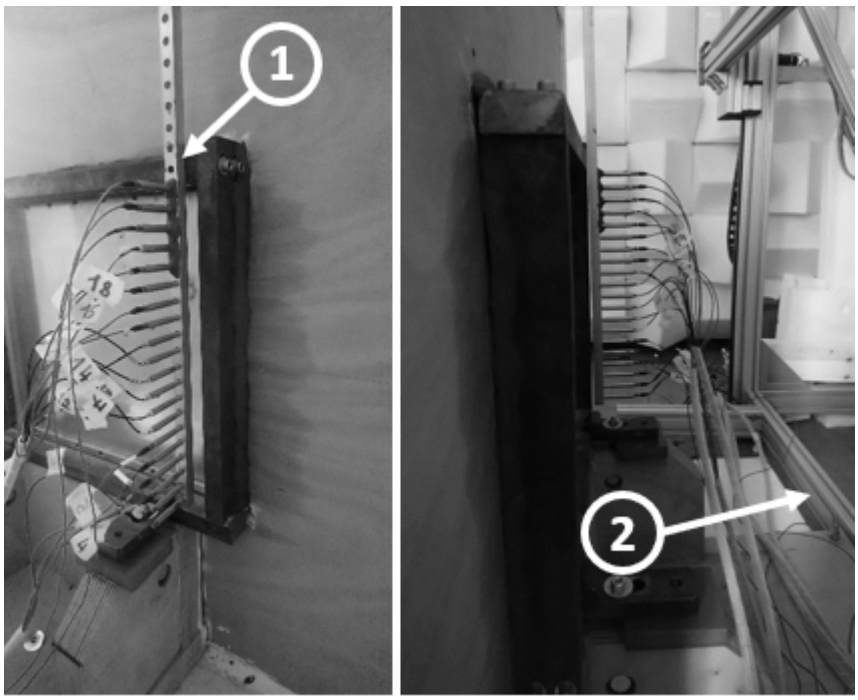

Figure 4.7: Particle velocity measurements: experimental setup. (1) linear array of microphones mounted on the $2D$ Cartesian robot and (2) $2D$ Cartesian robot.

Cette thèse est accessible à l'adresse : https://theses.insa-lyon.fr/publication/2022ISAL0077/these.pdf
© [A.D. Pouye], [2022], INSA Lyon, tous droits réservés

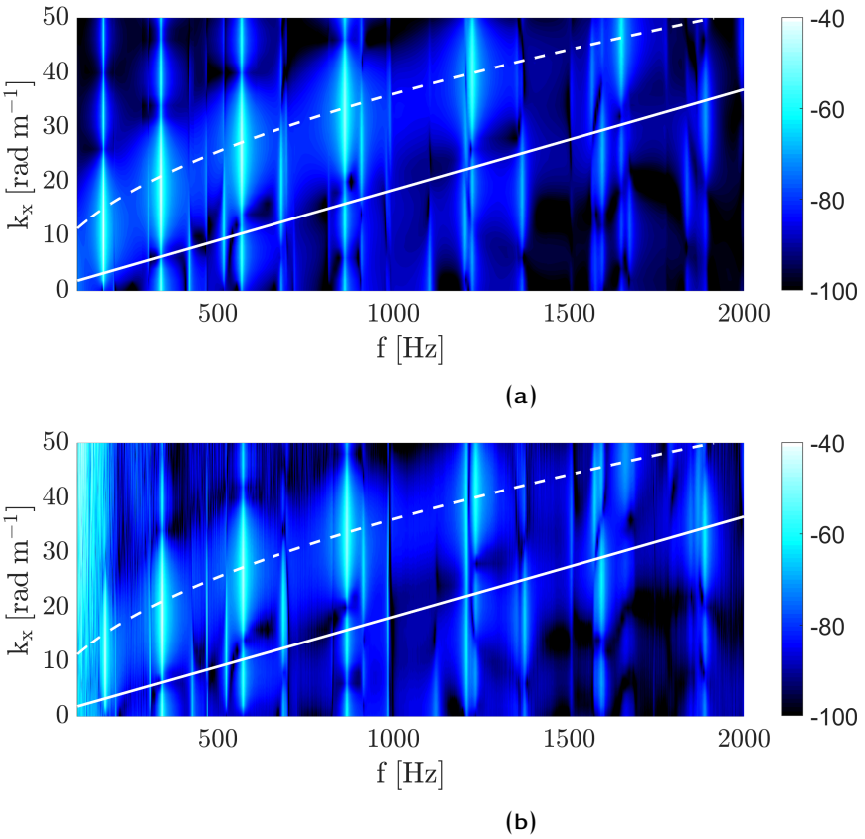

Figure 4.8: Velocity sensitivity functions $\left|H_v\left(\mathbf{x}, k_x, k_y = 0, \omega\right)\right|^2$ (dB, ref. 1 m^3 s^{-1} Pa^{-1}): (a) numerical and (b) SST. Continuous white line: acoustic wavenumber k_0. Dashed white line: panel flexural wavenumber k_f.

4.2 RESULTS AND DISCUSSION

4.2.1 Numerical validation

In order to assess the accuracy of the SST process on the test panel, one proposes in this section to compare its results with numerical ones. As evoked in Sec. 3.2.1, these latter were achieved using the analytical normal modes and the modal expansion method as described in Appendix A. First, let us compare the velocity sensitivity functions experimentally estimated with the SST process with the ones estimated numerically at

Cette thèse est accessible à l'adresse : https://theses.insa-lyon.fr/publication/2022ISAL0077/these.pdf
© [A.D. Pouye], [2022], INSA Lyon, tous droits réservés

point $\mathbf{x} = (0.06, 0.3, 0)$ m. The results are plotted in Fig. 4.8 as a function of the frequency and the wavenumber, k_x for $k_y = 0$. A good agreement between both results can be observed, even for wavenumbers above the acoustic wavenumbers (which are symbolized by the continuous white line in Fig. 4.8). This highlights that the SST approach is well adapted for reproducing subsonic plane waves, which is a limitation of past-developed reproduction techniques [14, 18, 76]. Below 300 Hz, one can however observe that the SST results are noisy. For these frequencies, the monopole source was not efficient and the measurements of the transfer functions were polluted by the background noise. On the other hand, in the higher part of the frequency range, some discrepancies between the two approaches appear. They can be attributed to the difference between the model that supposed a panel, perfectly simply supported on its four edges and the experiment that approaches these conditions with thin blades.

Fig. 4.9 and Fig. 4.10 show the ASD function of the structural velocity response at the receiving point $\mathbf{x} = (0.06, 0.3, 0)$ m (in dB units) when excited by a DAF and a TBL pressure field, respectively, as described in Sec. 1.1.2 and Sec. 1.1.3.

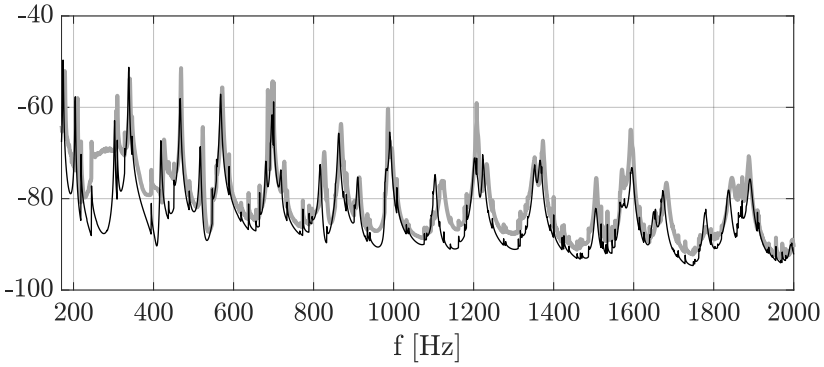

Figure 4.9: Velocity ASD function $S_{vv}(\mathbf{x}, \omega)$ (dB, ref. $1\,\mathrm{m^2\,s^{-2}\,Hz^{-1}}$) of the panel subjected to a DAF excitation: numerical (thin black line), SST (thick gray line).

It can be observed that the vibration responses, in both the DAF and TBL excitation cases, determined using SST do not match the numerical ones between approximately 230 Hz and 300 Hz: this is due to the fact that the source is not efficient in that frequency range as stated before. The vertical offsets that can be observed at some frequencies are due to

Cette thèse est accessible à l'adresse : https://theses.insa-lyon.fr/publication/2022ISAL0077/these.pdf
© [A.D. Pouye], [2022], INSA Lyon, tous droits réservés

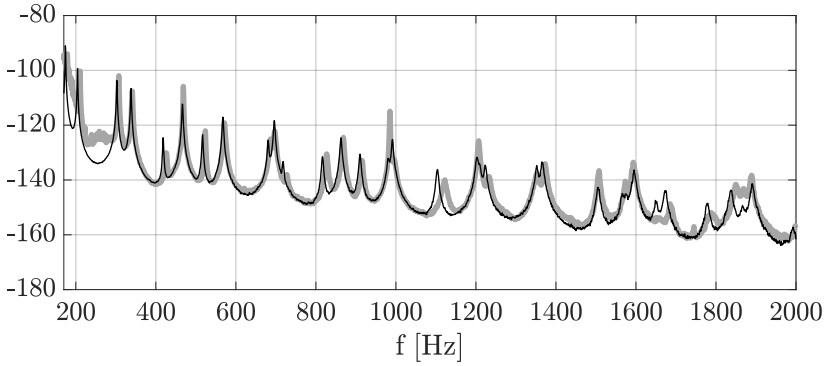

Figure 4.10: Velocity ASD function $S_{vv}(\mathbf{x}, \omega)$ (dB, ref. $1\,\mathrm{m^2\,s^{-2}\,Hz^{-1}}$) of the panel subjected to a TBL excitation: numerical (thin black line), SST (thick gray line).

the fact that for the numerical case, the modal damping of the panel is taken constant over the entire frequency range (i.e. $\eta = 0.005$) whereas it is certainly dependent on the panel modes in real conditions (see the values measured by Marchetto for the first modes in Table II, Ref. [58]). It can also be noticed that the vibration response in the DAF case is higher than in the case of the TBL excitation: this is due to the fact that the modes that contribute to the panel response under a diffuse field excitation are more efficiently excited than in the case of a TBL excitation [59].

Now, let us focus on the panel radiation. Fig. 4.11 and Fig. 4.12 show the inverse of the radiated power (in dB units) by the panel when excited by a DAF and a TBL pressure field, as described in Sec. 1.1.2 and Sec. 1.1.3 respectively.

The radiated power was determined using the two microphones method for the SST approach. For both cases (DAF and TBL), the experimental results do not match the theoretical results under approximately 700 Hz: this is probably due to the fact that the monopole source was not very efficient to induce a sufficient radiation amplitude for the measurement of the pressure and particle velocity sensitivity functions. Moreover, the estimation of the particle velocity with the two microphone measurements can amplify the uncertainties. From a practical point of view, one can conclude that an acoustic source more efficient in the low frequency range would be required. In general, this type of source (such as subwoofer loudspeakers) has a greater size than the considered one,

Cette thèse est accessible à l'adresse : https://theses.insa-lyon.fr/publication/2022ISAL0077/these.pdf
© [A.D. Pouye], [2022], INSA Lyon, tous droits réservés

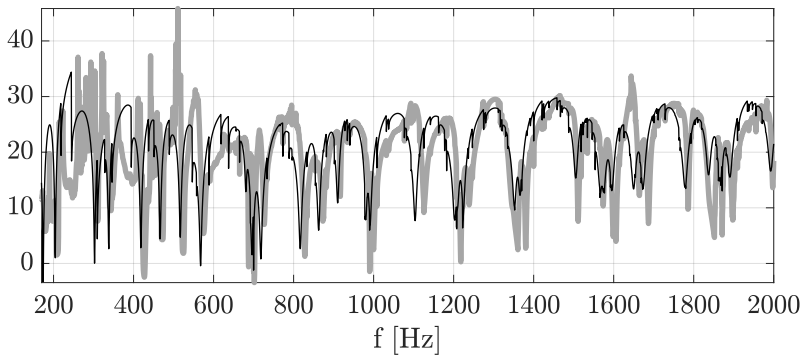

Figure 4.11: Transmission loss TL(ω) (dB, ref. 1) of the panel under DAF excitation: numerical (thin black line), SST (thick gray line).

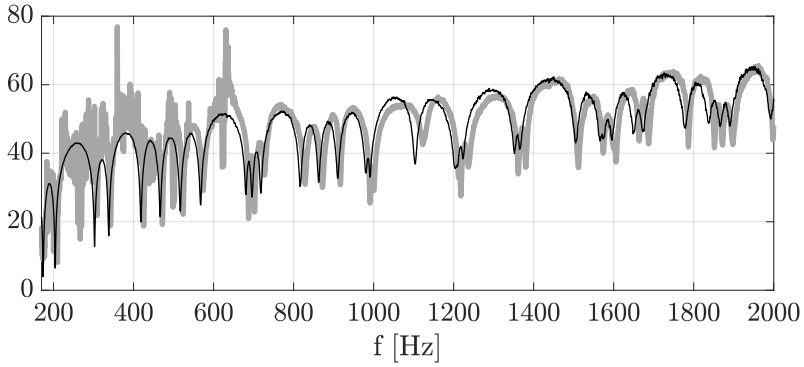

Figure 4.12: Transmission loss TL(ω) (dB, ref. 1) of the panel under TBL excitation: numerical (thin black line), SST (thick gray line).

that would require to define a coarser mesh for the source positions. With the present source, one can however observe a good agreement between the SST results and the numerical ones for both excitations. The two curves match very well above 700 Hz for the TBL excitation. That shows that the subsonic plane waves are well synthesized by the SST (as it has been already observed in Fig. 4.8).

In conclusion of this section, there is globally a good agreement between the numerical results and those obtained from the proposed method in terms of the panel vibrations and the radiated sound power. For this latter quantity, the strength of the acoustic source did not permit however a satisfactory reproduction below 700 Hz.

Cette thèse est accessible à l'adresse : https://theses.insa-lyon.fr/publication/2022ISAL0077/these.pdf
© [A.D. Pouye], [2022], INSA Lyon, tous droits réservés

4.2.2 Validation with direct measurements in standard test facilities

In this section, the experimental results obtained with the proposed SST method are compared to results obtained in standard test facilities. The results obtained in the standard test facilities have already been published [57, 58] and were done at the University of Sherbrooke by Marchetto *et al.* They concern the vibrations of a similar panel. In Ref. [57], the panel is excited by a DAF experimentally generated within a reverberant room whereas as in Ref. [58], it is excited by a turbulent flow generated in an anechoic wind tunnel at a flow speed of $20\,\mathrm{m\,s^{-1}}$. More details on these measurements can be found in these references.

Fig. 4.13 and Fig. 4.14 show for the DAF and the TBL, respectively, a comparison of the panel vibration responses obtained with the SST and the standard test facilities.

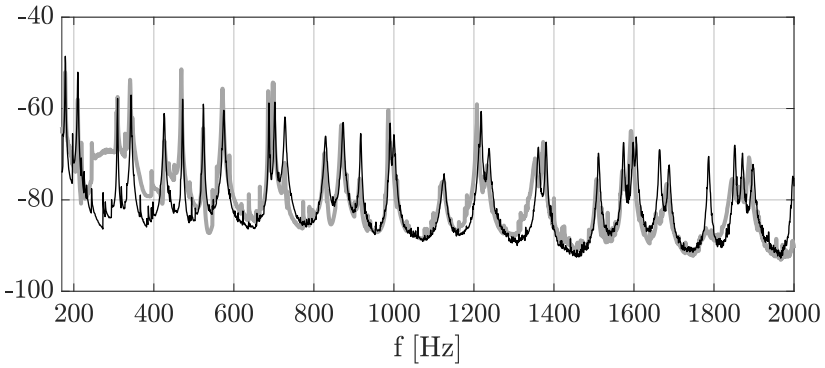

Figure 4.13: Velocity ASD function $S_{vv}(\mathbf{x},\omega)$ (dB, ref. $1\,\mathrm{m^2\,s^{-2}\,Hz^{-1}}$) of the panel subjected to a DAF excitation: reverberant chamber measurements at the University of Sherbrooke [57] (thin black line), SST (thick gray line).

There is globally a good agreement between the results obtained using SST and those measured in the test facilities. One can notice a shift of the responses along the frequency axis which is due to the fact that the panel used in the test facilities is not exactly the same as the one used in our experiment although both panels are made out of aluminum and have the same dimensions. This shift can also be explained by some minor differences in

Cette thèse est accessible à l'adresse : https://theses.insa-lyon.fr/publication/2022ISAL0077/these.pdf
© [A.D. Pouye], [2022], INSA Lyon, tous droits réservés

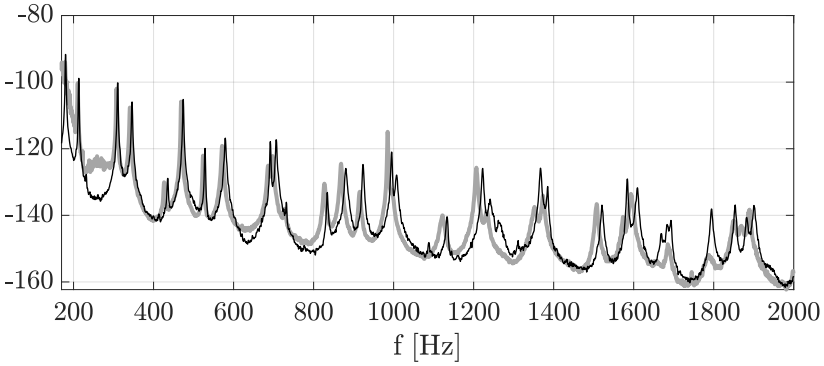

Figure 4.14: Velocity ASD function $S_{vv}(\mathbf{x}, \omega)$ (dB, ref. $1\,\mathrm{m^2\,s^{-2}\,Hz^{-1}}$) of the panel subjected to a TBL excitation: wind tunnel measurements at the University of Sherbrooke [58] (thin black line), SST (thick gray line).

the boundary conditions. These results show that the proposed SST is able to reproduce the excitation of a standard test facility.

4.3 SUMMARY

This chapter presented an experimental implementation of the SST approach. This process can be seen as alternative or complementary to standard test facilities such as reverberant rooms or wind tunnels. In the present study, our attention was focused on the validation of the process with comparisons against numerical and experimental results obtained with test facilities such as the reverberant room and the anechoic wind tunnel. A parametric study based on numerical simulations aiming at defining the ideal design of the array of virtual monopoles was done. This study allowed to define an optimal interval I_{opt}, for the distance between the panel and the source array, in which the synthesized pressure field is in good agreement with the target pressure field, allowing a good reproduction of the vibroacoustic response of the panel.
The proposed method was applied on a simply supported aluminum panel which was subject to either DAF or TBL excitation. Both the velocity response at a given point and

Cette thèse est accessible à l'adresse : https://theses.insa-lyon.fr/publication/2022ISAL0077/these.pdf
© [A.D. Pouye], [2022], INSA Lyon, tous droits réservés

the transmission loss of the panel were determined. A $3D$ Cartesian robot was used to move the acoustic source whereas a $2D$ Cartesian robot was used to move a linear array of microphones. This system was controlled by a MATLAB script that allows us to automatize the measurement process of the transfer functions between the source (at different positions) and the quantities of interest. To evaluate the radiated power for the computation of the transmission loss, the two microphone method was used to estimate the normal particle velocity. Apart from an overestimation of the panel responses between 230 and 300 Hz due to the low efficiency of the monopole source and the noisy transmission loss curve under approximately 600 Hz stemming from the two microphone method, there is a fairly good agreement between the three types of results (numerical, SST and direct measurements).

The total measurement time of the transfer functions needed to determine the velocity response as well as the radiated power by the panel is approximately 60 hours. The measurement of the transfer functions needed to determine the radiated power by the panel are the most time consuming (approximately 46 hours) as it required to measure the radiated pressure and to estimate the particle velocity using a linear array of microphone. These measurement times are however not completely penalizing as the process is fully automatized. The use of acoustic velocity probes as well as a larger microphone array could greatly reduce these measurement times. Moreover, compared to standard facilities, the process supplies the sensitivity functions that can give some insights on how the structure filters out the random excitation. Table 4.1 summarizes the measurement times for each quantity of interest.

Table 4.1: Measurement times during the experimental SST process.

Measured quantities	**Times**
Transfer matrix ($\mathbf{G}$)	13 hours
Vibration response (H_v)	45 minutes
Radiated power (H_p and H_{v_0})	46 hours

Cette thèse est accessible à l'adresse : https://theses.insa-lyon.fr/publication/2022ISAL0077/these.pdf
© [A.D. Pouye], [2022], INSA Lyon, tous droits réservés

Part III

EXTENSION TO CURVED RECTANGULAR PANELS

Cette thèse est accessible à l'adresse : https://theses.insa-lyon.fr/publication/2022ISAL0077/these.pdf
© [A.D. Pouye], [2022], INSA Lyon, tous droits réservés

Cette thèse est accessible à l'adresse : https://theses.insa-lyon.fr/publication/2022ISAL0077/these.pdf
© [A.D. Pouye], [2022], INSA Lyon, tous droits réservés

5 SST ON CURVED RECTANGULAR PANELS: THEORY AND NUMERICAL STUDIES

5.1 Scattering by a rigid and curved rectangular panel: transfer functions . . 82
5.1.1 Two-dimensional case 83
5.1.2 Three-dimensional case 87
5.1.3 Validation of the solutions 91
5.2 SST on curved rectangular panels: parametric studies 94
5.2.1 Two-dimensional case 94
5.2.2 Three-dimensional case 111
5.3 Summary 124

This chapter is dedicated to the theoretical and numerical study of SST applied on Curved Rectangular Panels (CRPs). In a first step, an analytical form of the transfer functions between a monopole source and an observation point on the structure of interest is established using Green's representation in the two-dimensional and three-dimensional cases. The established closed-form solutions for the $2D$ and $3D$ cases are then validated using numerical results obtained with OpenBEM[1]. Afterwards, parametric studies on the design parameters of the SST process for a CRP are proposed and discussed before closing the chapter with a brief summary.

1 Collection of MATLAB codes which can be used to solve the Helmholtz equation using the Boundary Element Method (BEM).

Cette thèse est accessible à l'adresse : https://theses.insa-lyon.fr/publication/2022ISAL0077/these.pdf
© [A.D. Pouye], [2022], INSA Lyon, tous droits réservés

5.1 SCATTERING BY A RIGID AND CURVED RECTANGULAR PANEL: TRANSFER FUNCTIONS

A thorough search of the relevant literature did not yield any analytical closed-form transfer functions between a monopole source located at a given point $\mathbf{x}_0$ and an observation point $\mathbf{y}$ located on the structure σ as depicted in Fig. 5.1. Thus, this section is dedicated to the resolution of the boundary value problem formulated in Eq. (5.1). We seek a function $p(\mathbf{x})$, solution of the following Neumann problem

$$\begin{cases} \Delta p(\mathbf{x}) + k^2 p(\mathbf{x}) = -\delta(\mathbf{x} - \mathbf{x}_0), \mathbf{x} \in \Omega \\ \partial_{\mathbf{n}(\mathbf{x})} p(\mathbf{x}) = 0, \mathbf{x} \in \sigma \end{cases} \tag{5.1}$$

where $\partial_{\mathbf{n}(\mathbf{x})}\bullet$ designates the partial normal derivative at point $\mathbf{x}$ in the direction $\mathbf{n}$ and $\mathbf{n}$ corresponds to an exterior unit vector on the boundary constituted by $\sigma \cup \beta$. The domain of propagation Ω corresponds to the upper half-space delimited by the baffle β and the structure σ.

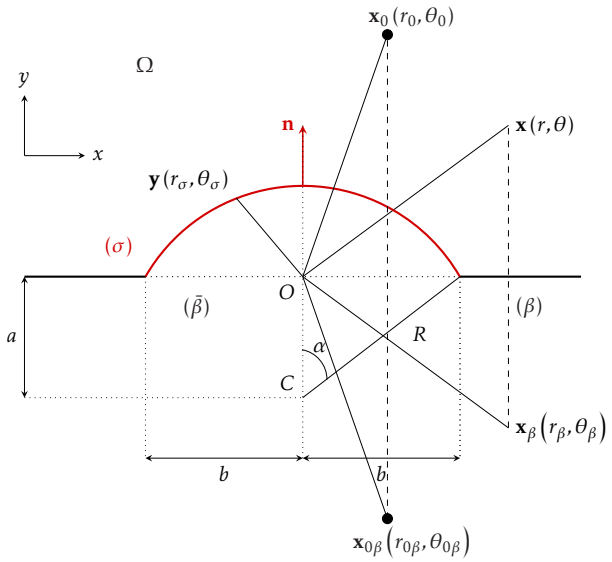

Figure 5.1: Problem geometry and parameters.

Cette thèse est accessible à l'adresse : https://theses.insa-lyon.fr/publication/2022ISAL0077/these.pdf
© [A.D. Pouye], [2022], INSA Lyon, tous droits réservés

In a first step, the two-dimensional case is studied and then follows the general three-dimensional case.

5.1.1 Two-dimensional case

In what follows, use will be made of the polar coordinates with the origin located at point O as shown in Fig. 5.1: the coordinates of a point $\mathbf{x}$ inside the propagation domain are denoted by (r, θ) while those of a point $\mathbf{y}$ on $\sigma \cup \beta$ are denoted by $(r_\sigma, \theta_\sigma)$ in the polar coordinates. $\mathbf{x}_\beta$ designates the image of point $\mathbf{x}$ with respect to the baffle plane (β) and $\mathbf{x}$ designates a point in Ω.
Note that since $\mathbf{x}$ is closer to σ than $\mathbf{x}_0$ in our application, it results that $r < r_0$.
From Eq. (3.51) in [38], Green's representation of the exterior pressure field p at $\mathbf{x}$ due to the source at point $\mathbf{x}_0$ and diffracted by the surface $\sigma \cup \beta$ reads

$$p(\mathbf{x}) = p_0(\mathbf{x}) + \int_{\sigma\cup\beta} \left\{ \mathrm{Tr}\left[\partial_{\mathbf{n}(\mathbf{y})} p(\mathbf{y})\right] G(\mathbf{x},\mathbf{y}) - \mathrm{Tr}\left[p(\mathbf{y})\right] \partial_{\mathbf{n}(\mathbf{y})} G(\mathbf{x},\mathbf{y}) \right\} \mathrm{d}S(\mathbf{y}) \tag{5.2}$$

where $\mathrm{Tr}[\bullet]$ represents the Cauchy trace operator and $\partial_{\mathbf{n}(\mathbf{y})}\bullet$ designates the partial normal derivative at point $\mathbf{y}$ in the direction $\mathbf{n}$.
Because the object is rigid, $\mathrm{Tr}\left[\partial_{\mathbf{n}(\mathbf{y})} p(\mathbf{y})\right] = 0$ on $\sigma \cup \beta$ and Eq. (5.2) reduces to

$$p(\mathbf{x}) = p_0(\mathbf{x}) - \int_{\sigma\cup\beta} \mathrm{Tr}\left[p(\mathbf{y})\right] \partial_{\mathbf{n}(\mathbf{y})} G(\mathbf{x},\mathbf{y}) \, \mathrm{d}S(\mathbf{y}) \tag{5.3}$$

A priori, the Green's function G is chosen to be the following free-field Green's function

$$G(\mathbf{x},\mathbf{y}) = \frac{\mathrm{i}}{4} H_0^{(1)}\left[k_0 d(\mathbf{x},\mathbf{y})\right], \ \mathbf{x} \in \Omega \text{ and } \mathbf{y} \in \sigma \cup \beta$$

where $H_0^{(1)}$ is the Hankel function of the first kind and order 0. In the remainder of this chapter, the superscript "(1)" in the considered function will be omitted as only Hankel or Bessel functions of the first kind are used.

Cette thèse est accessible à l'adresse : https://theses.insa-lyon.fr/publication/2022ISAL0077/these.pdf
© [A.D. Pouye], [2022], INSA Lyon, tous droits réservés

It is important to note that $\partial_{\mathbf{n}(\mathbf{y})} G(\mathbf{x},\mathbf{y}) \neq 0$ on β. One has a "certain" freedom of choice for the Green's function in the Green's representation in Eq. (5.3), see Eq. (5) of Ref. [84] for confirmation. Let us choose the half-space Green's function G_β whose normal derivative vanishes on $\beta(\cup\bar{\beta})$. It is given by

$$G_\beta(\mathbf{x},\mathbf{y}) = \frac{\mathrm{i}}{4} H_0^{(1)}[k_0 d(\mathbf{x},\mathbf{y})] + \frac{\mathrm{i}}{4} H_0^{(1)}\left[k_0 d\left(\mathbf{x},\mathbf{y}_\beta\right)\right] \tag{5.4}$$

where $\mathbf{x}_\beta$ is mirror-image point of $\mathbf{x}$ with respect to the plane baffle $\beta(\cup\bar{\beta})$. Thus, one has $\partial_{\mathbf{n}(\mathbf{y})} G_\beta(\mathbf{x},\mathbf{y}) = 0$ on $\beta\left(\cup\bar{\beta}\right)$. The integral representation in Eq. (5.3) thus reduces to

$$p(\mathbf{x}) = p_{0\beta}(\mathbf{x}) - \int_\sigma \mathrm{Tr}[p(\mathbf{y})]\, \partial_{\mathbf{n}(\mathbf{y})} G_\beta(\mathbf{x},\mathbf{y})\, \mathrm{d}S(\mathbf{y}) \tag{5.5}$$

where the integral term, which represents the sound field diffracted by $\sigma \cup \beta$ is now defined on a finite domain σ compared to Eq. (5.3) where the the integration domain was composed of the structure σ and the infinite baffle β.

Note that the free-field source term $p_0(\mathbf{x})$ has been replaced by $p_{0\beta}(\mathbf{x}) = p_0(\mathbf{x},\mathbf{x}_0) + p_0\left(\mathbf{x},\mathbf{x}_{0\beta}\right)$ such that $\partial_{\mathbf{n}(\mathbf{x})} p_{0\beta}(\mathbf{x}) = 0$ when $\mathbf{x} \in \beta(\cup\bar{\beta})$. This modification is reflected in the term ϕ_I of Eq. (5) in [84], but dealing with an incident plane wave instead of a point source as in our case.

We now proceed with a cylindrical harmonic expansion of $p_{0\beta}(\mathbf{x})$ and $\partial_{\mathbf{n}(\mathbf{y})} G_\beta(\mathbf{x},\mathbf{y})$.

- **Source term** $p_{0\beta}(\mathbf{x})$

  For $r < r_0$, we have (see Appendix D of Ref. [25])

  $$\frac{\mathrm{i}}{4} H_0^{(1)}[k_0 d(\mathbf{x},\mathbf{x}_0)] = \frac{\mathrm{i}}{4} \sum_{n=-\infty}^{+\infty} H_n(k_0 r_0) J_n(k_0 r) \mathrm{e}^{\mathrm{i}n(\theta-\theta_0)}$$

  where H_n and J_n are the Hankel function of the first kind and order n and the Bessel function of the first kind and order n, respectively. Note that $H_n J_n = H_{-n} J_{-n}$.

Cette thèse est accessible à l'adresse : https://theses.insa-lyon.fr/publication/2022ISAL0077/these.pdf
© [A.D. Pouye], [2022], INSA Lyon, tous droits réservés

We also have

$$\frac{\mathrm{i}}{4}H_0^{(1)}\left[k_0 d\left(\mathbf{x},\mathbf{x}_{0\beta}\right)\right]=\frac{\mathrm{i}}{4}\sum_{n=-\infty}^{+\infty}H_n\left(k_0 r_{0\beta}\right)J_n\left(k_0 r\right)\mathrm{e}^{\mathrm{i}n\left(\theta-\theta_{0\beta}\right)}\ \text{for}\ r<r_{0\beta}$$

Note that $r_{0\beta}=r_0$ and $\theta_{0\beta}=-\theta_0$. It follows

$$p_{0\beta}\left(\mathbf{x}\right)=\frac{\mathrm{i}}{4}\sum_{n=-\infty}^{+\infty}H_n\left(k_0 r_0\right)\mathrm{e}^{in\theta}\left[J_n\left(k_0 r\right)\mathrm{e}^{-\mathrm{i}n\theta_0}+J_n\left(k_0 r\right)\mathrm{e}^{\mathrm{i}n\theta_0}\right] \tag{5.6}$$

Using Euler's trigonometric formula yields

$$p_{0\beta}\left(\mathbf{x}\right)=\frac{\mathrm{i}}{2}\sum_{n=-\infty}^{+\infty}H_n\left(k_0 r_0\right)J_n\left(k_0 r\right)\mathrm{e}^{\mathrm{i}n\theta}\cos\left(n\theta_0\right) \tag{5.7}$$

- **Derivative of the half-space Green's function $\partial_{\mathbf{n}(\mathbf{y})}G_\beta\left(\mathbf{x},\mathbf{y}\right)$**

  G_β reads

$$G_\beta\left(\mathbf{x},\mathbf{y}\right)=\frac{\mathrm{i}}{4}H_0^{(1)}\left[k_0 d\left(\mathbf{x},\mathbf{y}\right)\right]+\frac{\mathrm{i}}{4}H_0^{(1)}\left[k_0 d\left(\mathbf{x},\mathbf{y}_\beta\right)\right]$$

  where $\mathbf{y}\left(r_\sigma,\theta_\sigma\right)$ is now on σ exclusively. Note that $r>r_{\sigma\beta}=r_\sigma$. G_β can thus be written as

$$G_\beta\left(\mathbf{x},\mathbf{y}\right)=\frac{\mathrm{i}}{4}\sum_{n=-\infty}^{+\infty}\left[H_n\left(k_0 r\right)J_n\left(k_0 r_\sigma\right)\mathrm{e}^{\mathrm{i}n\left(\theta-\theta_\sigma\right)}+H_n\left(k_0 r\right)J_n\left(k_0 r_{\sigma\beta}\right)\mathrm{e}^{\mathrm{i}n\left(\theta_{\sigma\beta}-\theta\right)}\right] \tag{5.8}$$

  and becomes

$$G_\beta\left(\mathbf{x},\mathbf{y}\right)=\frac{\mathrm{i}}{2}\sum_{n=-\infty}^{+\infty}H_n\left(k_0 r\right)J_n\left(k_0 r_\sigma\right)\mathrm{e}^{-\mathrm{i}n\theta}\cos\left(n\theta_\sigma\right) \tag{5.9}$$

  The partial normal derivative $\partial_{\mathbf{n}(\mathbf{y})}\bullet$ corresponds to the radial derivative in the polar coordinates $\partial_{r_\sigma}\bullet$, that is

$$\partial_{\mathbf{n}(\mathbf{y})}G_\beta\left(\mathbf{x},\mathbf{y}\right)=\partial_{r_\sigma}G_\beta\left(\mathbf{x},\mathbf{y}\right) \tag{5.10}$$

Cette thèse est accessible à l'adresse : https://theses.insa-lyon.fr/publication/2022ISAL0077/these.pdf
© [A.D. Pouye], [2022], INSA Lyon, tous droits réservés

and ultimately, one obtains

$$\partial_{\mathbf{n}(\mathbf{y})} G_\beta(\mathbf{x},\mathbf{y}) = \frac{\mathrm{i}k_0}{2} \sum_{n=-\infty}^{+\infty} H_n(k_0 r) J_n'(k_0 r_\sigma) \mathrm{e}^{-\mathrm{i}n\theta} \cos(n\theta_\sigma) \tag{5.11}$$

where the prime denotes derivative with respect to the argument.

Inserting Eqs. (5.7) and (5.11) into Eq. (5.5), one gets

$$p(\mathbf{x}) = \frac{\mathrm{i}}{2} \sum_{n=-\infty}^{+\infty} H_n(k_0 r_0) J_n(k_0 r) \mathrm{e}^{\mathrm{i}n\theta} \cos(n\theta_0)$$
$$-\frac{\mathrm{i}k_0}{2} \sum_{n=-\infty}^{+\infty} H_n(k_0 r) \mathrm{e}^{\mathrm{i}n\theta} \int_\sigma \mathrm{Tr}\left[p(\mathbf{y})\right] J_n'(k_0 r_\sigma) \cos(n\theta_\sigma) r_\sigma \mathrm{d}\theta_\sigma$$

Let $A_n = \int_\sigma \mathrm{Tr}\left[p(\mathbf{y})\right] J_n'(k_0 r_\sigma) \cos(n\theta_\sigma) r_\sigma \mathrm{d}\theta_\sigma$ be the unknowns, one can rewrite the previous equation as follows

$$p(\mathbf{x}) = \frac{\mathrm{i}}{2} \sum_{n=-\infty}^{+\infty} H_n(k_0 r_0) J_n(k_0 r) \mathrm{e}^{\mathrm{i}n\theta} \cos(n\theta_0) - \frac{\mathrm{i}k_0}{2} \sum_{n=-\infty}^{+\infty} H_n(k_0 r) \mathrm{e}^{\mathrm{i}n\theta} A_n \tag{5.12}$$

Let us determine $\partial_{\mathbf{n}(\mathbf{x})} p(\mathbf{x}) = \partial_r p(\mathbf{x})$. It reads

$$\partial_r p(\mathbf{x}) = \frac{\mathrm{i}k_0}{2} \sum_{n=-\infty}^{+\infty} H_n(k_0 r_0) J_n'(k_0 r) \mathrm{e}^{\mathrm{i}n\theta} \cos(n\theta_0) - \frac{\mathrm{i}k_0^2}{2} \sum_{n=-\infty}^{+\infty} H_n'(k_0 r) \mathrm{e}^{\mathrm{i}n\theta} A_n$$

Applying the Neumann boundary condition $\partial_{\mathbf{n}(\mathbf{x})} p(\mathbf{x})\big|_{\mathbf{x}=\mathbf{y}} = 0$, one obtains

$$\frac{\mathrm{i}k_0}{2} \sum_{n=-\infty}^{+\infty} H_n(k_0 r_0) J_n'(k_0 r_\sigma) \mathrm{e}^{\mathrm{i}n\theta_\sigma} \cos(n\theta_0) - \frac{\mathrm{i}k_0^2}{2} \sum_{n=-\infty}^{+\infty} H_n'(k_0 r_\sigma) \mathrm{e}^{\mathrm{i}n\theta_\sigma} A_n = 0 \tag{5.13}$$

A necessary condition for Eq. (5.13) to be satisfied requires

$$A_n = \frac{J_n'(k_0 r_\sigma)}{k_0 H_n'(k_0 r_\sigma)} H_n(k_0 r_0) \cos(n\theta_0) \tag{5.14}$$

Cette thèse est accessible à l'adresse : https://theses.insa-lyon.fr/publication/2022ISAL0077/these.pdf
© [A.D. Pouye], [2022], INSA Lyon, tous droits réservés

Substituting Eq. (5.14) into Eq. (5.12) one gets the pressure at any point $\mathbf{x} \in \Omega$

$$p(\mathbf{x}) = \frac{\mathrm{i}}{2} \sum_{n=-\infty}^{+\infty} H_n(k_0 r_0) J_n(k_0 r) \mathrm{e}^{\mathrm{i}n\theta} \cos(n\theta_0)$$
$$-\frac{\mathrm{i}k_0}{2} \sum_{n=-\infty}^{+\infty} H_n(k_0 r) \mathrm{e}^{\mathrm{i}n\theta} \frac{J_n'(k_0 r_\sigma)}{k_0 H_n'(k_0 r_\sigma)} H_n(k_0 r_0) \cos(n\theta_0)$$

Hence, one gets the following expression

$$p(\mathbf{x}) = \frac{\mathrm{i}}{2} \sum_{n=-\infty}^{+\infty} \mathrm{e}^{\mathrm{i}n\theta} \cos(n\theta_0) H_n(k_0 r_0) \left[J_n(k_0 r) - \frac{J_n'(k_0 r_\sigma)}{H_n'(k_0 r_\sigma)} H_n(k_0 r) \right] \tag{5.15}$$

Eq. (5.15) also represents the transfer function between a field point $\mathbf{x}$ and a unit point source located at $\mathbf{x}_0$. However, we are interested in the pressure at the surface of the structure σ.

Using one of the Wronskian relations $J_n(\xi) H_n'(\xi) - H_n(\xi) J_n'(\xi) = \dfrac{2\mathrm{i}}{\pi\xi}$ (see Ref. [85], p. 21), one can establish the following expansion for the pressure on the surface of the structure itself at $r = r_\sigma$

$$\boxed{p(\mathbf{x}_\sigma) = -\frac{1}{\pi} \sum_{n=-\infty}^{+\infty} \mathrm{e}^{\mathrm{i}n\theta_\sigma} \cos(n\theta_0) \frac{1}{k_0 r_\sigma} \frac{H_n(k_0 r_0)}{H_n'(k_0 r_\sigma)}} \tag{5.16}$$

5.1.2 Three-dimensional case

In this case, using Green's representation along with the cylindrical harmonics expansion would be rather complicated even though an expansion in cylindrical harmonics of the 3*D* Green's function is available [93].

In order to solve the 3*D* Helmholtz equation (see Eq. (5.1)), let us consider an infinite rigid half cylinder placed on a rigid infinite baffle plane and insonified by a monopole source located at $\mathbf{x}_0$ as shown in Fig. 5.2. The total sound field of the acoustic excitation

Cette thèse est accessible à l'adresse : https://theses.insa-lyon.fr/publication/2022ISAL0077/these.pdf
© [A.D. Pouye], [2022], INSA Lyon, tous droits réservés

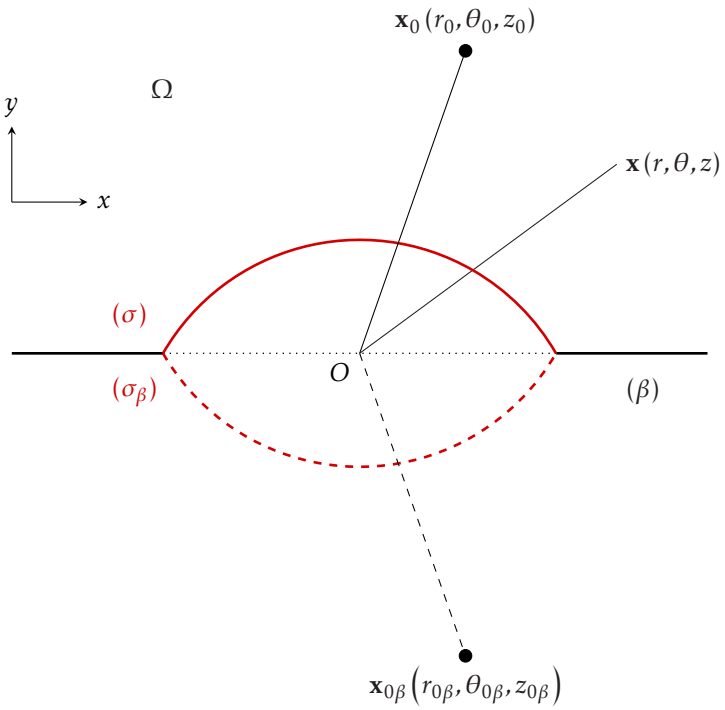

Figure 5.2: Problem geometry and parameters: section view of the $3D$ case. The z-axis is outgoing.

due to a point source on a long half cylinder above/on a hard ground can be expressed as [56, 85]

$$p(\mathbf{x}) = p_0(\mathbf{x}) + p_{0\beta}(\mathbf{x}) + p_\sigma(\mathbf{x}) + p_{\sigma\beta}(\mathbf{x}) \tag{5.17}$$

where $p_0(\mathbf{x})$ and $p_{0\beta}(\mathbf{x})$ represent respectively the pressure field due to the monopole source and its image with respect to the ground while $p_\sigma(\mathbf{x})$ and $p_{\sigma\beta}(\mathbf{x})$ correspond to the scattered pressure field by the infinite half cylinder and its image with respect to the ground, respectively.

Using the standard Fourier transform about the z variable, the free field pressure generated by the monopole source

$$p_0(\mathbf{x}) = \frac{e^{ik_0|\mathbf{x}-\mathbf{x}_0|}}{4\pi|\mathbf{x}-\mathbf{x}_0|} \tag{5.18}$$

Cette thèse est accessible à l'adresse : https://theses.insa-lyon.fr/publication/2022ISAL0077/these.pdf
© [A.D. Pouye], [2022], INSA Lyon, tous droits réservés

can be expanded in terms of its Fourier integral representation as follows

$$p_0(\mathbf{x}) = \frac{\mathrm{i}}{8\pi} \sum_{n=-\infty}^{+\infty} \mathrm{e}^{\mathrm{i}n(\theta-\theta_0)} \int_{-\infty}^{+\infty} J_n(k_r r) H_n(k_r r_0) \mathrm{e}^{\mathrm{i}k_z(z-z_0)} \mathrm{d}k_z \tag{5.19}$$

where $k_r^2 = k_0^2 - k_z^2$ corresponds to the axial wavenumber.
The same is done for the image of the source with respect to the ground/baffle. Hence

$$p_{0\beta}(\mathbf{x}) = \frac{\mathrm{e}^{\mathrm{i}k_0|\mathbf{x}-\mathbf{x}_{0\beta}|}}{4\pi|\mathbf{x}-\mathbf{x}_{0\beta}|} \tag{5.20}$$

and then, be expanded as

$$p_{0\beta}(\mathbf{x}) = \frac{\mathrm{i}}{8\pi} \sum_{n=-\infty}^{+\infty} \mathrm{e}^{\mathrm{i}n(\theta-\theta_{0\beta})} \int_{-\infty}^{+\infty} J_n(k_r r) H_n\left(k_r r_{0\beta}\right) \mathrm{e}^{\mathrm{i}k_z\left(z-z_{0\beta}\right)} \mathrm{d}k_z \tag{5.21}$$

Note that $r_{0\beta} = r_0$, $\theta_{0\beta} = -\theta_0$ and $z_{0\beta} = z_0$. Hence, one gets

$$p_{0\beta}(\mathbf{x}) = \frac{i}{8\pi} \sum_{n=-\infty}^{+\infty} \mathrm{e}^{\mathrm{i}n(\theta+\theta_0)} \int_{-\infty}^{+\infty} J_n(k_r r) H_n(k_r r_0) \mathrm{e}^{\mathrm{i}k_z(z-z_0)} \mathrm{d}k_z \tag{5.22}$$

The pressure field scattered by the structure σ and its image with respect to the ground are respectively given in convenient forms as [85]

$$p_\sigma(\mathbf{x}) = \sum_{n=-\infty}^{+\infty} \mathrm{e}^{\mathrm{i}n\theta} \int_{-\infty}^{+\infty} A_n H_n(k_r r) \mathrm{e}^{\mathrm{i}k_z z} \mathrm{d}k_z \tag{5.23}$$

and

$$p_{\sigma\beta}(\mathbf{x}) = \sum_{n=-\infty}^{+\infty} \mathrm{e}^{\mathrm{i}n\bar{\theta}} \int_{-\infty}^{+\infty} B_n H_n(k_r \bar{r}) \mathrm{e}^{\mathrm{i}k_z z} \mathrm{d}k_z \tag{5.24}$$

where $\bar{r}$ and $\bar{\theta}$ represent the coordinates of the field point with respect to the centerline of the image structure σ_β, which is the same as that of the structure σ itself.

Cette thèse est accessible à l'adresse : https://theses.insa-lyon.fr/publication/2022ISAL0077/these.pdf
© [A.D. Pouye], [2022], INSA Lyon, tous droits réservés

Noticing that the centerline of σ_β is the same as that of σ, it comes $\bar{r} = r$ and $\bar{\theta} = \theta$. Hence the total pressure scattered by the structure $p_s(\mathbf{x}) = p_\sigma(\mathbf{x}) + p_{\sigma\beta}(\mathbf{x})$ is

$$p_s(\mathbf{x}) = \sum_{n=-\infty}^{+\infty} \mathrm{e}^{\mathrm{i}n\theta} \int_{-\infty}^{+\infty} (A_n + B_n) H_n(k_r r) \mathrm{e}^{\mathrm{i}k_z z} \mathrm{d}k_z \tag{5.25}$$

which will be simply written as

$$p_s(\mathbf{x}) = \sum_{n=-\infty}^{+\infty} \mathrm{e}^{\mathrm{i}n\theta} \int_{-\infty}^{+\infty} C_n H_n(k_r r) \mathrm{e}^{\mathrm{i}k_z z} \mathrm{d}k_z \tag{5.26}$$

with $C_n = A_n + B_n$.

In the case where the centerline of the structure and its image are not superimposed as in the current configuration (see Fig. 5.2), one would have to use the Graf's translational addition theorem (see Chapter 9 of Ref. [2]) in order to transpose the cylindrical wave functions of the image structure to the cylindrical coordinates of the real structure and *vice versa*.

The total pressure field in Eq. (5.17) can now be expressed as

$$\begin{aligned} p(\mathbf{x}) = \frac{\mathrm{i}}{4\pi} \sum_{n=-\infty}^{+\infty} \mathrm{e}^{\mathrm{i}n\theta} \int_{-\infty}^{+\infty} & \cos(n\theta_0) J_n(k_r r) H_n(k_r r_0) \mathrm{e}^{\mathrm{i}k_z(z-z_0)} \\ & -4\pi\mathrm{i} C_n H_n(k_r r) \mathrm{e}^{\mathrm{i}k_z z} \mathrm{d}k_z \end{aligned} \tag{5.27}$$

Applying the Neumann boundary condition $\left.\dfrac{\partial p(\mathbf{x})}{\partial r}\right|_{r=r_\sigma} = 0$, one then obtain

$$C_n = \frac{1}{4\pi\mathrm{i}} \frac{J_n'(k_r r_\sigma)}{H_n'(k_r r_\sigma)} H_n(k_r r_0) \mathrm{e}^{-\mathrm{i}k_z z_0} \cos(n\theta_0) \tag{5.28}$$

Hence the sound pressure field of the acoustic excitation due to a monopole source on a long cylinder sector placed on rigid baffle can be written as

$$p(\mathbf{x}) = \frac{\mathrm{i}}{4\pi} \sum_{n=-\infty}^{+\infty} \mathrm{e}^{\mathrm{i}n\theta} \cos(n\theta_0) \int_{-\infty}^{+\infty} H_n(k_r r_0) \left[J_n(k_r r) - \frac{J_n'(k_r r_\sigma)}{H_n'(k_r r_\sigma)} H_n(k_r r) \right] \mathrm{e}^{\mathrm{i}k_z(z-z_0)} \mathrm{d}k_z$$

Cette thèse est accessible à l'adresse : https://theses.insa-lyon.fr/publication/2022ISAL0077/these.pdf
© [A.D. Pouye], [2022], INSA Lyon, tous droits réservés

(5.29)

Using the same Wronskian relation as for the $2D$ case allows one to establish the following equation for the pressure on the surface of the structure itself at $r = r_\sigma$

$$\boxed{p(\mathbf{x}_\sigma) = -\frac{1}{2\pi^2}\sum_{n=-\infty}^{+\infty} \mathrm{e}^{\mathrm{i}n\theta_\sigma}\cos(n\theta_0)\int_{-\infty}^{+\infty}\frac{1}{k_r r_\sigma}\frac{H_n(k_r r_0)}{H_n'(k_r r_\sigma)}\mathrm{e}^{\mathrm{i}k_z(z_\sigma - z_0)}\mathrm{d}k_z} \tag{5.30}$$

which is naturally very similar to the expression obtained for the $2D$ case in Eq. (5.16).

5.1.3 Validation of the solutions

Now that Eq. (5.1) has been solved, we need to validate the solutions of the two-dimensional and three-dimensional cases using numerical and/or experimental data. However, as we also need to validate the SST process for CRPs, the verification of these solutions will be done numerically using the Boundary Element Method (BEM) with OpenBEM [44] which is an open access code implemented in MATLAB. OpenBEM consists of three independent formulations: axisymmetrical (AxiBEM), bi-dimensional (2DBEM), and three-dimensional (3DBEM). They share a common structure and many of the features, but differ in the definition of the geometry and its implementation.
Comparisons of both amplitude and phase of the surface pressure will be carried out between OpenBEM results and analytical ones. All these steps towards the validation of the solutions are included in Appendix D. For both cases (two-dimensional and three-dimensional), a first study on the number of harmonics that must be considered in Eq. (5.16) and Eq. (5.30) for an accurate estimation of the transfer functions is proposed. For the three-dimensional case, the infinite integral needed to be estimated in a finite domain: all the steps towards this estimation can be consulted in Sec. D.2.1. Then the proper validation of the transfer functions is done by comparing the surface pressure obtained using OpenBEM to those yielded by our solutions.

Cette thèse est accessible à l'adresse : https://theses.insa-lyon.fr/publication/2022ISAL0077/these.pdf
© [A.D. Pouye], [2022], INSA Lyon, tous droits réservés

Naturally, 2DBEM is used for the validation of the two-dimensional transfer functions and 3DBEM for that of the three-dimensional transfer functions. Comparing 2DBEM results to those provided by Eq. (5.16) show a very good agreement between both methods, as shown in Fig. 5.3. In the case of the three-dimensional transfer functions, the results are also very accurate as it can been seen in Fig. 5.4. Although there are some minor discrepancies due to the limits of numerical methods (OpenBEM in this case), we can effectively validate the solution established in Eq. (5.30).

Fig. 5.3 and Fig. 5.4 show an example of comparisons between the pressure (amplitude and phase) at the surface of the considered structure obtained using OpenBEM with the analytical results for the two-dimensional case and the three-dimensional case, respectively. One can refer to Appendix D for more comparisons (Fig. D.8, Fig. D.9 and Fig. D.10 for the two-dimensional case; Fig. D.17, Fig. D.18, Fig. D.19 and Fig. D.20 for the three-dimensional case).

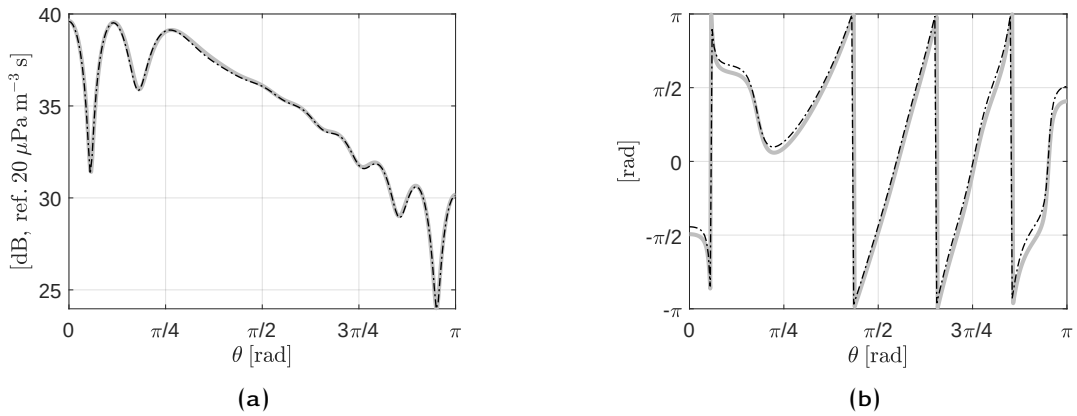

Figure 5.3: Comparison between the amplitudes and phases of the wall-pressure obtained with OpenBEM (gray continuous line) and those obtained using the developed analytical solution in Eq. (5.16) (dash-dotted black line) for one position of the monopole source $\left(r_0 = 1\,\text{m}, \theta_0 = \frac{\pi}{4}\right)$ at a frequency $f = 1000\,\text{Hz}$: two-dimensional case. (a) amplitudes (b) phases.

In the validation figures in Appendix D, one can notice that in the two-dimensional case, the match between the analytical solution and the numerical results is almost perfect. However, for the three-dimensional case, there are some minor discrepancies in the nu-

Cette thèse est accessible à l'adresse : https://theses.insa-lyon.fr/publication/2022ISAL0077/these.pdf
© [A.D. Pouye], [2022], INSA Lyon, tous droits réservés

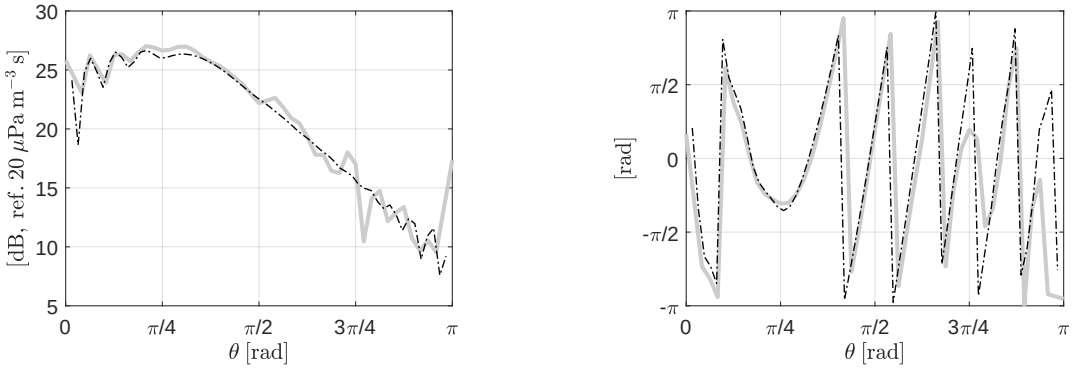

Figure 5.4: Comparison between the magnitudes and phases of the wall-pressure obtained with OpenBEM (gray continuous line) and those obtained using the developed analytical solution in Eq. (5.30) (dash-dotted black line) for one position of the monopole source $\left(r_0 = 0.6\,\text{m}, \theta_0 = \frac{\pi}{4}, z_0 = 0.5\,\text{m}\right)$ and at a frequency $f = 2000\,\text{Hz}$: three-dimensional case. The distance along the z-axis between the plane of the monopole source and that of the observation points is $|z - z_0| = 0.3\,\text{m}$.

merical results inherent to the BEM implementation. Indeed, it is important to note that although the boundary element method is nowadays a well established technique to solve acoustic problems, one of its most disadvantageous characteristics is the non-uniqueness of the solution. In fact, the exterior response is polluted by fictitious eigenfrequencies at the corresponding internal resonances. This purely mathematical issue is due to the ill-posed formulation of the method and strongly degrades the prediction accuracy. Several methodologies have been proposed to overcome this shortcoming. For Direct BEM, one of the most popular approaches is the Combined Helmholtz Integral Equation Formulation (CHIEF) method. It consists in applying internal over-determination points to improve the solution accuracy. Choosing these points is not straightforward since certain conditions have to be satisfied. In the past, methodologies have been developed to determine an efficient criterion. Nevertheless, practical applications are only limited to academic cases. Choosing the CHIEF points in an efficient way allows obtaining very accurate solutions with a limited increase of computational efforts. In our case, 5 CHIEF points were defined inside the mesh of the half cylinder shown in Fig. D.16.

Cette thèse est accessible à l'adresse : https://theses.insa-lyon.fr/publication/2022ISAL0077/these.pdf
© [A.D. Pouye], [2022], INSA Lyon, tous droits réservés

In the following table, a comparison of computation times between numerical (OpenBEM) and analytical solutions is proposed. The indicated computation times correspond to the time needed for each method to yield the transfer functions between one source position and a semi-circle of observation points (same number of points for each case) at one frequency.

Table 5.1: Transfer functions computation times.

	2D	**3D**
OpenBEM	$\sim 75\,\mathrm{s}$	$\sim 163.3\,\mathrm{s}$
Analytical	$\sim 0.86\,\mathrm{s}$	$\sim 3.5\,\mathrm{s}$

The computer processing times listed in Table 5.1 are all determined on the same computer with the following characteristics

- Processor: Intel Core i7-8650U CPU at 1.90 GHz
- RAM: 16.0 Go
- Operating system: Windows 10 64 bits

5.2 SST ON CURVED RECTANGULAR PANELS: PARAMETRIC STUDIES

5.2.1 Two-dimensional case

As described in Chapter 2, SST aims at reproducing Wall-Pressure Plane Waves (WPPWs) of the form $p(\mathbf{x},\mathbf{k}) = \mathrm{e}^{\mathrm{i}\mathbf{k}\mathbf{x}}$ which in turn will allow the synthesis of the vibroacoustic response of structures under random excitations. In the current geometry of the problem, illustrated in Fig. 5.5, these WPPWs are of the form

$$p(\mathbf{x},\mathbf{k}) = \mathrm{e}^{-\mathrm{i}k_\theta R\theta} \tag{5.31}$$

Cette thèse est accessible à l'adresse : https://theses.insa-lyon.fr/publication/2022ISAL0077/these.pdf
© [A.D. Pouye], [2022], INSA Lyon, tous droits réservés

where R is the radius of the structure and k_θ corresponds to the circumferential wavenumber related to the circumferential order n through the relation: $n = k_\theta R$.

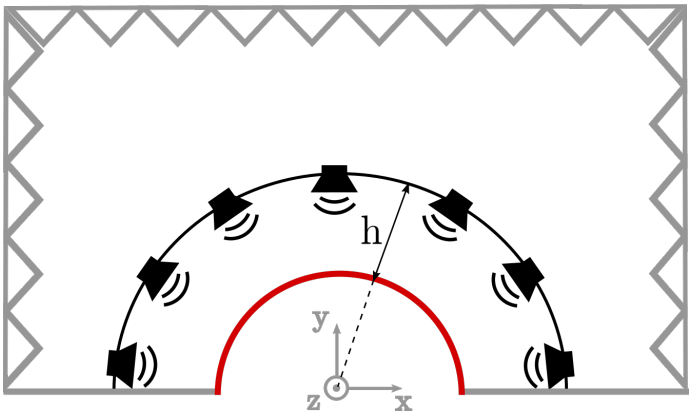

Figure 5.5: Section view of the SST setup for CRPs.

In the following, we go through the same steps as for the parametric study on SST for FRPs in order to define the optimal design parameters of the virtual array of monopoles in this new geometry of the problem. For the sake of simplicity, the structure of interest will be a half-circle with a radius $R = 0.5\,\mathrm{m}$.

5.2.1.1 *Studying the effect of the density of the array of monopoles*

From the results obtained with planar structures, a good reproduction of the target pressure field was obtained when the criterion of 4 monopoles per minimum wavelength is fulfilled [6, 62]. However, in the current case, there is a curvature on the studied structure which means that this criterion has to be validated or changed for these structures. In this context, we propose to study the behavior of SST on these structures when all other parameters of the process are fixed but one: n_s, the number of required monopole sources per minimum wavelength. We aim at synthesizing WPPWs which wavenumbers are in $[-k_{max}, k_{max}]$ with k_{max} arbitrarily set at $50\,\mathrm{rad\,m^{-1}}$. The spacing

Cette thèse est accessible à l'adresse : https://theses.insa-lyon.fr/publication/2022ISAL0077/these.pdf
© [A.D. Pouye], [2022], INSA Lyon, tous droits réservés

between two adjacent source positions is defined as a fraction of the lowest wavenumber to be reconstructed at the highest frequency of interest

$$\delta_s = \frac{\lambda_{min}}{n_s} \tag{5.32}$$

where n_s is a positive integer representing the number of monopole positions per minimum wavelength. Eq. (**??**) is simply a generalization of Eq. (3.5).

In these studies, the geometry of the virtual array of monopoles is the same as the structure of interest as shown in Fig. 5.5. The radius of this arc of sources is always greater than the radius of the structure. In comparison to the interplanar distance defined for rectangular structures, we define the radial height h as the difference between the radius of the arc of monopoles and that of the structure. In the following, the radial height is $h = 5\,\text{cm}$.

Fig. 5.6, Fig. 5.7 and Fig. 5.8 respectively show the reproduction error defined in Eq. (3.6) in the frequency-wavenumber domain, the real part and the imaginary part of the target and synthesized pressure fields at the surface of the structure (θ designates the angular position of the considered point on the structure) for four different values of n_s.

It is important to remember the criteria for an accurate reproduction process. This criteria was discussed in Sec. 3.3.2 of Chapter 2: the synthesis is considered accurate when the reproduction error is less than $-10\,\text{dB}$ which corresponds to a relative MSE of less than 10%. Comparing Fig. 5.6a, Fig. 5.6b, Fig. 5.6c and Fig. 5.6d, one can notice that the reproduction error covers an increasing area in the frequency-wavenumber domain when n_s varies from 1 to 4. This means that for an increasing number of monopoles per smallest wavelength, the reproduction process becomes more accurate. This observation is confirmed by comparing the target pressure fields and the synthesized ones. In Fig. 5.7a, Fig. 5.8a, 5.7b and Fig. 5.8b, one can clearly see that the reproduced pressure fields do not match the target ones. However, in Fig. 5.7c, Fig. 5.8c, 5.7d and Fig. 5.8d, the reproduction process is very accurate and the synthesized pressure fields perfectly match with the target ones. It is important to notice that only one example of WPPW is

Cette thèse est accessible à l'adresse : https://theses.insa-lyon.fr/publication/2022ISAL0077/these.pdf
© [A.D. Pouye], [2022], INSA Lyon, tous droits réservés

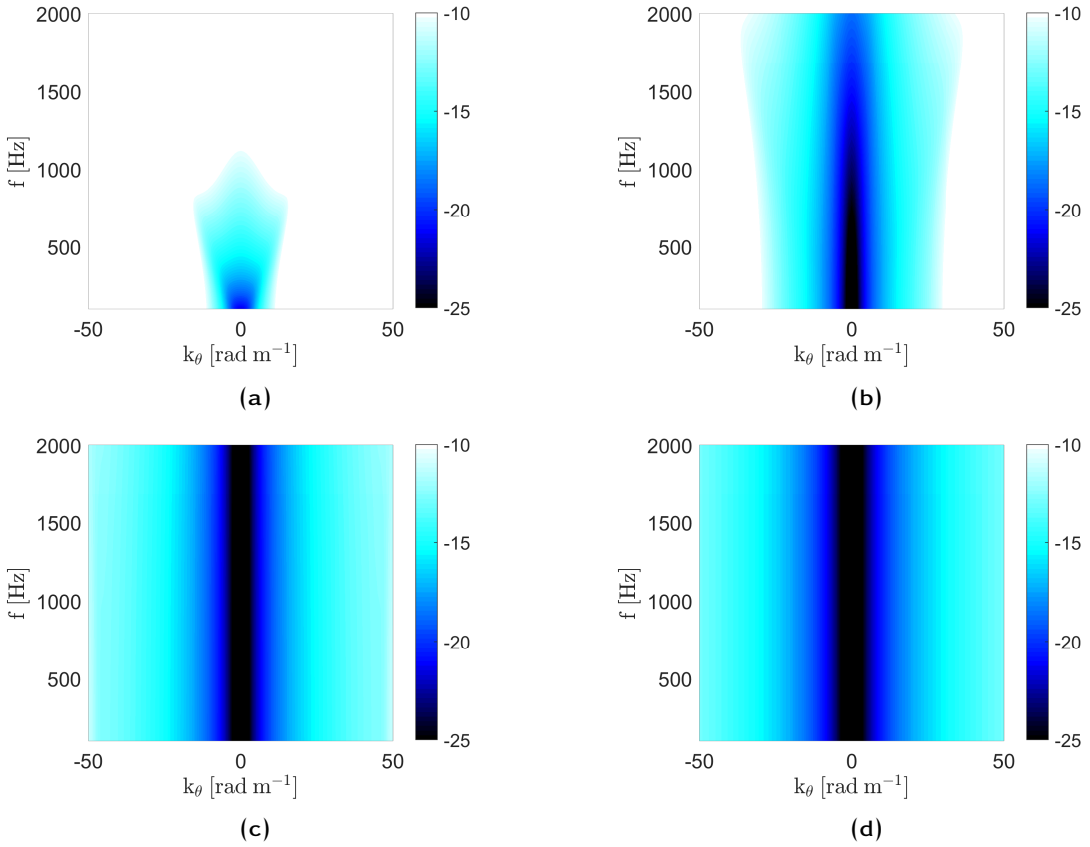

Figure 5.6: Reproduction error in the frequency-wavenumber domain: (a) $n_s = 1$, (b) $n_s = 2$, (c) $n_s = 3$ and (d) $n_s = 4$.

showed in these figures, the results for other WPPWs can be deduced by consulting the reproduction error maps in Fig. 5.6 and choosing one frequency and one wavenumber. In conclusion, the WPPWs are accurately synthesized when $n_s \geq 3$ which is consistent with the criteria that was defined for rectangular structures. Thus, we define the same criteria as in Sec. 3.3.1, that is $n_s = 4$ for the remainder of this chapter.

Let us now discuss the influence of the radial height on the conformal geometry setup of SST.

Cette thèse est accessible à l'adresse : https://theses.insa-lyon.fr/publication/2022ISAL0077/these.pdf
© [A.D. Pouye], [2022], INSA Lyon, tous droits réservés

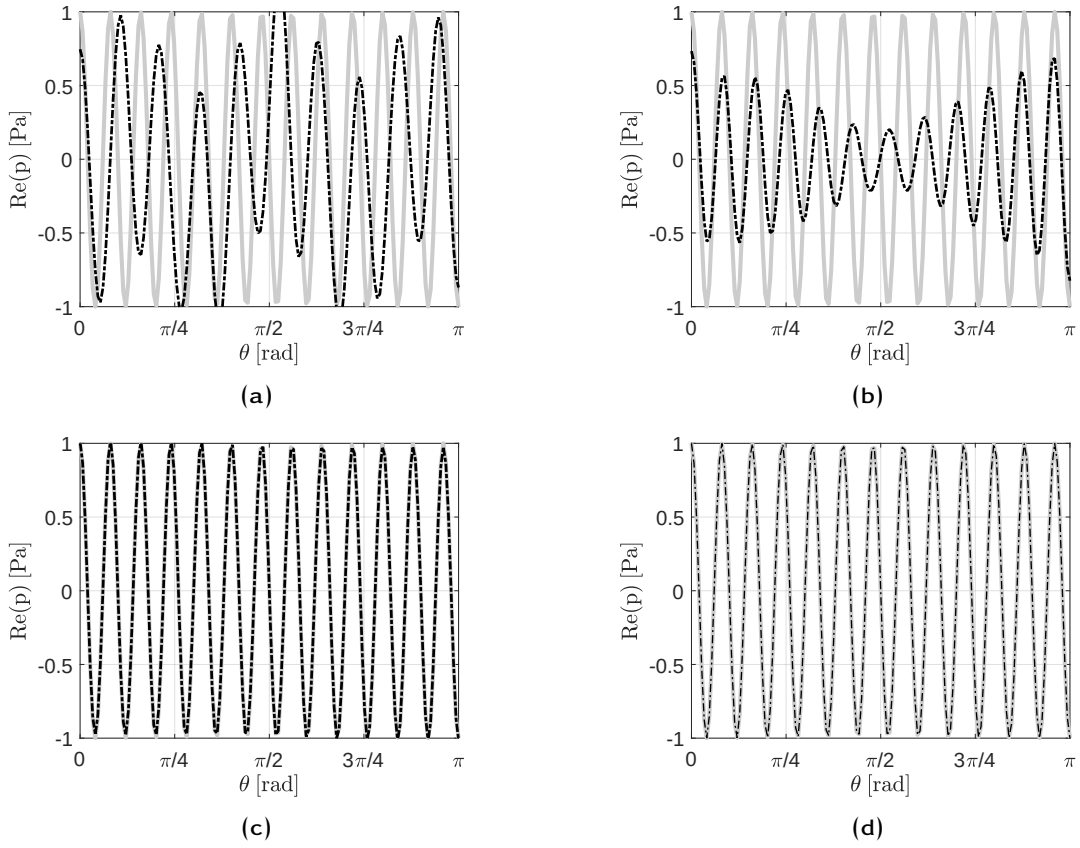

Figure 5.7: Real part of the target pressure field (continuous grey line) and the reconstructed pressure (dashed black line) of the WPPW defined by the wavevector $(-50, 50)$ rad m^{-1} at a frequency $f = 2000$ Hz: (a) $n_s = 1$, (b) $n_s = 2$, (c) $n_s = 3$ and (d) $n_s = 4$.

Cette thèse est accessible à l'adresse : https://theses.insa-lyon.fr/publication/2022ISAL0077/these.pdf
© [A.D. Pouye], [2022], INSA Lyon, tous droits réservés

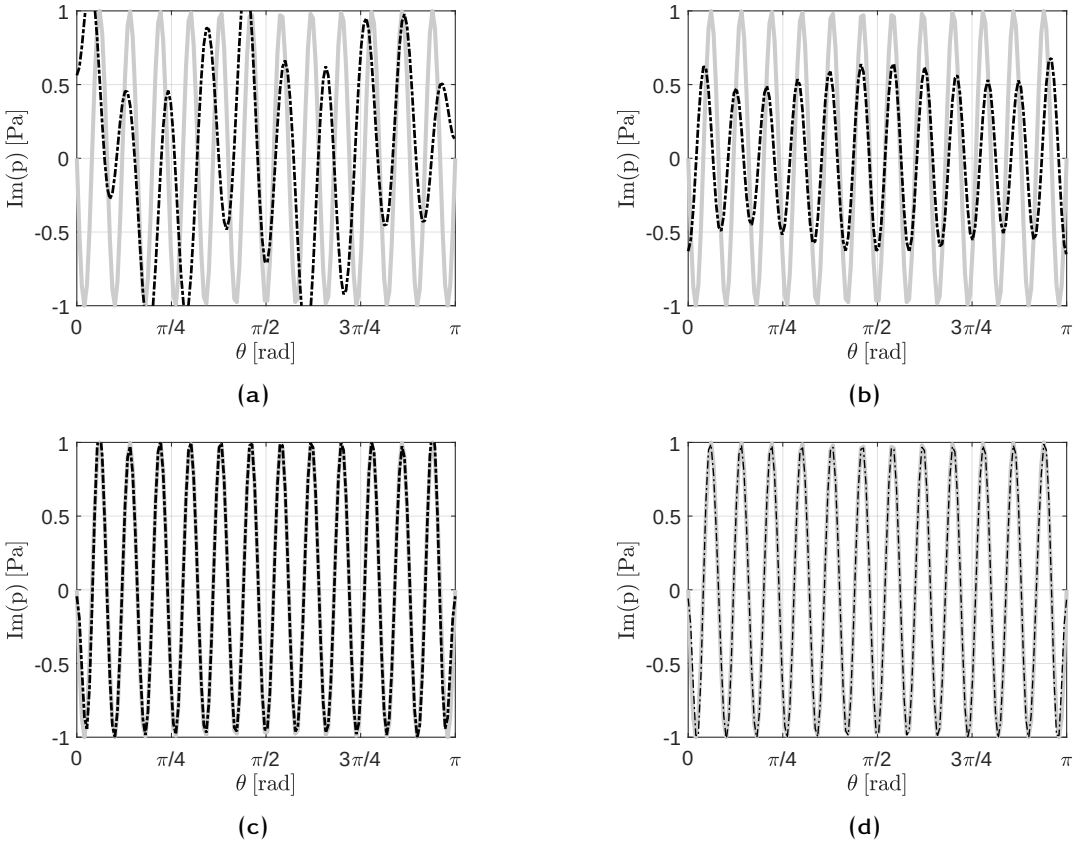

Figure 5.8: Imaginary part of the target pressure field (continuous grey line) and the reconstructed pressure (dashed black line) of the WPPW defined by the wavevector $(-50, 50)$ rad m^{-1} at a frequency $f = 2000$ Hz: (a) $n_s = 1$, (b) $n_s = 2$, (c) $n_s = 3$ and (d) $n_s = 4$.

Cette thèse est accessible à l'adresse : https://theses.insa-lyon.fr/publication/2022ISAL0077/these.pdf
© [A.D. Pouye], [2022], INSA Lyon, tous droits réservés

5.2.1.2 Influence of the radial height

Now that the criteria of four monopoles per smallest wavelength is verified, we will study the influence of the radial height on the reproduction process by modifying its value and discussing the results in terms of the indicators established in Chapter 2.

STANDARD SST WITHOUT ADDED NOISE

Fig. 5.9 shows the results of the parametric studies in determining the optimal radial height for an accurate reproduction process: one can respectively observe the reproduction error in the frequency-wavenumber domain, the condition number of the transfer matrix **G**, the real part and the imaginary part of the target and reconstructed pressure fields.

Similar results as in Fig. 5.9 are obtained for the other two radial heights of interest: $h = 10\,\text{cm}$ and $h = 20\,\text{cm}$.

Let us now take a look at the condition number of the transfer matrix **G** for each radial height in Fig. 5.10. One can notice that the condition number does not vary that much as a function of the frequency: the same result was observed in Fig. 3.2a in Chapter 3 fro FRPs. However, comparing these results for each of the radial heights, we can notice a rapidly increasing condition number when the arc of monopoles is displaced farther from the structure: from $\sim 10^3$ for $h = 5\,\text{cm}$ to $\sim 10^9$ for $h = 20\,\text{cm}$. It is important to note that this SST process is "numerical" and subject to only numerical errors. In practice the experimental process can be subject to multiple sources of errors and thus the less ill-posed the problem, the better. This means that the condition number of the transfer matrix must not be very high in practical applications. Otherwise, the errors induced by the hypothetical noise around the setup will be amplified due to the sensitivity of the system.

In order to illustrate these observations, let us intentionally add some noise during the numerical reconstruction process.

Cette thèse est accessible à l'adresse : https://theses.insa-lyon.fr/publication/2022ISAL0077/these.pdf
© [A.D. Pouye], [2022], INSA Lyon, tous droits réservés

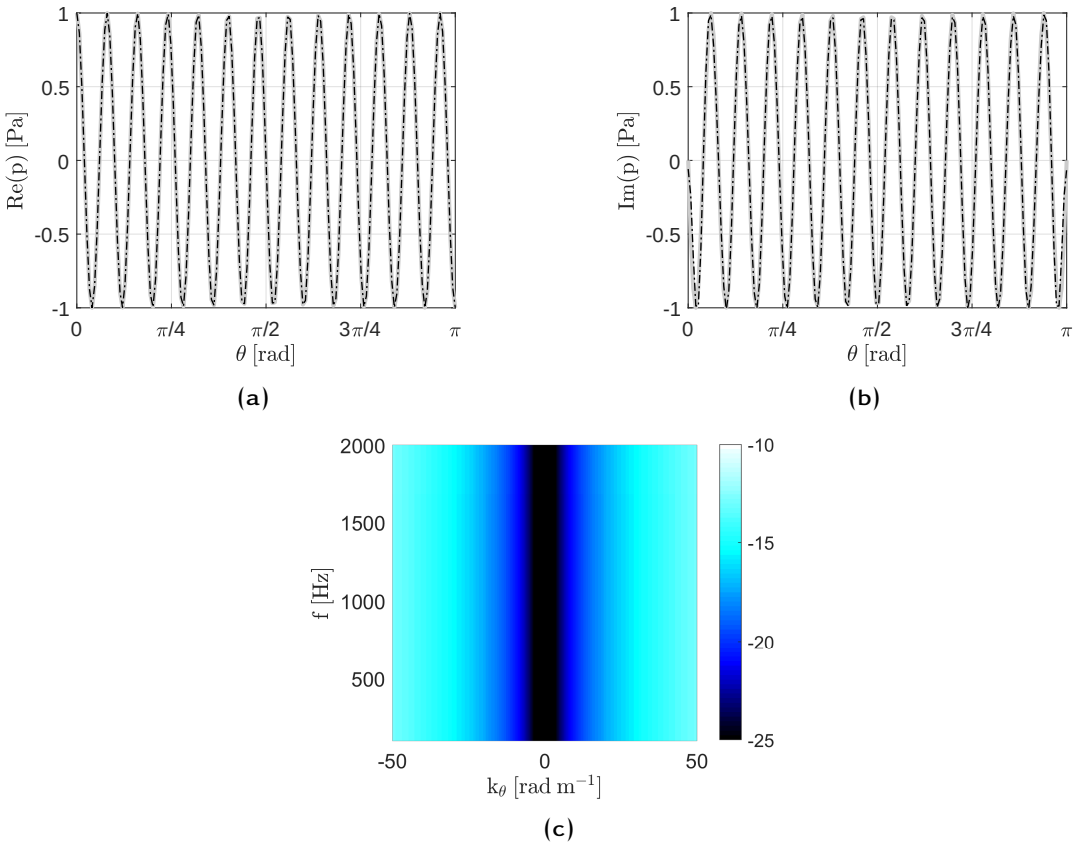

Figure 5.9: Parametric studies for $h = 5\,\text{cm}$: (a) real part and (b) imaginary part of the target pressure (continuous grey line) and reconstructed pressure (dashed black line) of the WPPW defined by the wavevector $(-50, 50)\,\text{rad}\,\text{m}^{-1}$ at a frequency $f = 2000\,\text{Hz}$ and (c) reproduction error.

Adding noise to the standard SST process

The reconstruction of the pressure field is done using the following equation

$$\mathbf{p} = \hat{\mathbf{G}}\mathbf{q} \tag{5.33}$$

where $\mathbf{p}$ is the reconstructed pressure field and $\mathbf{q}$ represents the monopole amplitude at each position. Eq. (**??**) can be written as follows

$$p_r = \hat{G}_{rs} q_s \tag{5.34}$$

Cette thèse est accessible à l'adresse : https://theses.insa-lyon.fr/publication/2022ISAL0077/these.pdf
© [A.D. Pouye], [2022], INSA Lyon, tous droits réservés

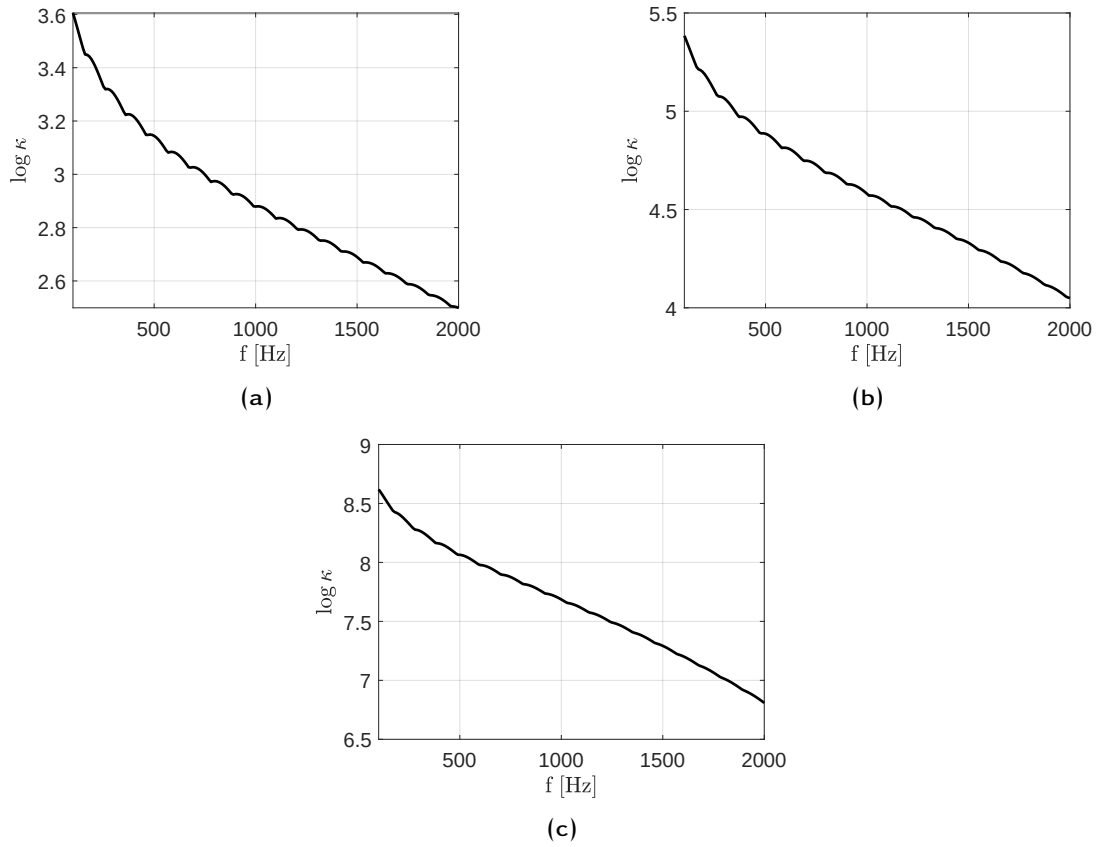

Figure 5.10: Condition number ($\log_{10}(\kappa)$) of the transfer matrix **G** for three different radial heights: (a) $h = 5$ cm, (b) $h = 10$ cm and (c) $h = 20$ cm.

where $\hat{G}_{rs} = G_{rs} + \epsilon_{rs}$, G_{rs} the usual reconstruction transfer matrix computed using Eq. (5.16) and $\epsilon_{rs} \in [0, 0.01]$ is a normally distributed random noise.

In the following, we discuss the influence of the background noise on the reproduction process of the target pressure field for the three radial heights that seemingly yielded the same results and choose the optimal radial height for the experimental SST on this type of geometry.

In Fig. 5.11, we propose a comparison of the reproduction error in the frequency-wavenumber domain and under the conditions presented above. One can now easily see the difference between the three radial heights: the further the arc of monopoles is from the structure, the more sensitive to background noise the system becomes. Fig.

Cette thèse est accessible à l'adresse : https://theses.insa-lyon.fr/publication/2022ISAL0077/these.pdf
© [A.D. Pouye], [2022], INSA Lyon, tous droits réservés

5.9c and Fig. 5.11a represent plots of the reproduction error during the SST process: one without added noise and the other with added noise. The comparison shows that the added noise induces a less accurate synthesis for frequencies less than 1500 Hz. In the wavenumber domain, it seems to affect high wavenumbers: this is understandable given that the higher the wavenumber, the more constrained the system is. However, it can be specifically designed to reproduce a target wavenumber.

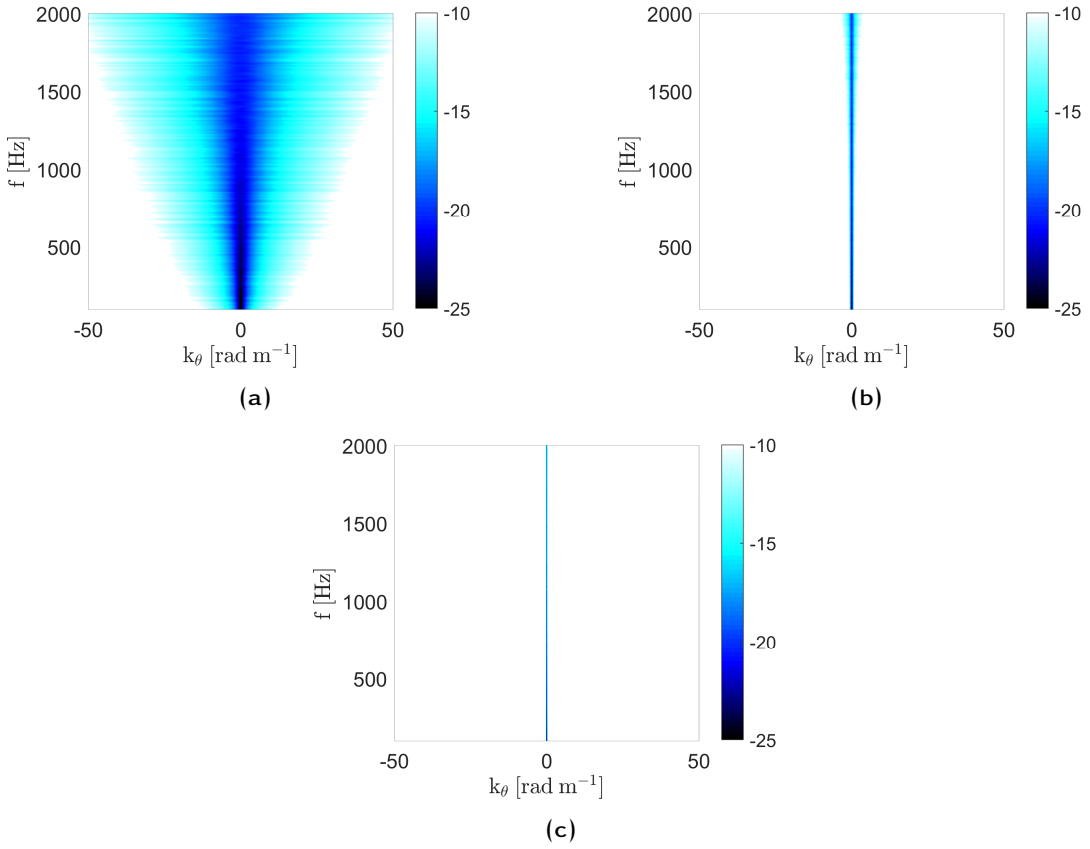

Figure 5.11: Parametric studies for an added normally distributed noise which values vary between 0 and 0.01. Reproduction errors in the frequency-wavenumber domain for (a) $h = 5$ cm, (b) $h = 10$ cm and (c) $h = 20$ cm.

Fig. 5.11b and Fig. 5.11c respectively show the reproduction error for a radial height $h = 10$ cm and $h = 20$ cm. One can notice that, with the added noise, SST succeeds only in a narrow band around 0 rad m^{-1} and for all frequencies. Therefore, one can only expects

Cette thèse est accessible à l'adresse : https://theses.insa-lyon.fr/publication/2022ISAL0077/these.pdf
© [A.D. Pouye], [2022], INSA Lyon, tous droits réservés

that the reconstructed pressure fields will not be successful. This is confirmed by Fig. 5.12 and Fig. 5.13 which respectively compare the real part and the imaginary part of the reconstructed pressure field to the target values of both quantities. We notice that for a radial height $h = 5\,\text{cm}$, the added noise barely affects the SST process. However, for $h = 10\,\text{cm}$ and specially for $h = 20\,\text{cm}$, the added noise strongly disturbs the process. It is even more disturbed on the sides of the structure, i. e. for $\theta \in \left[0, \frac{\pi}{4}\right] \cup \left[\frac{3\pi}{4}, \pi\right]$, approximately.

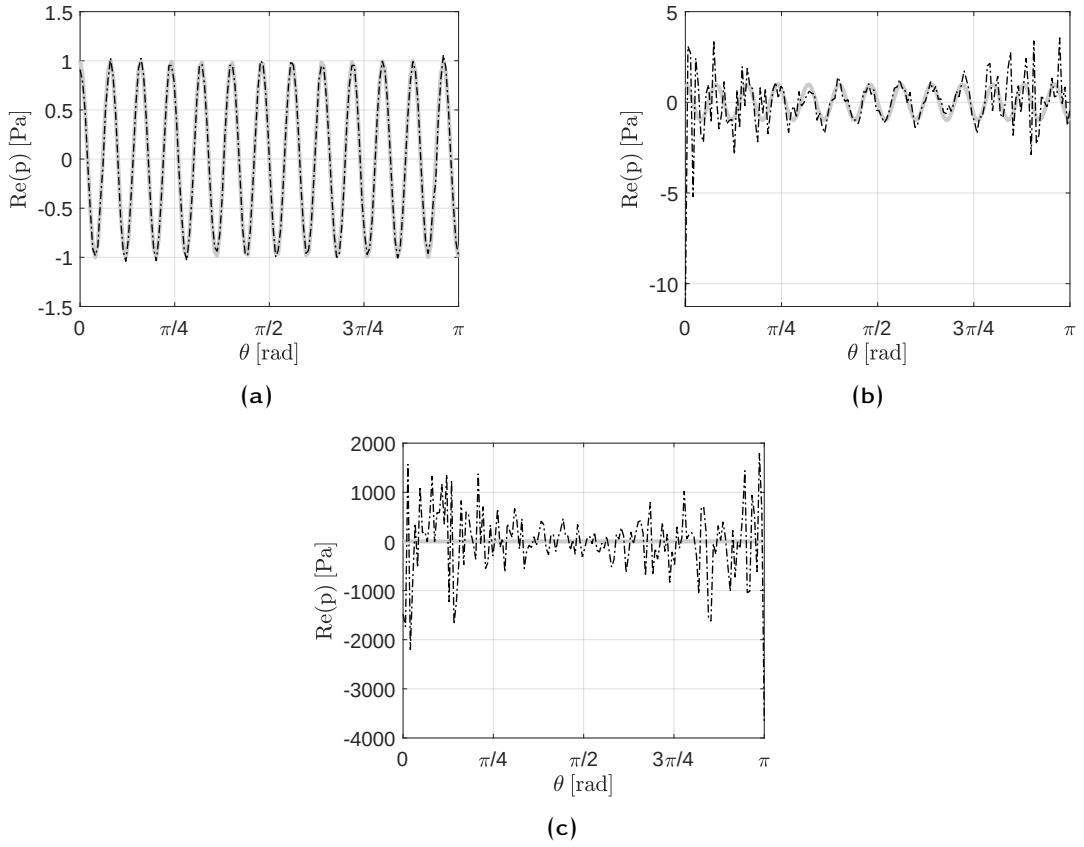

Figure 5.12: Parametric studies for an added normally distributed noise which values vary between 0 and 0.01. Real part of the target pressure (continuous grey line) and reconstructed pressure (dashed black line) for (a) $h = 5\,\text{cm}$, (b) $h = 10\,\text{cm}$ and (c) $h = 20\,\text{cm}$. The WPPW is defined by the wavevector $(-50, 50)\,\text{rad}\,\text{m}^{-1}$ at a frequency $f = 2000\,\text{Hz}$.

Cette thèse est accessible à l'adresse : https://theses.insa-lyon.fr/publication/2022ISAL0077/these.pdf
© [A.D. Pouye], [2022], INSA Lyon, tous droits réservés

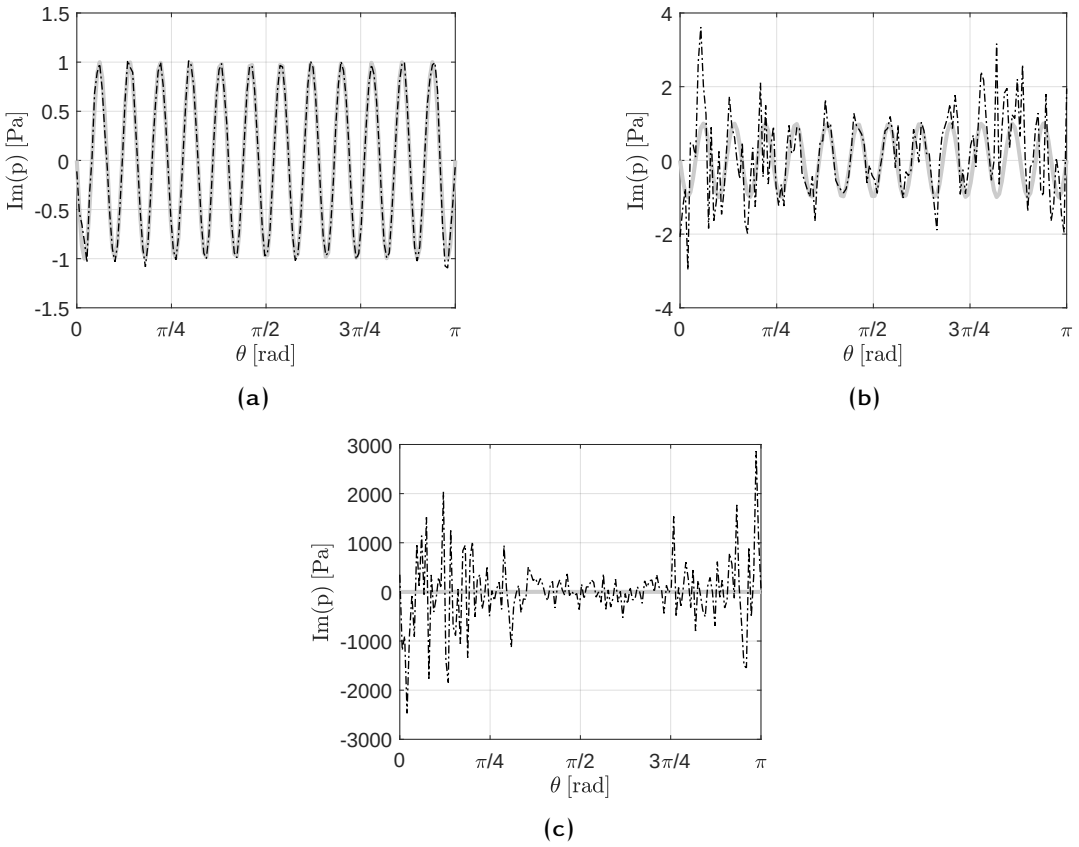

Figure 5.13: Parametric studies for an added normally distributed noise which values vary between 0 and 0.01. Imaginary part of the the target pressure (continuous grey line) and reconstructed pressure (dashed black line) for (a) $h = 5\,\text{cm}$, (b) $h = 10\,\text{cm}$ and (c) $h = 20\,\text{cm}$. The WPPW is defined by the wavevector $(-50, 50)\,\text{rad}\,\text{m}^{-1}$ at a frequency $f = 2000\,\text{Hz}$.

Considering all of the reasons discussed above, it is safe to state that the closer the arc of monopoles is to the structure, the less the condition number of the transfer matrix inducing a more accurate synthesis of the target pressure fields.

Prior to presenting the three-dimensional case, let us consider a different structure-monopole array configuration than the conformal geometric configuration presented in Fig. 5.5.

Cette thèse est accessible à l'adresse : https://theses.insa-lyon.fr/publication/2022ISAL0077/these.pdf
© [A.D. Pouye], [2022], INSA Lyon, tous droits réservés

5.2.1.3 *Non-conformal geometry*

Let us consider Fig. 5.14. In this new configuration, the array of monopole is organized as a line array in the two-dimensional case and in the three-dimensional case, it would be a rectangular array of monopoles. In the following, we will study the impact of the non-conformal structure-monopole array geometry in the results yielded by the SST process for the two-dimensional case: note that the length of the monopole line must be at least equal to the chord length of the structure.

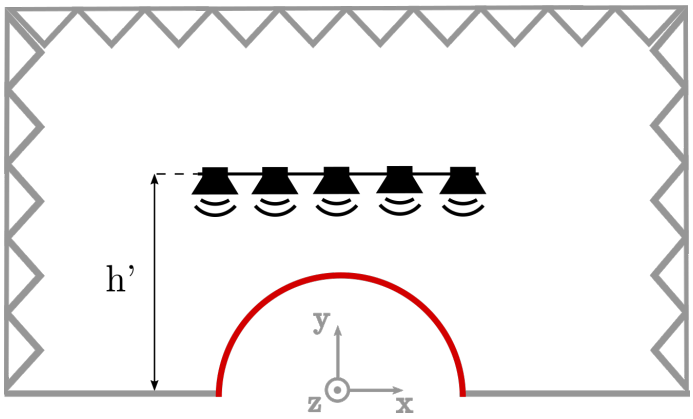

Figure 5.14: Section view of the non conformal SST geometry setup for CRPs.

Note that in the new configuration, the radial height h is replaced by the height h' which corresponds to the distance between the ground where the structure is positioned and the line of monopoles.

Fig. 5.15, Fig. 5.16 and Fig. 5.17 show the SST results for three different heights h'. Comparing Fig. 5.15a, Fig. 5.16a and Fig. 5.17a, one can notice that the surface covered by the reproduction error in the frequency-wavenumber domain becomes smaller and smaller when the height h' is increased from 55 cm to 70 cm. This result was already pointed out in the case of the conformal geometry which has better results than the current geometry configuration. However, comparing Fig. 5.15b, Fig. 5.16b and Fig. 5.17b, one can notice that the condition number does not vary that much among the three heights h': from 10^{14} to 10^{17}. Compared to the conformal configuration (see Fig.

Cette thèse est accessible à l'adresse : https://theses.insa-lyon.fr/publication/2022ISAL0077/these.pdf
© [A.D. Pouye], [2022], INSA Lyon, tous droits réservés

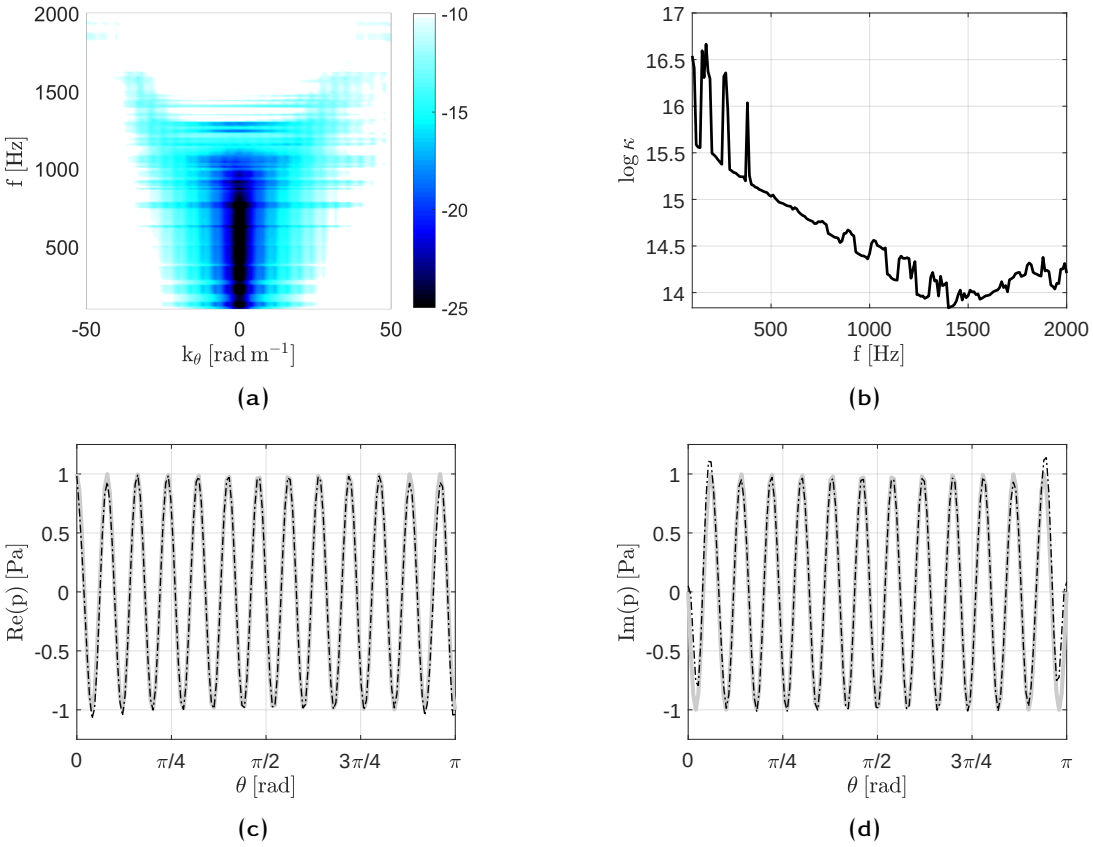

Figure 5.15: Parametric studies for a non conformal geometry configuration and for $h' = 55\,\text{cm}$: (a) reproduction error, (b) logarithm of the condition number ($\log_{10}\kappa$), (c) real part and (d) imaginary part of the target pressure (continuous grey line) and reconstructed pressure (dashed black line) of the WPPW defined by the wavevector $(-50, 50)$ rad m^{-1} at a frequency $f = 2000\,\text{Hz}$.

5.10a, Fig. 5.10b and Fig. 5.10c), these condition numbers for the current configuration are very high.

Let us take a look at the reconstructed WPPW for each of the arbitrarily chosen heights h'. For $h' = 55\,\text{cm}$, the reconstructed pressure matches almost perfectly the target pressure field, see Fig. 5.15c and Fig. 5.15d. When $h' = 60\,\text{cm}$, some discrepancies between the reconstructed WPPW and the target one start to appear on the sides of the structure, that is for $\theta \in \left[0, \frac{\pi}{4}\right] \cup \left[\frac{3\pi}{4}, \pi\right]$ as can be noticed in Fig. 5.16c and Fig. 5.16d. This observation is even more visible when $h' = 70\,\text{cm}$ in Fig. 5.17c and Fig. 5.17d.

Cette thèse est accessible à l'adresse : https://theses.insa-lyon.fr/publication/2022ISAL0077/these.pdf
© [A.D. Pouye], [2022], INSA Lyon, tous droits réservés

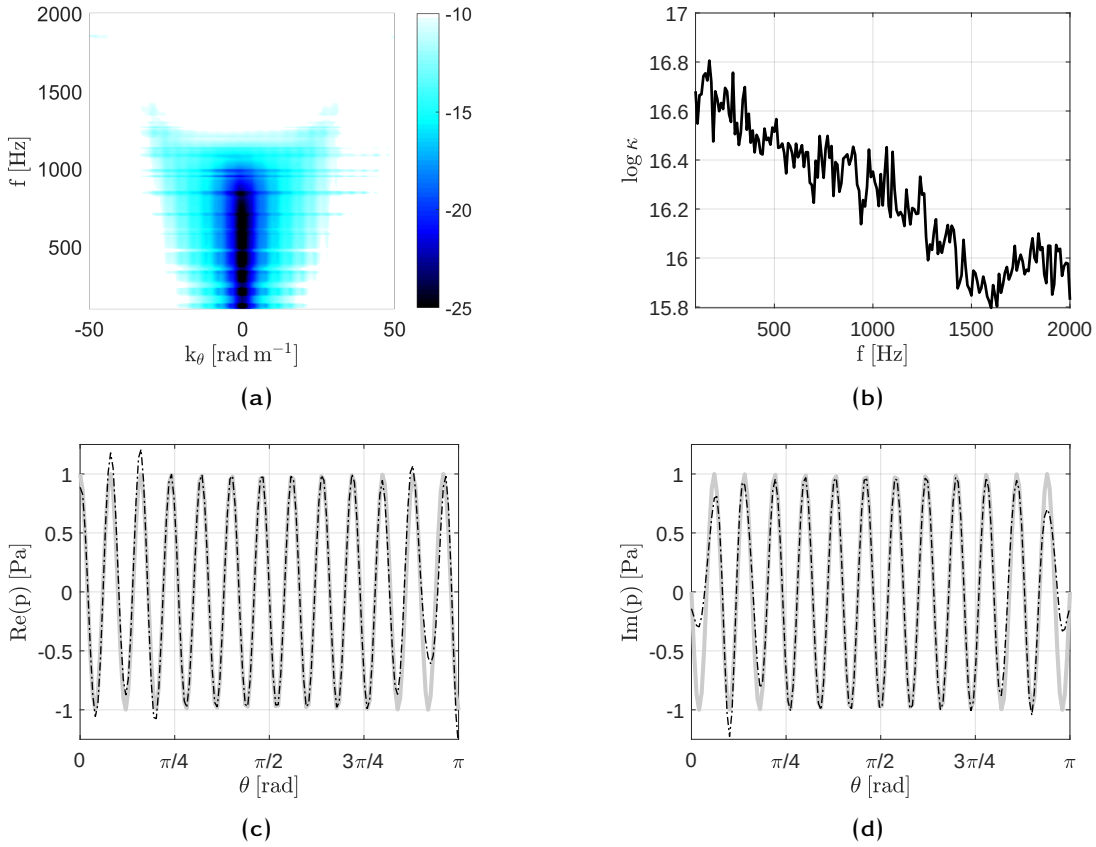

Figure 5.16: Parametric studies for a non conformal geometry configuration and for $h' = 60\,\text{cm}$: (a) reproduction error, (b) logarithm of the condition number ($\log_{10}\kappa$), (c) real part and (d) imaginary part of the target pressure (continuous grey line) and reconstructed pressure (dashed black line) of the WPPW defined by the wavevector $(-50, 50)\,\text{rad}\,\text{m}^{-1}$ at a frequency $f = 2000\,\text{Hz}$.

In summary, the non conformal geometry allows a good reconstruction process in a reduced frequency-wavenumber domain when compared to the conformal geometry. We have also noticed that the condition number of the transfer matrix $\mathbf{G}$ in this case is very high and that better results are obtained with the conformal geometry configuration even though there is a good reproduction of some WPPWs in the current configuration. As one would expect, the conformal configuration is better suited for an accurate reconstruction of the target pressure field as the monopole source covers more area on the structure even though the line array of monopoles is denser in the non conformal geometry. In

Cette thèse est accessible à l'adresse : https://theses.insa-lyon.fr/publication/2022ISAL0077/these.pdf
© [A.D. Pouye], [2022], INSA Lyon, tous droits réservés

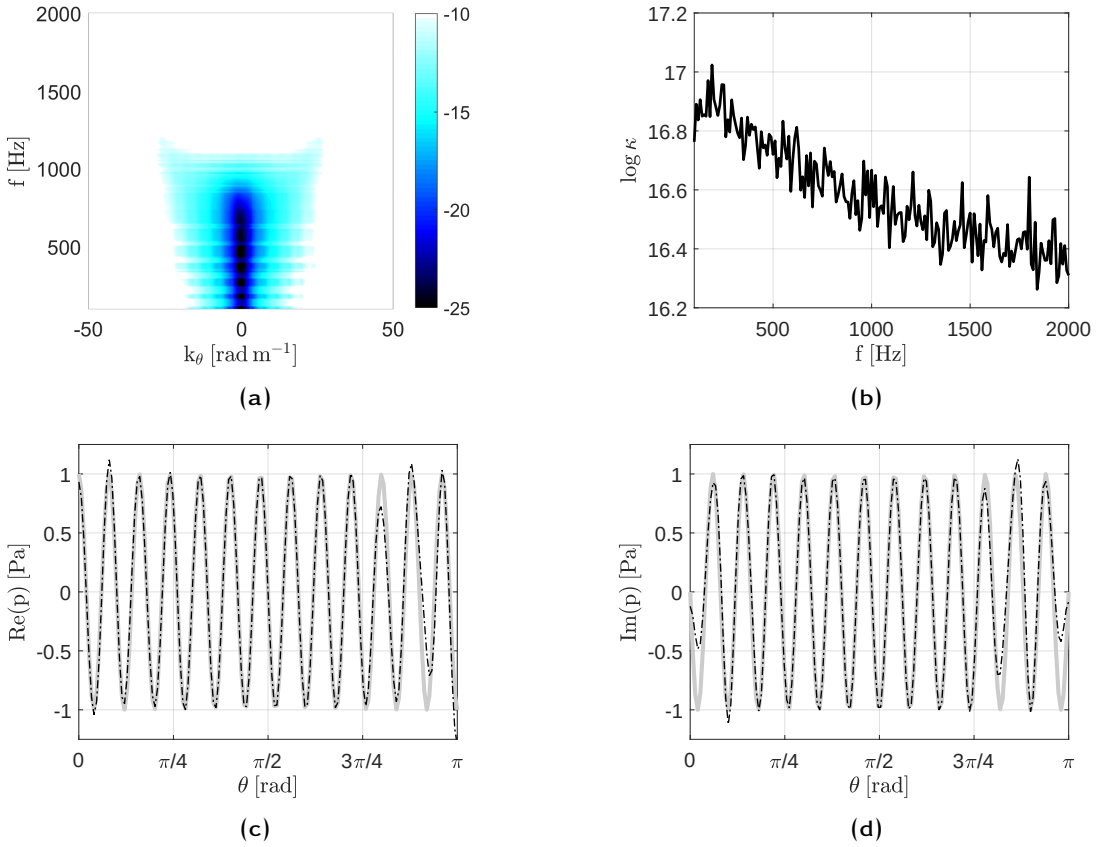

Figure 5.17: Parametric studies for a non conformal geometry configuration and for $h' = 70\,\text{cm}$: (a) reproduction error, (b) logarithm of the condition number ($\log_{10}\kappa$), (c) real part and (d) imaginary part of the target pressure (continuous grey line) and reconstructed pressure (dashed black line) of the WPPW defined by the wavevector $(-50, 50)\,\text{rad}\,\text{m}^{-1}$ at a frequency $f = 2000\,\text{Hz}$.

fact in the case of the conformal geometry, the monopole sources are placed along an arc of length πR and in the case of the non conformal geometry, the monopoles are placed along a line of length $2R$.

Fig. 5.18 shows a comparison between the reproduction error obtained using the conformal geometry and that obtained using a non-conformal geometry for "equivalent" setups, i. e. , a radial height $h = 5\,\text{cm}$ and a height $h' = 55\,\text{cm}$, respectively.

Cette thèse est accessible à l'adresse : https://theses.insa-lyon.fr/publication/2022ISAL0077/these.pdf
© [A.D. Pouye], [2022], INSA Lyon, tous droits réservés

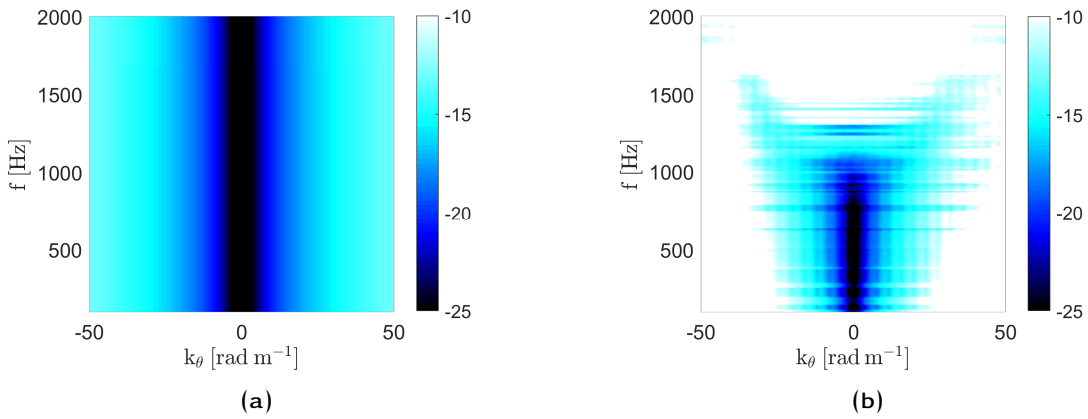

Figure 5.18: Comparison between the reproduction error induced by the (a) conformal geometry configuration and the (b) non-conformal configuration in the frequency-wavenumber domain.

In conclusion, a conformal geometry configuration between the structure and the array of monopoles is better suited for an accurate SST process for these types of shells and will be considered for the remainder of this chapter.

Cette thèse est accessible à l'adresse : https://theses.insa-lyon.fr/publication/2022ISAL0077/these.pdf
© [A.D. Pouye], [2022], INSA Lyon, tous droits réservés

5.2.2 Three-dimensional case

Let us consider Fig. 5.5 with the z-axis as shown on the figure. In the three-dimensional case and considering the cylindrical coordinates, the WPPWs are of the following form

$$p(\mathbf{x}, \mathbf{k}) = \mathrm{e}^{-\mathrm{i}(k_\theta R\theta + k_z z)} \tag{5.35}$$

where k_θ is the circumferential wavenumber, k_z is the longitudinal wavenumber and R is the curvature radius of the structure.
The structure of interest is a rigid half-cylinder with the following dimensions

Table 5.2: Dimensions of the rigid half-cylinder.

Parameter	Symbol	Value
Radius	R	0.5 m
Length	L	1 m

5.2.2.1 *Influence of the density of the array of monopoles*

In this section, we want to study the number of sources n_s needed per minimum wavelength in order to achieve an accurate reproduction process. Let us consider Eq. (5.32) where n_s represents the number of monopoles per minimum wavelength. The goal is to study which values of n_s allow an accurate reproduction of the target pressure field as was done in Sec. 5.2.1.1 for the two-dimensional case.
As in previous parametric studies, the accuracy of the reproduction process will be assessed using the reproduction error defined in Eq. (3.6). The accuracy of the reproduction process is established by comparing the reproduction error to an arbitrarily set threshold of −10 dB corresponding to a relative error of 10% between the target and reconstructed pressure fields. Note that this reproduction error is actually a spatial average over the whole structure of the MSE between the target and reconstructed pressure fields at each point on the structure.

Cette thèse est accessible à l'adresse : https://theses.insa-lyon.fr/publication/2022ISAL0077/these.pdf
© [A.D. Pouye], [2022], INSA Lyon, tous droits réservés

Once the reproduction error is determined, one can verify the accuracy of the reproduction process by comparing the target wall-pressure field to the synthesized one. The condition number of the transfer matrix **G** allows one to choose which setup is more adequate for an experimental implementation of SST. We start by looking at the reproduction error when n_s is given values in the set $\{1, 2, 3, 4\}$.

Reproduction error

Fig. 5.19, Fig. 5.20 and Fig. 5.21 show the reproduction error in the wavenumber domain for each value of n_s, for the following frequencies: $f = 500\,\text{Hz}$, $f = 1000\,\text{Hz}$ and $f = 2000\,\text{Hz}$, respectively. One should remember that for an accurate reproduction process, the reproduction error must be less than $-10\,\text{dB}$.

Fig. 5.19a, Fig. 5.20a and Fig. 5.21a represent the reproduction error for $n_s = 1$ for the three frequencies of interest: 500 Hz, 1000 Hz and 2000 Hz, respectively.

Observing Fig. 5.19a, one can notice that the synthesis process is accurate when the wavevector of the WPPWs is in a circle of radius $12\,\text{rad}\,\text{m}^{-1}$. For all other wavevectors and considering the set threshold of $-10\,\text{dB}$, the synthesis process is not accurate.

In Fig. 5.20a and Fig. 5.21a, which correspond to the reproduction error for $n_s = 1$ and for $f = 1000\,\text{Hz}$ and $f = 2000\,\text{Hz}$, respectively, one can clearly see that the reproduction is not accurate at all as the MATLAB colorbar upper and lower limits are intentionally left floating and not set to $-10\,\text{dB}$ and $-25\,\text{dB}$, respectively, as for the other figures representing reproduction errors in the wavenumber domain.

Increasing the density of the monopole array from $n_s = 1$ to $n_s = 2$ improves the process as the reproduction error decreases and there is less *white* area on the reproduction error maps in the wavenumber domain as it can be noticed in Fig. 5.19b, Fig. 5.20b and Fig.5.21b for all three frequencies.

Starting from $n_s = 3$, one can already notice in Fig. 5.19c, Fig. 5.20c and Fig.5.21c a good reproduction process over almost all the wavevectors in the wavenumber domain of interest $[-50, 50] \times [-50, 50]\,\text{rad}^2\,\text{m}^{-2}$.

Cette thèse est accessible à l'adresse : https://theses.insa-lyon.fr/publication/2022ISAL0077/these.pdf
© [A.D. Pouye], [2022], INSA Lyon, tous droits réservés

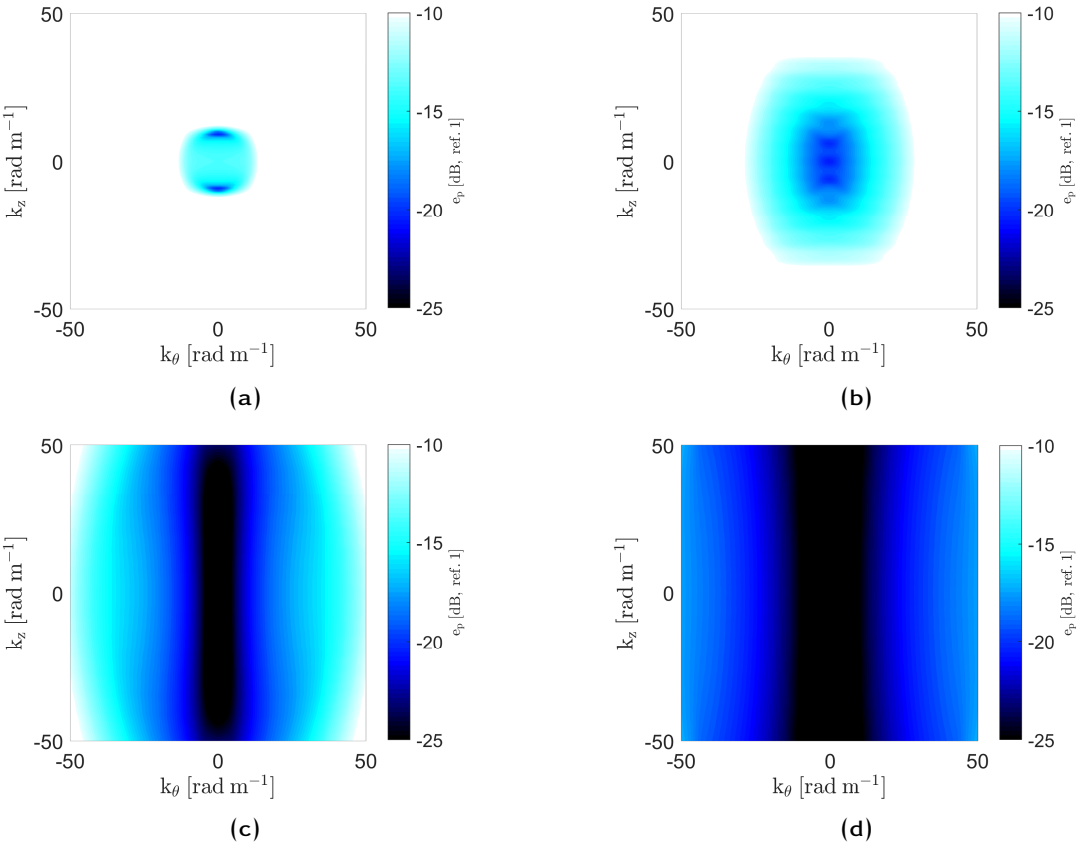

Figure 5.19: Parametric studies: influence of the density of the array of monopoles on the reproduction error e_p at a frequency $f = 500$ Hz. (a) $n_s = 1$, (b) $n_s = 2$, (c) $n_s = 3$ and (a) $n_s = 4$.

Finally, Fig. 5.19d, Fig. 5.20d and Fig.5.21d representing maps of the reproduction error in the wavenumber domain for an array density corresponding to $n_s = 4$ show an accurate synthesis process for all the wavevectors of interest.

In conclusion, these parametric studies confirm that we need at least four monopoles per minimum wavelength in order to have an accurate SST process as was the case for the two-dimensional case and Flat Rectangular Panels (FRPs).

Cette thèse est accessible à l'adresse : https://theses.insa-lyon.fr/publication/2022ISAL0077/these.pdf
© [A.D. Pouye], [2022], INSA Lyon, tous droits réservés

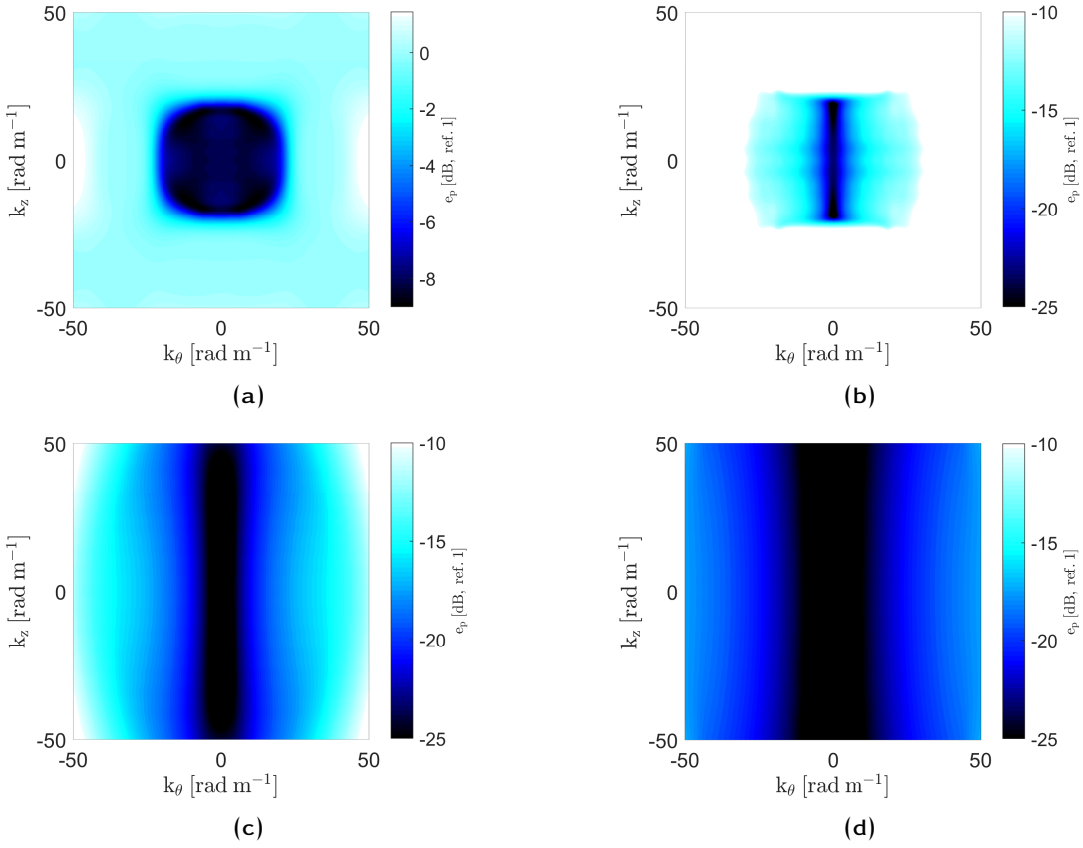

Figure 5.20: Parametric studies: influence of the density of the array of monopoles on the reproduction error e_p at a frequency $f = 1000\,\text{Hz}$. (a) $n_s = 1$, (b) $n_s = 2$, (c) $n_s = 3$ and (a) $n_s = 4$.

Cette thèse est accessible à l'adresse : https://theses.insa-lyon.fr/publication/2022ISAL0077/these.pdf
© [A.D. Pouye], [2022], INSA Lyon, tous droits réservés

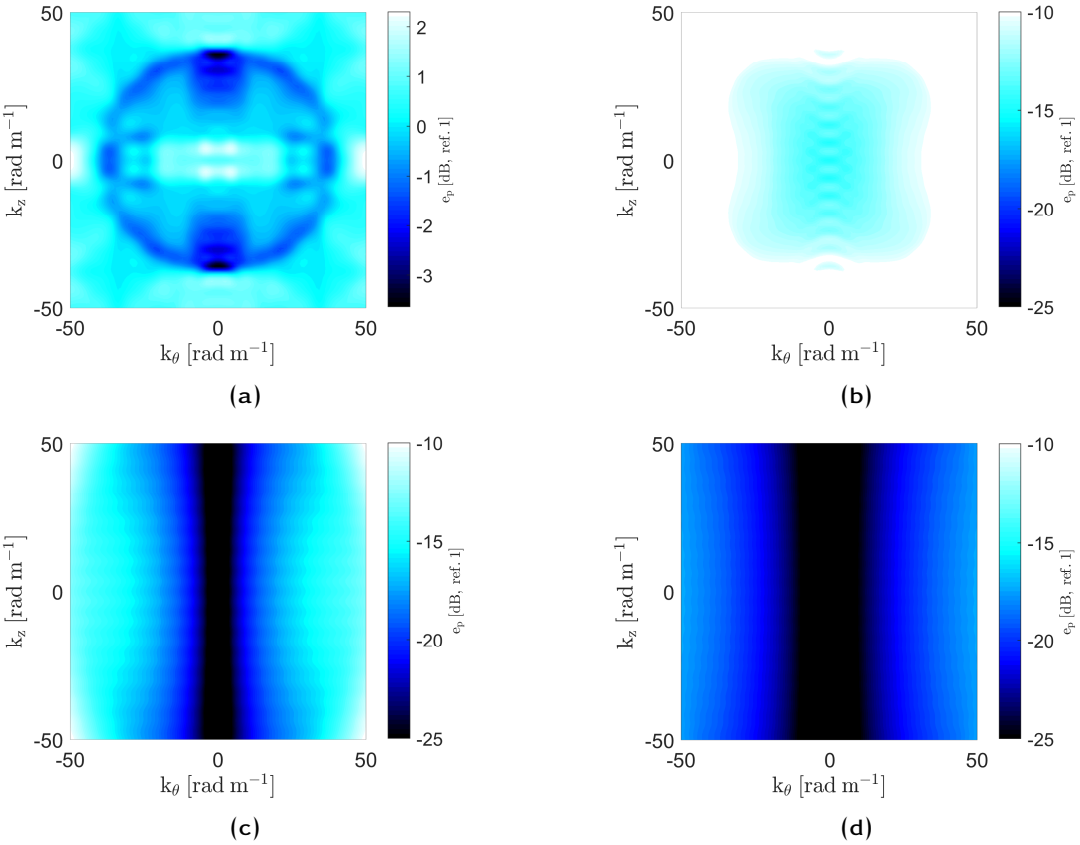

Figure 5.21: Parametric studies: influence of the density of the array of monopoles on the reproduction error e_p at a frequency $f = 2000$ Hz. (a) $n_s = 1$, (b) $n_s = 2$, (c) $n_s = 3$ and (a) $n_s = 4$.

Cette thèse est accessible à l'adresse : https://theses.insa-lyon.fr/publication/2022ISAL0077/these.pdf
© [A.D. Pouye], [2022], INSA Lyon, tous droits réservés

Reconstructed pressure fields

Now let us take a look at the reconstructed pressure fields when n_s is consequently given values from the set $\{1, 2, 3, 4\}$.

Let us consider the WPPW depicted on the surface of the structure in Fig. 5.22.

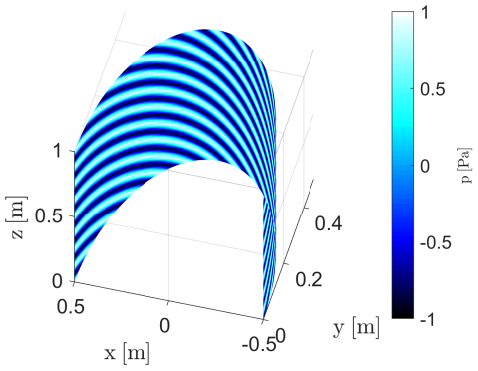

Figure 5.22: Target WPPW defined by the wavevector $(50, 50)$ rad m^{-1} mapped on the surface of the half-cylindrical structure.

Fig. 5.23, Fig. 5.24 and Fig. 5.25 represent plots on the surface of the half-cylinder of the reconstructed wall-pressure field of the WPPW defined by the wavevector $(k_\theta, k_z) = (50, 50)$ rad m^{-1} for $f = 500$ Hz, $f = 1000$ Hz and $f = 2000$ Hz, respectively. in order to assess the quality of the synthesis process, let us compare these figures to Fig. 5.22.

As expected after the analysis of the reproduction errors for $n_s = 1$ and $n_s = 2$ in Fig. 5.23a and Fig. 5.23b for $f = 500$ Hz, the synthesized wall-pressure fields do not match the target wall-pressure field in Fig. 5.22 as there is not enough monopole positions per minimum wavelength for an accurate SST process. The same conclusions can be drawn for the other two frequencies $f = 1000$ Hz and $f = 2000$ Hz in Fig. 5.24a and Fig. 5.24b and in Fig. 5.25a and Fig. 5.25b, respectively.

One can notice in Fig. 5.23c, Fig. 5.24c and Fig. 5.25c, that the synthesized wall-pressure field matches the target one in Fig. 5.22 for all three frequencies. There is no noticeable difference between the results obtained for $n_s = 3$ and those obtained for $n_s = 4$. Indeed,

Cette thèse est accessible à l'adresse : https://theses.insa-lyon.fr/publication/2022ISAL0077/these.pdf
© [A.D. Pouye], [2022], INSA Lyon, tous droits réservés

one can see in Fig. 5.23d, Fig. 5.24d and Fig. 5.25d that the SST process is very accurate for the WPPW with the maximum wavevector $(50, 50)$ rad m^{-1}.

These comparisons allow us to state that one needs at least four monopoles per minimum wavelength for an accurate reconstruction process.

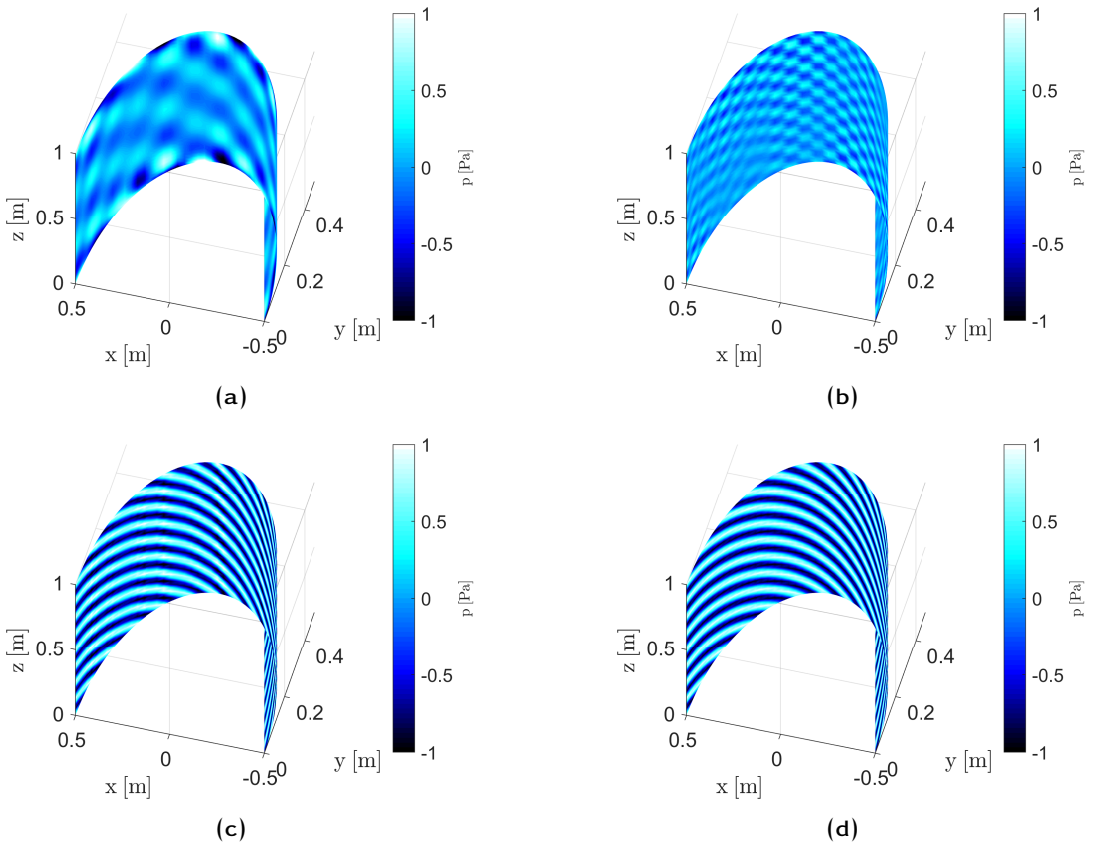

Figure 5.23: Parametric studies: influence of the density of the array of monopoles on the reconstructed pressure fields at a frequency $f = 500$ Hz. (a) $n_s = 1$, (b) $n_s = 2$, (c) $n_s = 3$ and (a) $n_s = 4$.

Cette thèse est accessible à l'adresse : https://theses.insa-lyon.fr/publication/2022ISAL0077/these.pdf
© [A.D. Pouye], [2022], INSA Lyon, tous droits réservés

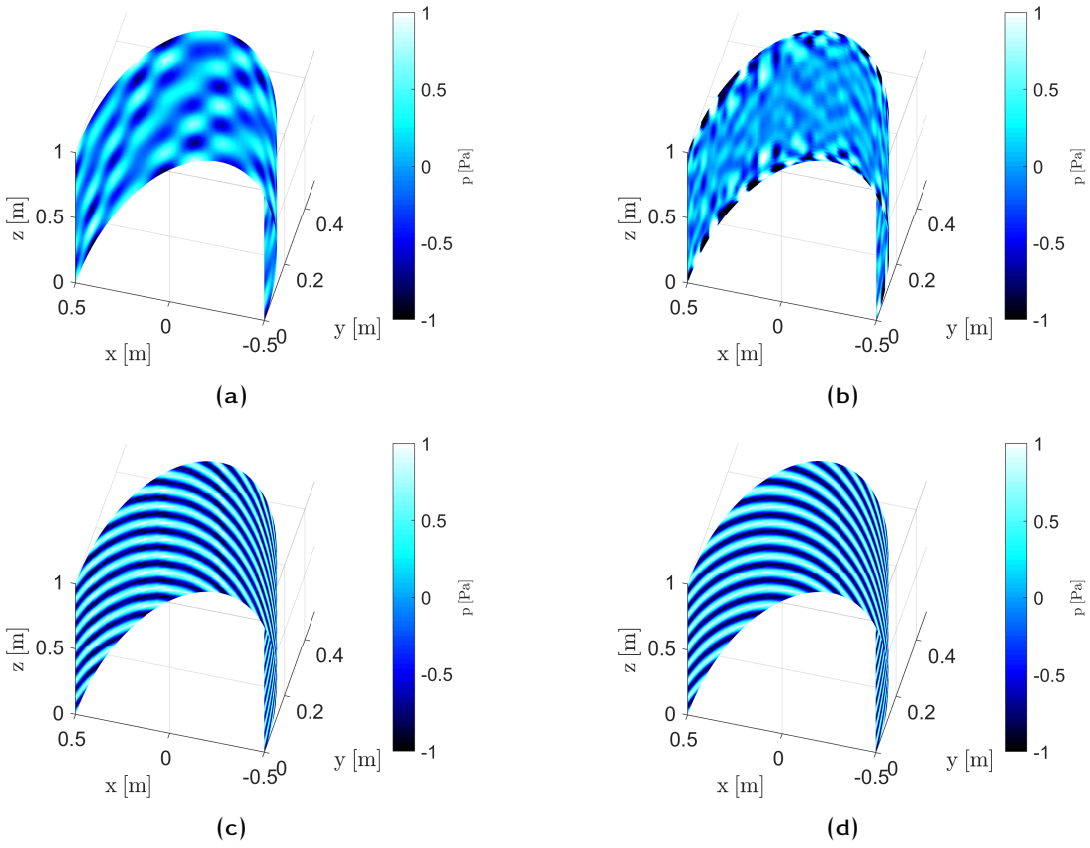

Figure 5.24: Parametric studies: influence of the density of the array of monopoles on the reconstructed pressure fields at a frequency $f = 1000\,\text{Hz}$. (a) $n_s = 1$, (b) $n_s = 2$, (c) $n_s = 3$ and (a) $n_s = 4$.

Cette thèse est accessible à l'adresse : https://theses.insa-lyon.fr/publication/2022ISAL0077/these.pdf
© [A.D. Pouye], [2022], INSA Lyon, tous droits réservés

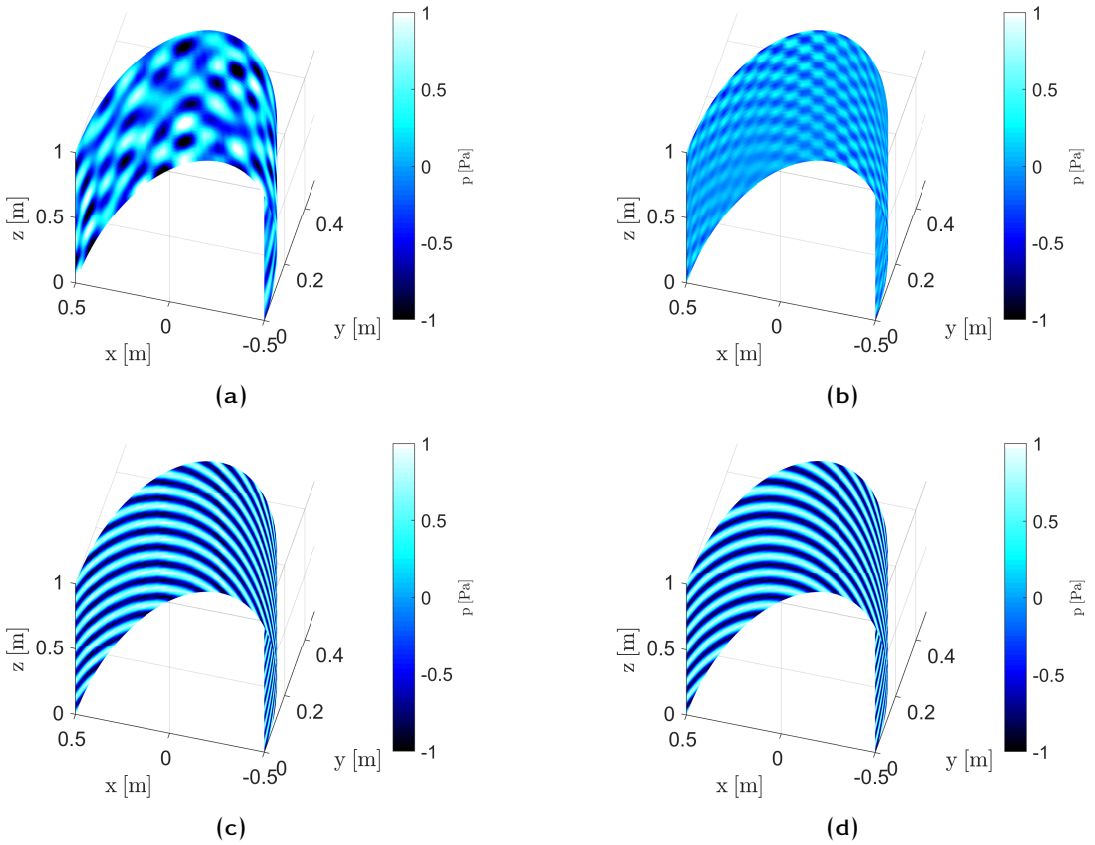

Figure 5.25: Parametric studies: influence of the density of the array of monopoles on the reconstructed pressure fields at a frequency $f = 2000$ Hz. (a) $n_s = 1$, (b) $n_s = 2$, (c) $n_s = 3$ and (a) $n_s = 4$.

Cette thèse est accessible à l'adresse : https://theses.insa-lyon.fr/publication/2022ISAL0077/these.pdf
© [A.D. Pouye], [2022], INSA Lyon, tous droits réservés

5.2.2.2 *Studying the effect of the radial height*

Let us now study the influence of the radial height h depicted in Fig. 5.5 by considering the following two radial heights: $h = 5\,\text{cm}$ and $h = 10\,\text{cm}$.
In these parametric studies, we will compare the reproduction errors induced by both radial heights as well as the reconstructed wall-pressure fields on the surface of the structure. The target wall-pressure field is the one depicted in Fig. 5.22 and corresponds to the WPPW defined by the wavevector $(50, 50)\,\text{rad}\,\text{m}^{-1}$. We will also discuss the condition numbers of the transfer matrices obtained using Eq. (5.16) in order to assess which radial height is more suitable for an experimental implementation of the SST process.

Reproduction error

Fig. 5.26, Fig. 5.27 and Fig. 5.28 show maps of the reproduction error defined in Eq. (3.6) for both radial heights and for $f = 500\,\text{Hz}$, $f = 1000\,\text{Hz}$ and $f = 2000\,\text{Hz}$, respectively. Observing these figures, one can clearly notice that the reproduction error is always below the threshold of $-10\,\text{dB}$ which is required in order to state that the synthesis technique is accurate for both radial heights and at all three studied frequencies.

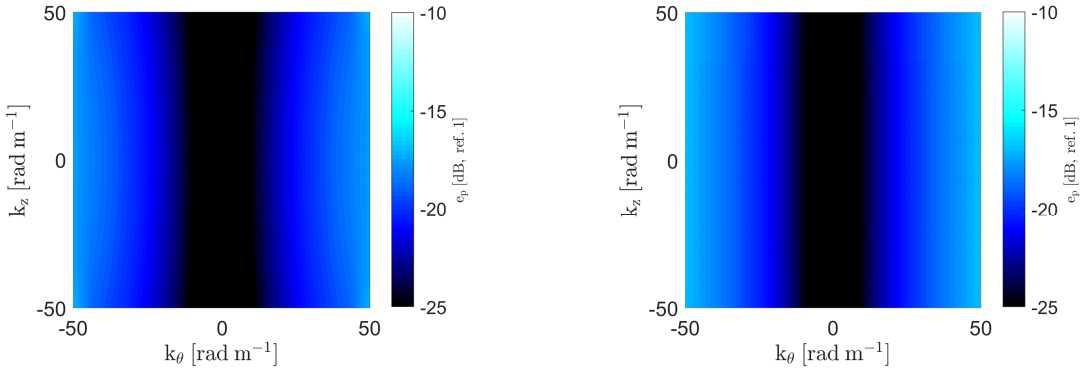

Figure 5.26: Influence of the radial height on the reproduction error at a frequency $f = 500\,\text{Hz}$ for two different radial heights: (a) $h = 5\,\text{cm}$ and (b) $h = 10\,\text{cm}$.

Cette thèse est accessible à l'adresse : https://theses.insa-lyon.fr/publication/2022ISAL0077/these.pdf
© [A.D. Pouye], [2022], INSA Lyon, tous droits réservés

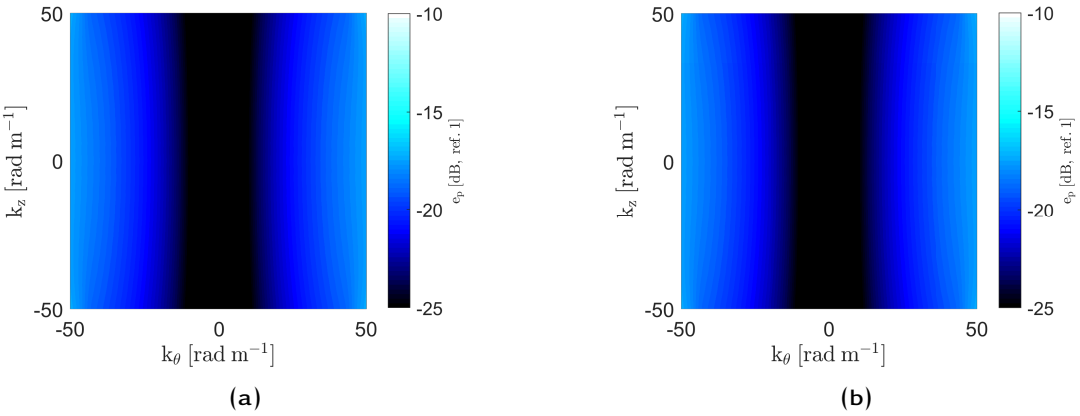

Figure 5.27: Influence of the radial height on the reproduction error at a frequency $f = 1000$ Hz for two different radial heights: (a) $h = 5$ cm and (b) $h = 10$ cm.

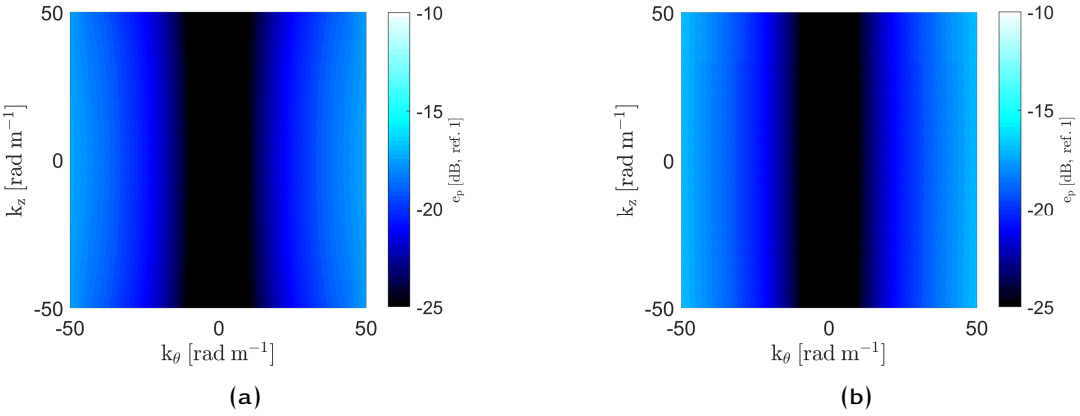

Figure 5.28: Influence of the radial height on the reproduction error at a frequency $f = 2000$ Hz for two different radial heights: (a) $h = 5$ cm and (b) $h = 10$ cm.

Reconstructed pressure fields

Fig. 5.29, Fig. 5.30 and Fig. 5.31 correspond to the synthesized wall-pressure fields for $f = 500$ Hz, $f = 1000$ Hz and $f = 2000$ Hz, respectively. The target wall-pressure field is the one presented in Fig. 5.22. Comparing these figures among them and with the target wall-pressure field, one can see that there is virtually no difference between these

Cette thèse est accessible à l'adresse : https://theses.insa-lyon.fr/publication/2022ISAL0077/these.pdf
© [A.D. Pouye], [2022], INSA Lyon, tous droits réservés

results, as one would expect after the analysis on the reproduction error that we carried out earlier.

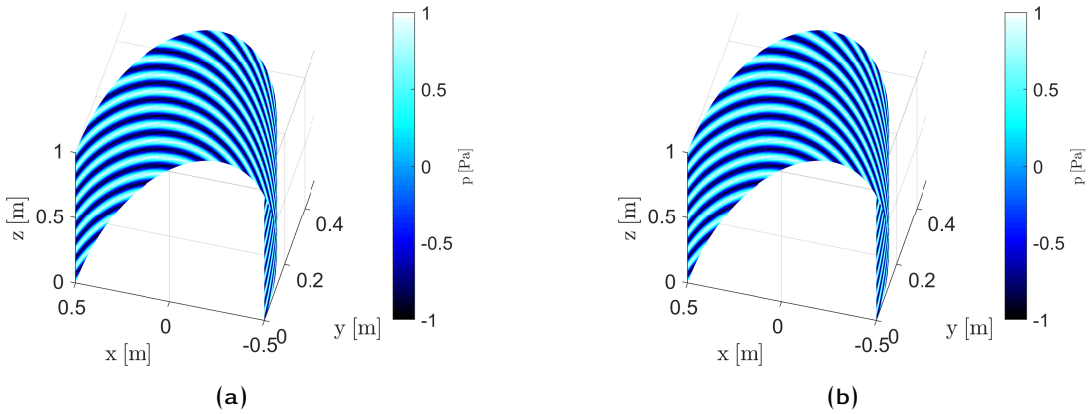

Figure 5.29: Reconstructed pressure fields using SST at a frequency $f = 500\,\text{Hz}$ for two different radial heights: (a) $h = 5\,\text{cm}$ and (b) $h = 10\,\text{cm}$.

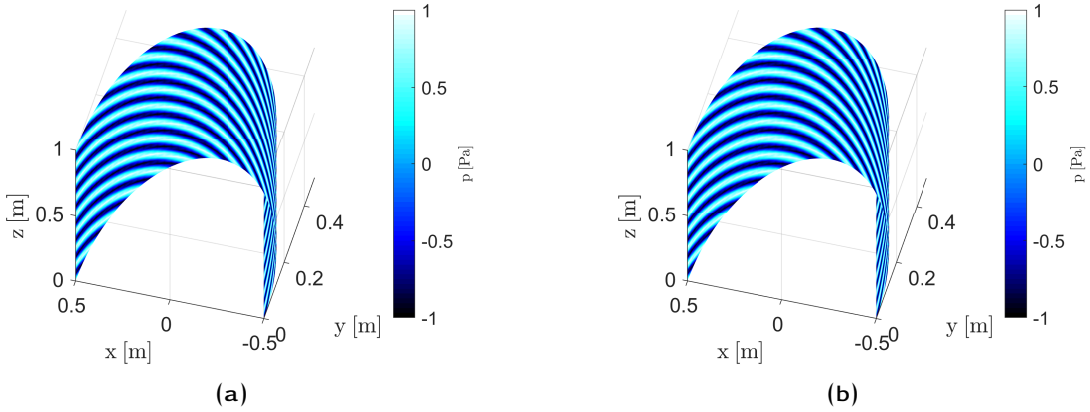

Figure 5.30: Reconstructed pressure fields using SST at a frequency $f = 1000\,\text{Hz}$ for two different radial heights: (a) $h = 5\,\text{cm}$ and (b) $h = 10\,\text{cm}$.

Condition number of the transfer matrix

The condition numbers of the transfer matrix $\mathbf{G}$ are given in table 5.3. One can notice that the condition number decreases when the frequency increases. This tendency has already been observed in the two-dimensional case. However its evolution is slow with

Cette thèse est accessible à l'adresse : https://theses.insa-lyon.fr/publication/2022ISAL0077/these.pdf
© [A.D. Pouye], [2022], INSA Lyon, tous droits réservés

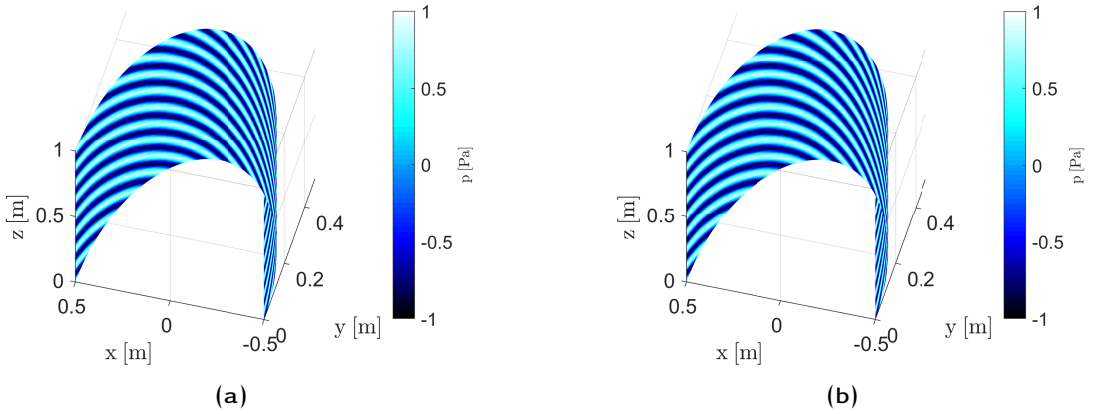

Figure 5.31: Reconstructed pressure fields using SST at a frequency $f = 2000$ Hz for two different radial heights: (a) $h = 5$ cm and (b) $h = 10$ cm.

respect to frequency. Finally, one can notice that there is not much difference between the two studied radial heights of 5 cm and 10 cm.

Table 5.3: Values of the condition number ($\log \kappa$) of the transfer matrix $\mathbf{G}$ for each frequency and radial height setup.

Frequency (Hz)	$h = 5$ cm	$h = 10$ cm
500	16.9	17
1500	~ 16.6	16.7
2000	~ 16.4	16.5

Nevertheless, the condition number for $h = 5$ cm is slightly better than that obtained for $h = 10$ cm for each of the three frequencies of interest which is in accordance with the results we have obtained up to this point when the height of the monopole array is increased. That being said, one must remember that the distance between the monopole array and the structure must be at least equal to the separation between two adjacent monopoles in the array.

Cette thèse est accessible à l'adresse : https://theses.insa-lyon.fr/publication/2022ISAL0077/these.pdf
© [A.D. Pouye], [2022], INSA Lyon, tous droits réservés

5.3 SUMMARY

In this chapter, the feasibility of the extension of the Source Scanning Technique (SST) to Curved Rectangular Panels (CRPs) was studied. Analytical solutions to the Helmholtz problem defined by Eq. (5.1) have been established for the two-dimensional as well as the three dimensional case. These solutions were consequently validated using the Boundary Element Method (BEM) implemented in OpenBEM. Once the validation is done, parametric studies have been carried out in order to determine the optimal parameters for an implementation of the SST in the two-dimensional and three-dimensional cases. The parametric studies allowed us to establish the minimum number of monopole sources per smallest wavelength at **four monopoles** which is the same number that was established four Flat Rectangular Panels (FRPs). Two different structure-array geometry configurations were studied. It was found that the conformal geometry, where the array of monopoles has the same geometry as the structure, is more suitable for the SST process than the non-conformal geometry configuration. Finally, it was found that the closer the monopole array is to the structure, the more accurate the reproduction process.

Cette thèse est accessible à l'adresse : https://theses.insa-lyon.fr/publication/2022ISAL0077/these.pdf
© [A.D. Pouye], [2022], INSA Lyon, tous droits réservés

6 SST ON CURVED RECTANGULAR PANELS: EXPERIMENTS

6.1 Experimental implementation 126
6.1.1 Measurement devices 126
6.1.2 Experimental setup 128
6.2 Results and discussion 134
6.2.1 Two dimensional case: validation of the transfer functions and experimental SST 134
6.2.2 Three dimensional case: validation of the transfer functions 139
6.3 Summary 141

In the previous chapter, we introduced transfer functions between source positions and observation points located on a half-cylindrical-like structure. We also applied the SST process on CRPs in order to determine the optimal parameters using the established 2D and 3D transfer functions. However the ultimate goal is to implement experimental SST on CRPs: the current chapter is thus dedicated to this effect. In a first step, we will present the devices used during the experiment as well as the experimental setup. Then, for the two-dimensional, we will discuss the results concerning the experimental validation of the transfer functions as well as experimental SST results compared with analytical ones. As for the three-dimensional case, only an experimental validation of the 3D transfer functions is carried out.

Cette thèse est accessible à l'adresse : https://theses.insa-lyon.fr/publication/2022ISAL0077/these.pdf
© [A.D. Pouye], [2022], INSA Lyon, tous droits réservés

6.1 EXPERIMENTAL IMPLEMENTATION

6.1.1 Measurement devices

6.1.1.1 Monopole source

The excitation device used during the SST process is a monopole source similar to the one used for FRPs manufactured by Siemens and shown in Fig. 6.1. This monopole source is composed of a simple flexible hose at the end of which there is a 15 mm diameter nozzle with a reference sensor at the output and the whole is driven with a high impedance loudspeaker.



Figure 6.1: Siemens mid-high frequency volume source used during the SST process for CRPs.

6.1.1.2 Microphones

In order to measure the transfer functions G_{ps} between the S source positions and the P observation points, 1/4″ microphones manufactured by the Center for Transfer of Technologies of Le Mans or *Centre de Transfert de Techonologie* in French (CTTM) were used.

Cette thèse est accessible à l'adresse : https://theses.insa-lyon.fr/publication/2022ISAL0077/these.pdf
© [A.D. Pouye], [2022], INSA Lyon, tous droits réservés

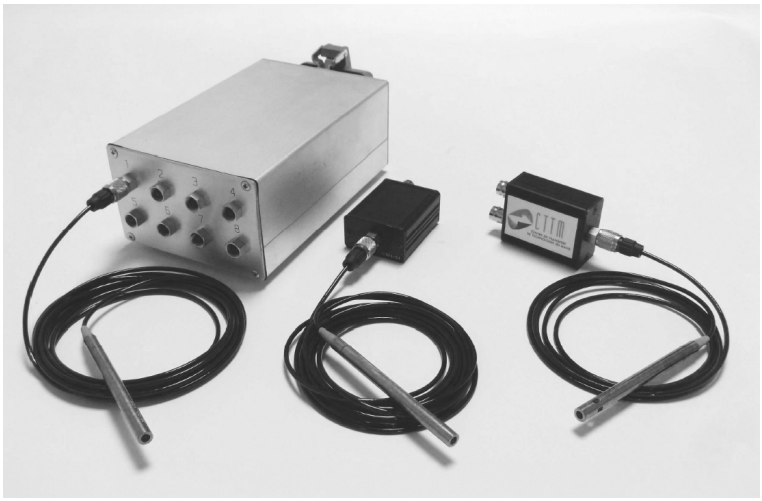

Figure 6.2: CTTM 1/4″ microphones.

These microphones were connected to 8 channel external conditioners such as the one shown in Fig. 6.3. The microphones were arranged in sets of 8 microphones per external conditioner.

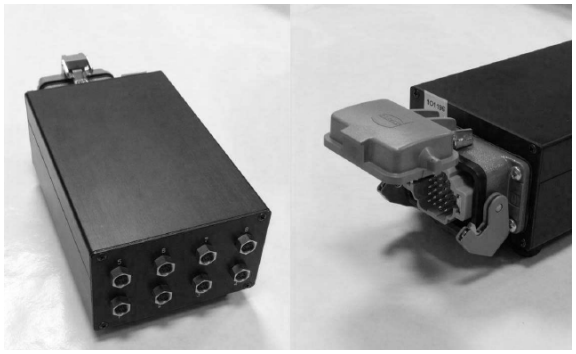

Figure 6.3: Eight channel conditioner with a Harting connector output.

6.1.1.3 Automation of the process

It is important to remember that one key feature of the SST process is that it uses only one monopole source which is spatially displaced to the desired locations. Naturally, the process is automatized as was done for FRPs. A 5 degrees-of-freedom robot arm

Cette thèse est accessible à l'adresse : https://theses.insa-lyon.fr/publication/2022ISAL0077/these.pdf
© [A.D. Pouye], [2022], INSA Lyon, tous droits réservés

manufactured by Igus and shown in different angles in Fig. 6.4 is used to displace the monopole source to different positions.

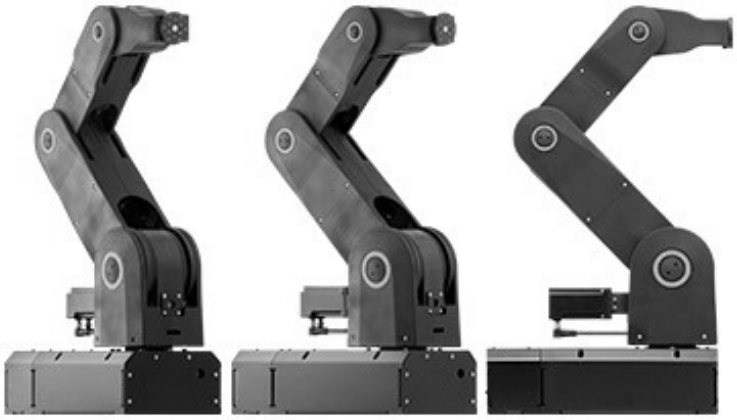

Figure 6.4: five degrees-of-freedom robot arm.

6.1.2 Experimental setup

In the following, the experimental setup is described and pictures of how each device is mounted will be shown.

Let us consider Fig. 6.5 where *chamber 1* designates the semi-anechoic room where the structure, the truss on which the monopole source is mounted and the monopole source itself are present. The robot arm is mounted upside down on a truss structure for the needs of the experiment. This robot arm can slide along a motorized rail of length 2 m which is parallel to the z axis on Fig. 6.5.

The 2 m motorized rail is aligned with the centerline of the structure (half open cylinder) in order to have an accurate positioning of the robot arm with respect to the structure. The monopole source is mounted on the robot using a 6 m flexible hose attached to an aluminum hollow tube which is fixed to the free end of the robot arm as shown in Fig. 6.6.

Cette thèse est accessible à l'adresse : https://theses.insa-lyon.fr/publication/2022ISAL0077/these.pdf
© [A.D. Pouye], [2022], INSA Lyon, tous droits réservés

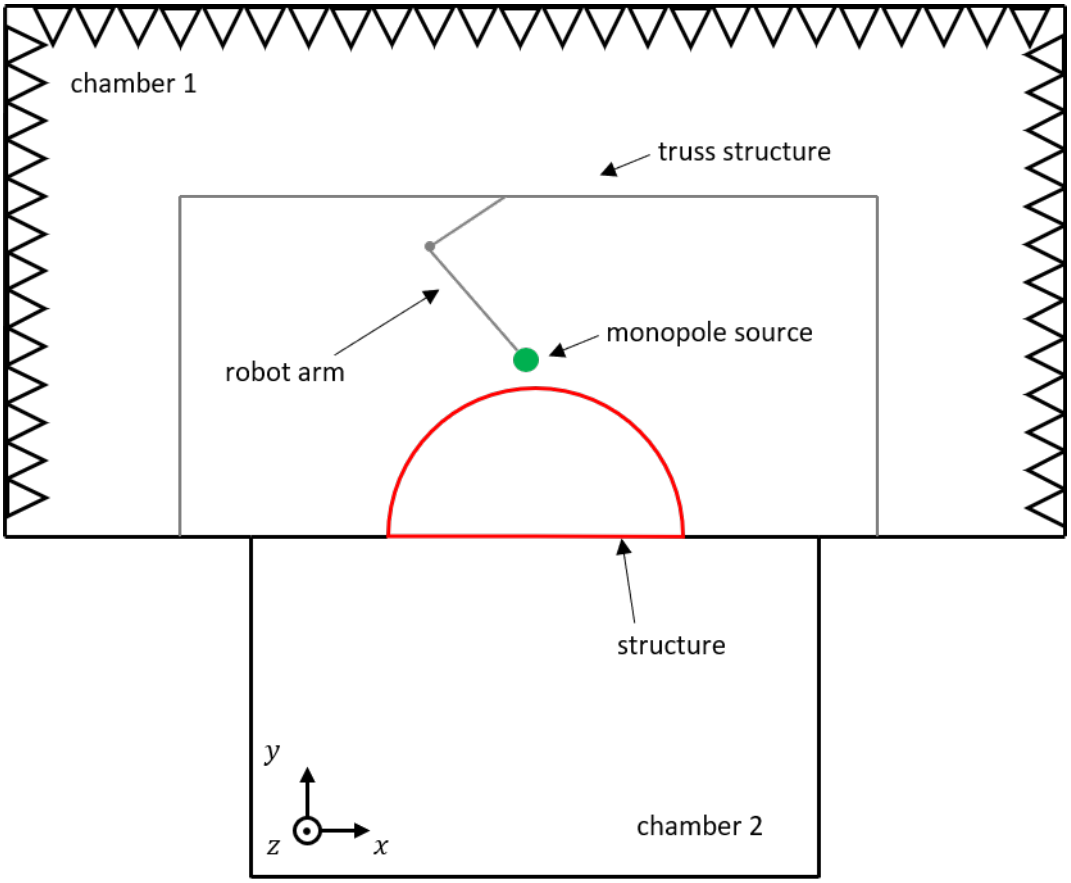

Figure 6.5: Sketch of the experimental setup for the SST process on CRPs.

In order to avoid using a plethora of microphones for the measurement of the transfer functions, the idea is to apply the same principle of invariance as it was done for FRPs, see Appendix C. Certainly, the structure of interest is more complex than the flat panel but this invariance of the measurements should remain valid in this new case study in view of the symmetry of the system. This principle consists in using only one semi-circular microphone array to perform transfer function measurements over the entire surface of the half cylinder. Instead of having to move the microphone array (which is impossible in our configuration) or having a multitude of microphones to manage over the entire surface of the half cylinder, one only needs to move the monopole source to the position facing the location of the "virtual" array of microphones where the transfer functions are to be measured.

Cette thèse est accessible à l'adresse : https://theses.insa-lyon.fr/publication/2022ISAL0077/these.pdf
© [A.D. Pouye], [2022], INSA Lyon, tous droits réservés

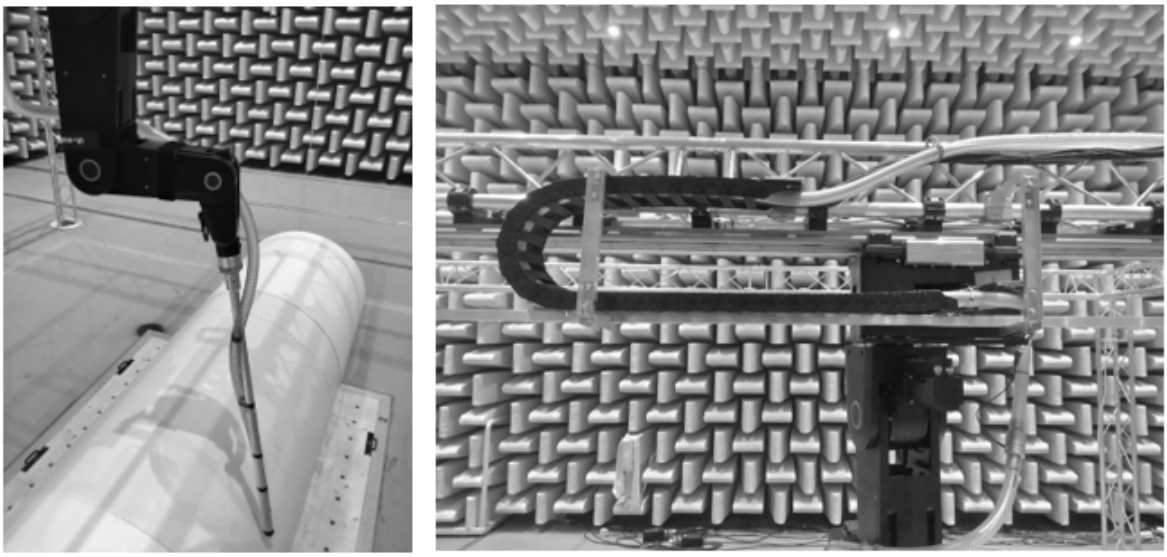

Figure 6.6: Monopole source mounted on the robot arm.

For instance, let us consider Fig. 6.7. In order to measure the transfer functions between the position s_1 of the source and the edge position of the microphones, one only needs to move the source to the position s_2 and measure the transfer functions between this position and the reference microphone position.

However, the ideal location of the semi-circular array of microphones would be the reference position shown in Fig. 6.8. In this configuration, there would be no problem if the measurements were to be made on only one half of the structure (from the reference position to one edge or the other). However, one needs to measure the transfer functions over the entire surface of the structure. Thus, one will have some issues during the measurement of transfer functions that are located at a distance greater than half the length of the structure. We would leave the measurement area as shown in Fig. 6.8 and considering the 2 m stroke on the robot rail, one would not be able to measure these transfer functions. Hence the choice of the location shown in Fig. 6.8.

The 63 microphones used during this experiment are flush-mounted on the rigid half open cylinder as shown in Fig. 6.9. They were assembled per sets of 8 microphones per external conditioner (see Fig. 6.3) except one which had 7 microphones.

Cette thèse est accessible à l'adresse : https://theses.insa-lyon.fr/publication/2022ISAL0077/these.pdf
© [A.D. Pouye], [2022], INSA Lyon, tous droits réservés

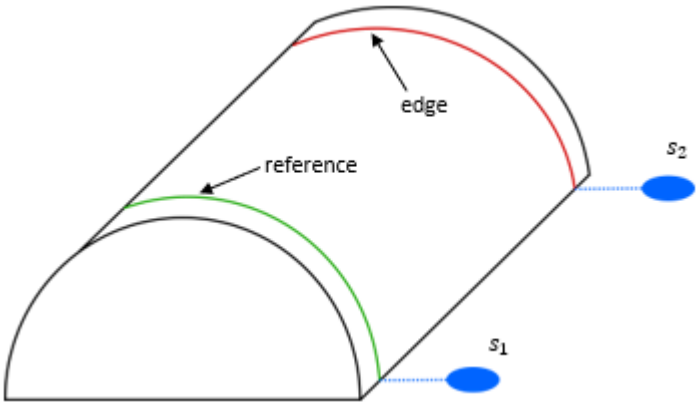

Figure 6.7: Chosen location of the semi-circular array of 63 microphones flush-mounted on the rigid half cylinder. The reference (green) position is where the microphones are actually located and the edge (red) corresponds to the farthest location from the reference where one needs to measure the transfer functions.

All the cables in *chamber 1* and *chamber 2* were plugged and retrieved in a control room where they were plugged in an OROS acquisition system. All the microphones were calibrated by taking into account the hypothetical attenuation due to the lengthy cables used to plug all the devices in the control room.

In Fig. 6.10, one can observe the complete experimental setup for the measurement during the SST process on CRPs.

Cette thèse est accessible à l'adresse : https://theses.insa-lyon.fr/publication/2022ISAL0077/these.pdf
© [A.D. Pouye], [2022], INSA Lyon, tous droits réservés

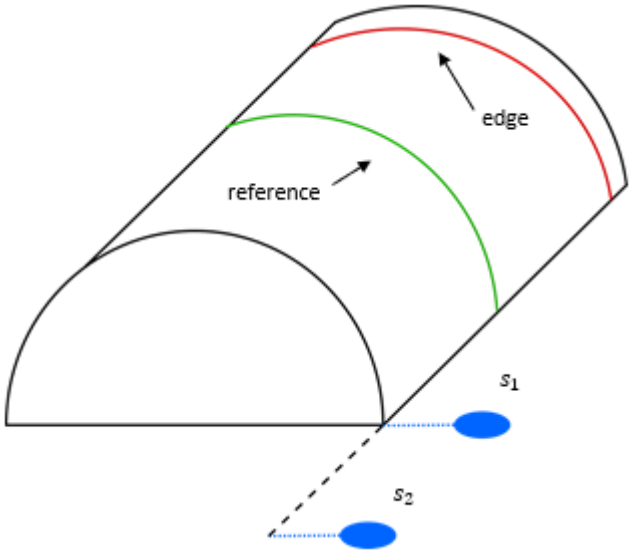

Figure 6.8: Optimal location of the semi-circular array of 63 microphones on the rigid half cylinder which reduces the diffraction effects on the measurements.



Figure 6.9: Flush-mounted microphones on the rigid open half cylinder. Left: view in *chamber 1* in Fig. 6.5. Right: view in *chamber 2* in Fig. 6.5.

Cette thèse est accessible à l'adresse : https://theses.insa-lyon.fr/publication/2022ISAL0077/these.pdf
© [A.D. Pouye], [2022], INSA Lyon, tous droits réservés

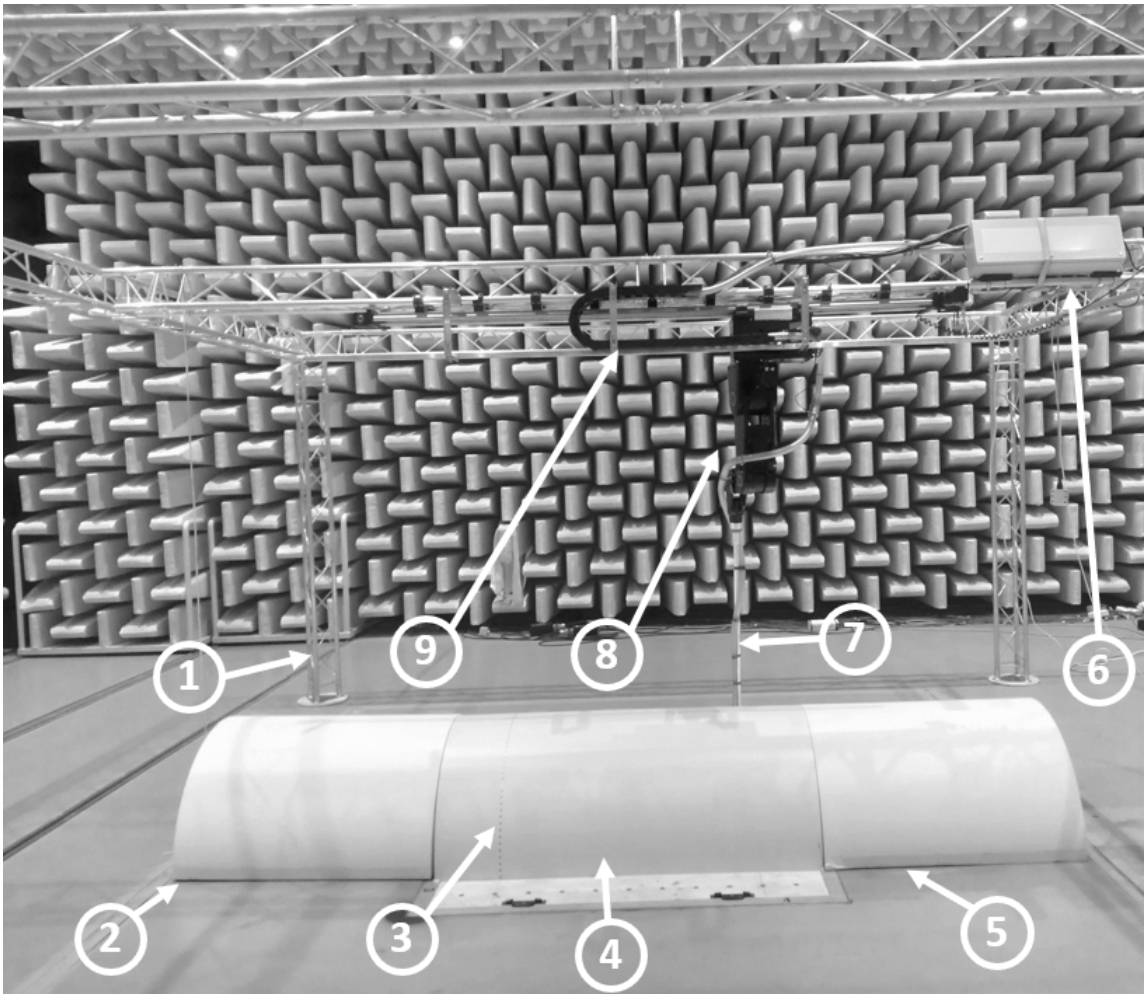

Figure 6.10: Experimental setup: simply supported rigid open half cylinder. The monopole source (7) is mounted on the robot arm (8) which can slide along the rail (9) and supported by the truss structure (1). The 63 microphones (3) are flush-mounted on the rigid open half cylinder (4) baffled by the half polystyrene cylinders (2) and (5). (6) corresponds to the robot arm control unit.

Cette thèse est accessible à l'adresse : https://theses.insa-lyon.fr/publication/2022ISAL0077/these.pdf
© [A.D. Pouye], [2022], INSA Lyon, tous droits réservés

6.2 RESULTS AND DISCUSSION

This section is dedicated to the experimental validation of the transfer functions studied in Chapter 5 as well as the experimental implementation of the SST process on Curved Rectangular Panels (CRPs). Naturally, we will study both the two-dimensional and the three-dimensional cases.

6.2.1 Two dimensional case: validation of the transfer functions and experimental SST

We will start with the experimental validation of the transfer functions defined in Eq. (5.16) and then we will apply the SST process.

6.2.1.1 Experimental validation of the transfer functions

Fig. 6.11, Fig. 6.12, Fig. 6.13 and Fig. 6.14 show comparisons of the analytical (see Sec. 5.1.1) and experimental transfer functions at two different frequencies for a given radial height and for one position (r_0, θ_0) of the monopole source through plots of the pressure at the surface of the structure (a semi-circular arc in the two-dimensional case) experimentally materialized by the arc of microphones (3) in Fig. 6.10 or in Fig. 6.9.
Observing Fig. 6.11 to Fig. 6.14, one can notice a good agreement between the analytical results and the experimental measurements done with an array of 63 microphones. One can notice that there are however some discrepancies of the pressure at structural points close to the monopole source position specially when the radial height is increased. In order to illustrate this statement, one can compare Fig. 6.11 and Fig. 6.14 where the pressure fields are plotted for the same monopole position but for two different radial heights: $h = 5\,\text{cm}$ and $h = 10\,\text{cm}$, respectively. One can see that the measurements are more accurate when the monopole source is close to the structure, this result was also discussed in Sec. 5.2.1.2 of Chapter 5.

Cette thèse est accessible à l'adresse : https://theses.insa-lyon.fr/publication/2022ISAL0077/these.pdf
© [A.D. Pouye], [2022], INSA Lyon, tous droits réservés

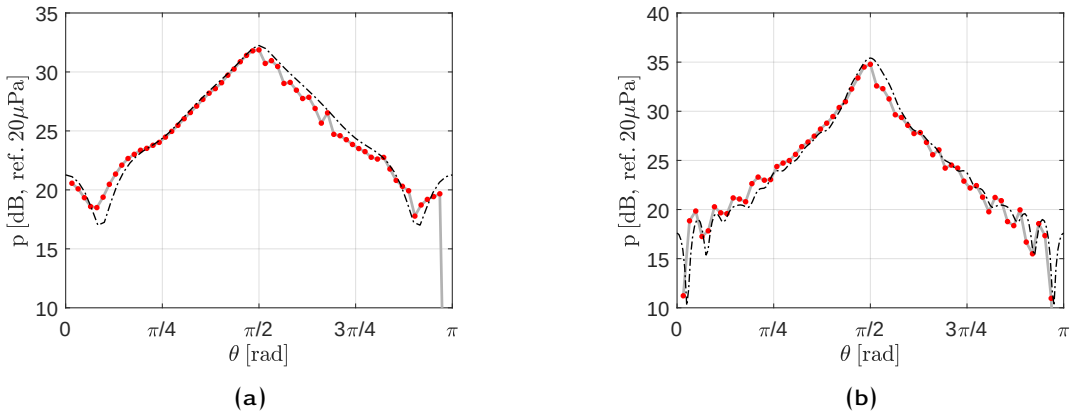

Figure 6.11: Pressure at the surface of the structure at two frequencies: (a) $f = 500\,\text{Hz}$ and (b) $f = 2000\,\text{Hz}$, for a radial height $h = 5\,\text{cm}$ and source angular position $\theta_0 = \frac{\pi}{2}$. Comparison between the analytical results (dash-dotted black line) and the experimental measurements (continuous gray line, the red dots correspond to the positions of the measurement points) for the two-dimensional case.

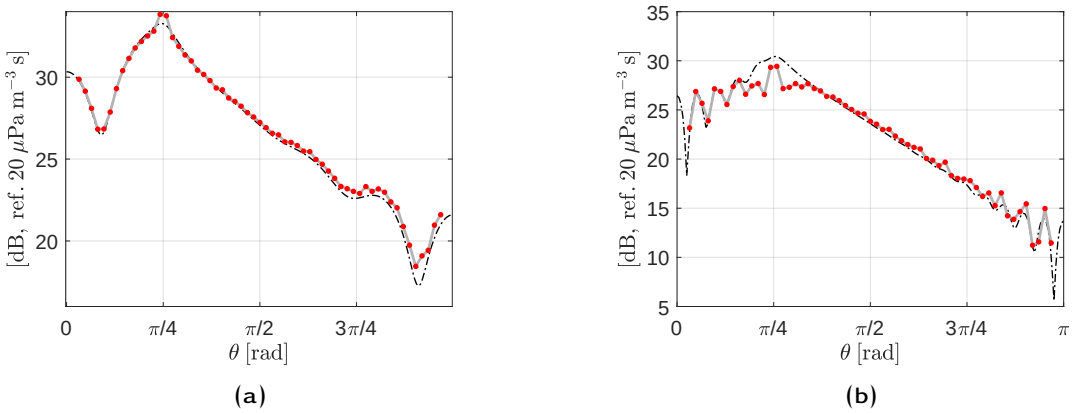

Figure 6.12: Pressure at the surface of the structure at two frequencies: (a) $f = 500\,\text{Hz}$ and (b) $f = 2000\,\text{Hz}$, for a radial height $h = 5\,\text{cm}$ and source angular position $\theta_0 = \frac{\pi}{4}$. Comparison between the analytical results (dash-dotted black line) and the experimental measurements (continuous gray line, the red dots correspond to the positions of the measurement points) for the two-dimensional case.

Given the results obtained in this case, one can completely validate the two-dimensional theoretical transfer functions defined by Eq. (5.16) which had also been compared to numerical results using OpenBEM.

Cette thèse est accessible à l'adresse : https://theses.insa-lyon.fr/publication/2022ISAL0077/these.pdf
© [A.D. Pouye], [2022], INSA Lyon, tous droits réservés

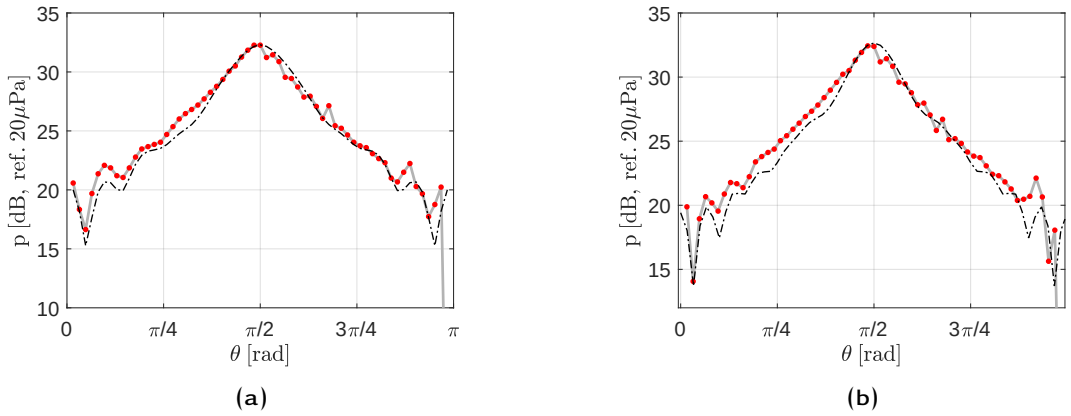

Figure 6.13: Pressure at the surface of the structure at two frequencies: (a) $f = 1000\,\text{Hz}$ and (b) $f = 1500\,\text{Hz}$, for a radial height $h = 10\,\text{cm}$ and source angular position $\theta_0 = \frac{\pi}{2}$. Comparison between the analytical results (dash-dotted black line) and the experimental measurements (continuous gray line, the red dots correspond to the positions of the measurement points) for the two-dimensional case.

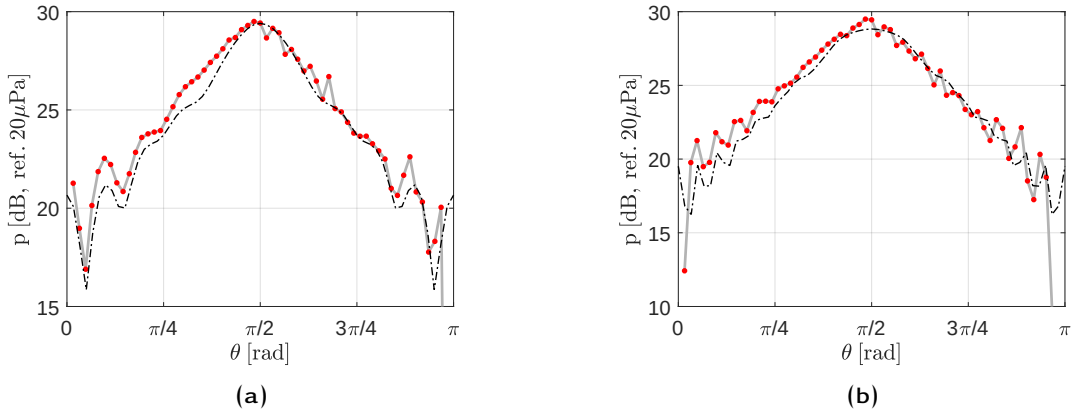

Figure 6.14: Pressure at the surface of the structure at two frequencies: (a) $f = 500\,\text{Hz}$ and (b) $f = 2000\,\text{Hz}$, for a radial height $h = 20\,\text{cm}$ and source angular position $\theta_0 = \frac{\pi}{2}$. Comparison between the analytical results (dash-dotted black line) and the experimental measurements (continuous gray line, the red dots correspond to the positions of the measurement points) for the two-dimensional case.

6.2.1.2 Experimental SST

The goal is to experimentally implement the SST process in the two-dimensional case using the same experimental setup introduced in Sec. 6.1.2.

Cette thèse est accessible à l'adresse : https://theses.insa-lyon.fr/publication/2022ISAL0077/these.pdf
© [A.D. Pouye], [2022], INSA Lyon, tous droits réservés

Let us consider a radial height of $h = 5\,\text{cm}$ and the WPPWs defined by wavenumbers $k_\theta \in [-50, 50]\,\text{rad}\,\text{m}^{-1}$.

Fig. 6.15 shows the condition number of the transfer matrix **G** measured between the 50 monopole positions and the 63 microphones of the arc array. One can notice a relatively acceptable condition number with regard to the measurement conditions.

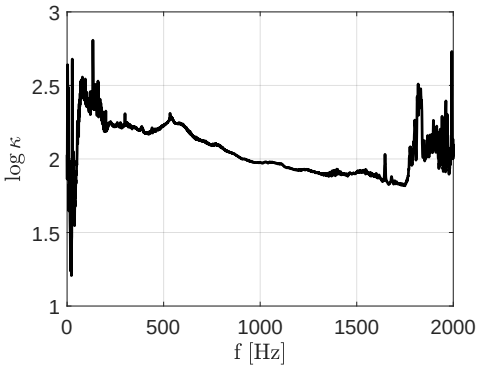

Figure 6.15: Condition number ($\log_{10}\kappa$) of the experimental transfer matrix **G** between the 50 monopole positions and the 63 microphone positions.

Fig. 6.16 shows plots of the real and imaginary part of the target pressure and the synthesized one obtained with the experimental SST process at a frequency $f = 2000\,\text{Hz}$ for a radial height $h = 5\,\text{cm}$ and for three different circumferential wavenumbers k_θ. Observing Fig. 6.16, one can verify a perfect reproduction process for the two-dimensional case.

Cette thèse est accessible à l'adresse : https://theses.insa-lyon.fr/publication/2022ISAL0077/these.pdf
© [A.D. Pouye], [2022], INSA Lyon, tous droits réservés

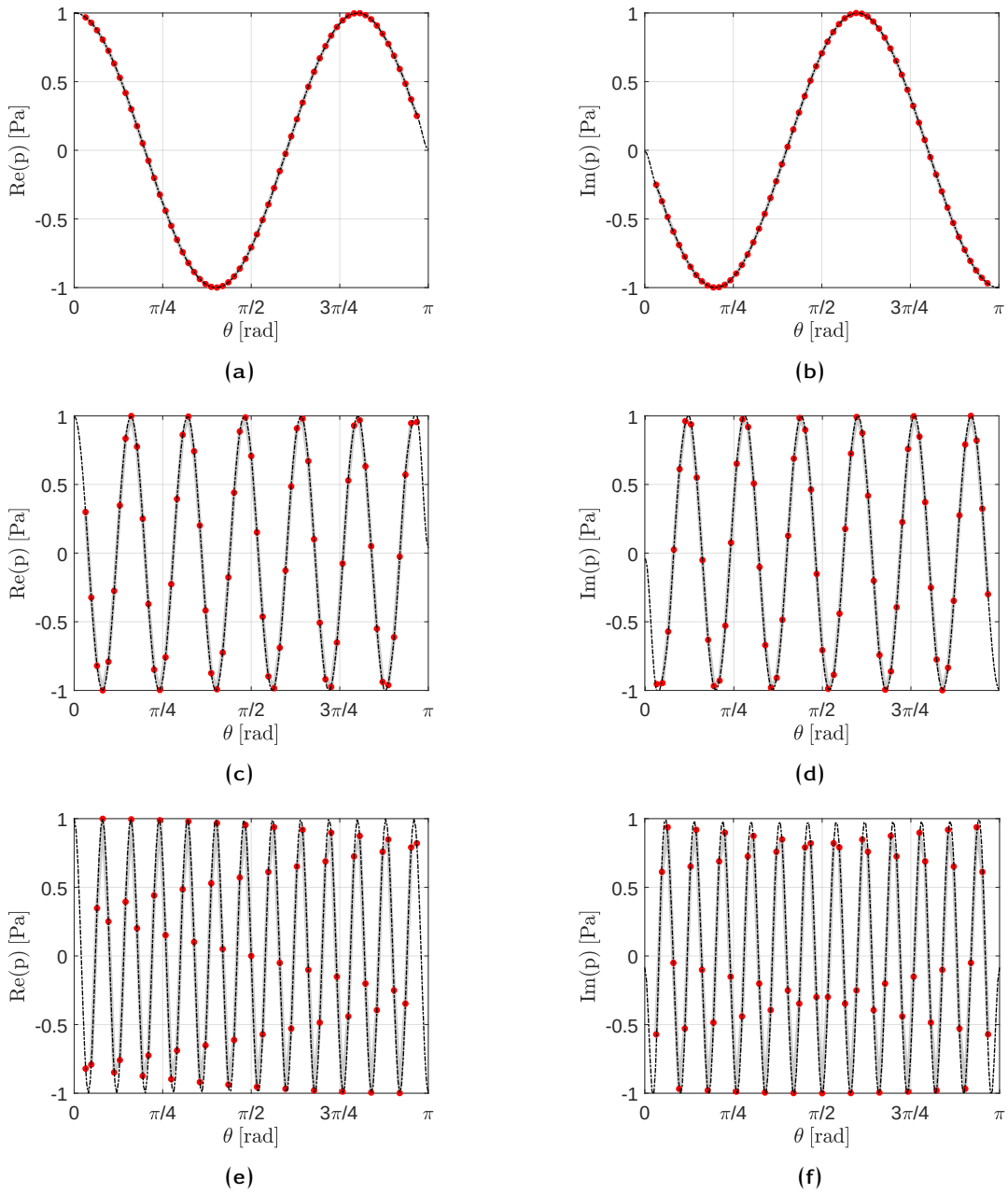

Figure 6.16: Comparison between the target pressure (dash-dotted black line) and the synthesized one (continuous gray line, the red dots correspond to the positions of the measurement points) using experimental SST at a frequency $f = 2000\,\text{Hz}$ for a radial height $h = 5\,\text{cm}$ and for three different WPPWs: (a) and (b): $k_\theta = 5\,\text{rad}\,\text{m}^{-1}$, (c) and (d): $k_\theta = 25\,\text{rad}\,\text{m}^{-1}$, (e) and (f): $k_\theta = 50\,\text{rad}\,\text{m}^{-1}$. Left column: real part of the pressure. Right column: imaginary part.

Cette thèse est accessible à l'adresse : https://theses.insa-lyon.fr/publication/2022ISAL0077/these.pdf
© [A.D. Pouye], [2022], INSA Lyon, tous droits réservés

6.2.2 Three dimensional case: validation of the transfer functions

As for the two-dimensional case, here we aim at validating the three-dimensional transfer functions defined in Eq. (5.30) using the experimental setup presented in Sec. 6.1.2. In this case, the structure of interest is the open rigid half-cylinder (4) in Fig. 5.30.
Fig. 6.17 and Fig. 6.18 show comparisons between the theoretical transfer functions defined in Eq. (5.30) and the measured transfer functions through plots of the pressure at the surface of the structure at two different frequencies, a given radial height and for one position (r_0, θ_0, z_0) of the monopole source. Regarding the experimental setup, the arc of microphones is at the same location as for the two-dimensional case. However, the monopole source is no longer on the same plane as the microphone arc array. Indeed, it can now be in a different z-plane as we are now in the three-dimensional case.

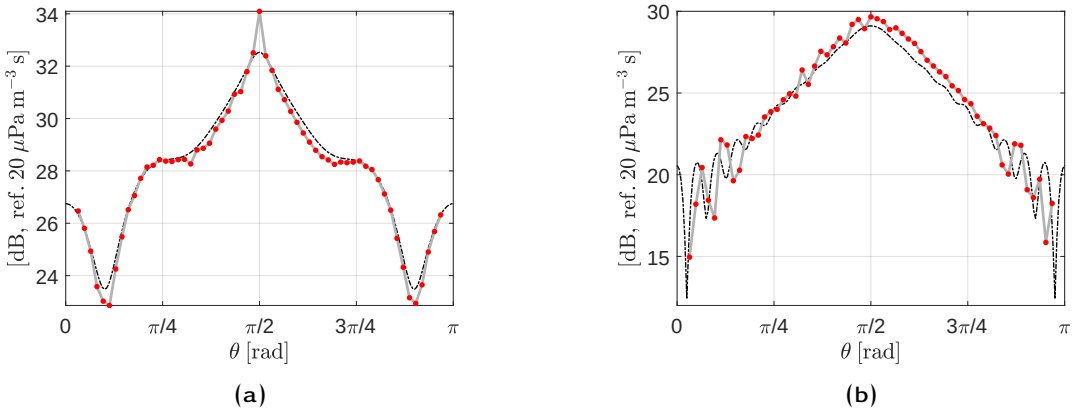

Figure 6.17: Pressure at the surface of the structure at two frequencies: (a) $f = 500\,\text{Hz}$ and (b) $f = 2000\,\text{Hz}$, for a radial height $h = 5\,\text{cm}$ and source angular position $\theta_0 = \frac{\pi}{2}$. Comparison between the analytical results (dash-dotted black line) and the experimental measurements (continuous gray line, the red dots correspond to the positions of the measurement points) for the three-dimensional case. The observation points are on a different section from the source's plane/section, i.e. $|z - z_0| = 50\,\text{cm}$.

In Fig. 6.17, the monopole source is located at $\left(r_0 = 55\,\text{cm}, \theta_0 = \frac{\pi}{2}, z_0 = 50\,\text{cm}\right)$ and the microphone array is always at the same position. Observing this figure, one can notice that despite some discrepancies, there is a good agreement between both types of results.

Cette thèse est accessible à l'adresse : https://theses.insa-lyon.fr/publication/2022ISAL0077/these.pdf
© [A.D. Pouye], [2022], INSA Lyon, tous droits réservés

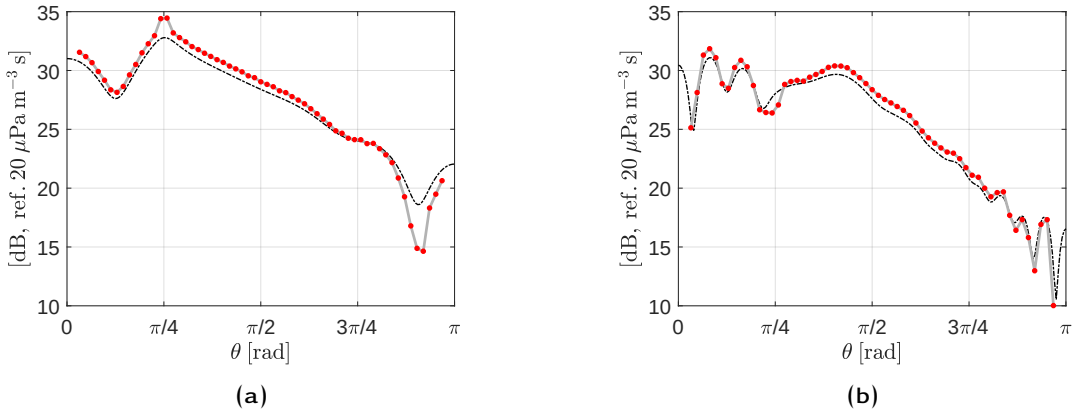

Figure 6.18: Pressure at the surface of the structure at two frequencies: (a) $f = 500\,\text{Hz}$ and (b) $f = 2000\,\text{Hz}$, for a radial height $h = 10\,\text{cm}$ and source angular position $\theta_0 = \frac{\pi}{4}$. Comparison between the analytical results (dash-dotted black line) and the experimental measurements (continuous gray line, the red dots correspond to the positions of the measurement points) for the three-dimensional case. The observation points are on a different section from the source's plane/section, i.e. $|z - z_0| = 25\,\text{cm}$.

As for Fig. 6.18, the monopole source is at the position $\left(r_0 = 60\,\text{cm}, \theta_0 = \frac{\pi}{4}, z_0 = 25\,\text{cm}\right)$. One can also notice that the measurements match the theoretical results. In conclusion, one can safely validate the three-dimensional transfer functions.

The measurement of the transfer matrix between each monopole source position and observation points on the surface of the half-cylinder for an experimental implementation of the SST process would be time consuming in the scope of this thesis. However, given the θ and z symmetry of the system and the results obtained in the two-dimensional case, we do not see any limitations to the implementation of the three-dimensional SST process over the cylindrical geometry. Moreover, the measured transfer functions agree well with the modeled ones and the simulated three-dimensional SST was assessed in Sec. 5.2.2 from modeled transfer functions.

Cette thèse est accessible à l'adresse : https://theses.insa-lyon.fr/publication/2022ISAL0077/these.pdf
© [A.D. Pouye], [2022], INSA Lyon, tous droits réservés

6.3 SUMMARY

In this chapter, the experimental devices (microphones, monopole source, robot arm) as well as the experimental setup were presented. The measurements were done using the devices along with an OROS acquisition system installed in the control room. The experimental validation of the transfer functions studied in Chapter 5 (see Eq. (5.16) and Eq. (5.30)) was then carried out for the two-dimensional case as well as for the three-dimensional case. The experimental implementation of the SST process was done for the two-dimensional case. The measurements were compared to analytical results with a very good agreement.

Cette thèse est accessible à l'adresse : https://theses.insa-lyon.fr/publication/2022ISAL0077/these.pdf
© [A.D. Pouye], [2022], INSA Lyon, tous droits réservés

Cette thèse est accessible à l'adresse : https://theses.insa-lyon.fr/publication/2022ISAL0077/these.pdf
© [A.D. Pouye], [2022], INSA Lyon, tous droits réservés

CONCLUSION

Cette thèse est accessible à l'adresse : https://theses.insa-lyon.fr/publication/2022ISAL0077/these.pdf
© [A.D. Pouye], [2022], INSA Lyon, tous droits réservés

Cette thèse est accessible à l'adresse : https://theses.insa-lyon.fr/publication/2022ISAL0077/these.pdf
© [A.D. Pouye], [2022], INSA Lyon, tous droits réservés

This thesis was focused on the reproduction of the vibroacoustic responses of structures under random pressure fields using the Source Scanning Technique (SST) which uses a single monopole source, displaced to several positions in order to mimic the effect of a full array, as an alternative or complementary method to the usual test facilities such as reverberant rooms and anechoic wind tunnels which are costly, difficult to implement and sometimes lack reproducibility. The random excitations of interest, the Diffuse Acoustic Field (DAF) and the Turbulent Boundary Layer (TBL), were considered stationary in time and homogeneous in space. We were interested in two types of structures: Flat Rectangular Panels (FRPs) and Curved Rectangular Panels (CRPs). In a first step, a validation of SST on FRPs was done. Subsequently, the proposed method was extended to CRPs.

Part II was concerned with the application of SST on FRPs. Our attention was focused on the validation of the process with comparisons against numerical and experimental results obtained in test facilities such as reverberant rooms and anechoic wind tunnels. A parametric study based on numerical simulations aiming at defining the ideal design of the array of virtual sources was done: it was established that for an accurate reproduction process, one needs at least 4 monopole positions per smallest wavelength to be synthesized accurately. This study allowed to define an optimal interval for the distance between the panel and the source array, in which the pressure field synthesis is in good agreement with the target pressure field, allowing a good reproduction of the vibroacoustic response of the considered structure. A case study involving a simply supported aluminum FRP subjected to either a DAF or TBL excitation was proposed. Both the velocity response at a given point and the radiated power by the panel were estimated. A $3D$ Cartesian robot was used to move the acoustic source whereas a $2D$ Cartesian robot was used to move a linear array of microphones. This system was controlled by a MATLAB script that allowed us to automatize the measurement process of the transfer functions between the source (at different positions) and the microphone array to determine the sensitivity functions and subsequently, the vibroacoustic responses. To evaluate the radiated power for the computation of the transmission loss, the two-microphone method

Cette thèse est accessible à l'adresse : https://theses.insa-lyon.fr/publication/2022ISAL0077/these.pdf
© [A.D. Pouye], [2022], INSA Lyon, tous droits réservés

was used to estimate the normal particle velocity. There was a fairly good agreement between the three types of results (numerical, SST and direct measurements) as can be visualized in Sec. 4.2.

Part III was dedicated to the extension of the SST process to CRPs. To the best of our knowledge, the closed-form transfer functions between a monopole source position and a point on a CRP as presented in the problem description in Sec. 5.1 and Fig. 5.1 was not yet established. Consequently, a preliminary work on the determination of these transfer functions was conducted to establish their analytical form. Once these transfer functions were numerically validated using OpenBEM, we investigated the optimal parameters of the monopole array for an accurate synthesis process through parametric studies. As for FRPs, it was also established that one needed at least 4 monopole positions per smallest wavelength to be reproduced. We also studied two different source array - structure geometric configurations: conformal configuration (monopole array with the same geometry as the test structure) and non-conformal (monopole array with a different geometry from the test structure). The results yielded that the conformal configuration is more suited for the proposed SST approach. Afterwards, we designed an experimental setup for the implementation of the SST process on CRPs. In order to automatize the process, the monopole source was mounted on an articulated robot arm. The measurements were done using an OROS acquisition system as was done for FRPs and the whole measurement operations were managed from a control room. The two-dimensional and three-dimensional measured transfer functions were compared to analytical ones. A good agreement between the two types of results was found thus validating each other. Finally, the SST process was implemented in the two-dimensional case and the results were very convincing as can be consulted in Sec. 6.2.1.2.

Several perspectives and applications are now considered. As one can notice, the three-dimensional experimental implementation of the broadband SST process in the case of CRPs was not done due to time consuming measurements induced by a large number of source positions over the size of the considered structure, see Table 5.2. Even though the experimental three-dimensional SST results should be, in theory, close to the analytical

Cette thèse est accessible à l'adresse : https://theses.insa-lyon.fr/publication/2022ISAL0077/these.pdf
© [A.D. Pouye], [2022], INSA Lyon, tous droits réservés

ones, it would be interesting to validate it in future works. Also, one needs to have a proper control on the mechanical boundary conditions of the structure of interest in order to accurately predict the vibroacoustic responses of CRPs to synthesized random pressure fields.

As the SST process has been validated and automatized, it can be used in the future to compare the responses of different complex panels (stiffened panels or multilayer panels) under DAF or TBL excitation. As the considered excitation is represented by a model, the comparison between different panels will not be perturbed by uncertainties and background noises related to the excitation. Moreover, the analysis of the measured sensitivity functions will be helpful to extract the physical phenomena contributing to the noise radiation of the panels. One can also compare different configurations (space between stiffeners, stiffeners damping, etc.) and analyze the impact on the results. Let us now consider a given panel for which all the sensitivity functions have already been measured and which is subjected to an unknown random pressure field. Using the measured sensitivity functions and measurements of the vibroacoustic response of the panel, one can estimate the wall-pressure fluctuations on the surface of the panel due to the unknown random excitation.

For future work, one can also imagine extending the SST process in order to synthesize inhomogeneous pressure fields and study the dispersion of the vibroacoustic response due to the inhomogeneity of the excitation. Finally, one can also imagine extending SST to dome-like structures for naval an aeronautical applications. For instance, the study of the vibroacoustic behavior of hulls or SONAR domes.

Cette thèse est accessible à l'adresse : https://theses.insa-lyon.fr/publication/2022ISAL0077/these.pdf
© [A.D. Pouye], [2022], INSA Lyon, tous droits réservés

Cette thèse est accessible à l'adresse : https://theses.insa-lyon.fr/publication/2022ISAL0077/these.pdf
© [A.D. Pouye], [2022], INSA Lyon, tous droits réservés

APPENDICES

Cette thèse est accessible à l'adresse : https://theses.insa-lyon.fr/publication/2022ISAL0077/these.pdf
© [A.D. Pouye], [2022], INSA Lyon, tous droits réservés

Cette thèse est accessible à l'adresse : https://theses.insa-lyon.fr/publication/2022ISAL0077/these.pdf
© [A.D. Pouye], [2022], INSA Lyon, tous droits réservés

A VELOCITY SENSITIVITY FUNCTIONS

The sensitivity functions characterize the dynamical behavior of a given structure and have been defined by Eq. (2.6). For the considered panel in this study, these sensitivity functions are calculated using the modal expansion method

$$H_v(\mathbf{x},\mathbf{k},\omega) = \mathrm{i}\omega \sum_{m,n} \frac{F_{mn}(\mathbf{k})\,\phi_{mn}(\mathbf{x})}{M_{mn}\left(\omega_{mn}^2 - \omega^2 + \mathrm{i}\eta_{mn}\omega_{mn}\omega\right)} \tag{A.1}$$

where m and n are both positive integers related to the summations.

- $\mathbf{x} = (x, y, 0)$ is the point of interest on the panel surface,
- $F_{mn}(\mathbf{k})$ is called the generalized force of the plane wave,
- $\phi_{mn}(\mathbf{x})$ represents the mode shape, M_{mn} the modal mass, ω_{mn} the modal angular frequency and η_{mn} the modal damping.

For a simply supported panel on all edges (as shown in Fig. 3.1), the modal parameters are given in the following equations

$$\omega_{mn} = \left[\left(\frac{m\pi}{L_1}\right)^2 + \left(\frac{n\pi}{L_2}\right)^2\right]\sqrt{\frac{D}{\rho h}} \tag{A.2}$$

$$\phi_{mn}(\mathbf{x}) = \sin\left(\frac{m\pi}{L_1}x_1\right)\sin\left(\frac{n\pi}{L_2}x_2\right) \tag{A.3}$$

Cette thèse est accessible à l'adresse : https://theses.insa-lyon.fr/publication/2022ISAL0077/these.pdf
© [A.D. Pouye], [2022], INSA Lyon, tous droits réservés

$$M_{mn} = \frac{\rho h L_1 L_2}{4} \tag{A.4}$$

The modal force is given by

$$F_{mn}(\mathbf{k}) = \iint_{\Sigma_p} p(\mathbf{x}, \mathbf{k}) \phi_{mn}(\mathbf{x}) \, \mathrm{d}\mathbf{x} \tag{A.5}$$

where Σ_p designates the area of the panel and $p(\mathbf{x}, \mathbf{k}) = \mathrm{e}^{-\mathrm{i}\mathbf{k}\mathbf{x}}$ is the prescribed pressure field corresponding to a unit wall plane wave characterized by the wave-vector $\mathbf{k}$. Equation (A.5) has a closed-form solution

$$F_{mn}(\mathbf{k}) = F_{mn}\left(k_x, k_y\right) = I_m^x(k_x) I_n^y\left(k_y\right) \tag{A.6}$$

where for $\xi \in \{x, y\}$ and $p \in \{m, n\}$

$$I_p^\xi\left(k_\xi\right) = \begin{cases} \left(\dfrac{p\pi}{L_\xi}\right) \dfrac{(-1)^p \mathrm{e}^{-\mathrm{i}k_\xi L_\xi} - 1}{k_\xi^2 - \left(\frac{p\pi}{L_\xi}\right)^2} & \text{if} \quad |k_\xi| \neq \dfrac{p\pi}{L_\xi} \\ \dfrac{1}{2}\mathrm{i}L_\xi \quad \text{otherwise} \end{cases} \tag{A.7}$$

Cette thèse est accessible à l'adresse : https://theses.insa-lyon.fr/publication/2022ISAL0077/these.pdf
© [A.D. Pouye], [2022], INSA Lyon, tous droits réservés

B RADIATED POWER BY A PANEL

The radiated power is defined by

$$\Pi_r(\omega) = \iint_{\Sigma_v} I_{act}(\mathbf{x},\omega)\,\mathrm{d}\mathbf{x} \tag{B.1}$$

where d$\mathbf{x}$ is the surface element and I_{act} is the normal component of the active sound intensity at point $\mathbf{x}$.
The active sound intensity is directly related to the CSD function $S_{pv_0}(\mathbf{x},\omega)$ between the sound pressure and the particle velocity at point $\mathbf{x}$ [36]

$$I_{act}(\mathbf{x},\omega) = \Re\mathfrak{e}\left[S_{pv_0}(\mathbf{x},\omega)\right] \tag{B.2}$$

with

$$S_{pv_0}(\mathbf{x},\omega) = \frac{1}{4\pi^2}\iint_{\mathbf{k}} H_p(\mathbf{x},\mathbf{k},\omega)\,H^*_{v_0}(\mathbf{x},\mathbf{k},\omega)\,S_{pp}(\mathbf{k},\omega)\,\mathrm{d}\mathbf{k} \tag{B.3}$$

Theoretically, the radiated power is obtained by solving the formal integral in Eq. (B.1). A discretized version of this equation is

$$\Pi_r(\omega) = \sum_{\sigma_v} I_{act}(\mathbf{x},\omega)\,\delta\mathbf{x} \tag{B.4}$$

where σ_v represents the set of points defined on Σ_v and $\delta\mathbf{x}$ is the elementary point area. The pressure and particle velocity sensitivity functions can respectively be written as

$$H_p(\mathbf{x},\mathbf{k},\omega) = \frac{1}{4\pi^2}\iint_{\tilde{\mathbf{k}}} \tilde{H}_p\left(\tilde{\mathbf{k}},\mathbf{k},\omega\right)\mathrm{e}^{\mathrm{i}\tilde{\mathbf{k}}\mathbf{x}}\mathrm{d}\tilde{\mathbf{k}} \tag{B.5}$$

Cette thèse est accessible à l'adresse : https://theses.insa-lyon.fr/publication/2022ISAL0077/these.pdf
© [A.D. Pouye], [2022], INSA Lyon, tous droits réservés

$$H_{v_0}(\mathbf{x},\mathbf{k},\omega)=\frac{1}{4\pi^2}\iint_{\tilde{\mathbf{k}}}\tilde{H}_{v_0}\left(\tilde{\tilde{\mathbf{k}}},\mathbf{k},\omega\right)\mathrm{e}^{\mathrm{i}\tilde{\tilde{\mathbf{k}}}\mathbf{x}}\mathrm{d}\tilde{\tilde{\mathbf{k}}} \tag{B.6}$$

Introducing Eq. (B.5) and Eq. (B.6) into Eq. (B.2), then the previous result is introduced in Eq. (B.3) then in Eq. (B.4) and after rearranging, one can obtain the following expression for the radiated power by the panel

$$\Pi_r(\omega)=\Re\mathfrak{e}\left[\left(\frac{1}{4\pi^2}\right)^3\iint_{\mathbf{k}}\iint_{\tilde{\mathbf{k}}}\iint_{\tilde{\tilde{\mathbf{k}}}}\tilde{H}_p\left(\tilde{\mathbf{k}},\mathbf{k},\omega\right)\tilde{H}_{v_0}\left(\tilde{\tilde{\mathbf{k}}},\mathbf{k},\omega\right)\iint_{\Sigma_p}\mathrm{e}^{\mathrm{i}\left(\tilde{\mathbf{k}}-\tilde{\tilde{\mathbf{k}}}\right)}\mathrm{d}\mathbf{x}\times\mathrm{d}\tilde{\mathbf{k}}\mathrm{d}\tilde{\tilde{\mathbf{k}}}S_{pp}(\mathbf{k},\omega)\,\mathrm{d}\mathbf{k}\right] \tag{B.7}$$

Note that

$$\frac{1}{4\pi^2}\iint_{-\infty}^{+\infty}\mathrm{e}^{\mathrm{i}\left(\tilde{\mathbf{k}}-\tilde{\tilde{\mathbf{k}}}\right)}\mathrm{d}\mathbf{x}=\delta\left(\tilde{\mathbf{k}}-\tilde{\tilde{\mathbf{k}}}\right)=\begin{cases}1 \text{ if } \tilde{\mathbf{k}}=\tilde{\tilde{\mathbf{k}}}\\ 0 \text{ if } \tilde{\mathbf{k}}\neq\tilde{\tilde{\mathbf{k}}}\end{cases} \tag{B.8}$$

The previous relation can be used in the case of a baffled panel as the outgoing intensity is null on on the baffle. The radiated power can now be written as

$$\Pi_r(\omega)=\Re\mathfrak{e}\left[\left(\frac{1}{4\pi^2}\right)^2\iint_{\mathbf{k}}\iint_{\tilde{\mathbf{k}}}\tilde{H}_p\left(\tilde{\mathbf{k}},\mathbf{k},\omega\right)\tilde{H}_{v_0}\left(\tilde{\mathbf{k}},\mathbf{k},\omega\right)\mathrm{d}\tilde{\mathbf{k}}S_{pp}(\mathbf{k},\omega)\,\mathrm{d}\mathbf{k}\right] \tag{B.9}$$

One has

$$\tilde{H}_{v_0}\left(\tilde{\mathbf{k}},\mathbf{k},\omega\right)=\sum_{m,n}a_{mn}(\mathbf{k})\,\tilde{\phi}_{mn}\left(\tilde{\mathbf{k}}\right) \tag{B.10}$$

where

$$\tilde{\phi}_{mn}\left(\tilde{\mathbf{k}}\right)=\int_0^{L_x}\int_0^{L_y}\phi_{mn}(\mathbf{x})\,\mathrm{e}^{-\mathrm{i}\tilde{\mathbf{k}}\mathbf{x}}\mathrm{d}\mathbf{x}=I_m^x I_n^y \tag{B.11}$$

Cette thèse est accessible à l'adresse : https://theses.insa-lyon.fr/publication/2022ISAL0077/these.pdf
© [A.D. Pouye], [2022], INSA Lyon, tous droits réservés

The theoretical radiated power by a simply supported plate under random excitation is given by the following equation

$$\Pi_r(\omega) = \mathfrak{Re}\left[\left(\frac{1}{4\pi^2}\right)^2 \sum_{\mathbf{k}} \sum_{\tilde{\mathbf{k}}} \tilde{H}_p\left(\tilde{\mathbf{k}}, \mathbf{k}, \omega\right) \tilde{H}^*_{v_0}\left(\tilde{\mathbf{k}}, \mathbf{k}, \omega\right) \Delta\tilde{\mathbf{k}} S_{pp}(\mathbf{k}, \omega) \Delta\mathbf{k}\right] \tag{B.12}$$

The particle velocity over the wall of a panel excited by a WPPW of wavenumber $\mathbf{k}$ can be written as a function of the acoustic pressure

$$\tilde{H}_p\left(\tilde{\mathbf{k}}, \mathbf{k}, \omega\right) = \frac{\omega\rho_0}{k_z} \tilde{H}_{v_0}\left(\tilde{\mathbf{k}}, \mathbf{k}, \omega\right) \tag{B.13}$$

where ρ_0 is the density of the fluid and $k_z = \sqrt{k_0^2 - \tilde{k}_x^2 - \tilde{k}_y^2}$ if $\tilde{k}_x^2 + \tilde{k}_y^2 \leq k_0^2$, otherwise $k_z = j\sqrt{\tilde{k}_x^2 + \tilde{k}_y^2 - k_0^2}$. Using Equation (B.13), the radiated power can be written as follows

$$\Pi_r(\omega) = \mathfrak{Re}\left[\omega\rho_0\left(\frac{1}{4\pi^2}\right)^2 \sum_{\mathbf{k}} \sum_{\tilde{\mathbf{k}}} \frac{1}{k_z} \left|\tilde{H}_{v_0}\left(\tilde{\mathbf{k}}, \mathbf{k}, \omega\right)\right|^2 \delta\tilde{\mathbf{k}} S_{pp}(\mathbf{k}, \omega) \delta\mathbf{k}\right] \tag{B.14}$$

Cette thèse est accessible à l'adresse : https://theses.insa-lyon.fr/publication/2022ISAL0077/these.pdf
© [A.D. Pouye], [2022], INSA Lyon, tous droits réservés

Cette thèse est accessible à l'adresse : https://theses.insa-lyon.fr/publication/2022ISAL0077/these.pdf
© [A.D. Pouye], [2022], INSA Lyon, tous droits réservés

C | INVARIANCE PRINCIPLE

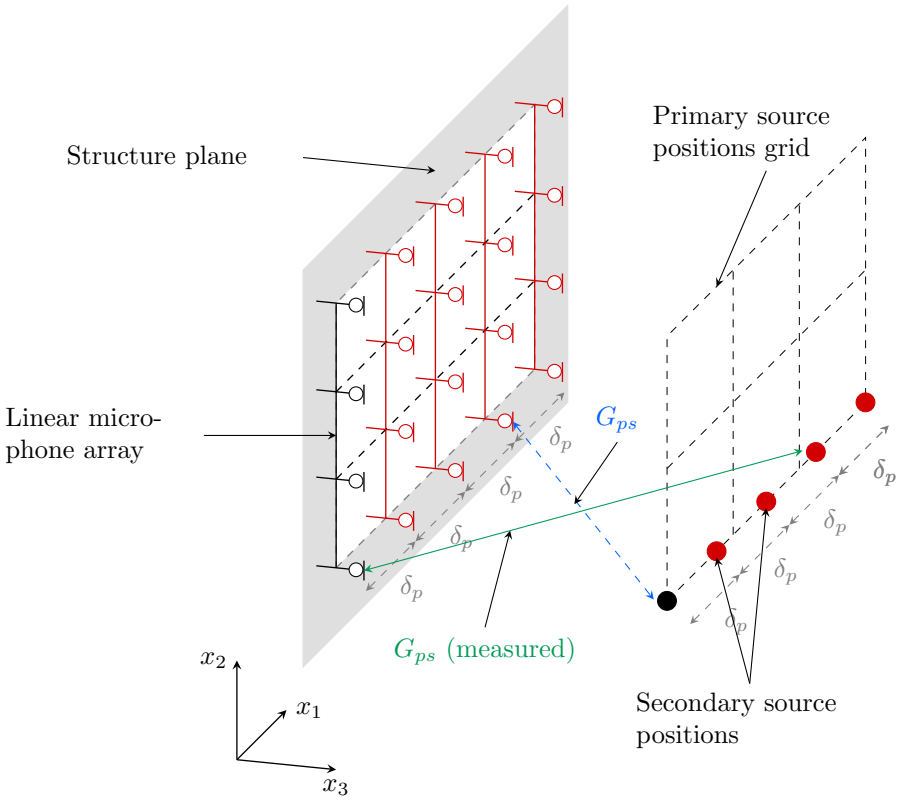

Figure C.1: FRFs measurements using a non-displaceable microphone array

The second step of the SST process requires the measurement of the FRFs G_{ps} between the source position s and the observation p on the reconstruction surface. A linear flush-mounted microphone array was used to achieve this measurement. As this array does not cover the whole reconstruction surface, one used the invariance property in translation of the idealized considered system (i.e. source, flat baffle, semi-anechoic room) to deduce the required transfer functions. This is highlighted in Fig. C.1.

Cette thèse est accessible à l'adresse : https://theses.insa-lyon.fr/publication/2022ISAL0077/these.pdf
© [A.D. Pouye], [2022], INSA Lyon, tous droits réservés

The blue grid shows the primary positions occupied by the source if we had a rectangular array or a displaceable (with an actuator for instance) linear array of microphones. The secondary source positions in red are the additional source positions needed to measure the FRFs if one had a single non-displaceable linear array of microphones considering the invariance property in translations. Thus, instead of measuring, for instance, the blue (dashed) FRF (see Fig. C.1), one would displace the source at the position facing the linear microphone array (same x coordinate but different z coordinate) and measure the green (solid line) FRF G_{ps}. As the linear array is along the y axis, there is no need to displace the source along the y coordinate. With this methodology, one can measure the transfer function G_{ps} for any point on the reconstruction surface with the considered linear array.

Cette thèse est accessible à l'adresse : https://theses.insa-lyon.fr/publication/2022ISAL0077/these.pdf
© [A.D. Pouye], [2022], INSA Lyon, tous droits réservés

D VALIDATION OF THE TRANSFER FUNCTIONS FOR CURVED PANELS

D.1 Two dimensional case 159
D.1.1 Convergence of the harmonic expansion 159
D.1.2 Comparison with OpenBEM 167
D.2 Three dimensional case 171
D.2.1 Integration domain 171
D.2.2 Validation with OpenBEM 175

This appendix contains supplementary material to Sec. 5.1.3 which purpose is to validate the analytical solutions of the two-dimensional and three-dimensional formulations respectively given by Eq. (5.16) and Eq. (5.30).

D.1 TWO DIMENSIONAL CASE

D.1.1 Convergence of the harmonic expansion

The goal in this section is the study of the convergence of the expansion present in Eq. (5.15) as a function of the monopole coordinate (either r_0 or θ_0) and the number of harmonics effectively used in that same equation. Four different points have been arbitrarily chosen as checking points: see Fig. D.1. In order to do so, we are going to determine the surface pressure for the structure depicted in Fig. 5.1 with the geometrical parameters in Table D.1. One can easily notice that, considering the geometrical values

Cette thèse est accessible à l'adresse : https://theses.insa-lyon.fr/publication/2022ISAL0077/these.pdf
© [A.D. Pouye], [2022], INSA Lyon, tous droits réservés

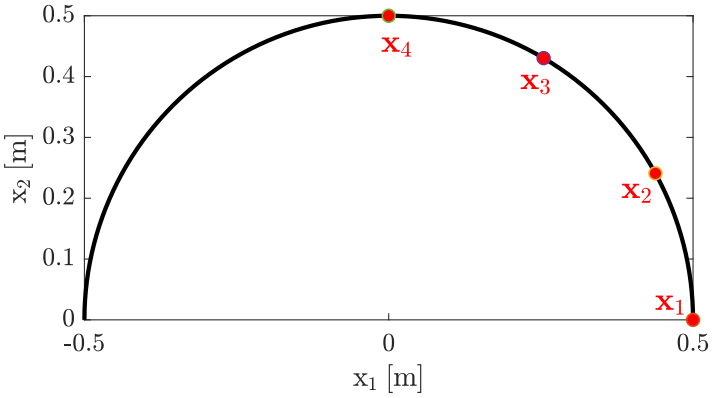

Figure D.1: Localization of arbitrarily chosen test points $\mathbf{x}_1$, $\mathbf{x}_2$, $\mathbf{x}_3$ and $\mathbf{x}_4$ where the pressure is plotted in order to study the number of necessary harmonics for a convergence of the pressure.

in Table D.1, the structure corresponds to a half cylinder with radius $R_s = \sqrt{a^2 + b^2} = 500\,\text{mm}$ and an apothem[1] a.

Table D.1: Geometrical properties of the structure

Parameters	Values
Apothem	$a = 0\,\text{mm}$
Chord length	$2b = 1000\,\text{mm}$

In the following, several (series of figures from Fig. D.2 to Fig. D.4) maps representing the evolution of the pressure at those specific points for a monopole positioned at $\left(r_0, \theta_0 = \frac{\pi}{2}\right)$ with $r_0 \in]0.5, 1]$ m and for three different frequencies: 100 Hz, 1000 Hz and 2000 Hz.

Observing Fig. D.2, Fig. D.3 and Fig. D.4 one can notice that the higher the frequency, the slower the convergence of the series. However, there is not much difference in the

1 Given a circle, the apothem is the perpendicular distance from the midpoint of a chord to the circle's center. For a regular polygon, the apothem simply is the distance from the center to a side. See circular segment.

Cette thèse est accessible à l'adresse : https://theses.insa-lyon.fr/publication/2022ISAL0077/these.pdf
© [A.D. Pouye], [2022], INSA Lyon, tous droits réservés

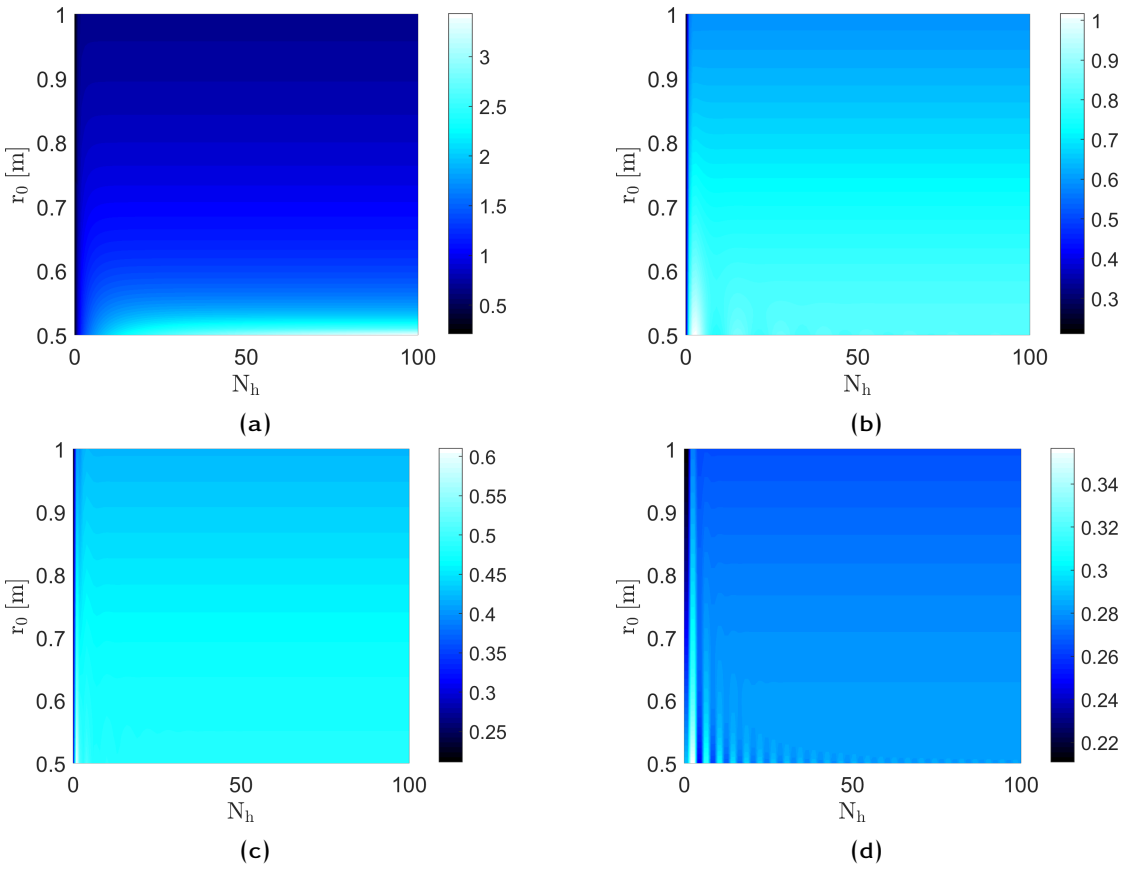

Figure D.2: Evolution of the pressure at four different points (see Fig. D.1) on the structure as a function of the source position r_0 for $\theta_0 = \frac{\pi}{2}$ and the number of harmonics N_h used in Eq. (5.15) at a frequency $f = 100\,\text{Hz}$ (a) $\mathbf{x}_1$, (b) $\mathbf{x}_2$, (c) $\mathbf{x}_3$, and (d) $\mathbf{x}_4$.

number of necessary harmonics for the series to converge for the three frequencies studied. In conclusion, for the considered frequency range ($[100, 2000]$ Hz), it is safe to say that above approximately $N_h = 30$ harmonics, the estimation of the surface pressure is accurate enough.

Fig. D.5, Fig. D.6 and Fig. D.7 show maps of the evolution of the pressure at the same four checking points ($\mathbf{x}_1$ to $\mathbf{x}_4$), the only difference from previous maps is that this time the pressure field is plotted as a function of the coordinate $\theta_0 \in [0, \pi]$ for $r_0 = 0.8\,\text{m}$.

Cette thèse est accessible à l'adresse : https://theses.insa-lyon.fr/publication/2022ISAL0077/these.pdf
© [A.D. Pouye], [2022], INSA Lyon, tous droits réservés

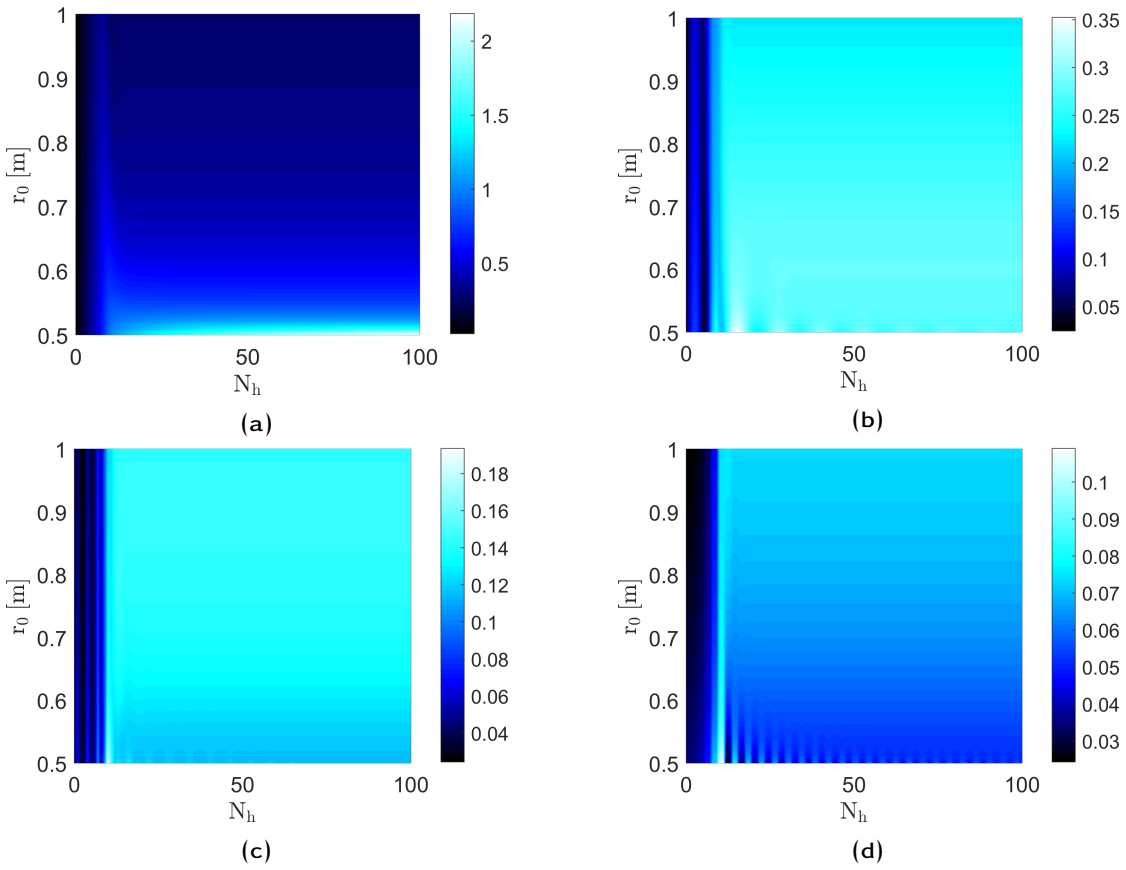

Figure D.3: Evolution of the pressure at four different points (see Fig. D.1) on the structure as a function of the source position r_0 for $\theta_0 = \frac{\pi}{2}$ and the number of harmonics N_h used in Eq. (5.15) at a frequency $f = 1000\,\text{Hz}$ (a) $\mathbf{x}_1$, (b) $\mathbf{x}_2$, (c) $\mathbf{x}_3$, and (d) $\mathbf{x}_4$.

Looking at these maps of the pressure for a varying angular position of the monopole source (θ_0), one can notice the same behavior of the series regarding the number of necessary harmonics for a good estimation of the surface pressure, i.e. above $N_h = 30$.

Cette thèse est accessible à l'adresse : https://theses.insa-lyon.fr/publication/2022ISAL0077/these.pdf
© [A.D. Pouye], [2022], INSA Lyon, tous droits réservés

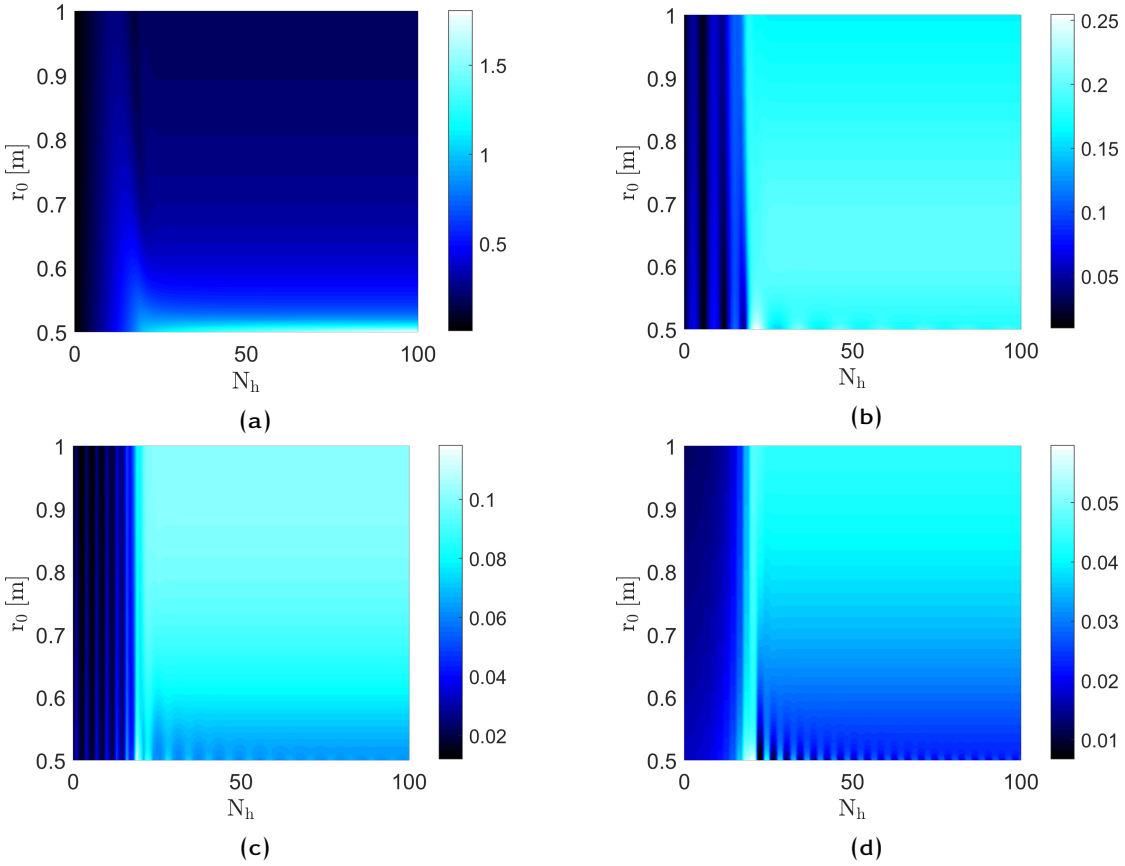

Figure D.4: Evolution of the pressure at four different points (see Fig. D.1) on the structure as a function of the source position r_0 for $\theta_0 = \frac{\pi}{2}$ and the number of harmonics N_h used in Eq. (5.15) at a frequency $f = 2000\,\text{Hz}$ (a) $\mathbf{x}_1$, (b) $\mathbf{x}_2$, (c) $\mathbf{x}_3$, and (d) $\mathbf{x}_4$.

Cette thèse est accessible à l'adresse : https://theses.insa-lyon.fr/publication/2022ISAL0077/these.pdf
© [A.D. Pouye], [2022], INSA Lyon, tous droits réservés

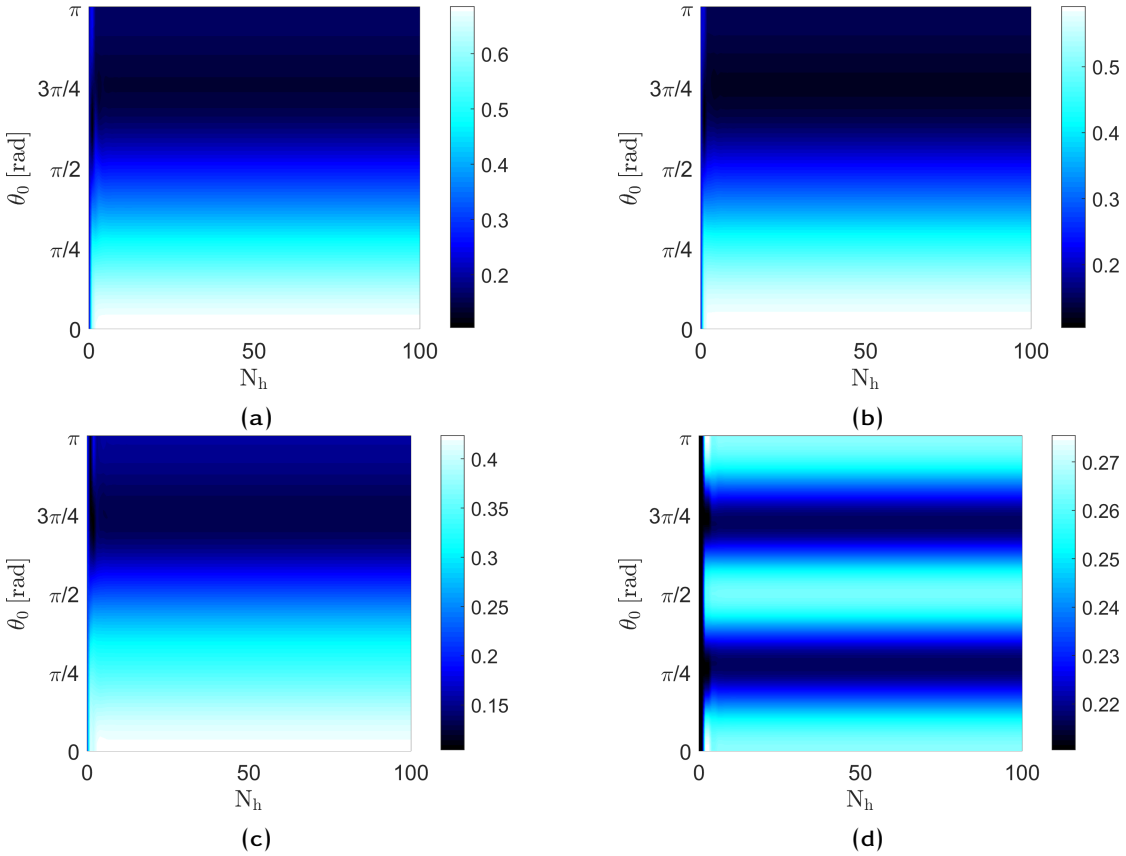

Figure D.5: Evolution of the pressure at four different points (see Fig. D.1) on the structure as a function of the source position θ_0 for $r_0 = 0.8\,\mathrm{m}$ and the number of harmonics N_h used in Eq. (5.15) at a frequency $f = 100\,\mathrm{Hz}$ (a) $\mathbf{x}_1$, (b) $\mathbf{x}_2$, (c) $\mathbf{x}_3$, and (d) $\mathbf{x}_4$.

Cette thèse est accessible à l'adresse : https://theses.insa-lyon.fr/publication/2022ISAL0077/these.pdf
© [A.D. Pouye], [2022], INSA Lyon, tous droits réservés

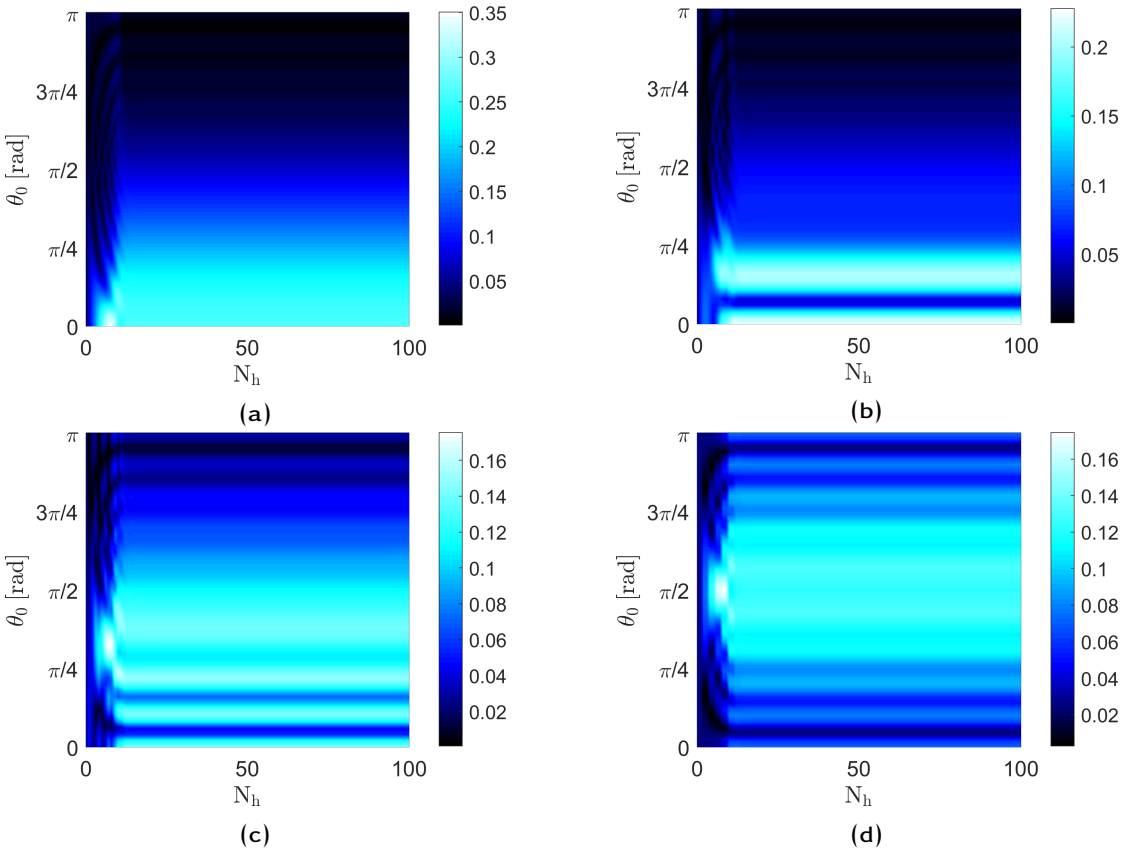

Figure D.6: Evolution of the pressure at four different points (see Fig. D.1) on the structure as a function of the source position θ_0 for $r_0 = 0.8\,\text{m}$ and the number of harmonics N_h used in Eq. (5.15) at a frequency $f = 1000\,\text{Hz}$ (a) $\mathbf{x}_1$, (b) $\mathbf{x}_2$, (c) $\mathbf{x}_3$, and (d) $\mathbf{x}_4$.

Cette thèse est accessible à l'adresse : https://theses.insa-lyon.fr/publication/2022ISAL0077/these.pdf
© [A.D. Pouye], [2022], INSA Lyon, tous droits réservés

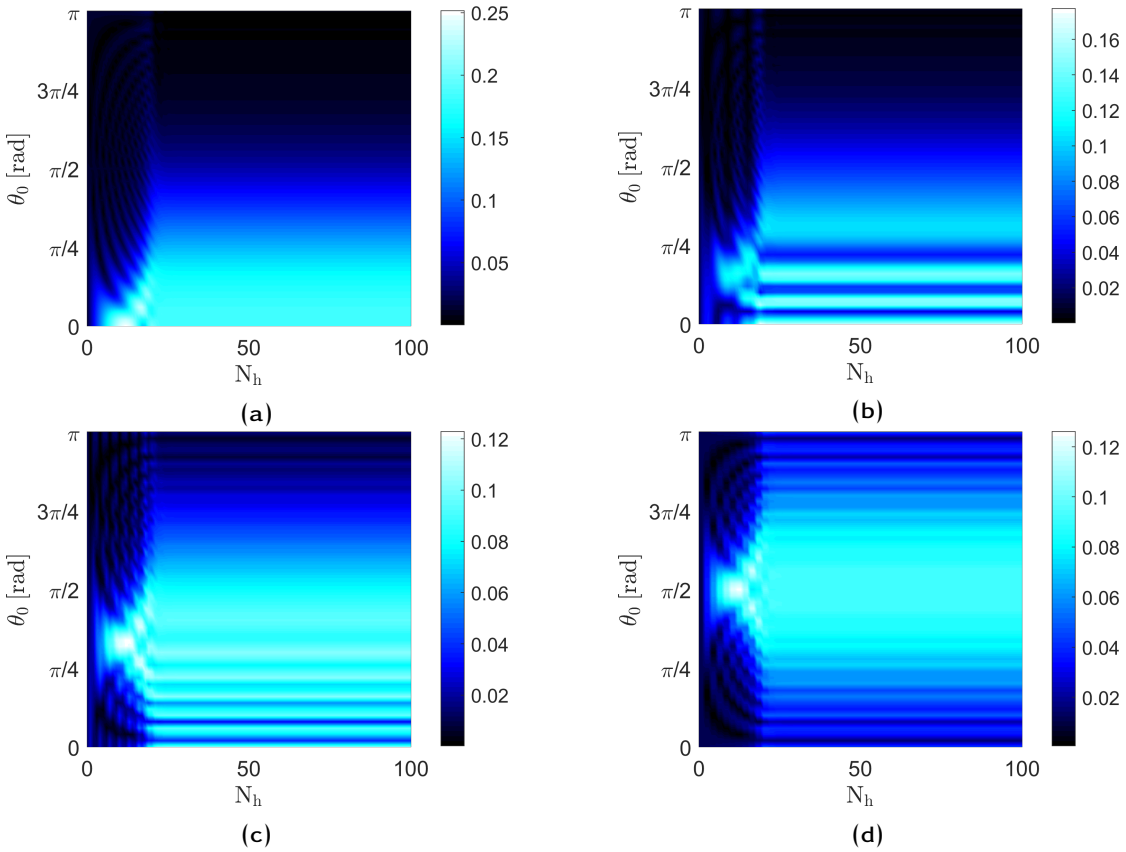

Figure D.7: Evolution of the pressure at four different points (see Fig. D.1) on the structure as a function of the source position θ_0 for $r_0 = 0.8\,\mathrm{m}$ and the number of harmonics N_h used in Eq. (5.15) at a frequency $f = 2000\,\mathrm{Hz}$ (a) $\mathbf{x}_1$, (b) $\mathbf{x}_2$, (c) $\mathbf{x}_3$, and (d) $\mathbf{x}_4$.

Cette thèse est accessible à l'adresse : https://theses.insa-lyon.fr/publication/2022ISAL0077/these.pdf
© [A.D. Pouye], [2022], INSA Lyon, tous droits réservés

D.1.2 Comparison with OpenBEM

Fig. D.8, Fig. D.9 and Fig. D.10 show a comparison between the numerical and analytical results of the magnitudes and phases of the surface pressure for three different positions of the monopole source and at three frequencies: 100, 1000 and 2000 Hz. Note that for these studies, $N_h = 50$.
Examining these results, one can deduce a very good agreement between both types of results thus confirming the validity of the established solution in Eq. (5.15).

Cette thèse est accessible à l'adresse : https://theses.insa-lyon.fr/publication/2022ISAL0077/these.pdf
© [A.D. Pouye], [2022], INSA Lyon, tous droits réservés

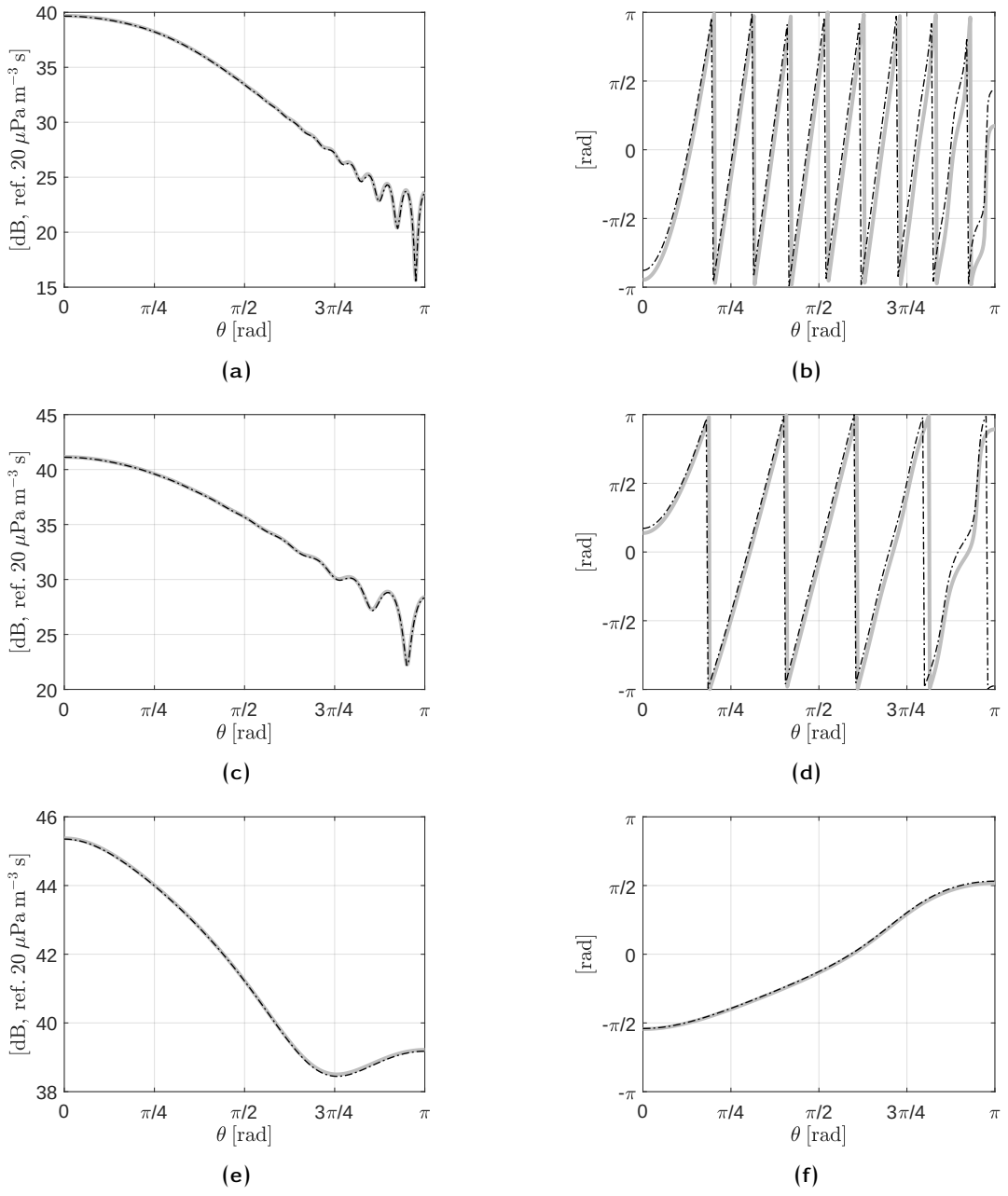

Figure D.8: Comparison between the amplitudes ((a), (c) and (e)) and phases ((b), (d) and (f)) of the transfer functions obtained with OpenBEM (gray continuous line) and those obtained using the developed analytical solution (dash-dotted black line) for one position of the unit amplitude monopole source ($r_0 = 1\,\mathrm{m}, \theta_0 = 0$) and at three different frequencies. (a) and (b): $f = 2000\,\mathrm{Hz}$; (c) and (d): $f = 1000\,\mathrm{Hz}$ and (e) and (f): $f = 100\,\mathrm{Hz}$.

Cette thèse est accessible à l'adresse : https://theses.insa-lyon.fr/publication/2022ISAL0077/these.pdf
© [A.D. Pouye], [2022], INSA Lyon, tous droits réservés

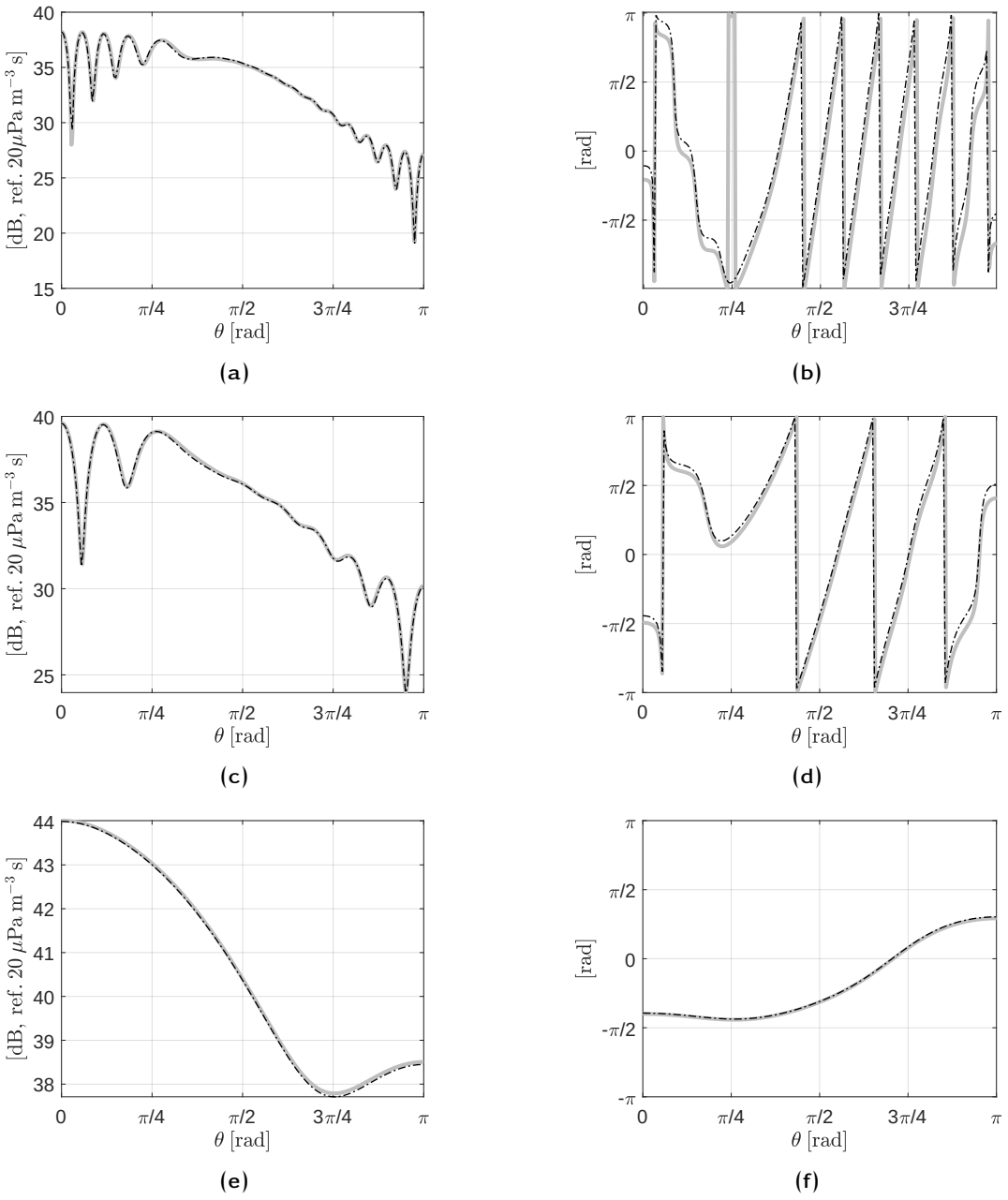

Figure D.9: Comparison between the amplitudes ((a), (c) and (e)) and phases ((b), (d) and (f)) of the transfer functions obtained with OpenBEM (gray continuous line) and those obtained using the developed analytical solution (dash-dotted black line) for one position of the unit amplitude monopole source $\left(r_0 = 1\,\text{m}, \theta_0 = \frac{\pi}{4}\right)$ and at three different frequencies. (a) and (b): $f = 2000\,\text{Hz}$; (c) and (d): $f = 1000\,\text{Hz}$ and (e) and (f): $f = 100\,\text{Hz}$.

Cette thèse est accessible à l'adresse : https://theses.insa-lyon.fr/publication/2022ISAL0077/these.pdf
© [A.D. Pouye], [2022], INSA Lyon, tous droits réservés

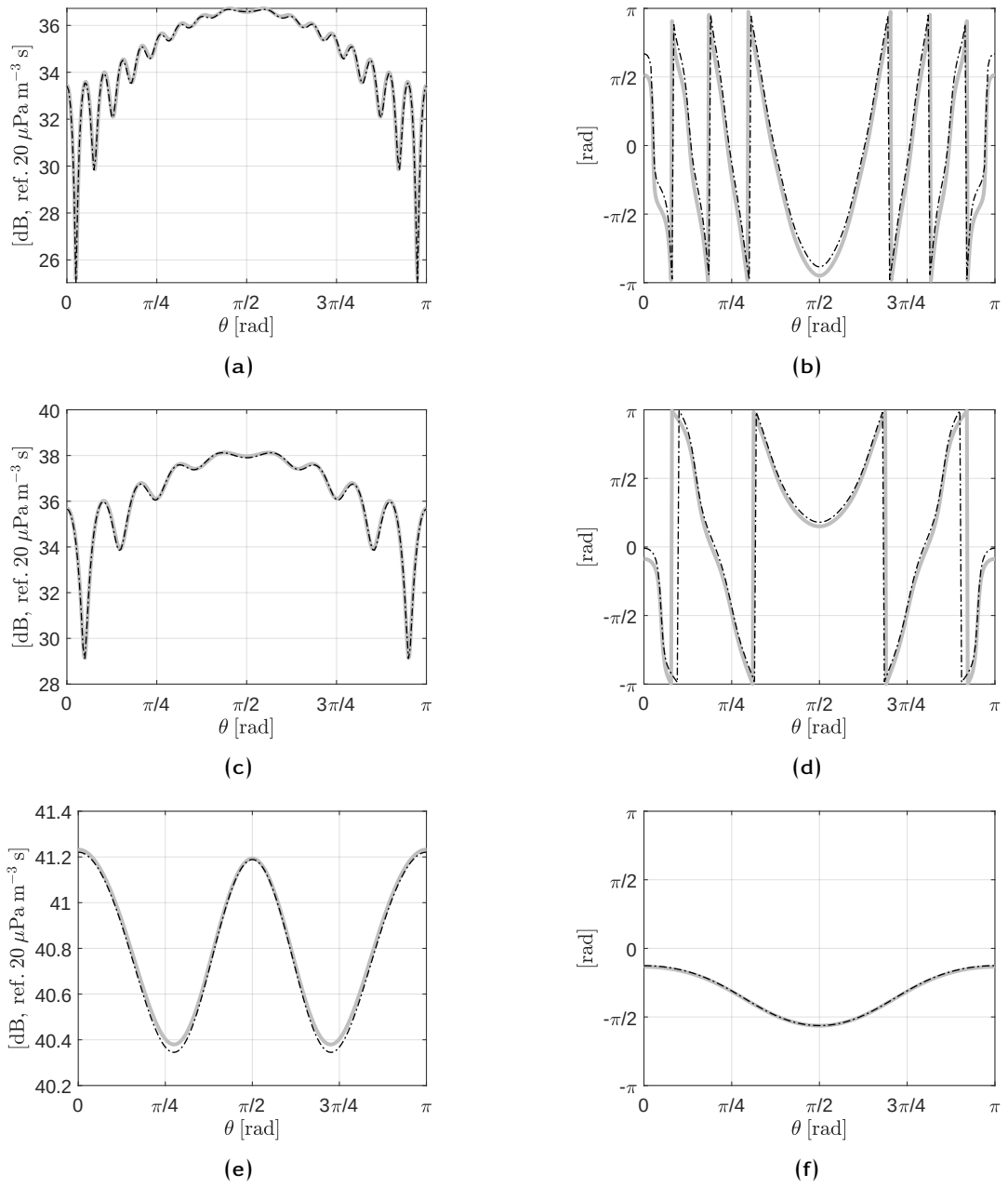

Figure D.10: Comparison between the amplitudes ((a), (c) and (e)) and phases ((b), (d) and (f)) of the transfer functions obtained with OpenBEM (gray continuous line) and those obtained using the developed analytical solution (dash-dotted black line) for one position of the unit amplitude monopole source $\left(r_0 = 1\,\text{m}, \theta_0 = \frac{\pi}{2}\right)$ and at three different frequencies. (a) and (b): $f = 2000\,\text{Hz}$; (c) and (d): $f = 1000\,\text{Hz}$ and (e) and (f): $f = 100\,\text{Hz}$.

Cette thèse est accessible à l'adresse : https://theses.insa-lyon.fr/publication/2022ISAL0077/these.pdf
© [A.D. Pouye], [2022], INSA Lyon, tous droits réservés

D.2 THREE DIMENSIONAL CASE

As for the two dimensional case, we must determine the optimal number of harmonics allowing an accurate computation of the transfer functions defined in Eq. (5.30). One can notice that this equation is very similar to Eq. (5.16) and a study on the number of cylindrical harmonics N_h shows an identical behavior of the three dimensional transfer functions when compared to the two dimensional ones. Hence, we will focus on the integration domain in Eq. (5.30) and their validation using the three dimensional functions of OpenBEM.

D.2.1 Integration domain

In order to determine the three dimensional transfer functions defined by Eq. (5.30), one must integrate the following expression over an infinite domain

$$I(k_z) = \sum_{n=-N_h}^{+N_h} \mathrm{e}^{\mathrm{i}n\theta_\sigma} \cos(n\theta_0) \frac{1}{k_r r_\sigma} \frac{H_n(k_r r_0)}{H_n'(k_r r_\sigma)} \mathrm{e}^{\mathrm{i}k_z(z_\sigma - z_0)} \tag{D.1}$$

However, it is not necessary to integrate this expression over an infinite domain. Fig. D.11 to Fig. D.15 represent plots of $I(k_z)$ for $k_z \in [-k_z^{max}, k_z^{max}]$ and for different source positions, frequencies and observation points. k_z^{max} is arbitrarily set to $500\,\mathrm{rad\,m^{-1}}$ for this study. The integral in Eq. (D.1) is numerically computed using Gauss-Legendre n-point quadrature [55].

Observing these figures, one can notice that the values of $I(k_z)$ are zero or very close to zero when $k_z > k_0$: this statement is also verified by setting the y-axis of these plots on a logarithmic scale and taking the absolute value of the real or imaginary part of the $I(k_z)$. This means that for an estimation of the integral defined in Eq. (5.30), one only needs to

Cette thèse est accessible à l'adresse : https://theses.insa-lyon.fr/publication/2022ISAL0077/these.pdf
© [A.D. Pouye], [2022], INSA Lyon, tous droits réservés

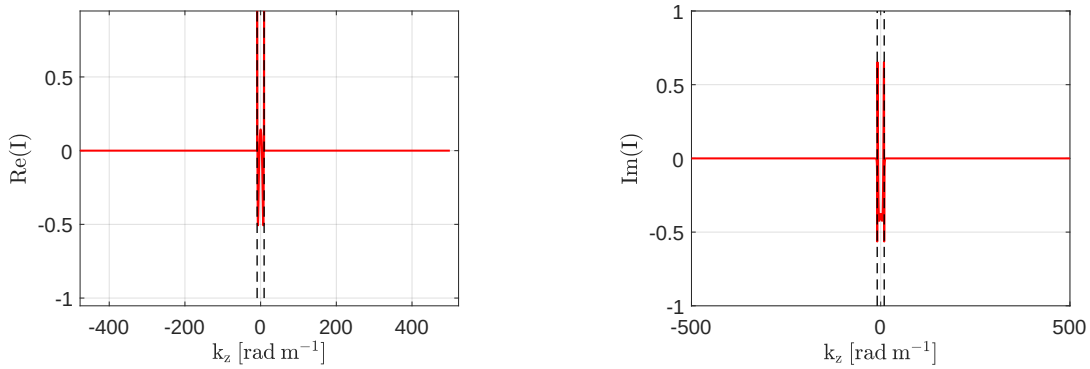

Figure D.11: Values of $I(k_z)$ for $k_z \in [-k_z^{max}, k_z^{max}]$: (a) real part and (b) imaginary part at a frequency $f = 500\,\text{Hz}$ and for a source position defined by $\left(r_0 = 0.7\,\text{m}, \theta_0 = \frac{\pi}{2}, z_0 = 0.5\,\text{m}\right)$. The observation point located at $(r = 0.5\,\text{m}, \theta = 0, z = 0.5\,\text{m})$ and the dashed black lines correspond to values of the acoustic wavenumber at the considered frequency.

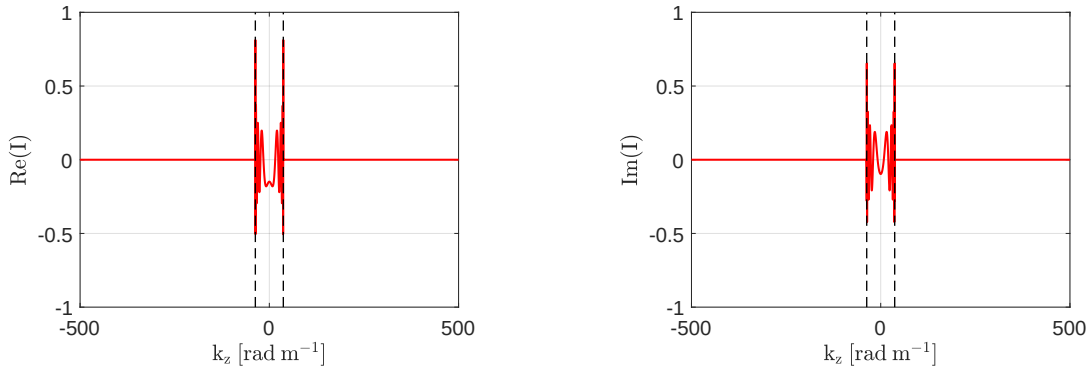

Figure D.12: Values of $I(k_z)$ for $k_z \in [-k_z^{max}, k_z^{max}]$: (a) real part and (b) imaginary part at a frequency $f = 2000\,\text{Hz}$ and for a source position defined by $\left(r_0 = 0.7\,\text{m}, \theta_0 = \frac{\pi}{2}, z = 0.5\,\text{m}\right)$. The observation point located at $(r = 0.5\,\text{m}, \theta = 0, z_0 = 0.5\,\text{m})$ and the dashed black lines correspond to values of the acoustic wavenumber at the considered frequency.

integrate over the wavenumber domain $[-k_0, k_0]$. Thus Eq. (5.30) can be estimated with the following equation

$$p(\mathbf{x}_\sigma) \approx -\frac{1}{2\pi^2} \sum_{n=-\infty}^{+\infty} e^{in\theta_\sigma} \cos(n\theta_0) \int_{-k_0}^{+k_0} \frac{1}{k_r r_\sigma} \frac{H_n(k_r r_0)}{H_n'(k_r r_\sigma)} e^{ik_z(z_\sigma - z_0)} dk_z \tag{D.2}$$

Cette thèse est accessible à l'adresse : https://theses.insa-lyon.fr/publication/2022ISAL0077/these.pdf
© [A.D. Pouye], [2022], INSA Lyon, tous droits réservés

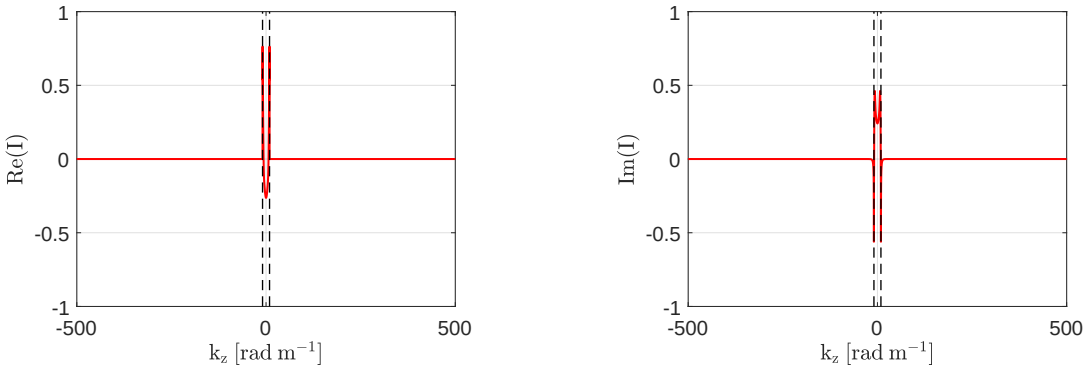

(a) (b)

Figure D.13: Values of $I(k_z)$ for $k_z \in [-k_z^{max}, k_z^{max}]$: (a) real part and (b) imaginary part at a frequency $f = 500\,\text{Hz}$ and for a source position defined by $\left(r_0 = 0.7\,\text{m}, \theta_0 = \frac{\pi}{2}, z_0 = 0.5\,\text{m}\right)$. The observation point located at $\left(r = 0.5\,\text{m}, \theta = \frac{\pi}{2}, z = 0.5\,\text{m}\right)$ and the dashed black lines correspond to values of the acoustic wavenumber at the considered frequency.

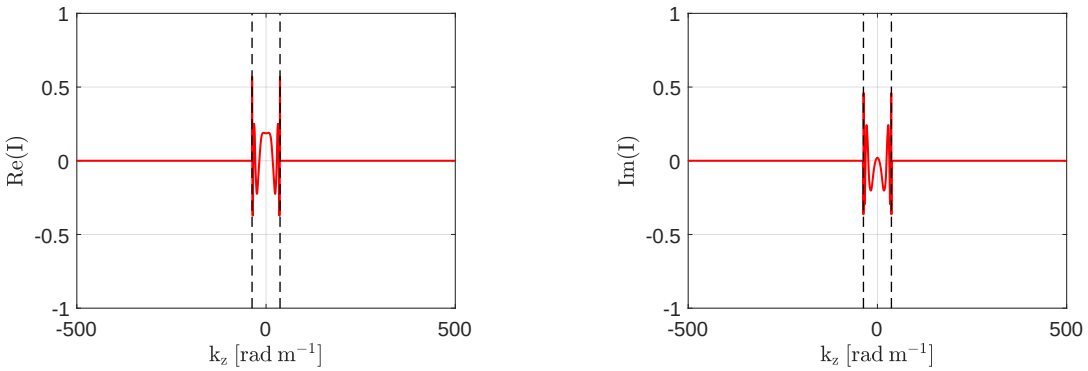

(a) (b)

Figure D.14: Values of $I(k_z)$ for $k_z \in [-k_z^{max}, k_z^{max}]$: (a) real part and (b) imaginary part at a frequency $f = 2000\,\text{Hz}$ and for a source position defined by $\left(r_0 = 0.7\,\text{m}, \theta_0 = \frac{\pi}{2}, z_0 = 0.5\,\text{m}\right)$. The observation point located at $\left(r = 0.5\,\text{m}, \theta = \frac{\pi}{2}, z = 0.5\,\text{m}\right)$ and the dashed black lines correspond to values of the acoustic wavenumber at the considered frequency.

Cette thèse est accessible à l'adresse : https://theses.insa-lyon.fr/publication/2022ISAL0077/these.pdf
© [A.D. Pouye], [2022], INSA Lyon, tous droits réservés

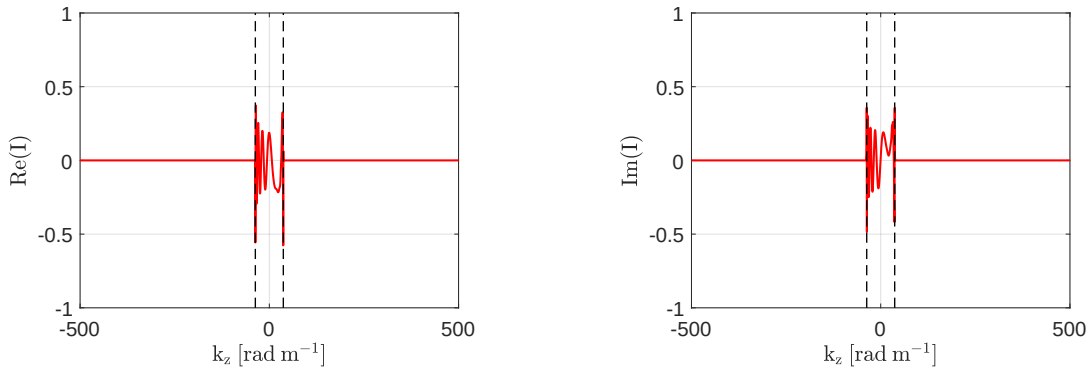

Figure D.15: Values of $I(k_z)$ for $k_z \in [-k_z^{max}, k_z^{max}]$: (a) real part and (b) imaginary part at a frequency $f = 2000\,\text{Hz}$ and for a source position defined by $\left(r_0 = 0.7\,\text{m}, \theta_0 = \frac{\pi}{3}, z_0 = 0.5\,\text{m}\right)$. The observation point located at $\left(r = 0.5\,\text{m}, \theta = \frac{\pi}{2}, z = 0.75\,\text{m}\right)$ and the dashed black lines correspond to values of the acoustic wavenumber at the considered frequency.

Cette thèse est accessible à l'adresse : https://theses.insa-lyon.fr/publication/2022ISAL0077/these.pdf
© [A.D. Pouye], [2022], INSA Lyon, tous droits réservés

D.2.2 Validation with OpenBEM

In this section, we aim at validating the three dimensional transfer functions established in Chapter 5 by comparing the results to those yielded by OpenBEM. In order to do so, a comparison between the magnitudes and phases of the analytical results and the numerical ones (OpenBEM) is proposed for different source positions, frequencies and configurations. Fig. D.16 shows the mesh generated with *Gmsh 2.2*[2].

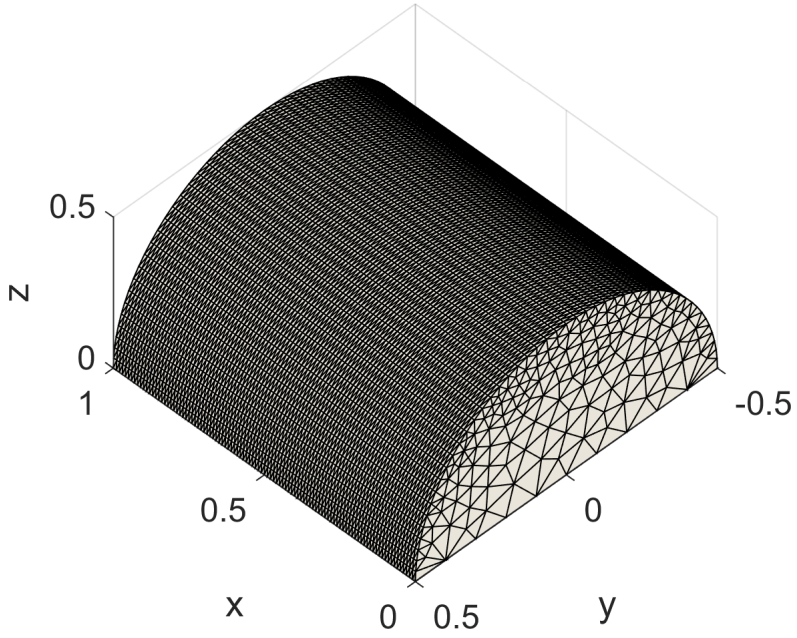

Figure D.16: Generated mesh for OpenBEM computations.

Fig. D.17 shows the results for a configuration where the source position and the observation points are on the same section/plane for three different frequencies. In Fig. D.18, the source and the observation points are not on the same section. Fig. D.19 shows the results for two frequencies and a configuration where source and observation are on different planes and Fig. D.20 shows the results for one frequency and another source-observation points configuration.

2 Gmsh is an open source 3D finite element mesh generator with a built-in CAD engine and post-processor [40].

Cette thèse est accessible à l'adresse : https://theses.insa-lyon.fr/publication/2022ISAL0077/these.pdf
© [A.D. Pouye], [2022], INSA Lyon, tous droits réservés

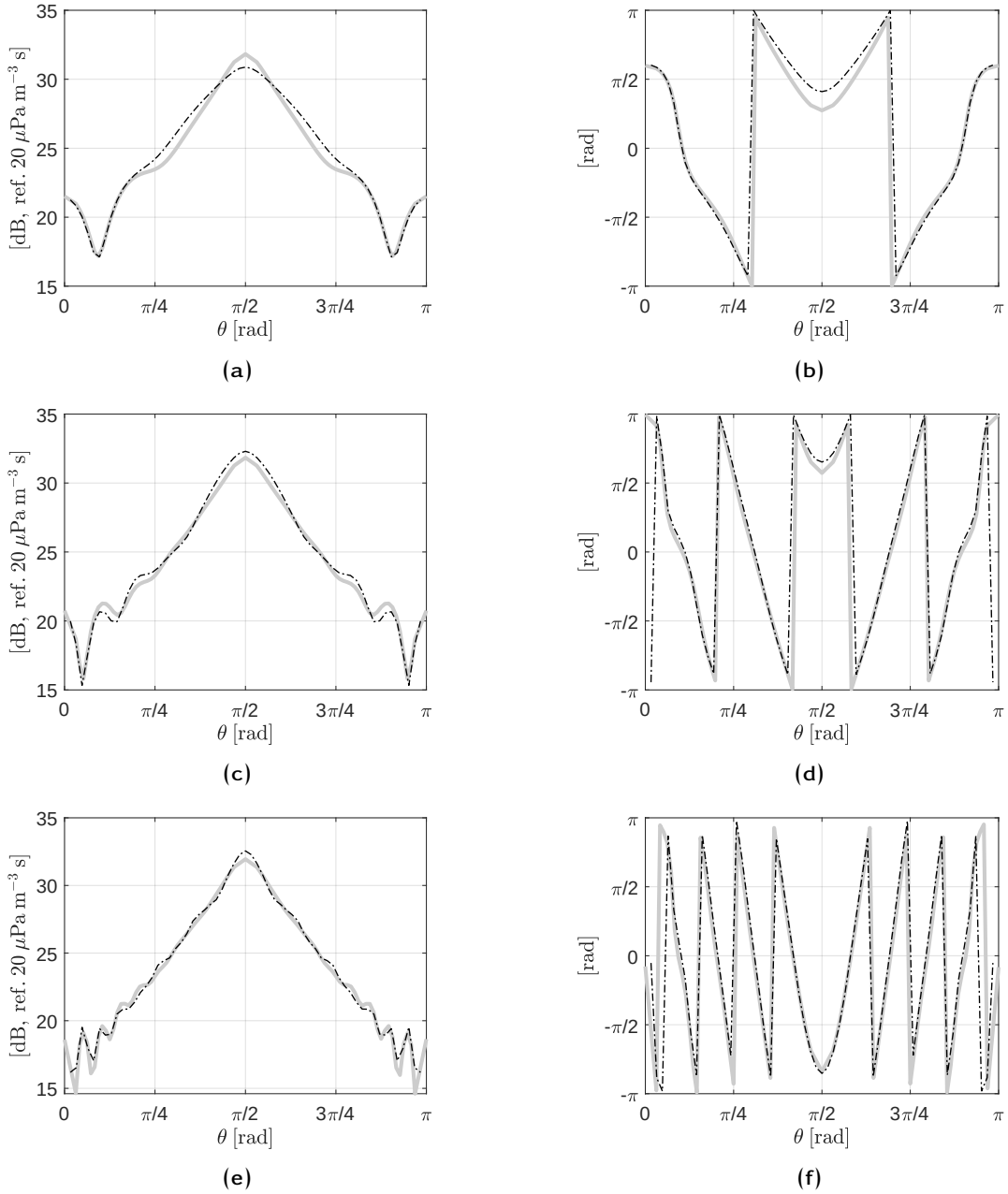

Figure D.17: Comparison between the magnitudes ((a), (c) and (e)) and phases ((b), (d) and (f)) of the transfer functions obtained with OpenBEM (gray continuous line) and those obtained using the developed analytical solution (dash-dotted black line) for one position of the unit amplitude monopole source $\left(r_0 = 0.6\,\text{m}, \theta_0 = \frac{\pi}{2}, z_0 = 0.5\,\text{m}\right)$ and at three different frequencies. (a) and (b): $f = 500\,\text{Hz}$; (c) and (d): $f = 1000\,\text{Hz}$ and (e) and (f): $f = 2000\,\text{Hz}$. The observation points are on the same section as the source, i.e. $z = z_0$.

Cette thèse est accessible à l'adresse : https://theses.insa-lyon.fr/publication/2022ISAL0077/these.pdf
© [A.D. Pouye], [2022], INSA Lyon, tous droits réservés

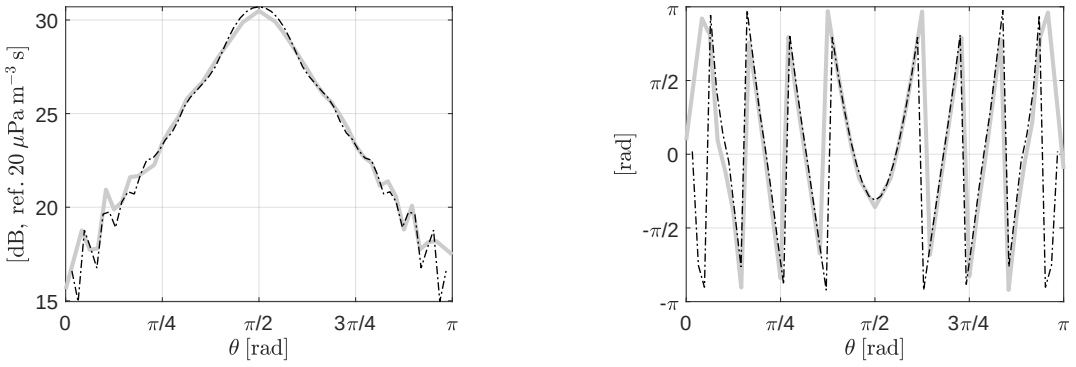

Figure D.18: Comparison between the magnitudes (a) and phases (b) of the transfer functions obtained with OpenBEM (gray continuous line) and those obtained using the developed analytical solution (dash-dotted black line) for one position of the unit amplitude monopole source $\left(r_0 = 0.6\,\mathrm{m}, \theta_0 = \frac{\pi}{2}, z_0 = 0.5\,\mathrm{m}\right)$ and at the frequency $f = 2000\,\mathrm{Hz}$. The observation points are on a different section from the source's plane/section, i.e. $|z - z_0| = 0.1\,\mathrm{m}$.

Cette thèse est accessible à l'adresse : https://theses.insa-lyon.fr/publication/2022ISAL0077/these.pdf
© [A.D. Pouye], [2022], INSA Lyon, tous droits réservés

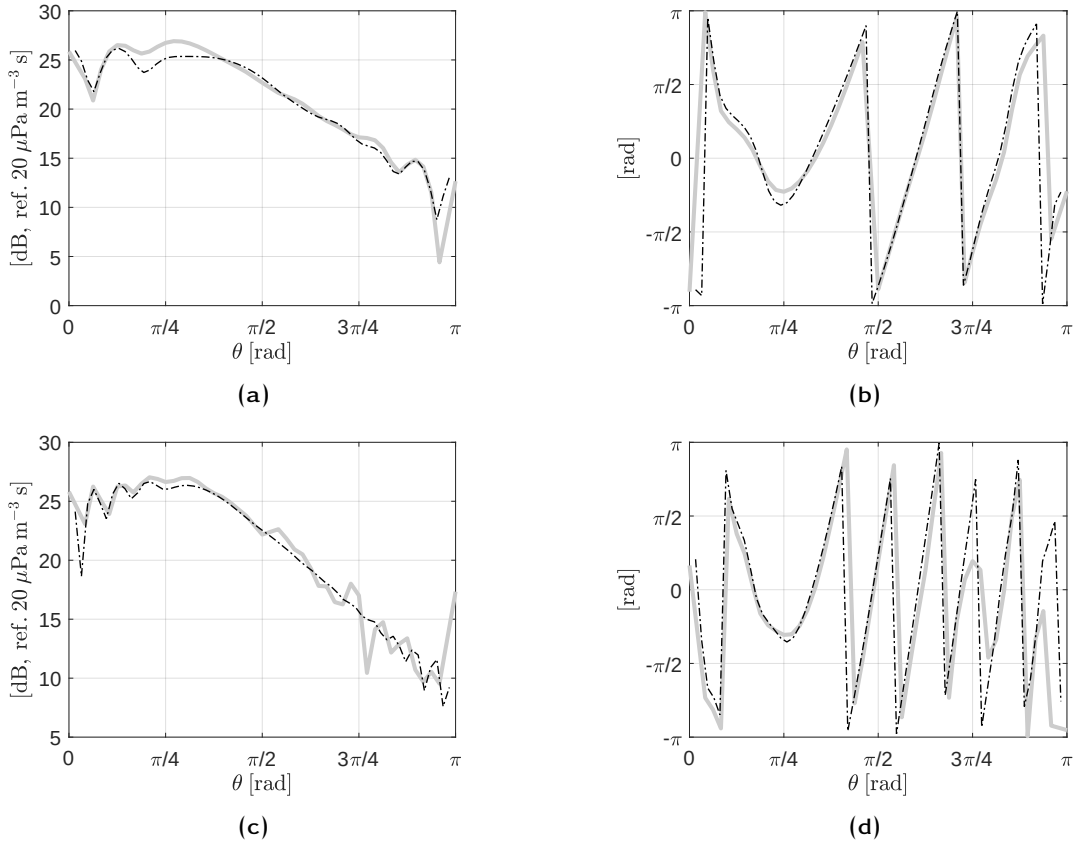

Figure D.19: Comparison between the magnitudes ((a), (c) and (e)) and phases ((b), (d) and (f)) of the transfer functions obtained with OpenBEM (gray continuous line) and those obtained using the developed analytical solution (dash-dotted black line) for one position of the unit amplitude monopole source $\left(r_0 = 0.6\,\mathrm{m}, \theta_0 = \frac{\pi}{4}, z_0 = 0.5\,\mathrm{m}\right)$ and at two different frequencies. (a) and (b): $f = 1000\,\mathrm{Hz}$ and (c) and (d): $f = 2000\,\mathrm{Hz}$. The observation points are on a different section from the source's, i.e. $|z - z_0| = 0.3\,\mathrm{m}$.

Cette thèse est accessible à l'adresse : https://theses.insa-lyon.fr/publication/2022ISAL0077/these.pdf
© [A.D. Pouye], [2022], INSA Lyon, tous droits réservés

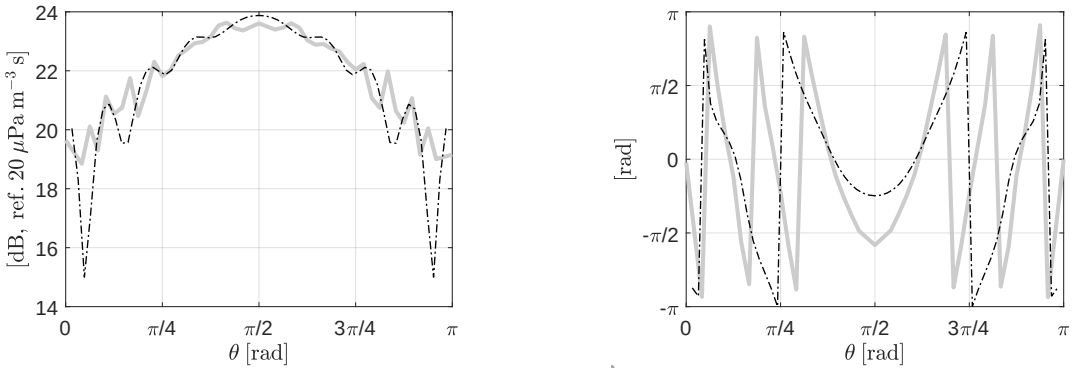

Figure D.20: Comparison between the magnitudes (a) and phases (b) of the transfer functions obtained with OpenBEM (gray continuous line) and those obtained using the developed analytical solution (dash-dotted black line) for one position of the unit amplitude monopole source $\left(r_0 = 1\,\text{m}, \theta_0 = \frac{\pi}{2}, z_0 = 0.5\,\text{m}\right)$ and at the frequency $f = 2000\,\text{Hz}$. The observation points are on a different section from the source's and close to the edge, i.e. $|z - z_0| = 0.4\,\text{m}$.

Cette thèse est accessible à l'adresse : https://theses.insa-lyon.fr/publication/2022ISAL0077/these.pdf
© [A.D. Pouye], [2022], INSA Lyon, tous droits réservés

Cette thèse est accessible à l'adresse : https://theses.insa-lyon.fr/publication/2022ISAL0077/these.pdf
© [A.D. Pouye], [2022], INSA Lyon, tous droits réservés

E RÉSUMÉ ÉTENDU EN FRANÇAIS

E.1 Contexte de la thèse 181
E.2 Technique de balayage de source 183
E.3 Application à des panneaux plans 186
E.4 Extension à des panneaux courbes 188
E.5 Conclusions générales 189

E.1 CONTEXTE DE LA THÈSE

De nos jours, dans le cadre du développement de moyens de transport plus durables, de nouveaux matériaux généralement très légers avec de bonnes propriétés mécaniques se répandent très rapidement. Cependant, ces nouveaux matériaux ont souvent des propriétés acoustiques très médiocres. Afin d'améliorer les propriétés acoustiques de ces derniers, il est nécessaire de déterminer expérimentalement leur comportement vibroacoustique lorsqu'ils sont soumis à des excitations aléatoires telles que l'excitation induite par une couche limite dans l'industrie du transport aéronautique. Il existe actuellement des installations expérimentales permettant de déterminer les propriétés vibroacoustiques de telles structures mais celles-ci sont souvent très coûteuses et la reproductibilité des mesures effectuées dans ces installations peut être remise en question, rendant difficile la comparaison de différentes solutions. Il est donc d'un intérêt considérable de disposer d'un outil ou d'un procédé expérimental pouvant être utilisé lors de la phase de conception des ouvrages considérés et permettant d'évaluer avec

Cette thèse est accessible à l'adresse : https://theses.insa-lyon.fr/publication/2022ISAL0077/these.pdf
© [A.D. Pouye], [2022], INSA Lyon, tous droits réservés

précision et à moindre coût les propriétés vibroacoustiques. Toutes ces raisons ont donné naissance au projet VIRTECH (VIRTualisation de moyens Expérimentaux en vibro-aCoustique par syntHèse de champ de pression) financé par l'ANR [1]. L'un des principaux objectifs de VIRTECH est l'optimisation de réseaux de sources pour synthétiser un champ de pression pariétal ayant les caractéristiques d'un champ acoustique diffus ou d'une couche limite turbulente sur la surface d'une structure donnée. Puis, en exploitant le phénomène de filtrage des structures dans le domaine des nombres d'onde, il s'agira de déterminer leurs réponses vibroacoustiques par rapport au champ excitateur. L'optimisation portera sur différents critères : rapidité de mise en œuvre, résolution spatiale, sensibilité aux erreurs, coût et reproductibilité. Un autre objectif du projet VIRTECH consiste à identifier les composantes utiles du champ acoustique par des mesures directes à l'aide de microphones et par des mesures indirectes en examinant le comportement vibroacoustique de la structure testée complétée par une analyse d'un modèle numérique du champ de pression.

Le travail présenté dans cette thèse s'inscrit dans le volet du projet VIRTECH qui vise à optimiser les réseaux de sources pour la synthèse d'excitations aléatoires afin de déterminer le comportement vibroacoustique des structures sous ces champs de pression aléatoires à travers les réponses vibratoires et acoustiques avec une attention particulière porté au champ acoustique diffus et à la couche limite turbulente. Comme indiqué précédemment, la caractérisation expérimentale des structures sous excitations stochastiques intéresse beaucoup de chercheurs ainsi que l'industrie du transport pour des raisons de confort acoustique principalement. L'objectif de ce travail de recherche est de mettre en place un procédé expérimental permettant de déterminer les réponses vibroacoustiques de structures à l'aide de la méthode de balayage de source introduite il y a quelques années.

1 Agence Nationale de la Recherche, en France

Cette thèse est accessible à l'adresse : https://theses.insa-lyon.fr/publication/2022ISAL0077/these.pdf
© [A.D. Pouye], [2022], INSA Lyon, tous droits réservés

E.2 TECHNIQUE DE BALAYAGE DE SOURCE

Cette partie sera consacrée à la description de la méthode proposée appelée méthode de balayage de source ou *source scanning technique* (SST) en anglais.
L'approche proposée est basée sur la formulation mathématique du problème dans le domaine des nombres d'onde. Cette formulation est très appropriée car elle permet, à travers l'Eq. (E.1), une séparation explicite des contributions de l'excitation *via* l'interspectre de pression pariétale $S_{p_b p_b}(\mathbf{k}, \omega)$ de celles du comportement vibroacoustique de la structure *via* les fonctions de sensibilité $H_\alpha(\mathbf{x}, \mathbf{k}, \omega)$.

$$S_{\alpha\alpha'}(\mathbf{x}, \omega) = \frac{1}{4\pi^2} \iint_{-\infty}^{+\infty} H_\alpha(\mathbf{x}, \mathbf{k}, \omega)\, S_{p_b p_b}(\mathbf{k}, \omega)\, H^*_{\alpha'}(\mathbf{x}, \mathbf{k}, \omega)\, \mathrm{d}\mathbf{k} \tag{E.1}$$

Considérons une onde plane pariétale unitaire définie par le vecteur d'onde $\mathbf{k}$ et la fréquence angulaire ω. La pression à la surface de la structure qui sera appelée surface de reproduction est simplement donnée par $p(\mathbf{x}, \mathbf{k}, \omega) = \mathrm{e}^{-\mathrm{i}\mathbf{k}\mathbf{x}}$. Le processus de la méthode de balayage de source peut être divisé en quatre grandes étapes qui permettront de synthétiser le champ de pression cible à partir des positions prédéfinies de la source monopolaire.

1. **Définition de la pression cible :** on suppose que la surface de reproduction est régulièrement discrétisée en une grille de P points d'observation et on définit le vecteur pression cible comme le vecteur dont les composantes correspondent à la pression d'une onde plane pariétale unitaire aux points P. L'espacement entre les points doit être suffisamment petit pour décrire la variation spatiale de l'onde plane pariétale.

2. **Détermination de la matrice des fonctions de transfert :** on détermine les fonctions de transfert (G_{ps}) entre les positions de la source $s \in [1, S]$ et les points d'observation $p \in [1, P]$ sur la structure comme indiqué sur la Fig. 2.3, puis on définit la matrice des fonctions de transfert $\mathbf{G}$ comme la matrice ayant les fonctions G_{ps} comme composantes.

Cette thèse est accessible à l'adresse : https://theses.insa-lyon.fr/publication/2022ISAL0077/these.pdf
© [A.D. Pouye], [2022], INSA Lyon, tous droits réservés

3. **Calcul du vecteur des amplitudes de la source q** en inversant l'équation matricielle suivante

$$\mathbf{Gq} = \mathbf{p} \tag{E.2}$$

qui peut être réécrite explicitement comme

$$\sum_{s=1}^{S} G_{ps}(\omega)\, q_s(\mathbf{k}, \omega) = p_p(\mathbf{k}, \omega),\ \forall p \in [1, P] \tag{E.3}$$

où $q_s(\mathbf{k}, \omega)$ est l'amplitude de la source à la position s et $p_p(\mathbf{k}, \omega) = \mathrm{e}^{-\mathrm{i}\, pak_x x_p + k_y y_p}$ représente la pression cible au point d'observation p dont les coordonnées sont x_p et y_p sur la structure.

Lorsque le nombre de points d'observation P est inférieur au nombre de positions de source S, le système de l'Eq. (E.2) est sous-déterminé et a un nombre infini de solutions. Cependant, lorsque $P > S$, le système est surdéterminé et n'a pas une seule solution exacte. Néanmoins, une solution minimisant l'erreur entre la pression cible et celle synthétisée peut être déterminée. La matrice **G** est alors rectangulaire, l'Eq. (E.2) est résolu au sens des moindres carrés comme suit

$$\mathbf{q} = \mathbf{G}^{\dagger}\mathbf{p} \tag{E.4}$$

La dague dans l'Eq. (E.4) indique la pseudo-inverse de Moore-Penrose. La reproduction d'un champ de pression cible à l'aide d'un réseau de sources acoustiques est donc un problème inverse qui conduit à certains problèmes de conditionnement.

4. **Synthèse du champ de pression cible et de la fonction de sensibilité :** afin d'évaluer la qualité du champ de pression reconstruit, on considère Q points sur la surface de reproduction. Ces Q points doivent être différents des P points de référence afin d'estimer la capacité de la technique à reproduire correctement le

Cette thèse est accessible à l'adresse : https://theses.insa-lyon.fr/publication/2022ISAL0077/these.pdf
© [A.D. Pouye], [2022], INSA Lyon, tous droits réservés

champ de pression entre les points de référence. Une fois que la matrice de la fonction de transfert $\hat{\mathbf{G}}$ entre les S positions source et les Q points de reconstruction est déterminée, le vecteur de la pression reconstruite $\hat{\mathbf{p}}$ peut-être calculé avec l'expression suivante : $\hat{\mathbf{p}} = \hat{\mathbf{G}}\mathbf{q}$. On utilisera cette expression dans la suite pour estimer l'efficacité de la méthode et pour définir les paramètres optimaux de l'antenne synthétique. Les fonctions de sensibilité sont données par l'équation suivante

$$H_\alpha(\mathbf{x}, \mathbf{k}, \omega) = \sum_{s=1}^{S} q_s(\mathbf{k}, \omega) \Gamma^s_{alpha}(\mathbf{x}, \omega) \tag{E.5}$$

où $\alpha = (v, p, v_0)$ et $\Gamma^s_\alpha(\mathbf{x}, \omega)$ représente la réponse fréquentielle entre le point $\mathbf{x}$ et la source à la position s et est défini comme la réponse α au point $\mathbf{x}$ lorsque la source est située au point s.

L'étape 2 est généralement réalisée une seule fois alors que les autres étapes peuvent être répétées pour couvrir l'ensemble des vecteurs d'onde d'intérêt dans l'Eq. (E.1). Une fois que les fonctions de sensibilité ont été déterminées à l'aide de l'Eq. (E.5) pour l'ensemble de vecteurs d'onde d'intérêt, la réponse de la structure à l'excitation stochastique peut être estimée avec l'Eq. (E.6) et le modèle du champ de pression pariétal correspondant, champ acoustique diffus ou couche limite turbulente.

$$S_{\alpha\alpha'}(\mathbf{x}, \omega) \approx \frac{1}{4\pi^2} \sum_{\mathbf{k}\in\Omega_\mathbf{k}} H_\alpha(\mathbf{x}, \mathbf{k}, \omega) S_{p_b p_b}(\mathbf{k}, \omega) H^*_{\alpha'}(\mathbf{x}, \mathbf{k}, \omega) \delta\mathbf{k} \tag{E.6}$$

Naturellement, il existe des paramètres de conception qui sont inhérents à cette approche et dont les valeurs doivent être soigneusement choisies pour un bon processus de reproduction. Ces paramètres sont

- le nombre d'onde de coupure $\bar{k}$ qui permet de définir l'ensemble des vecteurs d'onde $\Omega_\mathbf{k}$ sur lesquels on a une synthèse précise de la réponse de la structure,

Cette thèse est accessible à l'adresse : https://theses.insa-lyon.fr/publication/2022ISAL0077/these.pdf
© [A.D. Pouye], [2022], INSA Lyon, tous droits réservés

- la distance d_m entre deux positions monopolaires adjacentes (voir Fig. 2.5), et
- la distance d entre la structure et le réseau de monopoles qui sera déterminée par une analyse du conditionnement de la matrice de transfert $\mathbf{G}$ et l'erreur quadratique moyenne relative entre pression pariétale cible et celle synthétisée. Voir Fig. 2.5 pour une représentation de cette distance.

E.3 APPLICATION À DES PANNEAUX PLANS

La méthode de balayage de source a été introduite il y a quelques années nécessite des validations qualitatives et quantitatives supplémentaires. C'est le premier des enjeux de cette thèse : valider numériquement et expérimentalement la méthode de balayage de source sur des panneaux plans par des mesures vibroacoustiques et par une comparaison à des mesures issues d'installations comme les chambres réverbérantes pour des excitations de type champ acoustique diffus ou les tunnels aérodynamique pour des excitations de type couche limite turbulente.

Dans un premier temps, une brève revue bibliographique des réponses vibroacoustiques théoriques des panneaux plans sous excitations aléatoires a été présentée. Les grandeurs d'intérêt étaient la réponse vibratoire et la perte en transmission du panneau soumis à un champ pression aléatoire. Par la suite, des études paramétriques sur le processus de la méthode de balayage de source ont été réalisées afin de déterminer les valeurs optimales des paramètres de l'antenne synthétique pour une synthèse précise. Ces paramètres sont principalement le nombre d'onde de coupure $\bar{k}$ et la distance *interplanaire* d entre le plan du panneau et le plan du réseau synthétique (voir Fig. 2.5).

Dans un second temps, après avoir défini le montage expérimental, nous avons réalisé des mesures issues de l'application expérimentale de la méthode de balayage de source. Ce procédé peut être vu comme une alternative ou complémentaire aux moyens d'essais standards tels que les salles réverbérantes ou les souffleries. Dans la présente étude, notre

Cette thèse est accessible à l'adresse : https://theses.insa-lyon.fr/publication/2022ISAL0077/these.pdf
© [A.D. Pouye], [2022], INSA Lyon, tous droits réservés

attention s'est concentrée sur la validation du processus avec des comparaisons avec des résultats numériques et expérimentaux obtenus dans une salle réverbérante et une soufflerie anéchoïque. Une étude paramétrique basée sur des simulations numériques visant à définir les paramètres idéaux du réseau synthétique de monopoles a été réalisée. Cette étude a permis de définir un intervalle optimal pour la distance entre le panneau plan et le réseau de sources.

La méthode proposée a été appliquée sur un panneau en aluminium simplement appuyé et soumis à une excitation aux deux types d'excitations d'intérêt : le champ acoustique diffus et la couche limite turbulente. La réponse en vitesse à un point donné et la perte de transmission du panneau ont été déterminées. Un robot cartésien $3D$ a été utilisé pour déplacer la source acoustique tandis qu'un robot cartésien $2D$ a été utilisé pour déplacer un réseau linéaire de microphones. Ce système était contrôlé par un script MATLAB qui nous permettait d'automatiser le processus de mesure des fonctions de transfert entre la source (à différentes positions) et les quantités d'intérêt. Pour évaluer la puissance rayonnée pour le calcul de la perte en transmission, la méthode des deux microphones a été utilisée pour estimer la vitesse normale particulaire. Hormis une surestimation des réponses du panneau entre 230 et 300 Hz due au faible rendement de la source monopole et à la courbe de perte en transmission bruitée sous environ 600 Hz résultant de la méthode des deux microphones, il y a un assez bon accord entre les trois types de résultats (numériques, méthode de balayage de source et mesures directes).

Le temps total de mesure des fonctions de transfert nécessaires pour déterminer la réponse en vitesse ainsi que la puissance rayonnée par le panneau est d'environ 60 heures. La mesure des fonctions de transfert nécessaires pour déterminer la puissance rayonnée par le panneau a duré environ 46 heures et a nécessité de mesurer la pression rayonnée et d'estimer la vitesse particulaire à l'aide d'un réseau linéaire de microphone. Ces temps de mesure ne sont cependant pas complètement pénalisant car le processus est entièrement automatisé. L'utilisation de sondes de vitesse particulaire ainsi qu'un plus grand réseau de microphones pourraient réduire considérablement ces temps de mesure. De plus, par rapport aux installations standards, le procédé fournit les fonctions

Cette thèse est accessible à l'adresse : https://theses.insa-lyon.fr/publication/2022ISAL0077/these.pdf
© [A.D. Pouye], [2022], INSA Lyon, tous droits réservés

de sensibilité qui peuvent donner des indications sur la façon dont la structure filtre l'excitation aléatoire.

E.4 EXTENSION À DES PANNEAUX COURBES

Après l'application de la méthode de balayage de source sur des panneaux plans, l'extension de la de celle-ci à des panneaux courbes été étudiée. Les solutions analytiques au problème de Helmholtz défini en Eq. (5.1) ont été établis pour le cas bidimensionnel ainsi que pour le cas tridimensionnel. Ces solutions ont été validées à l'aide d'OpenBEM, un ensemble de scripts MATLAB permettant de résoudre des problèmes avec la méthode des éléments de frontières. Une fois la validation effectuée, des études paramétriques ont été réalisées afin de déterminer les paramètres optimaux de l'antenne synthétique pour une bonne synthèse en utilisant la méthode de balayage de source dans les cas bidimensionnel et tridimensionnel. Les études paramétriques nous ont permis d'établir le nombre minimum de sources monopolaires par plus petite longueur d'onde à 4 monopoles qui est le même critère que celui établi pour les panneaux plans. Deux configurations différentes de géométrie structure-réseau de monopoles ont été étudiées : la configuration géométrique conforme (l'antenne de monopoles a une géométrie similaire à celle de la structure étudiée) et la configuration géométrique non-conforme (l'antenne de monopoles a une géométrie différente de celle de la structure étudiée). Il a été constaté que la configuration conforme est plus adaptée au processus de balayage de source que la configuration non conforme. Enfin, il a été montré que plus le réseau de monopoles est proche de la structure, plus le processus de reproduction est précis. Une fois que ces études analytiques et numériques ont été effectuées, il a fallu passer à l'étape expérimentale. Les dispositifs expérimentaux (microphones, source monopolaire, robot articulé) ainsi que le montage expérimental ont été présentés. Les mesures ont été réalisées avec un système d'acquisition OROS installé en salle de contrôle. La validation expérimentale des fonctions de transfert étudiées au chapitre 5 (voir Eq. (5.16)

Cette thèse est accessible à l'adresse : https://theses.insa-lyon.fr/publication/2022ISAL0077/these.pdf
© [A.D. Pouye], [2022], INSA Lyon, tous droits réservés

et Eq. (5.30)) a ensuite été effectuée pour le cas bidimensionnel ainsi que pour le cas tridimensionnel. L'implémentation expérimentale du processus de balayage de source a été réalisée pour le cas bidimensionnel. Les mesures ont été comparées aux résultats analytiques avec un très bon accord.

E.5 CONCLUSIONS GÉNÉRALES

Cette thèse s'est concentrée sur la reproduction des réponses vibroacoustiques de structures soumis à des champs de pression aléatoires à l'aide de la technique de balayage de source. Cette méthode utilise une seule source monopolaire, déplacée à un nombre arbitraire de positions afin de mimer l'effet d'un réseau complet de sources, comme méthode alternative ou complémentaire aux moyens d'essais habituels tels que les chambres réverbérantes et les souffleries anéchoïques qui sont parfois très coûteux, difficiles à mettre en œuvre et manquent souvent de reproductibilité. Les excitations aléatoires d'intérêt, le champ acoustique diffus et la couche limite turbulente, ont été considérées stationnaires temporellement et homogènes spatialement. Nous nous sommes intéressés à deux types de structures : les panneaux plans et les panneaux courbes. Dans un premier temps, une validation de la méthode de balayage de source sur des panneaux plans a été effectuée. Par la suite, la méthode proposée a été étendue aux panneaux courbes. Concernant les panneaux courbes, notre attention s'est concentrée sur la validation du processus avec des comparaisons avec des résultats numériques et expérimentaux obtenus dans des installations d'essais telles que les salles réverbérantes et les souffleries anéchoïques. Une étude paramétrique basée sur des simulations numériques visant à définir les paramètres optimaux du réseau de sources virtuel a été réalisée : il a été établi que pour un processus de reproduction fidèle, il faut au moins 4 positions monopolaires par plus petite longueur d'onde à synthétiser. Cette étude a permis de définir un intervalle optimal pour la distance entre le panneau et le réseau de sources, dans lequel la pression synthétisée est en bon accord avec le champ de pression cible,

Cette thèse est accessible à l'adresse : https://theses.insa-lyon.fr/publication/2022ISAL0077/these.pdf
© [A.D. Pouye], [2022], INSA Lyon, tous droits réservés

permettant une bonne reproduction de la réponse vibroacoustique de la structure considérée. Une étude de cas impliquant un panneau plan en aluminium en appuis simples et soumis à une excitation de types champ acoustique diffus et couche limite turbulente a été proposée. La réponse en vitesse en un point donné et la puissance rayonnée par le panneau ont été estimées. Un robot cartésien $3D$ a été utilisé pour déplacer la source monopolaire tandis qu'un robot cartésien $2D$ a été utilisé pour déplacer le réseau linéaire de microphones. Ce système était contrôlé par un script MATLAB qui nous a permis d'automatiser le processus de mesure des fonctions de transfert entre la source (à différentes positions) et le réseau de microphones pour déterminer les fonctions de sensibilité et, par la suite, les réponses vibroacoustiques. Pour évaluer la puissance rayonnée pour le calcul de la perte en transmission, la méthode des microphones a été utilisée pour estimer la vitesse normale des particulaire. Un très bon accord entre les trois types de résultats (numériques, méthode de balayage de source et mesures directes) a été mis en évidence en Sec. 4.2.

Une fois l'étude des panneaux plans terminées, nous sommes passés à l'extension de la méthode de balayage de source à des panneaux courbes. Au meilleur de notre connaissance, les fonctions de transfert analytiques entre une position de monopole et un point sur un panneau courbe comme présenté dans la description du problème en Sec. 5.1 et la Fig. 5.1 n'avaient pas encore été établies. En conséquence, un travail préliminaire sur la détermination de ces fonctions de transfert a été mené pour établir leur forme analytique. Une fois ces fonctions de transfert validées numériquement à l'aide d'OpenBEM, nous avons étudié les paramètres optimaux du réseau de monopoles pour un processus de synthèse précis grâce à des études paramétriques. Comme pour les panneaux plans, il a également été établi qu'il fallait au moins 4 positions monopolaires par plus petite longueur d'onde pour que le processus de reproduction soit précis. Nous avons également étudié deux configurations géométriques réseau de sources - structure : configuration conforme (le réseau de monopoles a une géométrie similaire à celle de la structure étudiée) et non conforme (le réseau de monopoles a une géométrie différente de celle de la structure étudiée). Les résultats ont montré que la configuration

Cette thèse est accessible à l'adresse : https://theses.insa-lyon.fr/publication/2022ISAL0077/these.pdf
© [A.D. Pouye], [2022], INSA Lyon, tous droits réservés

conforme est plus adaptée pour une bonne synthèse avec la méthode de balayage de source. Ensuite, nous avons conçu un dispositif expérimental pour l'implémentation du processus sur des panneaux courbes. Afin d'automatiser le processus, la source monopolaire a été fixée sur un bras robotique articulé. Les mesures ont été effectuées à l'aide d'un système d'acquisition OROS comme pour les panneaux plans et l'ensemble des opérations de mesure était géré depuis une salle de contrôle. Les fonctions de transfert bidimensionnelles et tridimensionnelles mesurées ont été comparées aux fonctions de transfert analytiques. Un bon accord entre les deux types de résultats a été établi, se validant ainsi mutuellement. Enfin, le processus de balayage de source a été implémenté expérimentalement dans le cas bidimensionnel et les résultats ont été très probants comme on peut le constater en Sec. 6.2.1.2.

Plusieurs perspectives sont désormais envisagées. Le processus de balayage de source ayant été validé et automatisé, il pourra être utilisé dans le futur pour comparer les réponses de différents panneaux complexes sous excitation de types champ acoustique diffus ou couche limite turbulente. L'excitation considérée étant représentée par un modèle, la comparaison entre différents panneaux ne sera pas perturbée par les incertitudes et les bruits de fond liés à l'excitation. De plus, l'analyse des fonctions de sensibilité mesurées sera utile pour extraire les phénomènes physiques contribuant au rayonnement sonore des panneaux. Comme on peut le remarquer, la mise en œuvre expérimentale tridimensionnelle du processus de balayage de source à large bande dans le cas des panneaux courbes n'a pas été effectuée en raison de mesures chronophages induites par un grand nombre de positions de source sur la surface de la structure considéré, voir Tableau 5.2 pour les dimensions de la structure. Même si les résultats tridimensionnels expérimentaux de la méthode de balayage de source devraient être, en théorie, proches des résultats analytiques, il serait intéressant de les valider dans des travaux futurs. De plus, il est nécessaire d'avoir un contrôle approprié sur les conditions aux limites mécaniques de la structure d'intérêt afin de prédire avec précision les réponses vibroacoustiques de panneaux courbes aux champs de pression aléatoires synthétisés. Une autre piste pour de futures études dans cette thématique serait la mise

Cette thèse est accessible à l'adresse : https://theses.insa-lyon.fr/publication/2022ISAL0077/these.pdf
© [A.D. Pouye], [2022], INSA Lyon, tous droits réservés

en place d'une méthodologie pour obtenir de bonnes conditions limites mécaniques pour une bonne maîtrise de ces dernières.

Cette thèse est accessible à l'adresse : https://theses.insa-lyon.fr/publication/2022ISAL0077/these.pdf
© [A.D. Pouye], [2022], INSA Lyon, tous droits réservés

BIBLIOGRAPHY

Cette thèse est accessible à l'adresse : https://theses.insa-lyon.fr/publication/2022ISAL0077/these.pdf
© [A.D. Pouye], [2022], INSA Lyon, tous droits réservés

Cette thèse est accessible à l'adresse : https://theses.insa-lyon.fr/publication/2022ISAL0077/these.pdf
© [A.D. Pouye], [2022], INSA Lyon, tous droits réservés

[1] I. 15186-1:2000. *Acoustics – Measurement of sound insulation in buildings and of building elements using sound intensity – Part 1: Laboratory measurements*. Standard. Geneva, CH: International Organization for Standardization, 2000 (cit. on p. 22).

[2] M. Abramowitz and I. A. Stegun, eds. *Handbook of Mathematical Functions: with Formulas, Graphs, and Mathematical Tables*. English. 0009-Revised edition. New York, NY: Dover Publications, June 1965 (cit. on p. 90).

[3] R. K. Amiet. "Noise due to turbulent flow past a trailing edge." en. In: *Journal of Sound and Vibration* 47.3 (Aug. 1976), pp. 387–393 (cit. on p. 19).

[4] B. Arguillat. "Etude expérimentale et numérique de champs de pression pariétale dans l'espace des nombres d'onde, avec application aux vitrages automobiles." PhD thesis. Ecole Centrale de Lyon, 2006 (cit. on p. 17).

[5] B. Arguillat, D. Ricot, C. Bailly, and G. Robert. "Measured wavenumber: frequency spectrum associated with acoustic and aerodynamic wall pressure fluctuations." eng. In: *The Journal of the Acoustical Society of America* 128.4 (Oct. 2010), pp. 1647–1655 (cit. on p. 17).

[6] M. Aucejo, L. Maxit, and J. L. Guyader. "Experimental simulation of turbulent boundary layer induced vibrations by using a synthetic array." In: *Journal of Sound and Vibration* 331.16 (July 2012), pp. 3824–3843 (cit. on pp. 29, 56, 95).

[7] M. Aucejo, L. Maxit, and J.-L. Guyader. "Source Scanning Technique for Simulating TBL-Induced Vibrations Measurements." In: *Flinovia - Flow Induced Noise and Vibration Issues and Aspects*. Dec. 2014 (cit. on p. 29).

[8] M. Aucejo. "Vibro-acoustique des structures immergées sous écoulement turbulent." PhD thesis. INSA de Lyon, 2010 (cit. on p. 29).

[9] S. W. Autrey. "Passive synthetic arrays." In: *The Journal of the Acoustical Society of America* 84.2 (Aug. 1988), pp. 592–598 (cit. on p. 34).

Cette thèse est accessible à l'adresse : https://theses.insa-lyon.fr/publication/2022ISAL0077/these.pdf
© [A.D. Pouye], [2022], INSA Lyon, tous droits réservés

[10] M. R. Bai, S.-W. Juan, and C.-C. Chen. "Particle velocity estimation based on a two-microphone array and Kalman filter." In: *The Journal of the Acoustical Society of America* 133.3 (Mar. 2013). Publisher: Acoustical Society of America, pp. 1425–1432 (cit. on p. 70).

[11] A. J. Berkhout. "A Holographic Approach to Acoustic Control." In: *J. Audio Eng. Soc* 36.12 (1988), pp. 977–995 (cit. on p. 26).

[12] A. J. Berkhout. "Wave-front synthesis: A new direction in electroacoustics." In: *The Journal of the Acoustical Society of America* 92.4 (Oct. 1992), pp. 2396–2396 (cit. on p. 26).

[13] A. J. Berkhout, D. de Vries, and P. Vogel. "Acoustic control by wave field synthesis." In: *The Journal of the Acoustical Society of America* 93.5 (May 1993), pp. 2764–2778 (cit. on p. 26).

[14] A. Berry, R. Dia, and O. Robin. "A wave field synthesis approach to reproduction of spatially correlated sound fields." In: *The Journal of the Acoustical Society of America* 131.2 (Feb. 2012), pp. 1226–1239 (cit. on pp. 27, 73).

[15] W. V. Bhat. "Flight test measurement of exterior turbulent boundary layer pressure fluctuations on Boeing model 737 airplane." en. In: *Journal of Sound and Vibration* 14.4 (Feb. 1971), pp. 439–457 (cit. on p. 24).

[16] W. V. Bhat and J. F. Wilby. "Interior noise radiated by an airplane fuselage subjected to turbulent boundary layer excitation and evaluation of noise reduction treatments." en. In: *Journal of Sound and Vibration* 18.4 (Oct. 1971), pp. 449–464 (cit. on p. 24).

[17] W. K. Blake. *Mechanics of Flow-Induced Sound and Vibration, Volume 1: General Concepts and Elementary Sources*. en. Academic Press, June 2017 (cit. on pp. 17, 20).

[18] T. Bravo and C. Maury. "The experimental synthesis of random pressure fields: Methodology." In: *The Journal of the Acoustical Society of America* 120.5 (Oct. 2006), pp. 2702–2711 (cit. on pp. 28, 73).

Cette thèse est accessible à l'adresse : https://theses.insa-lyon.fr/publication/2022ISAL0077/these.pdf
© [A.D. Pouye], [2022], INSA Lyon, tous droits réservés

[19] T. Bravo and C. Maury. "A synthesis approach for reproducing the response of aircraft panels to a turbulent boundary layer excitation." In: *The Journal of the Acoustical Society of America* 129.1 (Jan. 2011), pp. 143–153 (cit. on p. 29).

[20] H.-E. de Bree and T. Basten. "Microflown based monopole sound sources for reciprocal measurements." In: *SAE Brasil Noise and Vibration Conference*. SAE International, 2008 (cit. on p. 64).

[21] M. K. Bull. "Wall-Pressure Fluctuations Beneath Turbulent Boundary Layers: Some Reflections on Forty Years of Research." In: *Journal of Sound and Vibration* 190.3 (Feb. 1996), pp. 299–315 (cit. on pp. 18, 21).

[22] M. R. Catlett, J. Forest, J. M. Anderson, and D. Stewart. "Empirical Spectral Model of Surface Pressure Fluctuations beneath Adverse Pressure Gradients." In: *20th AIAA/CEAS Aeroacoustics Conference*. AIAA AVIATION Forum. American Institute of Aeronautics and Astronautics, June 2014 (cit. on p. 19).

[23] J.-D. Chazot, O. Robin, J.-L. Guyader, and N. Atalla. "Diffuse Acoustic Field Produced in Reverberant Rooms: A Boundary Diffuse Field Index." en. In: (June 2016) (cit. on p. 22).

[24] E. Cheney and D. Kincaid. *Numerical Mathematics and Computing*. Cengage Learning, Aug. 2007 (cit. on p. 57).

[25] W. C. Chew. *Waves and Fields in Inhomogeneous Media*. en. IEEE Press, July 1996. ISBN: 978-0-19-859224-2 (cit. on p. 84).

[26] R. K. Cook, R. V. Waterhouse, R. D. Berendt, S. Edelman, and M. C. Thompson. "Measurement of Correlation Coefficients in Reverberant Sound Fields." In: *The Journal of the Acoustical Society of America* 27.6 (Nov. 1955), pp. 1072–1077 (cit. on p. 11).

[27] G. M. Corcos. "Resolution of Pressure in Turbulence." In: *The Journal of the Acoustical Society of America* 35.2 (Feb. 1963), pp. 192–199 (cit. on p. 19).

Cette thèse est accessible à l'adresse : https://theses.insa-lyon.fr/publication/2022ISAL0077/these.pdf
© [A.D. Pouye], [2022], INSA Lyon, tous droits réservés

[28] J. C. Curlander and R. N. McDonough. *Synthetic Aperture Radar: Systems and Signal Processing*. English. 1 edition. New York: Wiley-Interscience, Nov. 1991 (cit. on p. 34).

[29] W. P. J. De Bruijn. "Application of Wave Field Synthesis in Videoconferencing." PhD thesis. Delft University of Technology, 2004 (cit. on p. 26).

[30] A. E90-09. *Standard Test Method for Laboratory Measurement of Airborne Sound Transmission Loss of Building Partitions and Elements*. Standard. West Conshohocken, PA: ASTM International, 2009 (cit. on p. 22).

[31] B. M. Efimtsov. "Characteristics of the field of turbulent wall pressure fluctuations at large reynolds numbers." In: *Soviet Physics Acoustics* (1982) (cit. on p. 20).

[32] S. J. Elliott, C. Maury, and P. Gardonio. "The synthesis of spatially correlated random pressure fields." In: *The Journal of the Acoustical Society of America* 117.3 (Mar. 2005), pp. 1186–1201 (cit. on p. 28).

[33] F. J. Fahy. "On simulating the transmission through structures of noise from turbulent boundary layer pressure fluctuations." In: *Journal of Sound and Vibration* 3.1 (Jan. 1966), pp. 57–81 (cit. on p. 25).

[34] F. J. Fahy. *Foundations of Engineering Acoustics*. en. Elsevier, Sept. 2000 (cit. on p. 54).

[35] F. J. Fahy and P. Gardonio. *Sound and Structural Vibration: Radiation, Transmission and Response*. Anglais. 2nd ed. Amsterdam ; Boston: Academic Press, 2006 (cit. on pp. 35, 52).

[36] F. Fahy. *Sound intensity*. en. Elsevier Applied Science, 1989 (cit. on pp. 38, 153).

[37] F. M. Fazi. "Sound Field Reproduction." PhD thesis. University of Southampton, 2010 (cit. on p. 26).

[38] P. Filippi, A. Bergassoli, D. Habault, and J. P. Lefebvre. *Acoustics: Basic Physics, Theory, and Methods*. English. 1 edition. San Diego: Academic Press, Oct. 1998 (cit. on p. 83).

Cette thèse est accessible à l'adresse : https://theses.insa-lyon.fr/publication/2022ISAL0077/these.pdf
© [A.D. Pouye], [2022], INSA Lyon, tous droits réservés

[39] P.-A. Gauthier. "Synthèse de champs sonores adaptative (Adaptive sound field synthesis)." PhD thesis. Université de Sherbrooke, 2007 (cit. on p. 26).

[40] C. Geuzaine and J.-F. Remacle. "Gmsh: A 3-D finite element mesh generator with built-in pre- and post-processing facilities." In: *International Journal for Numerical Methods in Engineering* 79.11 (Sept. 2009). Publisher: Wiley, pp. 1309–1331 (cit. on p. 175).

[41] P. W. Goodwin. *An in-flight supersonic TBL surface pressure fluctuation model*. Contract No. NAS1-20013 D6-81571. Boeing Document, 1994 (cit. on p. 19).

[42] M. Goody. "Empirical Spectral Model of Surface Pressure Fluctuations." In: *AIAA Journal* 42.9 (2004), pp. 1788–1794 (cit. on p. 19).

[43] S. I. Hayek. "Nearfield Acoustical Holography." en. In: *Handbook of Signal Processing in Acoustics*. Ed. by D. Havelock, S. Kuwano, and M. Vorländer. New York, NY: Springer New York, 2008, pp. 1129–1139 (cit. on p. 27).

[44] V. C. Henríquez and P. M. Juhl. "OpenBEM - An open source Boundary Element Method software in Acoustics." en. In: (2010), p. 10 (cit. on p. 91).

[45] B. Hildebrand. *An Introduction to Acoustical Holography*. en. Springer US, 1972 (cit. on p. 27).

[46] C. Huygens. *Traité de la lumière*. Les maîtres de la pensée scientifique. Gauthier-Villars, 1920 (cit. on p. 26).

[47] Y. F. Hwang, W. K. Bonness, and S. A. Hambric. "Comparison of semi-empirical models for turbulent boundary layer wall pressure spectra." In: *Journal of Sound and Vibration* 319.1 (Jan. 2009), pp. 199–217 (cit. on pp. 18, 19).

[48] Y. Hwang and G. Maidanik. "A wavenumber analysis of the coupling of a structural mode and flow turbulence." en. In: *Journal of Sound and Vibration* 142.1 (Oct. 1990), pp. 135–152 (cit. on p. 16).

Cette thèse est accessible à l'adresse : https://theses.insa-lyon.fr/publication/2022ISAL0077/these.pdf
© [A.D. Pouye], [2022], INSA Lyon, tous droits réservés

[49] *ISO 16283-1:2014, Acoustics — Field measurement of sound insulation in buildings and of building elements — Part 1: Airborne sound insulation*. en. Tech. rep. Geneva, 2014 (cit. on p. 12).

[50] *ISO 354, Acoustics — Measurement of sound absorption in a reverberation room*. Standard. Geneva: International Organization for Standardization, 2003 (cit. on p. 10).

[51] F. Jacobsen and D. t. h. L. f. akustik. *The Diffuse Sound Field: Statistical Considerations Concerning the Reverberant Field in the Steady State*. Lyngby. Technical university of Denmark, Acoustics laboratory. Report. Acoustics Laboratory, Technical University of Denmark, 1979 (cit. on p. 23).

[52] F. Jacobsen and T. Roisin. "The coherence of reverberant sound fields." In: *The Journal of the Acoustical Society of America* 108.1 (June 2000), pp. 204–210 (cit. on p. 11).

[53] A. Klabes, M. Herr, and S. Callsen. "Fuselage Excitation During Cruise Flight Conditions: A New CFD Based Pressure Point Spectra Model." In: *INTER-NOISE and NOISE-CON Congress and Conference Proceedings* 253.7 (Aug. 2016), pp. 1018–1029 (cit. on p. 19).

[54] R. H. Kraichnan. "Pressure Fluctuations in Turbulent Flow over a Flat Plate." In: *The Journal of the Acoustical Society of America* 28.3 (May 1956), pp. 378–390 (cit. on p. 16).

[55] F. G. Lether. "On the construction of Gauss-Legendre quadrature rules." In: *Journal of Computational and Applied Mathematics* 4.1 (Jan. 1978), pp. 47–52. ISSN: 0377-0427 (cit. on p. 171).

[56] W. K. Lui and K. M. Li. "The scattering of sound by a long cylinder above an impedance boundary." en. In: *J. Acoust. Soc. Am.* 127.2 (2010), p. 12 (cit. on p. 88).

[57] C. Marchetto, L. Maxit, O. Robin, and A. Berry. "Vibroacoustic response of panels under diffuse acoustic field excitation from sensitivity functions and reciprocity

Cette thèse est accessible à l'adresse : https://theses.insa-lyon.fr/publication/2022ISAL0077/these.pdf
© [A.D. Pouye], [2022], INSA Lyon, tous droits réservés

principles." In: *The Journal of the Acoustical Society of America* 141.6 (June 2017), pp. 4508–4521 (cit. on pp. xv, 25, 76).

[58] C. Marchetto, L. Maxit, O. Robin, and A. Berry. "Experimental prediction of the vibration response of panels under a turbulent boundary layer excitation from sensitivity functions." In: *The Journal of the Acoustical Society of America* 143.5 (May 2018), pp. 2954–2964 (cit. on pp. xv, 25, 55, 68, 74, 76, 77).

[59] C. Maury, P. Gardonio, and S. J. Elliott. "A Wavenumber Approach to Modelling the Response of a Randomly Excited Panel, Part I: General Theory." In: *Journal of Sound and Vibration* 252.1 (Apr. 2002), pp. 83–113 (cit. on pp. 35, 36, 74).

[60] C. Maury and T. Bravo. "Focussed Synthesis of a Turbulent Boundary Layer Excitation." In: *22nd AIAA/CEAS Aeroacoustics Conference*. Aeroacoustics Conferences (May 2016) (cit. on p. 29).

[61] C. Maury, S. J. Elliott, and P. Gardonio. "Turbulent Boundary-Layer Simulation with an Array of Loudspeakers." In: *AIAA Journal* 42.4 (2004), pp. 706–713 (cit. on p. 28).

[62] C. Maury and T. Bravo. "The experimental synthesis of random pressure fields: Practical feasibility." In: *The Journal of the Acoustical Society of America* 120 (Oct. 2006), pp. 2712–2723 (cit. on pp. 28, 29, 56, 95).

[63] L. Maxit and V. Denis. "Prediction of flow induced sound and vibration of periodically stiffened plates." In: *The Journal of the Acoustical Society of America* 133.1 (Jan. 2013), pp. 146–160 (cit. on p. 36).

[64] J. D. Maynard, E. G. Williams, and Y. Lee. "Nearfield acoustic holography: I. Theory of generalized holography and the development of NAH." In: *The Journal of the Acoustical Society of America* 78.4 (Oct. 1985), pp. 1395–1413 (cit. on p. 28).

[65] R. H. Mellen. "On modeling convective turbulence." In: *The Journal of the Acoustical Society of America* 88.6 (Dec. 1990), pp. 2891–2893 (cit. on pp. 20, 21).

Cette thèse est accessible à l'adresse : https://theses.insa-lyon.fr/publication/2022ISAL0077/these.pdf
© [A.D. Pouye], [2022], INSA Lyon, tous droits réservés

[66] T. S. Miller. "Turbulent boundary layer models for acoustic analysis." PhD thesis. Wichita, Kansas: Wichita State University, 2011 (cit. on p. 21).

[67] H. Nélisse and J. Nicolas. "Characterization of a diffuse field in a reverberant room." In: *The Journal of the Acoustical Society of America* 101.6 (June 1997), pp. 3517–3524 (cit. on p. 11).

[68] R. Oldfield. "The Analysis and Improvement of Focused Source Reproduction with Wave Field Synthesis." PhD thesis. University of Salford, 2013 (cit. on p. 26).

[69] F. K. Owen and A. K. Owen. "Measurement and assessment of wind tunnel flow quality." en. In: *Progress in Aerospace Sciences* 44.5 (July 2008), pp. 315–348 (cit. on p. 24).

[70] L. J. Peltier and S. A. Hambric. "Estimating turbulent-boundary-layer wall-pressure spectra from CFD RANS solutions." en. In: *Journal of Fluids and Structures* 23.6 (Aug. 2007), pp. 920–937 (cit. on p. 17).

[71] Phillips Owen Martin and Taylor Geoffrey Ingram. "On the aerodynamic surface sound from a plane turbulent boundary layer." In: *Proceedings of the Royal Society of London. Series A. Mathematical and Physical Sciences* 234.1198 (Feb. 1956), pp. 327–335 (cit. on p. 16).

[72] A. D. Pierce. *Acoustics: An Introduction to Its Physical Principles and Applications*. en. Acoustical Society of America, 1989 (cit. on pp. 39, 70).

[73] L. Prandtl. "Über Flüssigkeits bewegung bei sehr kleiner Reibung." In: *Verhaldlg III Int. Math. Kong* (1904), pp. 484–491 (cit. on p. 12).

[74] J. E. Robertson. *Prediction of in flight fluctuating pressure environments including protuberance induced flow*. Tech. rep. WR-71-10. Mar. 1971 (cit. on p. 19).

[75] O. Robin, A. Berry, and S. Moreau. "Reproduction of random pressure fields based on planar nearfield acoustic holography." In: *The Journal of the Acoustical Society of America* 133.6 (June 2013), pp. 3885–3899 (cit. on p. 28).

Cette thèse est accessible à l'adresse : https://theses.insa-lyon.fr/publication/2022ISAL0077/these.pdf
© [A.D. Pouye], [2022], INSA Lyon, tous droits réservés

[76] O. Robin, A. Berry, and S. Moreau. "Experimental vibroacoustic testing of plane panels using synthesized random pressure fields." In: *The Journal of the Acoustical Society of America* 135.6 (June 2014), pp. 3434–3445 (cit. on pp. 26, 73).

[77] O. Robin, J.-D. Chazot, R. Boulandet, M. Michau, A. Berry, and N. Atalla. "A Plane and Thin Panel with Representative Simply Supported Boundary Conditions for Laboratory Vibroacoustic Tests." en. In: (Feb. 2016) (cit. on p. 65).

[78] Y. Rozenberg. "Modélisation analytique du bruit aérodynamique à large bande des machines tournantes : utilisation de calculs moyennés de mécanique des fluides (*Analytical modeling of the broadband aerodynamic noise of rotating machines: use of average calculations of fluid mechanics*)." fr. PhD thesis. Ecole Centrale de Lyon, Dec. 2007 (cit. on p. 19).

[79] M. Sanalatii. "Synthèse d'un champ acoustique avec contraste spatial élevé (*Synthesis of an acoustic field with high spatial contrast*)." PhD thesis. Le Mans Université, 2018 (cit. on p. 26).

[80] H. Schlichting (Deceased) and K. Gersten. *Boundary-Layer Theory*. en. Springer, Oct. 2016 (cit. on p. 15).

[81] M. R. Schroeder. "Statistical Parameters of the Frequency Response Curves of Large Rooms." English. In: *Journal of the Audio Engineering Society* 35.5 (May 1987), pp. 299–306 (cit. on p. 23).

[82] M. R. Schroeder. "The "Schroeder frequency" revisited." In: *The Journal of the Acoustical Society of America* 99.5 (May 1996), pp. 3240–3241 (cit. on p. 23).

[83] T. J. Schultz. "Diffusion in reverberation rooms." In: *Journal of Sound and Vibration* 16.1 (May 1971), pp. 17–28. (Visited on 01/28/2019) (cit. on p. 10).

[84] A. F. Seybert and T. W. Wu. "Modified Helmholtz integral equation for bodies sitting on an infinite plane." In: *The Journal of the Acoustical Society of America* 85.1 (Jan. 1989). Publisher: Acoustical Society of America, pp. 19–23 (cit. on p. 84).

Cette thèse est accessible à l'adresse : https://theses.insa-lyon.fr/publication/2022ISAL0077/these.pdf
© [A.D. Pouye], [2022], INSA Lyon, tous droits réservés

[85] E. A. Skelton and J. H. James. *Theoretical Acoustics of Underwater Structures*. en. Published by Imperial College Press and Distributed by World Scientific Publishing Co., Dec. 1997 (cit. on pp. 87–89).

[86] A. V. Smol'Yakov, V. M. Tkachenko, and J. S. Wood. "Model of a field of pseudosonic turbulent wall pressures and experimental data." In: *Soviet physics. Acoustics* 37.6 (1991), pp. 627–631 (cit. on p. 20).

[87] A. V. Smol'yakov and V. M. Tkachenko. *The Measurement of Turbulent Fluctuations: An Introduction to Hot-Wire Anemometry and Related Transducers*. en. Ed. by P. Bradshaw. Berlin Heidelberg: Springer-Verlag, 1983 (cit. on p. 9).

[88] E. W. Start. "Direct Sound Enhancement by Wave Field Synthesis." PhD thesis. Delft University of Technology, 1997 (cit. on pp. 26, 27).

[89] U. M. Stephenson. "Different assumptions - Different reverberation formulae." en. In: *Proceedings of INTERNOISE*. New York, 2012 (cit. on p. 10).

[90] R. Vaicaitis and M. Slazak. "Noise transmission through stiffened panels." In: *Journal of Sound and Vibration* 70 (June 1980). NTRS Author Affiliations: Columbia Univ., Columbia University NTRS Document ID: 19800057523 NTRS Research Center: Legacy CDMS (CDMS) (cit. on p. 35).

[91] E. Verheijen. "Sound Reproduction by Wave Field Synthesis." PhD thesis. Delft University of Technology, 1997 (cit. on p. 26).

[92] P. Vogel. "Application of Wave Field Synthesis in Room Acoustics." PhD thesis. Delft University of Technology, 1993 (cit. on p. 26).

[93] W.-X. WANG. "Expansion of the Green's Funcion in a Cylindrical Coordinate System." In: *Quarterly of Applied Mathematics* 48.3 (1990). Publisher: Brown University, pp. 499–501 (cit. on p. 87).

[94] J. F. Wilby and F. L. Gloyna. "Vibration measurements of an airplane fuselage structure I. Turbulent boundary layer excitation." en. In: *Journal of Sound and Vibration* 23.4 (Aug. 1972), pp. 443–466 (cit. on p. 24).

Cette thèse est accessible à l'adresse : https://theses.insa-lyon.fr/publication/2022ISAL0077/these.pdf
© [A.D. Pouye], [2022], INSA Lyon, tous droits réservés

[95] C. A. Wiley. "Pulsed Doppler Radar Methods and Apparatus." Pat. 3196436. 1965 (cit. on p. 33).

[96] E. G. Williams and J. D. Maynard. "Holographic Imaging without the Wavelength Resolution Limit." In: *Physical Review Letters* 45.7 (Aug. 1980), pp. 554–557 (cit. on p. 28).

[97] W. W. Willmarth and F. W. Roos. "Resolution and structure of the wall pressure field beneath a turbulent boundary layer." en. In: *Journal of Fluid Mechanics* 22.1 (May 1965). Publisher: Cambridge University Press, pp. 81–94 (cit. on p. 19).

[98] W. W. Willmarth and C. E. Wooldridge. "Measurements of the fluctuating pressure at the wall beneath a thick turbulent boundary layer." en. In: *Journal of Fluid Mechanics* 14.2 (Oct. 1962), pp. 187–210 (cit. on pp. 19, 24).

[99] L. Yeh. "High intensity acoustic testing to determine structural fatigue life and to improve reliability in nuclear reactor and aerospace structures." en. In: *Materials Science and Engineering* 48.2 (May 1981), pp. 167–179 (cit. on p. 22).

Cette thèse est accessible à l'adresse : https://theses.insa-lyon.fr/publication/2022ISAL0077/these.pdf
© [A.D. Pouye], [2022], INSA Lyon, tous droits réservés

FOLIO ADMINISTRATIF

THESE DE L'INSA LYON, MEMBRE DE L'UNIVERSITE DE LYON

NOM : POUYE DATE de SOUTENANCE : 22/09/2022

Prénoms : Augustin Djibane

TITRE : Optimisation de réseaux de sources pour la synthèse de champs de pression aléatoire pour la reproduction de la réponse vibroacoustique de structures

NATURE : Doctorat Numéro d'ordre : 2022LYSEI0077

Ecole doctorale : MEGA

Spécialité : Acoustique

RESUME : La reproduction des réponses vibratoires et acoustiques de structures sous excitations aléatoires telles que le champ acoustique diffus ou la couche limite turbulente intéresse particulièrement le monde de la recherche et l'industrie des transports. La caractérisation de structures sous ces types d'excitations nécessite de réaliser des mesures in-situ ou d'utiliser des moyens d'essais tels que les souffleries anéchoïques ou les salles réverbérantes, qui sont des méthodes complexes et coûteuses. La nécessité de trouver des méthodes alternatives simples, rentables et reproductibles, devient évidente sous les considérations précédentes. Dans cette thèse, une méthode alternative appelée la méthode de balayage de source ou Source Scanning Technique (en anglais) est présentée. Le premier objectif est d'évaluer la validité de la technique proposée en comparant ses résultats avec des résultats numériques et expérimentaux pour des structures simples telles que les panneaux plans. Pour ce faire, une étude de cas d'un panneau en aluminium en appuis simples et soumis à une des excitations aléatoires est considérée. La réponse expérimentale vibratoire du panneau ainsi que la perte en transmission sont comparées aux résultats théoriques d'une part. D'autre part, ces mêmes résultats obtenus avec la méthode de balayage de source sont comparés aux résultats obtenus avec des mesures directes en salle réverbérante et en soufflerie. Ensuite, il s'agit d'étendre la méthode à des structures plus complexes telles que les panneaux courbes. Après avoir effectué des études théoriques et numériques et défini un montage expérimental pour l'application de la méthode à des panneaux courbes, les fonctions de transfert sont validées expérimentalement en comparant les mesures aux solutions analytiques. La comparaison montre un très bon accord entre les deux types de résultats. Une implémentation expérimentale de la technique de balayage de source est faite pour le cas bidimensionnel et les résultats montrent des applications prometteuses de la méthode pour les structures courbes convexes.

MOTS-CLÉS : Couche Limite Turbulente – Champ Acoustique Diffus – Vibroacoustique – Transparence Acoustique – Synthèse de champs de pression – Méthode de balayage de source – Panneaux Rectangulaires Plans – Panneaux Rectangulaires Courbes – Source monopolaire

Laboratoire (s) de recherche : Laboratoire Vibrations-Acoustique (INSA Lyon), Laboratoire de Mécanique et d'Acoustique (CNRS Marseille)

Directeur de thèse : Laurent MAXIT

Président de jury : Manuel MELON

Composition du jury : Elena CIAPPI (rapportrice), Sergio DE ROSA (rapporteur), Mahmoud KARIMI (examinateur), Cédric MAURY (co-directeur de thèse), Laurent MAXIT (directeur de thèse), Manuel MELON (examinateur)

Cette thèse est accessible à l'adresse : https://theses.insa-lyon.fr/publication/2022ISAL0077/these.pdf
© [A.D. Pouye], [2022], INSA Lyon, tous droits réservés